UNIVERSITÀ DEGLI STUDI DI NAPOLI FEDERICO II

SCUOLA POLITECNICA E DELLE SCIENZE DI BASE

Department of Chemical, Materials and Industrial Process Engineering

Electric field-assisted flame synthesis of Carbon Nanoparticle films

Arianna Parisi

Tutor
Prof. Francesco Di Natale

Scientific Committee
Prof. Andrea D’Anna
Prof. Amedeo Lancia
Prof. Claudia Carotenuto

A thesis presented for the degree of Doctor of Philosophy in Industrial Product and Process Engineering

XXXV Cycle- 2023

PhD Candidate:

Arianna Parisi, PhD program in Industrial Product and Process Engineering, XXXV cycle

Tutor:

Prof. Francesco Di Natale

Scientific Committee:

Prof. Andrea D'Anna

Prof. Amedeo Lancia

Prof. Claudia Carotenuto

PhD Program Coordinator:

Prof. Andrea D'Anna

The PhD thesis has been revised by:

- Prof. Anatol Jaworek, Institute of Fluid Flow Machinery, Polish Academy of Sciences (Warsaw).
- Prof. Luis Modesto, Ingeniería Aeroespacial y Mecánica de Fluidos, Universidad de Sevilla (Sevilla).

Abstract

In the last years, the scientific discovery of the many special features of nanoparticles has driven the research toward the production of carbon nanoparticles (CNPs) as promising solutions in the field of bioimaging, nanomedicine, catalysis and energy storage applications, with some advantages compared to the conventional carbon-based materials, such as candle soot and carbon black. The easiest way to produce CNPs is the flame synthesis with carbon-to-oxygen ratios slightly higher than the stoichiometric one. In this process, the deposition mechanism – known as thermophoresis – is very slow, and gives rise to high porosity, low-density deposits of agglomerates composed of the pristine CNPs found in the flame at the harvesting position of the substrate. These films are characterized by low mechanical resistance and low temperature-dependent conductivity which limit their direct application. However, the primary CNPs particles can be easily detached from the support and suspended in liquids or other means, since they are deposited in the form of unstable agglomerates.

The longstanding experience in the field of particle filtration by electrostatic forces suggested that the superimposition of an electric field to the flame may fasten the deposition rate of CNPs during flame harvesting, improving the process efficiency. The new process, named Electric field-assisted flame synthesis, is the topic of this PhD thesis. In this research work, a mathematical model has been developed to investigate the dynamics of particle deposition under the effect of the electric field. The model reveals that, compared to the conventional thermophoretic deposition, the electric field-assisted flame synthesis has a faster deposition rate, preferentially capturing particles larger than 5 nm, and producing more compact films.

The experimental results provide an extensive and brand-new set of data on the characteristics of aged CNP films and agglomerates that can be formed: UV-vis Absorption and Raman spectroscopy, Atomic Force Microscopy, Size Exclusion

Chromatography, Surface Texture Analysis, Contact Angle and Current Voltage Measurements have been used to highlight the similitudes and the differences between thermophoretic and electric field-assisted CNP films. The results confirm the increased harvesting rate and the selective deposition of non-fluorescent CNPs larger than 5 nm. The film morphology is irregular with large mesoscopic structures, the deposits have higher compactness and stability. Finally, the experiments indicate that the hydrophilic character of the thermophoretic deposits is preserved in the electric field-assisted flame synthesis deposits, despite their larger roughness and graphitic behaviour, and the higher and temperature-independent electrical conductivity.

In conclusion, electric field-assisted flame synthesis emerges as a technology able to overcome the limits of conventional flame synthesis methods and to add a new degree of freedom in synthesising nanoparticles and thin films with new and tunable properties, that can be proficiently used to produce electrodes for fuel cells and hydrolysers, as heat exchange surfaces for reboilers, as scaffolds for active phases, and as noble metal catalysts.

Keywords: Carbon Nanoparticles, Flame Synthesis, Electrophoresis, Thin film deposition.

Summary

List of Symbols and Abbreviations

A_f	Top surface area of the film
A_i	Area occupied by a single CNP
A_s	Mica Substrate area
$Abs(\lambda)$	Absorbance at a specific wavelength
AC	Alternating current
AFM	Atomic Force Microscopy
C_c	Cunningham correction factor
CA	Contact Angle
CNP	Carbon nanoparticle
C/O	Carbon to oxygen ratio
$c_{p,g}$	Gas specific heat capacity at constant pressure
DC	Direct current
D_i/D	CNP diffusivity
d_p/d_{pi}	CNP diameter
E	Young's Modulus
$\mathbf{E}$	Electric field vector
E_g	Optical band gap energy
E_i	Natural electric field in a premixed flame
E_L	Energy of an incident photon
$E(m)$	Function of the refractive index of soot

e	elementary charge
f	Peclet number distribution
f_v	Soot volume fraction
f_w	Peclet number distribution weighted considering the CNPs mass distribution
$\boldsymbol{F}_B$	Brownian excitation amplitude
$\boldsymbol{F}_D$	Friction force on a spherical CNP
$\boldsymbol{F}_{DEP}$	Dielectrophoretic force for uncharged CNP
$\boldsymbol{F}_E$	Electrostatic force for charged CNP
$\boldsymbol{F}_i$	Interaction forces
$\boldsymbol{F}_G$	Gravity and buoyancy body force
$\boldsymbol{F}_T$	Thermophoretic force
$\boldsymbol{F}_t$	Tangential component of the friction forces to the CNP against the tangential component of velocity
$\boldsymbol{f}_{CM}$	Clausius-Mossotti factor
G	Electrical conductance
$\boldsymbol{g}$	Gravitational acceleration
H	Film Hardness
h	Distance between the burner mouth and the stabilizing plate
hv	Photon energy: product between the Planck's constant and the frequency of an incident light
HAB	Height above the burner
H/C	Hydrogen to carbon ratio

HIM	Helium Ion Microscope
HR-AFM	High-Resolution Atomic Force Microscopy
HRTEM	High-Resolution Transmission Electron Microscope
HV	High Voltage
I	Current
I_m	Moment of inertia
I-V	Current-Voltage
$\underline{\boldsymbol{I}}$	Identity tensor
I(D)	Intensity of the D peak in a Raman Spectrum
I(G)	Intensity of the G peak in a Raman Spectrum
k	Thermal conductivity
$k(\lambda)$	Extinction coefficient for homogeneous sample
k_B	Boltzmann constant
$k_g(\lambda)$	Extinction coefficient for air in porous medium
k_r	Exponent for the photon energy
$k_s(\lambda)$	Extinction coefficient for solid material in porous medium
L	Microelectrode length
L_a	In-plane crystallite size
$\boldsymbol{M}$	Net torque
m	Mass of a single CNP
m_f	Measured weight of the film

MOSFET	Metal-Oxide-Semiconductors field-effect transistor theory
$\boldsymbol{M}_F$	Resulting momenta related to the external long-range field
$\boldsymbol{M}_i$	Resulting torque acting between pair of CNPs
$\boldsymbol{M}_r$	Rolling friction force acting against the angular velocity
$N_{in,i}$	Number of injected CNPs
N_{i0}	Number of inlet CNPs in the real flame
N_{ins}	Number of insertions in flame
$N_{out,i}$	Number of harvested CNPs
N_p	Particle number concentration in flame
$\boldsymbol{n}$	Outward surface normal unit vector
n_-	Number density of negative ions
n_+	Number density of positive ions
P	Pressure
P_0	Incident radiant power through the sample
$P(\lambda)$	Transmitted radiant power through the sample
Pe_i	Peclet dimensionless number of each CNP
PL	Photoluminescence
p_{out}	Pressure outside the domain
PSD	Particles sized distribution
q	Total charged carried by a CNP
q_r	Heat flux by radiation

Q_{gen}	Heat sources other than viscous dissipation
$\mathrm{Re}(f_{CM})$	Real part of the Clausius-Mossotti factor
$\boldsymbol{R}_p$	Radius vector
S_a	Average roughness
S_{ku}	Kurtosis
S_p	Maximum heigh of peaks
S_q	Root mean square roughness
S_{sk}	Skewness
SEC	Size exclusion chromatography
SEM	Scanning Electron Microscopy
SMPS	Scanning Mobility Particles Sizer
T	Absolute Temperature
TFD	Thermophoretic Deposition
t_{ins}	Insertion time- time for a single insertion
t_p	Starting time for the experiment
$\boldsymbol{U}$	Relative CNP velocity
UV-Vis	Ultraviolet-light
$\boldsymbol{u}$	Flame velocity vector
$\boldsymbol{u}_{\mathrm{inlet}}$	Normal inflow inlet velocity vector
$\boldsymbol{u}_{\mathrm{wall}}$	Flame velocity vector on the physical walls of the domain
V	Electric potential

V_C	Critical value for electric potential
V_i	Intrinsic electric potential in a flame
V_0	Electric potential applied to the deposition substrate
V_b	Electric potential at the burner exit
V_p	Electric potential at the stabilization plate
v_i	CNP impact velocity modulus
v_{th}	Thermophoretic velocity
W	Microelectrode width
WE	Working Electrodes
z	Distance from the deposition surface
Z_{max}	Maximum value for the peak height
Z_{min}	Minimum value for the peak height
$\alpha(\lambda)$	Absorption coefficient for a specific wavelength
Δt	Time-step for integration of the equation for particle motion
δ	Optical thickness of the homogeneous sample
δ_{AFM}	Film thickness from AFM images
δ_{Abs} (δ_{eq})	Optical equivalent film thickness from UV-vis Absorption
δ_f	Film thickness determined by SEM
δ_g	Optical thickness of air in porous medium
δ_s	Optical thickness of solid in porous medium
Φ	Equivalence ratio

φ_{AFM}	Experimental degree of coverage obtained by AFM
φ_{sim}	Simulation degree of coverage
ε	Film packing density
ε_m	Medium (flame) permittivity
ε_p	CNP permittivity
ε^*_m	Complex permittivity for the flame
ε^*_p	Complex permittivity for CNP
θ	Young's contact angle
θ_{ap}	Apparent contact angle
λ	Fluid mean free path or wavelength
λ_l	Boundary layer for a laminar flame impinging on a flat plate
μ_i^-	Mobility of negative ionic species
μ_i^+	Mobility of positive ionic species
∇	Nabla operator
∇T	Temperature gradient
$\nabla \boldsymbol{V}$	Electric potential gradient
$\nabla \boldsymbol{u}$	Velocity gradient tensor
$\nabla \boldsymbol{u}^{\boldsymbol{T}}$	Transposed velocity gradient tensor
$\nabla \cdot \boldsymbol{u}$	Divergence of the velocity vector
ξ	Film growth rate
ξ_i	Collisional probability

ρ_g	Gas mass density
ρ_p	Particle density
ρ_{sc}	Net space charge density
σ	CNP electrical conductivity
σ_m	Flame electrical conductivity
ω	CNP Angular velocity
ω_e	Angular frequency of the electric filed
ζ	Zero-mean, unit-variance independent Gaussian random vector number

List of Figures

Chapter 1

Chapter 2

Chapter 3

Chapter 4

List of Tables

Chapter 1

Chapter 2

Chapter 3

Chapter 4

Chapter 5

Introduction

Carbon black is a fascinating material that has piqued the interest of people interested in its technology and applications and inspired a huge number of fundamental inquiries in scientific laboratories of universities and research institutes across the world. It can be ranked as being of the oldest manufactured products since its usage as a pigment in black ink refers to the third century B.C. [1]. Its industrial application dates back to the fifteenth century when the printed book became the most important means of communicating information. However, the most important event which was to have the greatest influence on the industrial utilization of carbon black occurred at the turn of the century and involved the discovery of the reinforcing effect of carbon black when added to natural rubber, a discovery that was destined to become the most significant milestone in the rubber and automotive industry [2–4]. Its proven effectiveness in various industrial applications is attributed to its nano-sized dimensions, large specific areas, chemical stability, mechanical strength, reasonable cost, good electrical conductivity and superhydrophobic proprieties [5,6]. All these proprieties depend on the morphology of aggregates and their microstructure. It essentially consists of elemental carbon fractal aggregates that can be larger than 500 nm in the form of nearly spherical particles, with sizes going from 10 to 40 nm, and is obtained by incomplete combustion of hydrocarbons [7]. In the last years, the scientific discovery of the many special features of nanoparticles has driven research toward the production of carbon nanoparticles, CNPs. According to the latest definition of the Commission of the European Union in 2011, a nanoparticle is defined as “a natural, incidental or manufactured material containing particles, in an unbound state or as an aggregate or as an agglomerate and where, for 50% or more of the particles in the number size distribution, one or more external dimensions are in the size ranges 1 nm-100 nm” [8]. CNPs can be manufactured following a top-bottom approach, namely starting from carbon black particles that are processed using different treatments in order to reduce their size to the nanoscale [9,10]. However, combustion science and technology provide sufficient know-how and facilities to produce CNPs with virtually tunable size and properties using a more efficient and green bottom-up approach: using a gaseous fuel with low molecular weight to sustain a highly controlled flame condition, and with accurate positioning and geometry of the CNP collector inside the flame, it is possible to drive the chemical processes that regulate the formation of aromatic structures, and tunable size and properties [11–17]. Furthermore, the process includes a highly efficient combustion process with minimal creation of harmful by-products and energy production. This bottom-up approach is known as flame synthesis. This process is based on the use of thermophoretic forces to deposit particles on a cold substrate immersed in the flame [18–20]. However, most of the research available in the pertinent literature is based on the production of inorganic films [21–25] and its application to CNPs is the subject of few studies, most of which were carried out by the Clean Combustion Research Lab in Naples [26,27]. By working at carbon-to-oxygen ratios in flame slightly higher than stoichiometric one (C/O=0.33 ethylene-air flames), or placing the collector at a very low distance above the burner, it is possible to produce CNPs having sizes close to 10-20 nm, that are very similar to the primary particles obtained from carbon black but have a higher oxygen content that makes them more hydrophilic, a unique property that can be used for specific surface coatings for heat exchangers, antifouling surfaces and specific water sensors [28,29]. However, in this flame, both the particle concentration and the thermophoretic deposition rate are low, undermining the process productivity.

The longstanding experience in the field of particle filtration by electrostatic forces [30–32] suggested that the presence of an electric field to the flame - a plasma characterized by the presence of positive ions, electrons and charged particles - can fasten the deposition rate of CNPs overcoming the limitations of conventional thermophoretic flame synthesis [33,34]. This new process, named Electric field-assisted flame synthesis, is the topic of this PhD work.

This is part of the PRIN 2017 MAGIC DUST project funded by the Italian Ministry of the University and the Research, which is devoted to the production of new CNPs with improved technological properties and to a better understanding of the physical and chemical mechanisms underpinning this process. The PhD project has been carried out in cooperation with the Clean Combustion Research Lab of Naples (University Federico II and CNR STEMS laboratories in Naples) and with the Rheology Lab of the Department of Engineering of the University of Campania. This work aims to improve the state of the art concerning the electric field-assisted flame synthesis applied to the production of CNPs in a slightly sooting C/O ethylene air flame, by performing selected experimental tests and presenting a mathematical model for particle collection which may guide the comprehension of the mechanisms underpinning the process.

The following graphical abstract summarizes the main objectives achieved in this PhD thesis project.

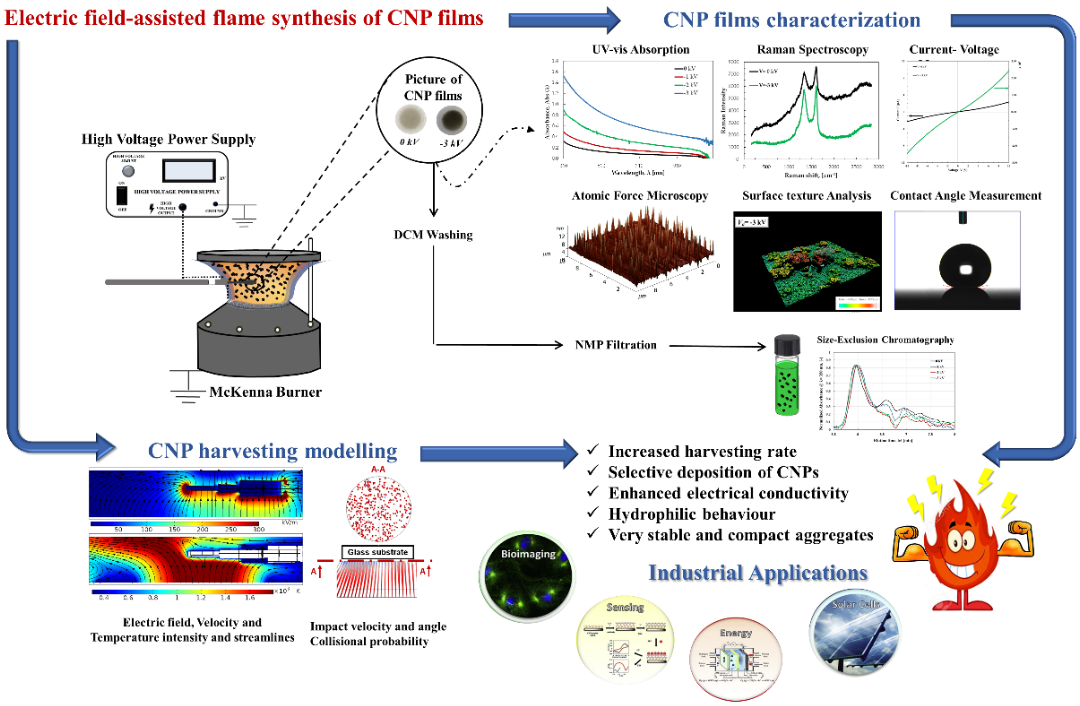

This PhD thesis is divided into five chapters.

Chapter 1 resumes the State-of-Art on the electric field-assisted flame synthesis of Carbon NanoParticle (CNP) films. In particular, the fundamentals and some experimental evidence on the thermophoretic flame synthesis of CNP films are reported. Then, the effects of the presence of external electric fields on flame behaviour and CNPs formation are discussed. Some experimental results based on inorganic nanoparticle films in terms of enhanced deposition rate and film properties are reviewed. The literature analysis suggests that CNP production by electric field-assisted flame synthesis is still an unexplored process, which justifies the need to address this topic in this PhD thesis work.

Chapter 2 contains two sections. Firstly, the experimental setup and procedures used to produce CNP films by electric field-assisted flame synthesis are described. Secondly, the ex-situ analytical techniques adopted for the morphological, chemical, structural, electrical, and surface-wetting characterization of the produced CNP films are discussed in detail. In particular, UV-vis Absorption and Raman Spectroscopy, Atomic Force Microscopy, Size Exclusion Chromatography, Surface Texture Analysis, Contact Angle and Current-Voltage Measurement techniques are described, underlying all the information that can be obtained by each of them.

Chapter 3 reports a numerical model based on momentum balance on single CNPs and on a simplified model for the flame environment, which has been validated against dedicated experimental data, and provides several insights into the physical mechanisms governing the electric field-assisted flame synthesis of CNPs.

Chapter 4 resumes the results of the experimental campaign using the different analytical techniques described in **Chapter 2**. In particular, the morphological, physicochemical, structural, electrical and wettability properties of CNP films produced by electric field-assisted flame synthesis are reported and critically commented, also in light of the particle collision modelling, providing an overview of the main features of the new process and showing the potential industrial applications of these CNP films.

Lastly, **Chapter 5** resumes the final remarks, the outcomes and the future perspective for this PhD Thesis work.

References

[1] Donnet J-B, Bansal RC, Wang M-J. Carbon black : science and technology. Dekker; 1993.

[2] Kim YS, Ha SC, Yang Y, Kim YJ, Cho SM, Yang H, et al. Portable electronic nose system based on the carbon black-polymer composite sensor array. Sens Actuators B Chem, vol. 108, 2005, p. 285–91. https://doi.org/10.1016/j.snb.2004.11.067.

[3] Pantea D, Darmstadt H, Kaliaguine S, Roy C. Electrical conductivity of conductive carbon blacks: Influence of surface chemistry and topology. Appl Surf Sci 2003;217:181–93. https://doi.org/10.1016/S0169-4332(03)00550-6.

[4] Saini D, Gunture N, Kaushik J, Aggarwal R, Tripathi KM, Sonkar SK. Carbon Nanomaterials Derived from Black Carbon Soot: A Review of Materials and Applications. ACS Appl Nano Mater 2021;4:12825–44. https://doi.org/10.1021/acsanm.1c02840.

[5] Kumar R, Joanni E, Singh RK, Singh DP, Moshkalev SA. Recent advances in the synthesis and modification of carbon-based 2D materials for application in energy conversion and storage. Prog Energy Combust Sci 2018;67:115–57. https://doi.org/10.1016/j.pecs.2018.03.001.

[6] Xie P, Yuan W, Liu X, Peng Y, Yin Y, Li Y, et al. Advanced carbon nanomaterials for state-of-the-art flexible supercapacitors. Energy Storage Mater 2021;36:56–76. https://doi.org/10.1016/j.ensm.2020.12.011.

[7] Lahaye J, Prado G. Morphology and Internal structure of soot and carbon blacks. In: Siegla DC, editor. Particulate Carbon. Springer Science, 1981.

[8] Potocnik J. Official Journal of the European Union. 2011.

[9] Lian W, Song H, Chen X, Li L, Huo J, Zhao M, et al. The transformation of acetylene black into onion-like hollow carbon nanoparticles at 1000 °C using an iron catalyst. Carbon N Y 2008;46:525–30. https://doi.org/10.1016/j.carbon.2007.12.024.

[10] Hu S, Dong Y, Yang J, Liu J, Cao S. Simultaneous synthesis of luminescent carbon nanoparticles and carbon nanocages by laser ablation of carbon black suspension and their optical limiting properties. J Mater Chem 2012;22:1957–61. https://doi.org/10.1039/c1jm14510j.

[11] Kammler HK, Mädler L, Pratsinis SE. Flame synthesis of nanoparticles. Chem Eng Technol 2001;24:583–96. https://doi.org/10.1002/1521-4125(200106)24:6<583::AID-CEAT583>3.0.CO;2-H.

[12] Sirignano M, Russo C, Ciajolo A. One-step synthesis of carbon nanoparticles and yellow to blue fluorescent nanocarbons in flame reactors. Carbon N Y 2020;156:370–7. https://doi.org/10.1016/j.carbon.2019.09.068.

[13] Martin JW, Salamanca M, Kraft M. Soot inception: Carbonaceous nanoparticle formation in flames: Soot inception. Prog Energy Combust Sci 2022;88. https://doi.org/10.1016/j.pecs.2021.100956.

[14] Minutolo P, Commodo M, D'Anna A. Optical properties of incipient soot. Proceedings of the Combustion Institute 2022. https://doi.org/10.1016/j.proci.2022.09.019.

[15] De Falco G, Commodo M, Minutolo P, D'Anna A. Flame-formed carbon nanoparticles: Morphology, interaction forces, and hamaker constant from AFM. Aerosol Science and Technology 2015;49:281–9. https://doi.org/10.1080/02786826.2015.1022634.

[16] Commodo M, De Falco G, Minutolo P, D'Anna A. Structure and size of soot nanoparticles in laminar premixed flames at different equivalence ratios. Fuel 2018;216:456–62. https://doi.org/10.1016/j.fuel.2017.12.032.

[17] Commodo M, De Falco G, Bruno A, Borriello C, Minutolo P, D'Anna A. Physicochemical evolution of nascent soot particles in a laminar premixed flame: From nucleation to early growth. Combust Flame 2015;162:3854–63. https://doi.org/10.1016/j.combustflame.2015.07.022.

[18] Zheng F. Thermophoresis of spherical and non-spherical particles: a review of theories and experiments. Adv Colloid Interface Sci 2002;97:255–78.

[19] Dobbins RA, Megaridis CM. Morphology of flame generated soot as determined by thermophoretic sampling. Langmuir American Chemical Society 1987;3:254–9.

[20] Russo C, Apicella B, Tregrossi A, Oliano MM, Ciajolo A. Thermophoretic sampling of large PAH (C ≥ 22–24) formed in flames. Fuel 2020;263. https://doi.org/10.1016/j.fuel.2019.116722.

[21] Primo A, Corma A, García H. Titania supported gold nanoparticles as photocatalyst. Physical Chemistry Chemical Physics 2011;13:886–910. https://doi.org/10.1039/c0cp00917b.

[22] De Falco G, Porta A, Petrone AM, del Gaudio P, el Hassanin A, Commodo M, et al. Antimicrobial activity of flame-synthesized nano-TiO2 coatings. Environ Sci Nano 2017;4:1095–107. https://doi.org/10.1039/c7en00030h.

[23] Tolmachoff ED, Abid AD, Phares DJ, Campbell CS, Wang H. Synthesis of nano-phase TiO2 crystalline films over premixed stagnation flames. Proceedings of the Combustion Institute 2009;32 II:1839–45. https://doi.org/10.1016/j.proci.2008.06.052.

[24] Zhang Y, Shuiqing L, Deng S, Yao Q, Tse SD. Direct synthesis of nanostructured TiO2 films with controlled morphologies by stagnation swirl flames. J Aerosol Sci 2012;44:71–82. https://doi.org/10.1016/j.jaerosci.2011.10.001.

[25] Vemury S, Pratsinis SE, Kibbey L. Electrically controlled flame synthesis of nanophase TiO2 , SiO2 , and SnO2 powders. J Mater Res 1997;12:1031–42.

[26] De Falco G, Commodo M, Barra M, Chiarella F, D'Anna A, Aloisio A, et al. Electrical characterization of flame-soot nanoparticle thin films. Synth Met 2017;229:89–99. https://doi.org/10.1016/j.synthmet.2017.05.008.

[27] De Falco G, Carbone F, Commodo M, Minutolo P, D'Anna A. Exploring nanomechanical properties of soot particle layers by atomic force microscopy nanoindentation. Applied Sciences (Switzerland) 2021;11. https://doi.org/10.3390/app11188448.

[28] Ahmad D, van den Boogaert I, Miller J, Presswell R, Jouhara H. Hydrophilic and hydrophobic materials and their applications. Energy Sources, Part A: Recovery, Utilization and Environmental Effects 2018;40:2686–725. https://doi.org/10.1080/15567036.2018.1511642.

[29] Tokudome Y, Nakane K, Takahashi M. Mesostructured carbon film with morphology-induced hydrophilic surface through a dewetting-free coating process. Carbon N Y 2014;77:1104–10. https://doi.org/10.1016/j.carbon.2014.06.028.

[30] Jaworek A, Marchewicz A, Sobczyk AT, Krupa A, Czech T. Two-stage electrostatic precipitators for the reduction of PM2.5 particle emission. Prog Energy Combust Sci 2018;67:206–33. https://doi.org/10.1016/j.pecs.2018.03.003.

[31] Jaworek A, Sobczyk AT, Krupa A, Marchewicz A, Czech T, Śliwiński L. Hybrid electrostatic filtration systems for fly ash particles emission control. A review. Sep Purif Technol 2019;213:283–302. https://doi.org/10.1016/j.seppur.2018.12.011.

[32] Di Natale F, Carotenuto C, Parisi A, Flagiello D, Lancia A. Wet electrostatic scrubbing for flue gas treatment. Fuel 2022;325. https://doi.org/10.1016/j.fuel.2022.124888.

[33] Calcote HF. Ion and electron profiles in flames. Symposium (International) on Combustion 1963;9:622–37.

[34] Calcote HF, Pease RN. Electrical properties of flames. Burner Flames in Longitudinal Electric Fields. Ind Eng Chem 2021;18:2726–31.

Chapter 1

Electric field-assisted flame synthesis of CNP films: State-of-art

This chapter resumes the State-of-art on the electric field-assisted flame synthesis of Carbon NanoParticle (CNP) films. First, the fundamentals and some experimental evidence on the flame synthesis of CNP films are reported. Then, the effects of external electric fields on flame behaviour are discussed. In a third section, the effects of external electric fields on CNPs formation in flame and the possibility of enhancing the deposition rate and modifying the film properties are discussed, focusing on experimental results based on inorganic nanoparticle films. Finally, the motivations behind this PhD thesis work are reported.

Contents

1.1 Flame Synthesis of Functional Carbon Nanoparticle films: fundamentals and experimental evidence

The rise of nanoscience and nanotechnology has opened up new horizons to scientists and engineers. In this field, carbon nanomaterials are considered the cornerstone of numerous investigations. Among various carbon nanostructures, Carbon NanoParticles (CNPs) have attracted a great deal of attention during the past few years because of their good electrical conductivity, high chemical and thermal stability and low toxicity. Based on these unique features along with their interesting optical behaviour, their exploitation is increasing in various applications, such as flexible/stretchable sensors for wearable electronics [1,2], energy storage [3–5], sensors [6,7], and smart biotechnology [8–11]. Moreover, their fascinating electrochemical properties including high effective surface area, excellent electrical conductivity, electrocatalytic activity as well as high porosity and adsorption capability, turn them into potential candidates for electrochemical purposes, particularly sensing [12,13]. It is worth mentioning the ever-increasing demand for lightweight and high-strength metals in various engineering sectors: CNPs are used as reinforcement materials, being helpful in enhancing various mechanical properties like ultimate tensile strength, yield strength and Young's modulus [14–16]. Recently, it has also become very interesting to use flame-formed Carbon Nanoparticles for the fabrication of coatings with enhanced properties. These films could be very useful as coatings for cylinders and valves in internal combustion engines which use soot-contaminated oil and lubricants and they could be applied also for designing diesel particulate filters and their regeneration processes [17–20]. Finally, it has been shown that CNPs are suitable for the preparation of nature-inspired superhydrophobic anti-icing, self-cleaning, strain-free smart coatings [12,21,22].

Flame synthesis is a low-cost continuous process with high-throughput production, fast processing time and proven scalability [23–28]. It makes use of in situ energy source provided by the exothermic combustion reactions, it has short production times, and CNPs with complex surface functionalization can be produced very cheaply and with low environmental impacts [29–32]. These features make flame synthesis one of the most advantageous methods for the manufacture of commercial quantities of CNPs compared to wet chemistry and other gas-phase processes [23,29,33–37]. Despite several investigations on chemical and physical processes involved in the combustion phenomena, the generation of carbonaceous particles in hydrocarbon flames has remained an unsolved, fascinating subject for many years. It has only been in the last decade, however, that experimental and computational techniques in combustion science have been able to reveal insights into the earliest formation mechanisms of carbonaceous particles in a flame [38,39]. Overall, carbonaceous particle formation proceeds continuously from gas-phase hydrocarbon molecules to carbonized, aggregated soot particles. Because of the vast number of molecular changes in this process, the overall process is described in terms of a series of simplified stages, namely inception (or precursor formation), fine-structure evolution growth with nanoparticle formation, primary particles formation by agglomeration, and aggregate formation (*see* **Figure 1.1**). There is no sharp transition between these stages and their relative importance depends on local combustion conditions (*i.e.* equivalence ratio, temperature, time, and pressure), as well as on the specific associated controlling chemistry.

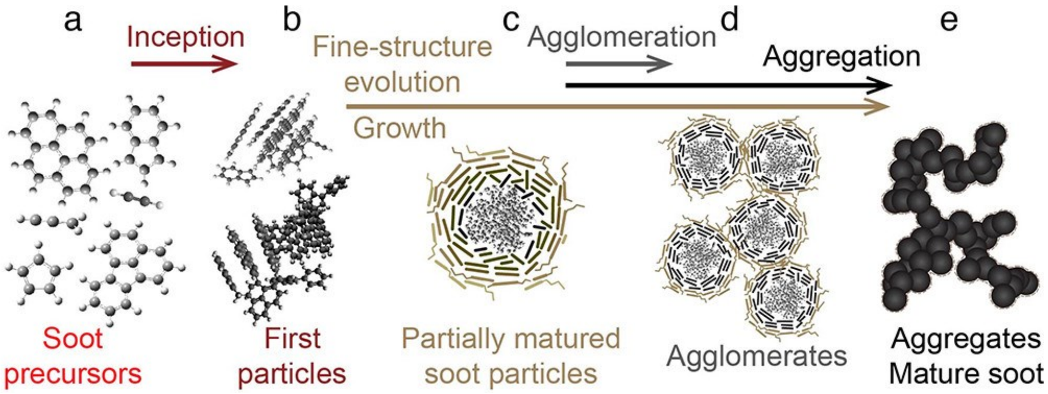

Figure 1.1. Simplified evolution steps from gas-phase hydrocarbon molecules to mature soot aggregates, adapted from Michelsen et al. [39].

Modelling and experimental activities have demonstrated that in fuel-rich flame conditions particles are formed in a bimodal distribution and thus can be distinguished into two main classes: organic carbon nanoparticles and soot particles with sizes in the range of 1-10 nm and 10-100 nm, respectively [40–49]. By changing the process conditions in terms of flame temperature, carbon-to-oxygen ratio (C/O) and particle residence time (namely the distance from the burner mouth, HAB), different relative amounts of organic nanoparticles and soot particles can be obtained. In particular, an increase in the proportion of soot particles with respect to nanoparticles is observed when one or more of these parameters increase.

For example, **Figure 1.2** shows particle size distributions in number and volume for premixed ethylene/air flames varying the C/O ratio and the distance from the burner mouth (HAB).

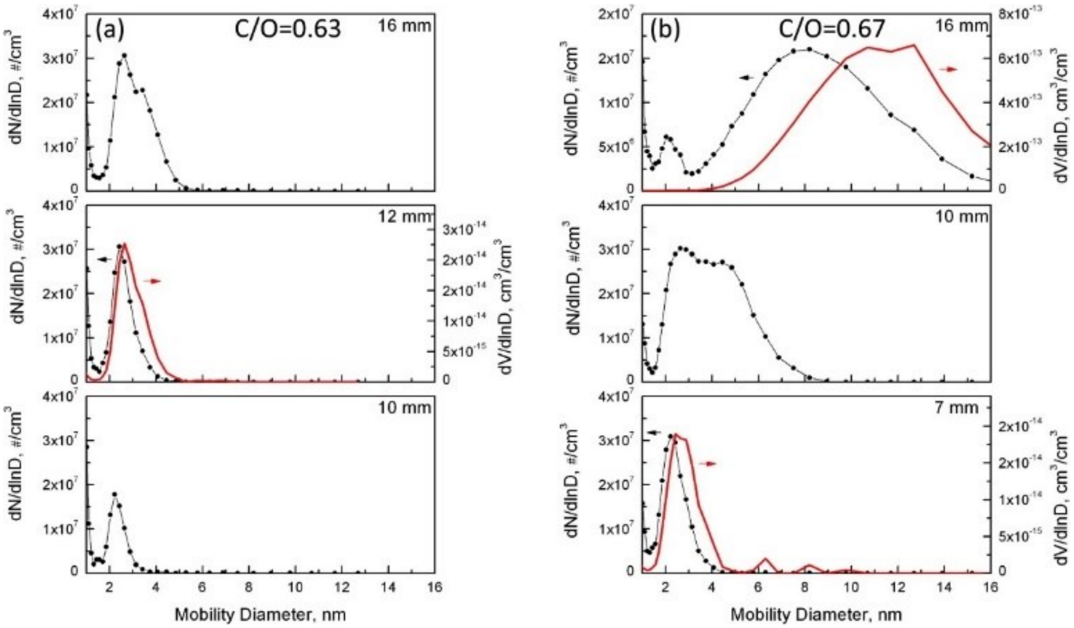

Figure 1.2. Particle size distributions in number (black line with symbols) and in volume (red line) for (a) C/O=0.63, HAB=10,12,16 mm and (b) C/O=0.67, HAB=7, 10, 16 mm, adapted from Commodo et al. [41].

These two classes are characterized by different sizes, chemical structures, morphology, optical and spectroscopic behaviours [42,50–52].

Early nucleated carbon nanoparticles are formed starting from large polyaromatic molecules (PAHs) through van der Waals forces and chemical cross-linking. These molecular constituents have been recently visualized by high-resolution atomic force microscopy [44]. These particles are about 2-4 nm in size. They are molecular-like species, composed of sp^2 carbon arranged in small aromatic islands with a bandgap of 1.5-2 eV, and a hydrogen/carbon ratio ranging from 0.5 to 1. Due to their chemical composition and morphological arrangement, these particles are partially soluble in water, and soluble in some organic solvents, such as dichloromethane. They absorb radiation predominantly in the ultraviolet range and emit fluorescence signals in the range of 300-900 nm [41,53]. Particularly relevant is that experiments have revealed that the band gap and HOMO/LUMO energy levels show a size-dependency similar to the optical characteristics of semiconductor nanocrystal quantum dots [53,54]. Furthermore, the light emissions of these organic carbon nanoparticles depend on the wavelength of the excitation light. All these characteristics make such particles of potential interest for next-generation technologies, like solar cells, light emitting diodes, biological labelling, sensors and catalysis [4,7,11,55–60].

With increasing their residence time in the flame, particles undergo a graphitization process to form soot particles with a mean size of 10-100 nm, often taking the form of fractal-like aggregates [61]. Mature soot particles have a turbostratic internal disposition for the aromatic planes with a H/C ratio of 0.1, similar to graphite, but with a larger interplanar spacing of about 0.35-0.5 nm. They absorb light in the visible and possess a large electrical conductivity [46,62].

Soot particles are formed in fuel-rich flames with an equivalence ratio higher than 2.1 (sooting fuel-rich flames), whereas carbon nanoparticles are generated both in sooting conditions, coexisting with larger primary soot particles and soot aggregated, and in less fuel-rich flame conditions, with an equivalence ratio between 1.7 and 2.1

(non-sooting fuel-rich flames) [63–65]. **Figure 1.3** resumes the carbonaceous particle formation route in a flame and some images of the representative produced species obtained by high-resolution microscopy techniques.

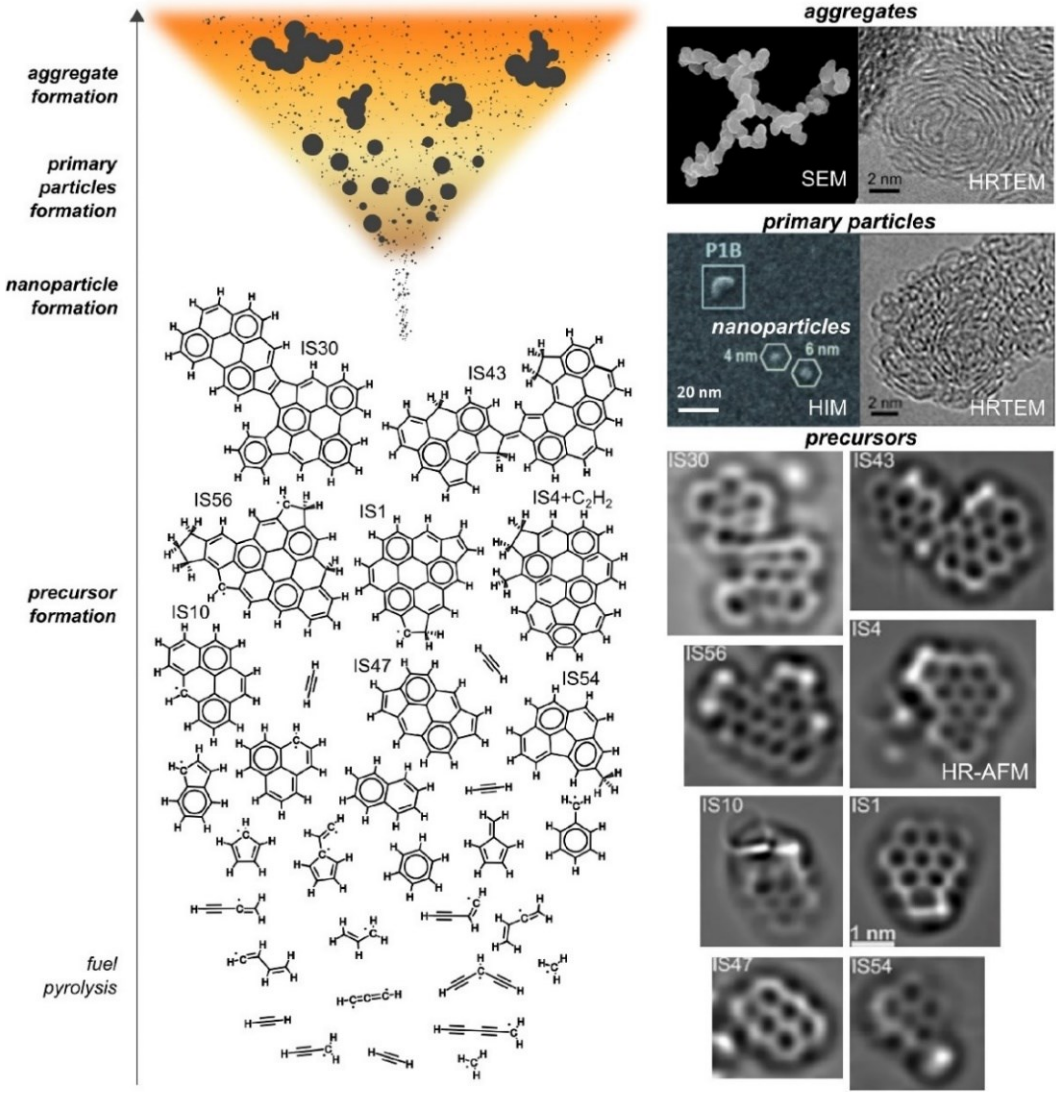

Figure 1.3. Schematic representation of the major steps in carbonaceous particles formation and images of representative species produced as the process proceeds: multiring aromatic structures by HR-AFM [44]; nanoparticles imaged with HIM [51]; primary particles imaged with HIM and HRTEM [66]; aggregates are shown with SEM and HRTEM [66]. HR-AFM: High-Resolution Atomic Force Microscopy; HIM: Helium Ion Microscope; HRTEM: High-Resolution Transmission Electron Microscope; SEM: Scanning Electron Microscopy [67].

Flame synthesis allows manufacturing either nanoparticles or aggregates, depending on the operating conditions. Fuchs [68] exploited the possibility of producing CNP films in flame though a low kinetic energy particles deposition mechanism based on the large temperature gradient (about 10^6 K/m) occurring in the thermal boundary layer [46] between the hot flame environment and a cold substrate inserted in flame: The discrete molecular structure of a gas causes small suspended particles to migrate from a region of high temperature to a region of low temperature with a velocity proportional to the modulus of the temperature gradient [69]. This mechanism, named thermophoresis, is an important route for nanoparticle deposition [70,71] and thermophoretic deposition is emerging as an attractive method for a low-cost, simple and one-step film preparation [24–28,41,47,72–75].

Bongiorno et al. [76] proved that the thermophoretic deposition mechanism consists of a random stacking of nanoparticles. Due to the low impact velocity, cluster fragmentation upon landing is minimal, the deposited structure is very similar to the aggregates formed in the gas phase and films have a low-density, fractal-like structure [77,78]. This memory effect offers the possibility to synthesize films with different structural and functional properties by controlling particle residence time in flame, temperature, pressure, fuel and burner-collector geometry. This possibility of tuning particle composition is particularly appealing for those applications in which precise control of the chemical-physical properties of the nanoparticles constituting the film is required. There are numerous papers in the literature referring to the thermophoretic deposition of films made up of inorganic nanoparticles, such as TiO_2 and SnO_2 [28,32,72,79–81].

In contrast, research on CNP films has been mostly limited to the use of thermophoresis as a diagnostic technique to analyse particle morphology and size [24,63,74,82–85]. Indeed, at the best of our knowledge, the largest majority of the researches on flame synthesis of CNP films by thermophoresis has been carried out by the Combustion Research group of the University Federico II and the CNR-

STEMS of Naples, Italy [46,86,87]. Since 2017 these groups have performed test on the harvesting and characterization of CNP films in well-established and deeply characterized flame conditions. The works developed by these groups in the past years are reviewed thereinafter.

The first paper investigated CNP film synthesis produced by thermophoretic deposition in flame (hereafter TFD), where morphological, and electrical properties of the thin films have been tested [46]. In this work, CNPs were produced by inserting a cold substrate in a flame for a given residence time using a flat laminar premixed ethylene-air C/O=0.72 flame stabilized on a water-cooled bronze McKenna Burner. From a technological viewpoint, the McKenna flat-burner is one of the prototypical reactors for the fundamental study of the evolution of particle growth [23,88] and for the calibration of optical diagnostic techniques [89,90]. This is considered the best choice to obtain stable and replicable conditions since in such a flame, the temperature and the species concentrations only depend on the height above the burner (HAB). The size distribution of the CNPs in the aerosol phase was measured online by SMPS (Scanning Mobility Particles Sizer) to identify the particle population available at a given HAB which will constitute the CNP film. Different nanoparticles were collected by changing HAB at a constant insertion time of the substrate in flame of 100 ms. A sequence of insertions has been performed to allow the deposition of an appreciable amount of CNPs. The number of insertions in the flame varied from 250 to 500.

CNP films were characterized by Atomic Force Microscopy, Raman and UV-Vis Absorption Spectroscopy in order to obtain chemical/ morphological information. Moreover, electrical characterization was performed.

Figure 1.4 shows the McKenna-type flame reactor, the experimental layout for the on-line characterization of the CNPs, the sketch for the thermophoretic deposition setup, and the silicon substrate with gold electrodes used for CNP films electrical characterization.

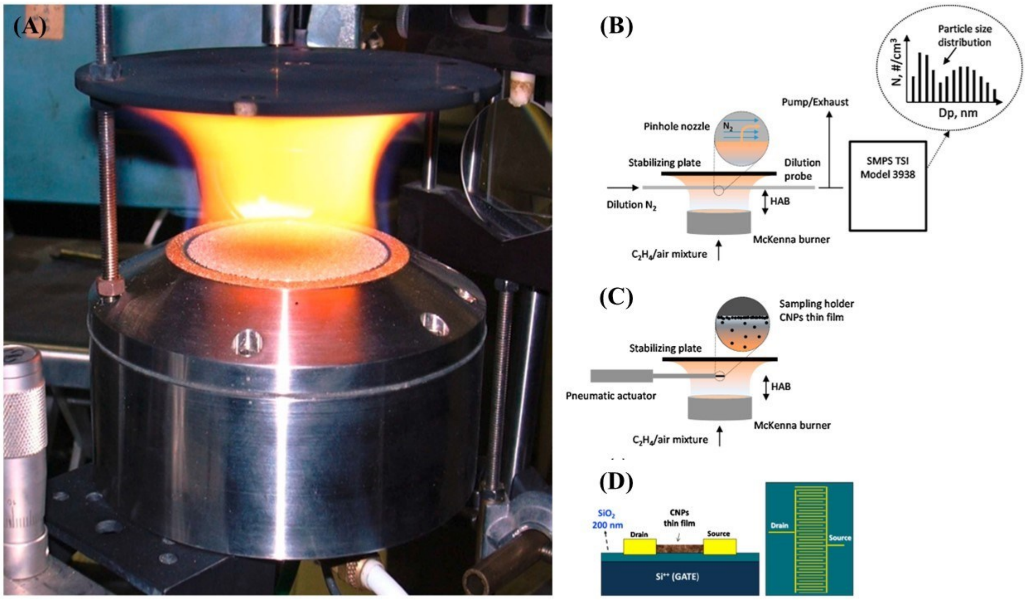

Figure 1.4. Summary of the experimental setup used for thermophoretic deposition (TFD) of CNPs by the Combustion Group of Federico II University and the CNR Stems: **(A)** Picture of McKenna type reactor; **(B)** Experimental layout for the online characterization of CNPs; **(C)** Sketch of the thermophoretic deposition; **(D)** Simplified side view of the substrate employed for electrical characterization (right) and interdigitated layout of the gold electrodes (left), adapted from De Falco et al. [46].

De Falco et al. [46] showed that the particle population formed in flame at the HAB=14 mm, whose average size is around 10 nm, represents a good compromise between the production of quasi-monodisperse small particles and an adequate production rate for practical applications [46]. Once deposited, Atomic Force Microscopy (AFM) has been applied to visualize CNP deposition. The AFM images obtained varying the number of insertions are reported in **Figure 1.5**.

These results reveal that thermophoretic deposition forms a thin film composed of nanoscale grains. Moreover, by increasing the deposition time, the morphology of the soot CNPs film changes, being formed by larger grains, higher values of roughness and enhanced void fraction. Apart from morphological analyses, the AFM images allow for estimating a thickness of the deposits, δ_{AFM}, which varies from 100 nm to 200 nm in the images of **Figure 1.5**.

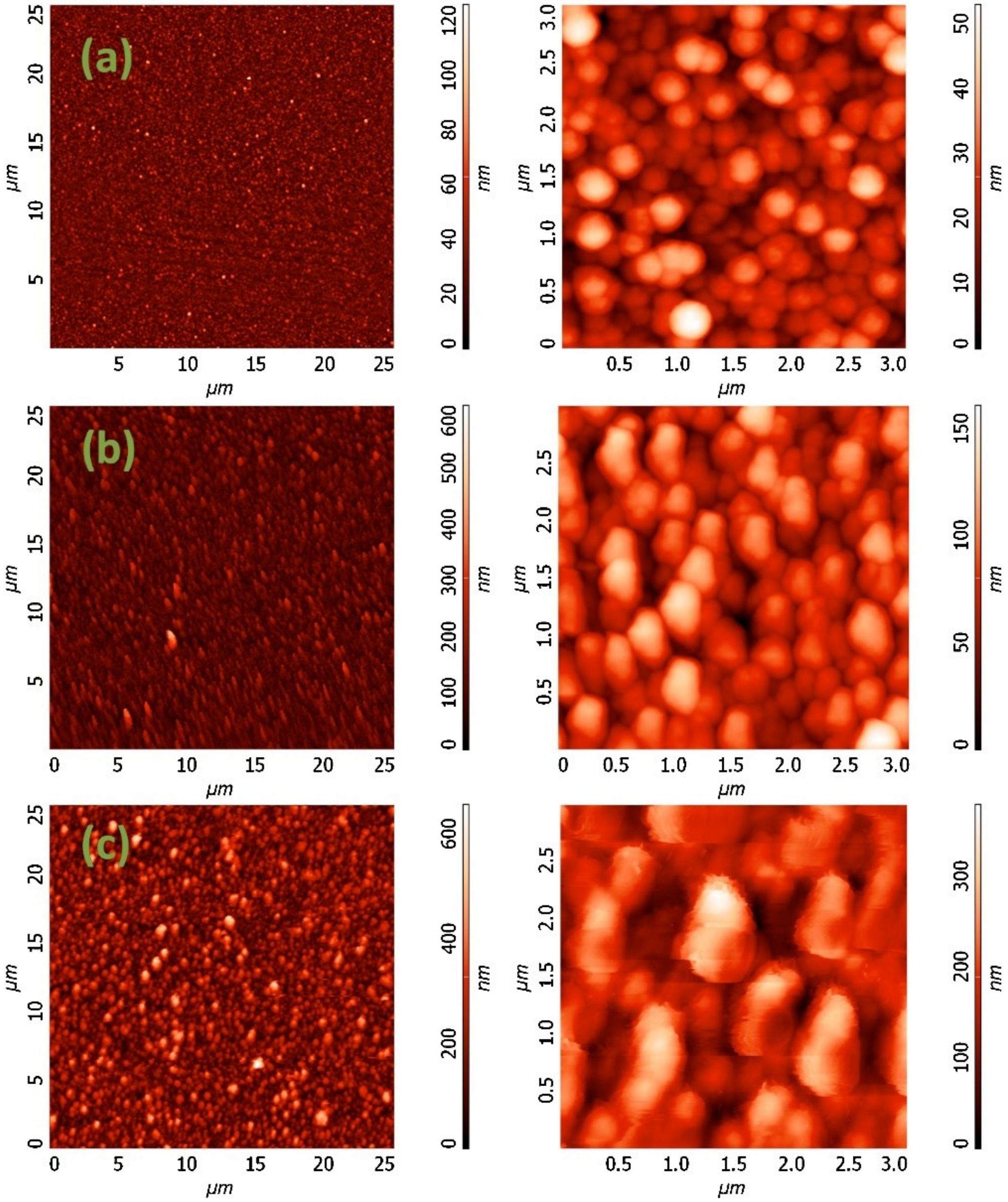

Figure 1.5. AFM images for films obtained at three different numbers of insertions for the substrate in flame: 250 (a), 375 (b), 500 (c), adapted from De Falco et al. [46].

Raman spectra of the CNP films (**Figure 1.6A**) reveal that they are made up of small size of the graphitic crystallites, with disorder and breathing modes of the aromatic islands [91].

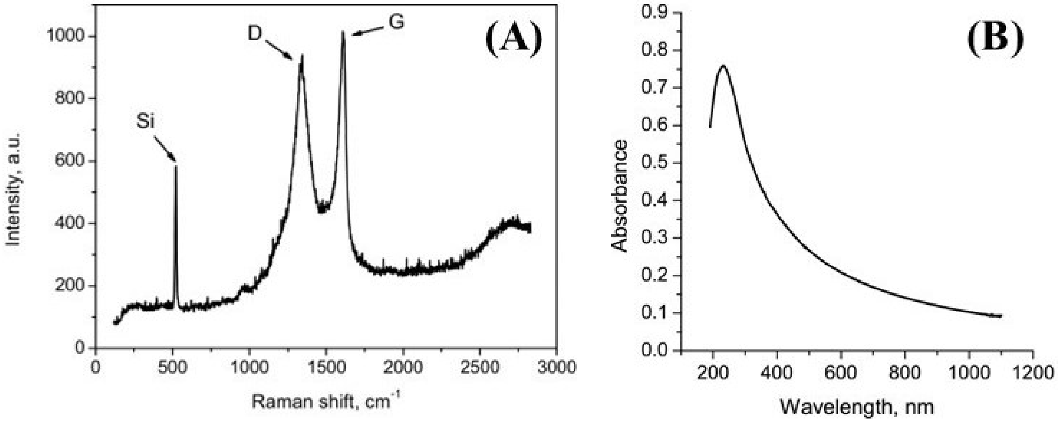

Figure 1.6. Examples of Raman spectrum (A) and UV-vis absorption spectrum (B) of a CNPs thin film, adapted from De Falco et al. [46].

Moreover, the intensity ratio of the D and G band, I(D)/I(G) allows estimating the in-plane crystallite size, L_a, which in these experiments is equal to 1.2 nm.

CNP films have been characterized by light absorption analysis. A typical spectrum for a thermophoretic harvesting CNP film is reported in **Figure 1.6B**: varying the number of insertions in flame, the spectra shape remains the same with absorbances that increase linearly with the number of insertions. This result suggests that the nature of the deposited particles is not altered by the insertion number and duration.

The absorption spectra can be analysed to estimate an equivalent optical thickness of the films and the optical band gap in light of the Tauc's relation [92]. For these CNP films the optical band gap remains equal to 0.5 eV, as for typical amorphous carbon materials. The equivalent thickness of the bulk carbon material in absence of voids δ_{Abs} is estimated using the Beer-Lambert equation [46,72,93]. De Falco et al [46] proposed that the ratio between δ_{AFM} and δ_{Abs} allows for estimating an average void fraction around 0.8 [46]. This void fraction has been used to evaluate the film growth rate as:

$$\xi = \frac{N_p v_{th}}{\lambda_l \left(1-\varphi\right)} \frac{\pi}{6} d^3 \approx 4 \pm 2 \frac{nm}{s} \tag{1.1}$$

where N_p is the particle number concentration in flame (experimentally obtained); v_{th} is the thermophoretic velocity; λ_l is the boundary layer for a laminar flame impinging on a flat plate (3 mm); φ is the void fraction.

As mentioned, CNP films are gaining increasing attention as reinforcing materials and for the production of coating with enhanced properties. In this perspective, mechanical characterization is a key issue in order to tune and modify the synthesis process for manufacturing more robust, durable and stable CNP films. De Falco et al. [86] proposes a first attempt to overcome the lack of experimental information on the mechanical properties of CNP films and provided direct experimental measurements on the hardness and the elastic modulus of nanostructured films by mean of Atomic Force Microscopy nanoindentation [94,95]. The approach behind this method is the combination between semi-contact AFM topography imaging, contact AFM topography imaging and AFM force spectroscopy to analyse CNP films deposited on mica substrates by means of the thermophoretic sampling system shown in **Figure 1.4**. The experimental procedure has been tested on pentacene (PEN) films, a medium soft material, and Highly oriented pyrolytic graphite (HOPG), a medium hard material. Two different samples of CNP films have been analyzed:

- Sample 1: flame with C/O ratio equal to 0.67, used to obtain a bimodal particle size distribution with a first particle mode of 2-4 nm and a second mode of 12-15 nm [40,41,44,45,47,49];
- Sample 2: flame with C/O ratio equal to 0.85, used to obtain particles larger than 10 nm and aggregates characterized by a higher graphitization degree compared to Sample 1 [43,48].

Results in terms of film Hardness *H* and Young's Modulus *E* are listed in **Table 1.1**.

Table 1.1. Hardness *H* and Young's modulus *E* measured by AFM nanoindentation on Sample 1 and Sample 2 and compared to PEN and HOPG. Mean standard deviation are reported referring to a number of independent measurements higher than 20. Adapted from De Falco et al. [86].

Sample	Hardness *H*, GPa	Young's modulus *E*, GPa
PEN	0.70 ± 0.05	3.8 ± 0.3
HOPG	2.40 ± 0.10	7.5 ± 0.3
Sample 1	0.75 ± 0.05	4.2 ± 0.3
Sample 2	0.90 ± 0.05	7.2 ± 0.4

Both Sample 1 and Sample 2 films have shown lower hardness and Young's modulus compared to HOPG. This can be explained by referring to the CNP film morphology. CNP films are composed of nanoscale grains, as suggested by De Falco et al. [46,62], packed together in a porous structure with porosity close to 80% [46]. So, the deformation of CNP films measured by indentation is governed by inter-grain mechanisms rather than intra-grain slippage and motion along the basal plane of the graphitic nano crystallites. Moreover, Sample 2 is characterized by higher hardness and Young's modulus, and the authors suggested this can be referred to the different properties of the nanograins that compose the two films in terms of internal nanostructure, size and aggregation degree of pristine particles, and of particles agglomeration in the nanograins during the deposition process.

Basic Current-Voltage (I-V) measurements have been performed as well [46]. In this case, the voltage applied between two gold electrodes was swept from 0 to 10 V, while the gate electrode was kept floating at 0 V. Two exemplificative I-V curves acquired in air and vacuum for the same CNP thin film are reported in **Figure 1.7A** [46].

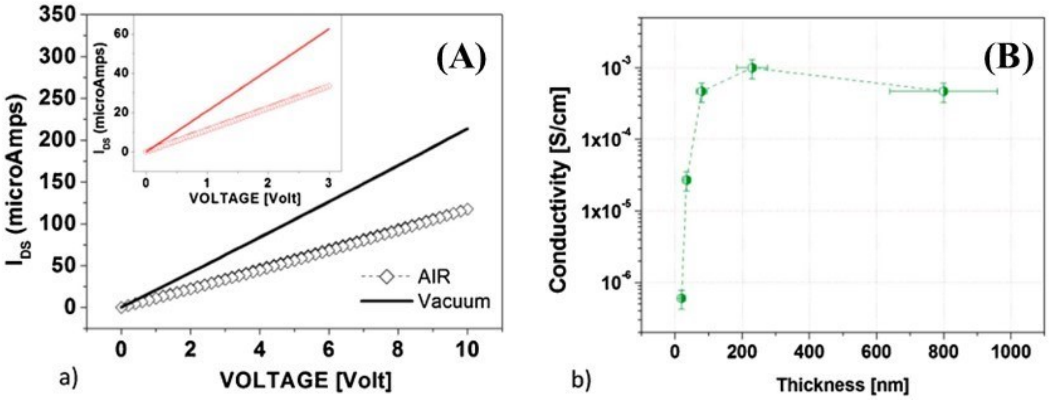

Figure 1.7. (A) Current-Voltage (I-V) measurements performed in air and vacuum for the same CNP film; **(B)** Conductivity values as a function of the thickness estimated in vacuum for the CNP films, adapted from De Falco et al. [46]. (C/O=0.72, HAB=14 mm, t_{ins}=100 ms, N_{ins}=500).

As shown, these films were found to be almost perfectly linear, exhibiting a basic ohmic behaviour up to 10 V. The linear behavior of I-V curves for each CNP film allowed an estimation of the equivalent conductivity (σ) of the thin film. As shown in **Figure 1.7B**, the value of σ depends on the equivalent film thickness. In particular, this result suggests that the films have an anisotropic morphological structure in the direction normal to the substrate surface. Increasing the film thickness, a simultaneous increase of grain size and roughness occur (*see* **Figure 1.5** and **Figure 1.6**). At small thickness, initially the conductivity increases with the grain size following a percolation-like behaviour, reaching a maximum at film thickness within 100-200 nm. Above this value, addition of further material does not enhance anymore the percolation paths and the conductivity reduces, probably because of the rise of roughness and void fraction [46]. Also, the charge carrier mobility values - obtained by using the MOSFET (Metal-Oxide-Semiconductors field-effect transistor) theory [96,97] - increase with thickness, allowing an estimation of the charge density equal to about $5\cdot10^{19}$cm^{-3} for the most conducting region of the films. Consequently, this work demonstrates the potentiality of CNP films to be employed as electrically-active components in electronic and sensing applications having properties similar to other carbonaceous materials as shown in the pertinent literature [98–101].

Finally, it is worth investigating the possibility of fabrication of CNPs-based synthetic superhydrophobic (water contact angles CA> 150° [22,102]) coatings. These smart superhydrophobic surfaces have recently evoked great interest to obtain self-cleaning, anti-bacterial and anti-icing properties. The superhydrophobic materials are special nature-inspired functional materials since they can replicate exactly the mechanism of the Lotus leaf to repel rain droplets and remain completely clean [12,21,22,103,104]. The oldest, simplest and most frequently used precursor in research involving the development of CNPs-based superhydrophobic surfaces is the simple candle soot since its flame's laminarity increases the coating's homogeneity in terms of morphological and chemical peculiarities. Unfortunately, the fresh candle soot may appear hydrophilic and water repellency is established only if the CNPs are collected from the middle flame region, where the amount of wax, organic compounds and non-conductive elements is higher. Although highly hydrophobic, the CNPs from the middle of the candle soot flame region could contain a small amount of PAH molecules that are highly toxic and additional treatments would be required to remove them and allow their safe use [12,103]. Commodo et al. [87] used thermophoretic flame synthesis in an ethylene/air McKenna Burner to produce CNP films with tunable wettability by varying combustion conditions, in terms of residence time, C/O ratio and HAB. In particular, carbon nanoparticles – namely the particles finer than 5 nm (*see* **Figure 1.2**) – appear to be the most hydrophilic, whereas those larger than 10 nm (*see* **Figure 1.2**) are the superhydrophobic ones. This suggests that very sooting flames (C/O>0.77) are expected to produce hydrophobic soot particles. Conversely, in slightly sooting flames (C/O< 0.77), hydrophilic/hydrophobic behaviour can be tuned by varying the HAB. In particular, since in their experiments for lower HAB values (<7 mm), all the collected particles have sizes smaller than 5 nm, hydrophilic films can be produced; as HAB increases, a higher relative contribution of particles larger than

10 nm determines an increase of the hydrophobic behaviour [87]. **Figure 1.8** shows examples of contact angle measurement for hydrophilic **(A)** and superhydrophobic **(B)** CNPs deposits [87].

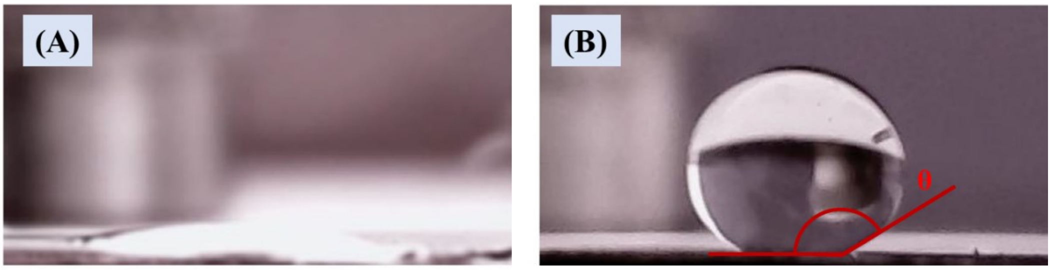

Figure 1.8. Example of sessile drop procedure and contact angle measurement for two selected flame conditions using an hydrophilic Teflon filter as substrate for CNPs deposition: **(A)** hydrophilic CNPs with C/O=0.63 and HAB=12 mm and **(B)** superhydrophobic (θ>150°) CNPs with C/O=0.67 and HAB=16 mm. Adapted from Commodo et al. [87].

In summary, the experimental studies of Federico II and STEMS pointed out that thermophoresis is a reliable process for deposition of CNPs and formation of thin films and by changing the flame parameters and the harvesting point, it is possible to obtain films with different morphological, electrical, mechanical, and wettability proprieties. Nevertheless, the industrial application of such a production process is limited to the use of flames characterized by relatively high C/O ratios (to obtain a massive deposition with higher throughput) and long production time to compensate the low thermophoretic harvesting rate. This suggests the need to identify a strategy able to guarantee the production of CNP films at a low C/O ratio and to allow CNP film productions with tunable properties possibly different from those generated by more sooting flames.

To this end, it is useful to remember that combustion is an exothermic self-sustaining reaction that involves the formation of a large number of ions, mostly positive, with a high concentration of free electrons. The concentration of these ions is measured in terms of a space charge density [105] and as a consequence of this presence an electric field forms between the burner and the surrounding environment. In a McKenna burner, the field is constrained between the burner mouth and the usually grounded stabilizing plate. Consequently, particles forming and moving along the flame naturally acquire an electric charge, mostly distributed according to a Boltzmann equilibrium charge distribution at a given temperature [49,106].

The existence of electric charges on particles can be used to enhance their deposition over a collector kept at a suitable bias potential. The deposition of charged particles by electric fields has been extensively studied, and it is well-known that electrostatic forces play an important role in many natural phenomena, including the deposition of particles in human airways [107]. When aerosols transport a high level of charge, the electrostatic forces significantly affect the particle motion, as well as the deposition rate. This high deposition rate is exploited in several applications, spanning from the microscopic devices for drug delivery [11,107] to the huge electrostatic precipitators and electric filters used in the industry and water treatment plants [108,109]. When neutral aerosols are immersed in a gas containing ions and under the effect of an external electric field, their motion is altered due to polarization phenomena and ionic wind effects [110,111].

The presence of charged species (in the form of electrons, ions and charged particles) in a flame suggests that the application of an external electric field can be used to improve CNPs deposition rate thanks to electrophoretic phenomena.

For example, Sardari et al. [112] studied the deposition of nanoparticles in a fully developed duct flow in the presence of an electric field using an Eulerian-Lagrangian particle tracking method. The simulation results showed that in the presence of an electric field, the electrostatic force dominated the Brownian effects for particles larger than around 10 nm: the deposition efficiencies for the combined effects of electrostatic and Brownian motion are, respectively, about 27% and 161.2% higher than for pure Brownian motion for charged 10 and 100 nm particles respectively.

To the best of our knowledge, there are not any studies on the electrophoretic deposition of CNPs. Some examples of electrophoretic in-flame synthesis of films can be found for inorganic nanoparticles such as TiO_2 and SnO_2 [32,79,81,98,113–115]. The studies referred to inorganic nanoparticle films may provide useful insights into the effectiveness of this process for the production of CNP films. However, it is also worth emphasizing that the presence of external electric fields not only influences nanoparticle dynamics and deposition in flame, but also the flame behaviour and these phenomena are likely to influence also the CNP formation pathways in a more complex way compared to the case of inorganic particles.

To have a suitable analysis of the State-of-Art regarding electric field-assisted CNP films formation several aspects must be considered:

1. The effect of electric field on flame properties (**Section 1.2**).
2. The experimental evidence of the effect of the application of electric fields on the in-flame CNPs production pathways and on the synthesis of inorganic nanoparticle films (**Section 1.3**).

1.2 Impact of electric field on flame behaviour

Electrical aspects of flames and the effects of electric field on flames have been of interesting subject area for several decades. One of the pioneers in this area, Lawton and Weinberg [116], published a book, Electrical Aspects of Combustion in 1969, summarizing state-of-art knowledge, which included theoretical models to describe the behaviours of charged species and phenomenological investigations.

A flame is a weakly ionized plasma with complex kinetical mechanisms which involve several species. While the majority is electrically neutral, some have a non-neutral electric potential and are balanced into two major groups, positive and negative. While the positive ones ($\sim 10^{12}/cm^3$) are composed only of positive ions, the negative ones are composed of free electrons and few negative ions [117].

Charged species are formed by ionization and destroyed by recombination. Ionization reactions typically occur in or nearby the flame front, while recombination reactions arise in the combustion products region.

Ionization in flames occurs mainly through four reaction types: collision, electron transfer, transfer excitation energy and lastly, chemi-ionization, which is the primary mechanism for ion formation [118]. It is a reaction which produces charged products from neutral reactants. An important primary chemi-ionization step in the flame front can be found in the following equations:

$$CH + O \rightarrow CHO^{+} + e^{-} \tag{1.2}$$

$$CHO^{+} + H_2O \rightarrow H_3O^{+} + CO \tag{1.3}$$

The CHO^+ is responsible for the formation of H_3O^+, **Eq. (1.3)**. This is the dominant ion in the flame zone and in the combustion products zone. Its concentration is superior to the other main positive ions due to the large concentration of H_2O produced by the flame [119]. Positive ions can recombine with either electrons or negative ions. The principal recombination process in flames also involves H_3O^+, as **Eq. (1.4)** reveals:

$$H_3O^{+} + e^{-} \rightarrow H + H_2O \tag{1.4}$$

The work of Call [120] confirms that H_3O^+ is formed later in the flames, above its front, upon reaction with CHO^+ ions. Therefore H_3O^+ are secondary ions.

Apart from CHO^+, other ions are found in lower concentrations, such as $C_3H_3^+$, $C_2H_3O^+$ and CH_3O^+. As in the other plasma processes, while some negative ions production exists, electrons are by far the most abundant [117,121]. Electrons, with their small mass and high mobility, have a high diffusion rate out of the flame, resulting in a charge spatial distribution in the flame. Electron and ion diffusion cannot be considered independent if quasi-neutrality, which is a characteristic quality of a plasma, is to be maintained. Therefore, in order to adjust the electron and ions fluxes in flames, there is a self-induced electric field E_i through the flame. This electric field accelerates positive ions and decelerates electrons, making them diffuse out of the flame front at equal rates. This movement of ions and electrons as a team is the essence of the phenomenon of ambipolar diffusion.

Consequently, the intrinsic electric field E_i is an important quantity when describing a flame containing charged species and electrons [64,65,105]. Pedersen and Brown [122] proposed the following model to determine the natural electric field E_i in a premixed flame:

$$\begin{aligned}
&\frac{dE_i}{dz} = -\frac{1}{\varepsilon_0} s_c = -\frac{1}{\varepsilon_0}\left(n_+ - n_-\right) e \\
&\frac{dV_i}{dz} = -E_i \\
&V_i\left(z = 0\right) = 0 \\
&V_i(z = h) = 0
\end{aligned} \tag{1.5}$$

Here, V_i is the intrinsic electric potential [V]; z is the flame direction [m]; e is the elementary charge [C]; n_+ and n_- are the number densities of positive and negative ions [#/m^3]; ρ_{sc} is the net space charge density [C/m^3]; h is the distance between the burner mouth and the stabilizing plate [m].

The net space charge density is a function of both flame fluid dynamics and local Carbon to Oxygen (C/O) ratio [64,65,105]. Delfau et al. [123] used an electrostatic probe and a multistage molecular beam sampling mass spectrometer to measure ion species concentration in laminar premixed ethylene-air flames at different C/O ratios. These experimental results have been also modeled with high accuracy by Cancian et al. [105]. **Figure 1.9** shows the net space charge density as a function of the C/O ratio for a laminar premixed ethylene-air flame in a McKenna burner [105,123].

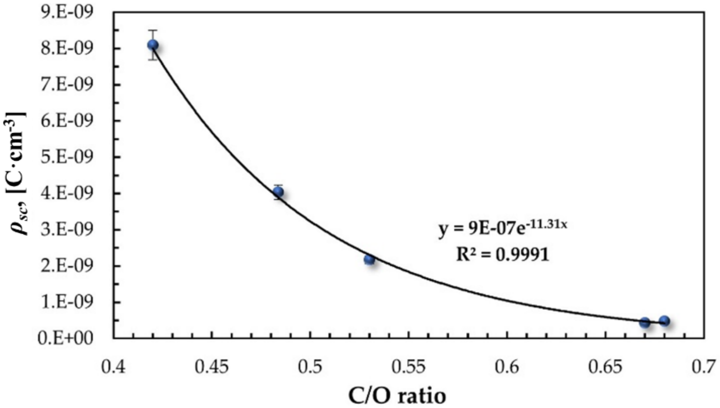

Figure 1.9. Net space charge density ρ_{sc} [C·cm^{-3}] as a function of the C/O ratio for a McKenna laminar premixed ethylene-air flame, adapted from Cancian et al. [105].

It has long been common knowledge that an external electric field has a dramatic visible effect upon a flame for the presence of charged particles: flame distortion, extinction in a sufficiently strong electric field and soot suppression have been evidenced since decennia [124–127]. Volkov et al. [127] studied the influence of a DC electric field on flame characteristics. The measurements were performed in premixed atmospheric-pressure stoichiometric CH_4/air flames stabilized on a burner using the heat flux method. The electric field was applied between the flat burner surface (grounded electrode) and an adjacent air-cooled electrode made of stainless-steel tube with outer diameter of 1 mm. Distance between the centres of the outer electrode and the burner is equal to 2.5 mm. The voltage is applied directly to the outer electrode. It was found that in this case the applied electric field leads to flame deformation both for positive and negative polarity (**Figure 1.10**).

Figure 1.10. Images of stoichiometric CH4/air flame: a) without EF, b) with EF of positive polarity and c) with EF of negative polarity. Distance between electrodes: 8 mm. Adapted from Volkov et al. [127].

The distortions of the flow can be explained by the action of volumetric electrical forces due to non-zero overall electrical charge in the reaction zone and in the combustion products. Observed effects of the electric field on gas flow suggest that positive excess volumetric charge is formed when high voltage is applied, regardless of the electric field direction. In the case of positive polarity, the electric field forces positive ions to move downward causing deceleration of the gas flow and, because of the integral flow continuity, the observed flow divergence. Conversely, the observed flow convergence in the case of negative polarity can be attributed to the upward acceleration of positively charged gas by electrical force. These effects are due to the different mobility between positive ions and electrons. Electrons have a higher mobility so they leave the inter-electrode space faster than the positive ions. Consequently, an excess of positive ions is formed in the flame and in the post-flame zone.

Another interesting observed phenomenon is the extinction of a flame in a sufficiently strong electric field. This effect was discovered by Malinowski [116] and has been studied under various experimental conditions. For example, Vinagradov et al. [126] measured the voltage-current characteristics (I-V curves) of flame-assisted electrical coronas in an inhomogeneous electric field. The experimental setup consists of a premixed CH_4/air flame stabilized on a copper Bunsen burner and a grounded conductive stainless steel mesh. The electric field was created by applying a voltage less than 25 kV DC to the burner. Both positive and negative polarities of the applied voltage V in the figures were studied in the presence of a premixed methane-air flame. The results were compared with the I-V curves measured for the same discharge gap in the absence of a flame. Typical I-V curves measured for the inter-electrode distance h=13 cm for no flame and in the presence of flame are shown in **Figure 1.11**.

It can be seen that in absence of a flame the plot corresponds to normal electrical breakdown and the electric current increases with the applied voltage (**Figure 1.11A**).

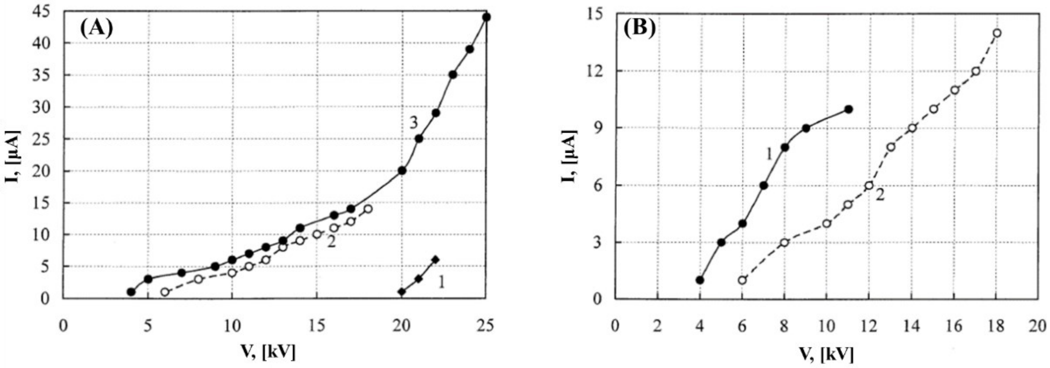

Figure 1.11. (A) I-V measurements for the inter-electrode distance *h*=13 cm. 1-no flame, both polarities; 2-flame assisted discharge, positive polarity; 3-flame-assisted discharge, negative polarity; **(B)** I-V curves with a flame for the case of positive polarity and (1) *h*=6.5 cm and (2) *h*=13 cm. Adapted from Vinogradov et al. [126].

The corona-type discharge for the cases $V>0$ and $V<0$ corresponds to positive and negative corona, respectively, since the sign of V is that of the space charge in the outer domain of the flame. The voltage polarity does not affect the I-V curves in the absence of a flame and there is no noticeable current, that is, the current's magnitude does not exceed the measurement error when the applied voltage is less than 20 kV. In the presence of a flame, a noticeable current appears when V exceeds the onset potential of 6 kV and 4 kV for positive and negative polarities, respectively. The current of the flame-assisted positive corona increases with voltage until the latter achieve some critical values V_C (18 kV for *h*=13 cm). For $V>V_C$ the flame is extinguished and the electric current drops abruptly to the value measured under flameless conditions. When the inter-electrode distance is decreased, the critical voltage V_C for flame extinction decreases; this is seen by comparing panels **A** and **B** in **Figure 1.11**. For negative corona, no flame extinction is observed within the 25 kV tested.

Wang et al. [128] investigated the effects of a uniform electric field, considering a series of one-dimensional laminar premixed ethylene/air flames, produced with a McKenna Burner. The burner was electrically grounded, whereas both positive and negative voltages were applied to the stabilizing plate, placed 23 mm above the burner surface. The study had three main goals. The first was to assess whether positively or negatively charged soot particles dominate in a flame. The second was to measure the variation of soot volume fractions and particle morphology under the effect of an electric field. The third aim was to assess the effect on flame flickering and extinction as a function of the applied electric field and of the equivalence ratio. This last part is presented below, while the first two aims will be discussed in more details in **Section 1.3**.

The authors argued that with sufficiently large values of electric field applied to the flame, the flame itself becomes unstable, firstly exhibiting flickering and then showing electric discharges. Indeed, **Figure 1.12** shows the flame stability diagrams, demarking the transitions to flickering and discharge as a function of the equivalence ratio (Φ=O/C) for negative and positive electric fields, respectively.

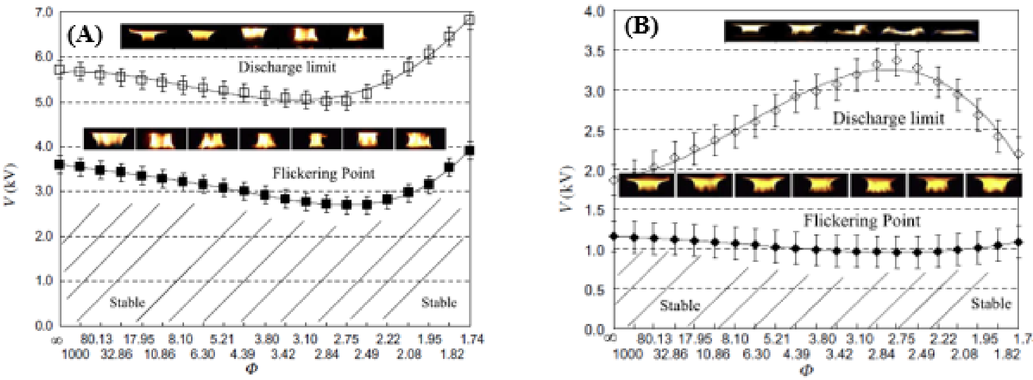

Figure 1.12. Maps of the critical values for negative E **(A)** and positive E **(B)** leading to flame flicker and discharge as a function of equivalence ratio, at a fixed ethylene gas flux of 2.1 mg/s and *h*=23mm. Adapted from Wang et al. [128].

A comparison between **(A)** and **(B)** reveals that the discharge voltages under a negative field are about two times higher than those in positive field. According to Paschen's law, in atmospheric air, a spark is triggered when the electric field strength exceeds approximately 3000 kV/m [129]. At this field strength, a very rapid increase in the number of free electrons and ions occurs in free air, temporarily causing the air to become an electrical conductor in a process called “dielectric breakdown”. The presence of charged species generated by the flame was found to reduce the dielectric field strength required to induce a discharge to one-seventh of that of air (~430 kV/m) [128,129].

As illustrated above, an external electric field has a dramatic visible effect on a flame. Since 1910, when Thompson [124,130,131] suggested that electrons are involved with combustion, the debate has been whether or not the observed effects of an electric field on a flame are due to the purely mechanical forces related to the ionic wind (which disrupt the physical parameters of the flame), or if the electric field actually alters the flame chemistry [124]. Recent findings suggest that both effects are occurring, with a relative importance depending upon the system geometry and the nature of the electric field. Hereafter, these two mechanisms are described with more details.

In a flame, the ionic wind is the flow of ions and neutral gases which occurs under the effects of an external electric field. The charged species, which are directly subjected to a displacement due to the electric field, transfer their momentum to the more numerous neutral species giving rise to an overall motion. In particular, under the influence of an external electric field, the charged components of a flame will experience a translation force proportional to the current density in flame and inversely proportional to the electrical mobility. Since the fuel and the oxidant for flames are initially neutral, by the law of charge conservation the current flow due to positive particles must be equal and opposite to the current flow due to the negative particles. Thus, the predominant direction of the force on the neutral gas is by the ionic species with the lowest mobility (*i.e.* the largest size). Since the positive ions are bigger than the electrons, which composed the majority of the negative ions, the ionic wind is primarily towards the negative electrode. Consider a positively charged mesh electrode placed above a one-dimensional premixed flat flame (**Figure 1.13**).

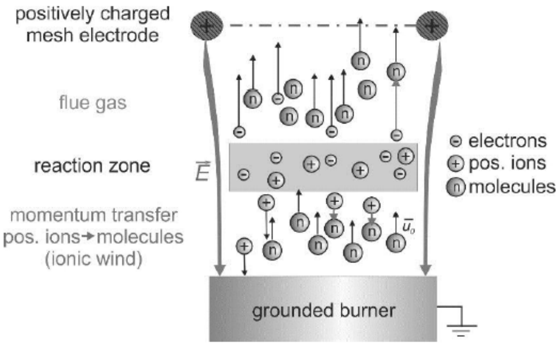

Figure 1.13. Electric field effect on premixed flames: schematic of the "ionic wind" for a laminar one-dimensional flame; a positively charged mesh electrode is positioned above the burner. Adapted from Zigan et al. [132,133].

If the burner acts as the cathode, then the positive ions move towards the burner while negative ions and electrons move towards the anode placed downstream. In other words, the electrons and negative ions are shifted to the positively charged electrode, whereas the positive ions move in counter-flow to the incoming fresh gas towards the grounded burner rim. The positive ions will collide with the neutral molecules of the incoming mixture after passing the mean free path length, on average. As the mean free path length is quite small and the positive ions are accelerated again by the electric field after each collision, each positive ion undergoes a multitude of collisions with neutral molecules. Therefore, small ion concentrations are enough for a noteworthy momentum transfer to the fresh gas. Unlike the ions, electrons play a minor role in total momentum in the flame front due to their low mass. Similarly, the impact of negative ions is rather low due to their lower concentration. As a result of ion-neutral collisions within the fresh gas region, a shift of the flame front appears.

As shown in the former pages, when an external electric field in applied across a flame, an electric current *I* can be measured. This is a useful indicator of the flux of charged species being displaced by the electric field and can be expressed as:

$$I = \left(\sum_i \mu_i^+ - \sum_j \mu_j^- \right) \cdot |e| \cdot |E| \tag{1.6}$$

Where μ_i^+ and μ_j^- are the mobility of positive and negative ionic species in flame; e is the elementary charge and E is the electric field generated by an applied voltage.

The relationship describing this behaviour is the I-V curves [134] shown in **Figure 1.11**, which result to be a macroscopic manifestation of the complex interaction of chemically-driven generation of charges and charge transport induced by the electric field to the applied voltage. These curves have a strong dependence on the type of fuel, flame stoichiometry, pressure, and position with respect to the electrode, but typically they have the generic form of **Figure 1.14** from which different electrical discharge regimes can be referred.

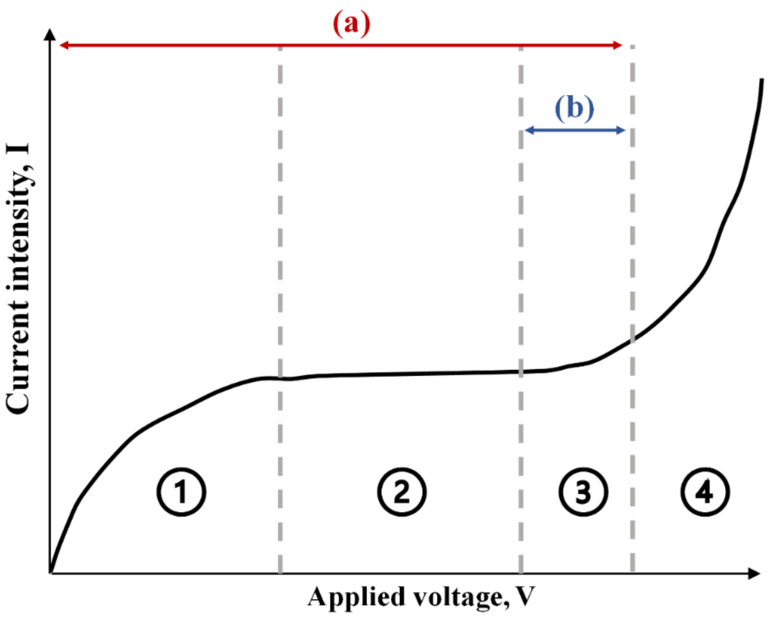

Figure 1.14. Generic *I-V* curve and discharge regimes. (1) sub-saturation; (2) saturation; (3) enhanced saturation; (4) breakdown. Indication about the controlling mechanism in flame: (a) voltages at which ionic wind occurs; (b) voltages at which alteration of the flame chemistry occurs. Adapted from Han et al. [134].

Zone (1) corresponds to the sub-saturation region, where the electric field dislocates more charged species from the flame front as the voltage increases, resulting in a current increase. In this regime the flame behaves similarly to a resistor. As the voltage increases, the electric field reaches a point at which all charged species are stripped away from the flame at the same rate as these are being formed: this is the saturation regime (2). By further increasing the voltage, secondary ionization mechanisms are triggered, and the electric field is capable of stripping free electrons from neutral molecules. This regime is known as enhanced saturation (3). Finally, in zone (4), the secondary ionization rate increases significantly, originating an electron avalanche which leads to electrical breakdown.

The authors [116] suggest that ionic wind effects do not completely explain the effects of an electric field upon a flame especially in the enhanced saturation region (3), where there is an exponential growth of the current with the applied voltage. Numerous experimental results have pointed out the change of flame chemistry due to the production of reactive radicals below the actual flame front. Jaggers and von Engel [124] studied the effect of DC and AC electric fields on the burning velocity of different gas flames. In a vertical tube 120 cm tall by 5 cm inside diameter, the burning velocity was measured as a function of the fuel/air mixture ratio under various electric fields. To eliminate the effects of the ionic wind, Jaggers and von Engel subsequently used a high frequency field of 5 MHz in their experiment. The electric field was applied both transversely along the flame front and longitudinally across the flame front. In both cases, a displacement of the flame towards the burner was seen, indicating an increase in the flame speed. There was no change in flame shape or stability, indicating that the effect of ionic wind can be effectively neglected. Jaggers and von Engel concluded that the displacement of the flame front is due to a change in the electron collision process in an electric field. They argued that the chain branching reaction:

$$H^{\cdot} + O_2 \rightarrow OH^{\cdot} + O^{\cdot} \tag{1.7}$$

controls the overall rate of reaction and therefore the flame speed.

The rate of this reaction is influenced by the vibrational energy level of O_2. The free electrons in the flame are involved in the following energy exchange reaction with O_2 molecules:

$$O_2(\nu = n) + e^- + energy \rightarrow O_2(\nu = n+1) + e^- \tag{1.8}$$

The free electrons translational energy makes possible an increase in O_2 internal vibrational energy and the rates of the chain branching reaction **(1.7)**. Consequently, the flame speed increases. Therefore, the application of an external electric field, by increasing the free-electron temperature (energy), causes an increase of the O_2 vibrational energy states, giving rise to a faster overall reaction rate and to an increase in flame speed.

1.3 Experimental evidence on the effect of an external electric field on the flame-synthesis of CNPs and inorganic nanoparticle films

In the previous sections, it was observed that flame distortion and extinction occur at sufficiently strong electric fields. These phenomena are not only due to mechanical forces acting on the molecules as an effect of the ionic wind, which affect sensibly physical parameters of the flame, but also to alteration of flame chemistry [110,120,124,130]. Despite all the knowledge gained about flame, the influence of an electric field on CNPs formation is not incompletely understood yet and only limited experimental evidence is available in the pertinent literature. Saito et al. [125] investigated the effects of applied voltage and electrode gap on the variation of the soot suppression in an acetylene diffusion flame by immersing in the flame a high voltage stainless-steel pipe and a grounded stainless-steel ring. DC voltages up 10 kV were applied between the electrodes and the electrode gap (*h*) was varied from 0-15 mm. **Figure 1.15** shows the effect of positive voltage on soot suppression. This chart shows the effect of positive voltage on soot suppression expressed as the ratio between collected mass of particles under the application of the given voltage, compared with the value at zero voltage.

As evident from **Figure 1.15**, soot suppression started rapidly at above 1-3 kV of positive applied voltages, and exceeds 90% over 7 kV. The experiments reveal that for a higher electrode gap the soot suppression is more efficient.

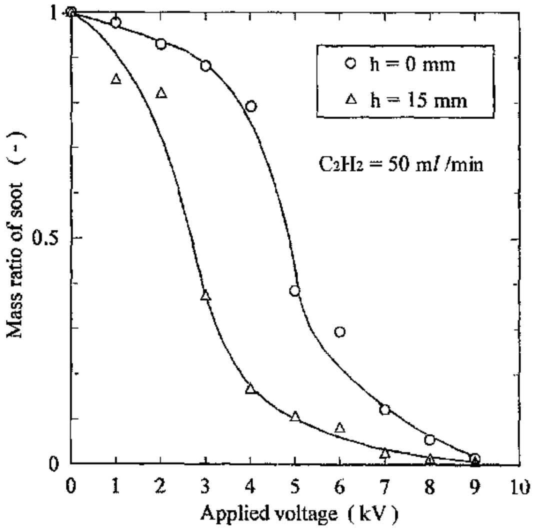

Figure 1.15. Effect of applied positive voltage on soot suppression for an electrode gap equal to h= 0 mm and h=15 mm. Adapted from Saito et al. [125].

On the contrary, the authors showed that when negative voltage was applied to the nozzle electrode, soot particle could not be collected because they deposited on the tip of the HV electrode. Therefore, the experiments concerning the effect of negative voltage were not reported in the original paper.

As suggested in **Section 1.2**, Wang et al. [128] investigated the effects of a uniform electric field, considering a series of one dimensional laminar premixed ethylene/air flames, produced with a grounded McKenna Burner, applying both positive and negative voltages to the stabilizing plate. In addition to studying the phenomena of flickering and flame instability, discussed in the previous section, the authors tried to assess whether positively or negatively charged soot particles dominate in a flame, and to measure the variation of soot volume fractions and particle morphology under the effect of an electric field. The measurements included both intrusive sampling probes and non-intrusive laser diagnostic techniques, as laser extinction and thermophoretic sampling/transmission electron microscopy. The laser extinction measurements are performed using a He-Ne CW polarized laser beam with power of 2 mW at λ=632.8 nm and diameter of less than 2 mm. Wang at al. [128] proposed the following equation to calculate the soot volume fraction:

$$f_v = \frac{\ln(P_0/P(\lambda))\lambda}{6\pi E(m)l} \tag{1.9}$$

where P_0 and $P(\lambda)$ are the intensities of the incident and the extinguished beams, respectively; λ is the wavelength of the laser; $E(m)$ is a function of the refractive index of the soot, set to 0.4 [90] and l is the laser path length through the flame axis. The time course of the soot volume fraction was measured for a Φ=1.82 flame setting the electric potential to 0, -0.4 and 0.4 kV at HAB equal to 15 mm. Results are reported in **Figure 1.16A**. Time t_p=0 of the experiments represents the moment at which the deposition on the sampling grid started, including 50 ms of delay time to insert the probe in the flame.

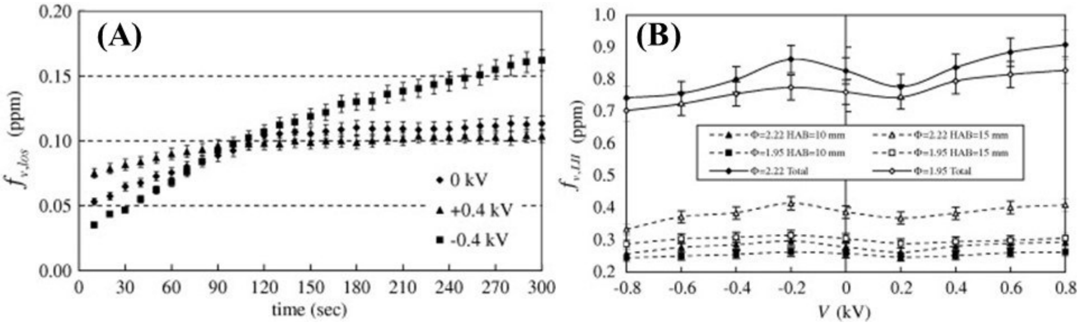

Figure 1.16. (A) The effect of an electric field on flame soot volume fraction during 300 s for HAB=15mm and Φ=1.82; **(B)** Variation of the soot volume fraction with the strength of the applied electric field for HAB=10 and 15 mm and Φ=1.95 and 2.22. Adapted from Wang et al. [128].

The thickness of the soot layer on the stabilizing plate (f_v) reaches an asymptotic value after about 2-3 min, when the deposition and oxidation processes were balanced. As shown in **Figure 1.16A**, for t_p<100 s, f_v was higher for positive applied polarity and lower for negative polarity, yet in both cases f_v profiles show approximately a linear behaviour; for t_p>100 s, f_v reached an asymptote for neutral and positive polarity, while for the negative polarity, additional deposition of the soot particles is observed. It is also noticeable that soot deposition rates (*i.e.* the slope of each f_v-t profile) are higher for the negative polarity. The Authors suggested that this behaviour can be ascribed to the fact that approximately 68% of soot particles are positively charged. In both cases, deposition rates progressively reduce over time due to space charge effect: as long as the accumulation of opposite polarity particles occurs on the substrate, a reduction of the overall electric field occurs and a deceleration of particles is observed.

Figure 1.16B shows how the f_v varies under different values of the applied potential and for various HAB and Φ values. For low voltages, as V=+0.2 kV, f_v is decreased by about 6% compared to V=0 for Φ=2.22; the opposite is observed for a negative applied electric field. Most of the visible effects are observed for the case of HAB=15mm Φ=2.22, while for lower HAB or Φ the electric field generated a negligible effect on soot deposition.

In addition, the Authors reported TEM images obtained at -0.8, 0 and 0.8 kV for a gap distance of 23 mm and HAB=10 and 15 mm in order to reveal soot particle structure and morphology (**Figure 1.17**). It is possible to notice that the morphology of individual particles at HAB=10 mm appears more “liquid-like, representing individual particles that have been recently formed. Instead, at HAB=15 mm the individual particles have undergone some agglomeration and, probably, an increased oxidation consistent with an increase of the CNPs residence time related to the positive electric field. On the contrary, the agglomerates look finer than those at V=0 when negative potentials are applied, due to their lower residence time in the flame.

In summary, electric field changes the particle size distribution by changing the residence time of charged particles in flame: a negative field attracts the positively charge particles, reducing their residence time. On the deduction that negatively charged particles dominate the root of the flame, while positively charged particles dominate the tip, it appears that the application of the electric field on the stabilizing plate makes both the particle formation and the oxidation processes to be shortened on average.

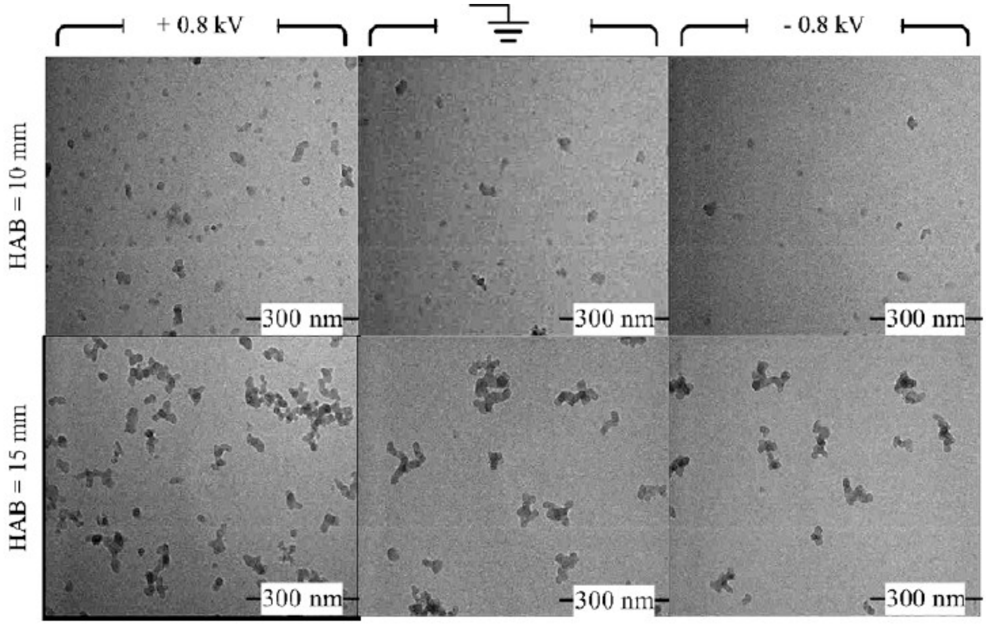

Figure 1.17. Morphologies of particles for +0.8, 0 and -0.8 kV for a gap distance of 23 mm and HAB=10 and 15 mm. Adapted from Wang et al. [128].

However, there are no studies in the pertinent literature referred to the effectiveness of the production of CNP films in presence of external electric field. For this reason, the production of films based on inorganic particles may provide useful insights.

Inorganic nanosized particles, such as TiO_2, SiO_2 and SnO_2, have distinctly different properties compared to their bulk materials, since they are characterized by lower melting point, better light absorption and structural properties. These features make them suitable for different industrial applications. In particular, titania nanoparticles are used as pigments, photocatalysts and as catalyst supports [135–137]; fumed silica nanoparticles are widely used for optical fibers, catalyst supports and as fillers and dispersing agents [138–140]; nanosized tin oxide powders are used as semiconductors and gas sensors [141,142]. The efficiency of these materials depends largely on film properties such as primary particle size, morphology, porosity, thickness and crystallinity. Effort have been made to tune and optimize these properties for specific applications. Flame synthesis has been utilized extensively for the production of particles and films [28,115] due to the low production cost and potentially high production rate, and because characteristics of the nanostructured films can be controlled by adjusting flame conditions, substrate temperature and precursor loading rate. Considerable research has been devoted to investigate the effect of external electric fields on particle characteristics in electro/thermophoretic harvesting processes. Early on, Hardesty and Winberg [143] injected hexamethyldisiloxane vapour into a Meker-burner using a premixed methane/air flame with an electric field applied parallel to the gas-stream lines. The primary particle size of the resulting SiO_2 powders was reduced by a factor of three for a -6 kV potential applied to the collecting substrate. This effect was attributed to the decreased residence time for sintering of the thermionically positively charged SiO_2 particles in the product gas. Much of the recent work in electrically-assisted flame synthesis has been done by Pratsinis and co-workers [25,27,31,37,75,81,144]. They produced TiO_2 nanoparticles by oxidation of $TiCl_4$ in a methane/air double diffusion flame using a corona discharge to charge the particles by two needle electrodes placed across the flame. They showed that the average primary particle diameter was reduced by a factor of two by increasing the applied potential from 1.2 to 2.0 kV/cm and that a reduction of the rutile-crystalline phase of harvested particles has been shown. Based on these earlier observations, Xiong et al. [113] have studied for the first time the electric-field-assisted flame synthesis of mesoporous titanium-dioxide films using a premixed stagnation swirl flame (**Figure 1.18**).

The setup includes a stainless steel grounded burner with an internal swirler and a stagnation aluminum plate positioned 20 mm from the burner exit. The main gas lines of methane, nitrogen and oxygen are preheated and mixed with the precursor that is titanium tetraisopropoxide heated to 130°C to avoid condensation of the precursor as it flows to the burner. A high-voltage power supply provides the voltage bias at the aluminum plate, creating the desired electric field between the grounded burner and the substrate.

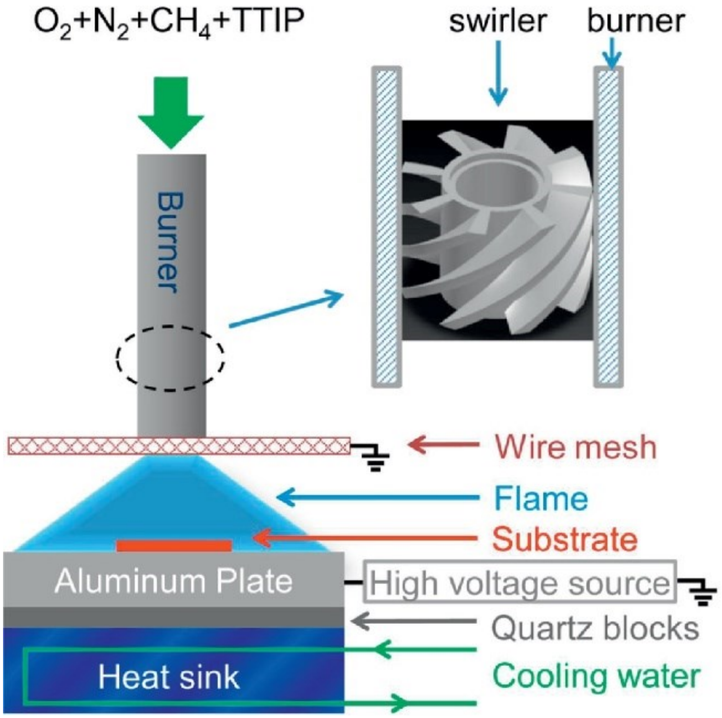

Figure 1.18. Sketch of the experimental setup for TiO2-nanoparticle-film deposition, adapted from Xiong et al. [113].

The work has focused on the effects of an electric field on the TiO_2-nanoparticle-film structure, porosity, and morphology for different substrate temperatures and precursor concentrations.

Figure 1.19 shows SEM images of cross-sections of nanostructured TiO_2 films for 116 ppm precursor concentration and 473 K substrate temperature.

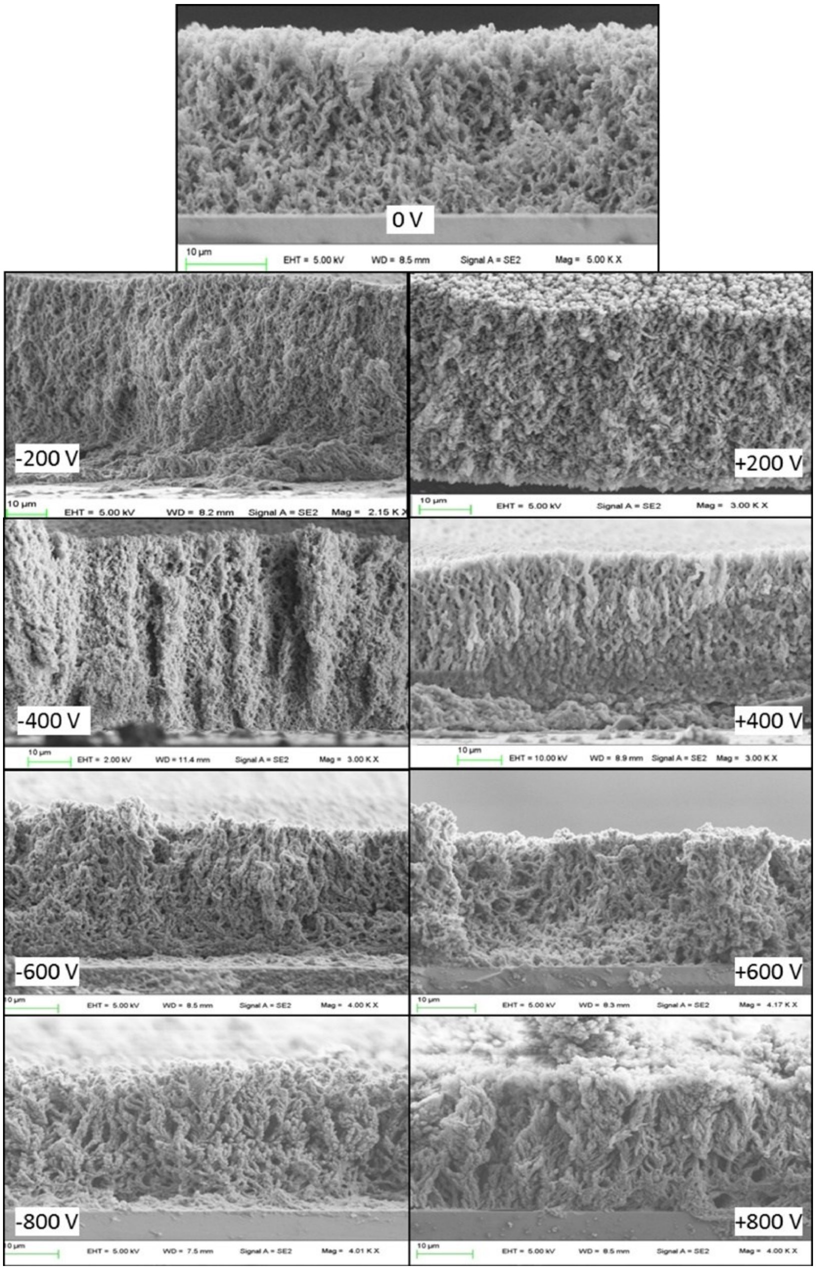

Figure 1.19. SEM images of TiO_2 film for substrate temperature 473 K and 116 ppm precursor concentration with voltages applied to the aluminum substrate from -800 V to +800V, adapted from Xiong et al. [113].

At 0 V (grounded substrate) it is possible to notice the formation of a tree-like branched fractal film. However, when the voltage magnitude increases to |±400| V, the authors argue that the films exhibit a more well-aligned columnar structure. Noteworthy, this trend is non-monotonic, since the film becomes less columnar as the voltage magnitude is set to |±800| V. In order to further understand the effects of electric field on particle growth, particles are collected from substrate and characterized by TEM (**Figure 1.20**) and XRD.

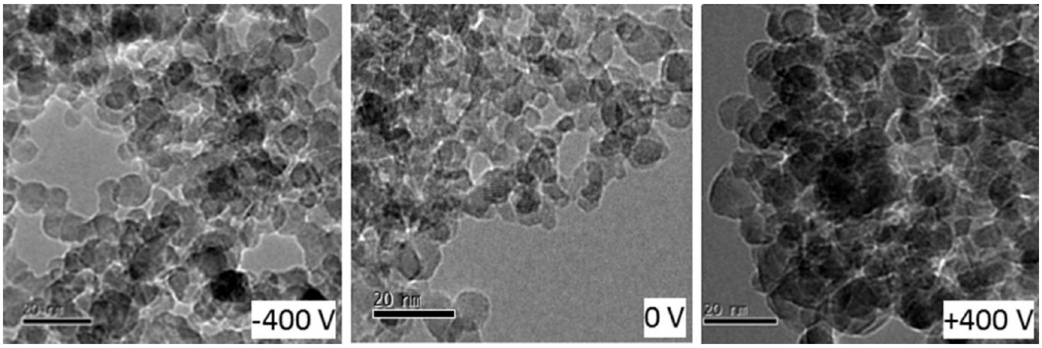

Figure 1.20. TEM images of titania nanoparticles from the films, adapted from Xiong et al. [113].

The average primary particle size are 5 nm, 4 nm, and 9 nm for a voltage bias equal to 0 V, -400 V to +400 V, respectively. These results indicate that more titania nanoparticles are positively charged. This can be justified considering that the applied electric field will impose a force on charged particles, affecting both the electrophoretic velocity and the residence time in flame: when a positive voltage is applied, positively charged titania particles spend more time in the flame since they are repelled by the collector and additional growth and agglomeration phenomena occur in flame respect to the 0 V case.

The XRD (not shown) reveals that the phase of the particles is anatase, irrespective of the voltage bias applied, demonstrating that the electrophoresis is not altering the chemistry of nanoparticles.

The authors also determined the TiO_2-film porosity by calculating the packing density of the film (ε), using the following equation:

$$\varepsilon = \frac{m_f}{\rho_p A_f \delta_f} \tag{1.10}$$

Where m_f is the measured weight of the film; ρ_p is the density of TiO_2 particles (3840 kg/m^3); A_f is the top surface area of the film; and δ_f is the thickness of the film, as determined by SEM. The packing density of the nanostructured TiO_2 films under substrate voltages from -800 V to +800 V is presented in **Figure 1.21**. The packing density data show a non-monotonic trend, with a minimum at |±400| V.

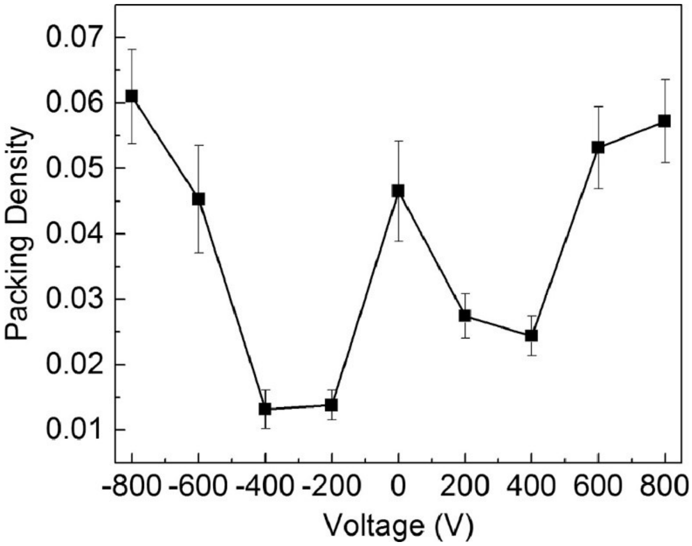

Figure 1.21. Packing density of titania films, varying the voltage bias on the aluminum plate, adapted from Xiong et al. [113].

1.4 Summary and aim of the work

This chapter summarized the current state of the art in the manufacture of Carbon Nanoparticles-based films through electric field-assisted in-flame deposition. Carbon Nanoparticles are receiving a lot of interest right now for their fascinating electrical, mechanical, electrochemical, and chemical properties that make them perfect candidates for a wide range of industrial applications, including the manufacture of sensors for wearable devices, energy storage and biotechnology applications [1–20]. It is a widespread understanding that CNPs are typically unwanted products of combustion processes. Under fuel-rich flame conditions, CNPs are generated from unburned hydrocarbons by complex mechanisms, which have long been unrecognized. Only in recent years these mechanisms have been thoroughly understood: by controlling combustion conditions (*i.e.* temperature, carbon/oxygen ratio, residence time and pressure) it is possible to obtain CNPs with specific sizes and properties [38,39]. In this way, a flame becomes the simplest and cheapest reactor for the production of CNPs, and by using thermophoretic forces, CNP deposits with low densities and fractal-like structures can be produced at low cost [68–70,76–78]. Numerous papers in the literature refers to the thermophoretic deposition of films made up of inorganic nanoparticles, such as titania and fumed silica [28,72,79–81,98,113–115], while in contrast, research on CNP films is limited to activities of the University Federico II and STEMS in Naples. These groups have carried out extensive characterisation of the films from a morphological, electrical and mechanical point of view [46,86]. However, the industrial application of CNP films produced by thermophoresis appears to be limited to flames at high C/O ratios, which guarantee higher throughput and long production time. However, the properties of CNPs depend on the C/O ratio and on the harvesting conditions, and it is desirable to produce deposits of CNPs from lower C/O ratio flames, which are likely to exploit specific features of interest for the project. To this end, the existence of electric charges on CNPs produced in flame can be used to enhance the deposition over a collector kept a suitable bias potential. Examples of the suitability of electric field-assisted flame synthesis are limited to the production of films based on inorganic nanoparticles, such as titania and fumed silica [113–115]. In these works, the burner is grounded and the stabiliser plate is electrically charged, and used as a collector. It was observed that in the presence of electric fields, there is an alteration in the size of the primary particles with changes in the morphology, porosity and structure of the deposited films. At the same time, the electric field gives rise to alterations in the flame properties. These distinctions depend on the presence of ionic wind and alterations in the chemistry of the flame [124,126,130–133], which also change the residence time of CNPs in flame and, consequently, the particle size distribution function [125,128].

However, as far as CNP film production is concerned, this is still an unexplored process, which justifies the need to address this topic in this PhD thesis work. Apart from the abovementioned alteration of flame properties and CNP characteristics, insights from the literature allow us to state that the same CNP films produced by electrophoresis exhibit properties different from those produced by pure thermophoresis. These statements can be partly supported by referring to the process of film growth and how this changes due to the presence of electric fields, as described by Castillo et al. [77,78,145]. The growth of CNP films comprised several steps: CNP collision on a substrate (or on deposit), CNP adhesion to the substrate or to the deposit and, finally, CNP deposit/film re-structuring. Each of these steps is characterized by a specific mechanism and it is possible to follow a rigorous description of the process including a large number of parameters [77,146–148]. However, it is possible to focus on the mechanism with plays a major role and neglect all the other effects. In particular, the work of Castillo et al. [78] for carbon black systems suggested a way of controlling the final deposit morphology by adjusting the dynamical behaviour of CNPs when approaching the collecting surface, assuming a complete passive deposit, for which CNP attachment and coagulation phenomena can be neglected [77,145]. CNPs suspended in a flame can be driven towards the substrate by different mechanisms, such as inertia, convection, diffusion and gravitation or phoretic forces, leading to the formation of CNP deposits. When CNPs are very small, inertia plays a negligible role and CNP motion can be split into two contributions: the first one, a deterministic mean particle velocity associated with convection thermophoresis or electrophoresis; a second one, a random walk diffusion motion linked to the Brownian motion of CNPs. Once CNPs get in the active zone close to a collector [77,145–148], this combination of deterministic motions and random walk may bring the CNPs onto the surface, leading to the collision and eventually to the formation of a deposit. The dimensionless Peclet number measures the relative importance of the deterministic CNPs motion to the Brownian random walk and it is defined as:

$$Pe_i = \frac{v_i d_{p,i}}{D_i} \tag{1.11}$$

Where v_i is the normal component of the particle arrival velocity and D_i is the CNP diffusion coefficient. From Monte Carlo Simulations it is possible to understand that in the limit case of *Pe* equal to zero, a purely diffusive CNPs motion in the absence of drift occurs and the generated deposits grow with the fractal structure predicted by the diffusion-limited aggregation model. On the other hand, if the *Pe* number tends to be infinite, there is a ballistic behaviour of the CNPs with vanishing diffusion, and the deposits will be compact and with a rough interface [78,149–151].

The results of the proposed theoretical model can be applied to obtain information on films that can be produced by electric field-assisted flame synthesis. It is known that thermophoresis is a low kinetic energy deposition mechanism in which fractal structures are formed [46,68,76]. Since the electric field determines an increase in the deposition rate [112,152], a transition from a pure diffusive to a ballistic deposition regime can be expected, resulting in the formation of more compact structures.

This is the background to this PhD thesis, whose aim is to improve the state of the art concerning to the electric field-assisted flame synthesis applied to the production of CNPs in a low C/O ethylene/air flame and to characterize the properties of CNP films produced with this new methodology. This research work has been developed considering a specific model condition: the production of CNP films by insertions at a specific HAB of a cold substrate, kept at a specific electric potential, varying from 0 to -3 kV, in a a laminar premixed ethylene/air flame with C/O ratio equal to 0.67 stabilized on a McKenna Burner. This reference conditions have been considered for its technological relevance, but also for the large amount of information on its characteristics provided over the last decade by the research groups involved in the project.

First, a mathematical model will be explained in order to investigate the dynamics of CNPs harvesting under the presence of electric fields, in order to understand the possible impact on harvesting rate and CNP trajectories. Moreover, this model will give information about the controlling forces for the harvesting rate for each CNP size and charge.

Then, the experimental results will provide data on the CNP film morphological, physicochemical and structural properties, by using a series of complementary techniques, such as UV-vis Absorption, Raman Spectroscopy, Atomic Force Microscopy, Surface texture analysis, and Size Exclusion Chromatography, highlighting the similitudes and the differences between thermophoretic and electric field-assisted in-flame CNP films deposition. The comparison between the experimental and model results will verify its validity and limitations.

Finally, Current-Voltage and Contact Angle measurement will be performed to suggest the possible application of the electric field-assisted flame synthesis deposits for technological applications.

1.5 References

[1] Trung TQ, Ramasundaram S, Hwang BU, Lee NE. An All-Elastomeric Transparent and Stretchable Temperature Sensor for Body-Attachable Wearable Electronics. Advanced Materials 2016;28:502–9. https://doi.org/10.1002/adma.201504441.

[2] Wang C, Xia K, Wang H, Liang X, Yin Z, Zhang Y. Advanced Carbon for Flexible and Wearable Electronics. Advanced Materials 2019;31. https://doi.org/10.1002/adma.201801072.

[3] Iqbal S, Khatoon H, Hussain Pandit A, Ahmad S. Recent development of carbon based materials for energy storage devices. Mater Sci Energy Technol 2019;2:417–28. https://doi.org/10.1016/j.mset.2019.04.006.

[4] Xiao J, Momen R, Liu C. Application of carbon quantum dots in supercapacitors: A mini review. Electrochem Commun 2021;132. https://doi.org/10.1016/j.elecom.2021.107143.

[5] Miao L, Song Z, Zhu D, Li L, Gan L, Liu M. Recent advances in carbon-based supercapacitors. Mater Adv 2020;1:945–66. https://doi.org/10.1039/d0ma00384k.

[6] Liu J, Bao S, Wang X. Applications of Graphene-Based Materials in Sensors: A Review. Micromachines (Basel) 2022;13. https://doi.org/10.3390/mi13020184.

[7] Asadian E, Ghalkhani M, Shahrokhian S. Electrochemical sensing based on carbon nanoparticles: A review. Sens Actuators B Chem 2019;293:183–209. https://doi.org/10.1016/j.snb.2019.04.075.

[8] Milcovich G, Lettieri S, Antunes FE, Medronho B, Fonseca AC, Coelho JFJ, et al. Recent advances in smart biotechnology: Hydrogels and nanocarriers for tailored bioactive molecules depot. Adv Colloid Interface Sci 2017;249:163–80. https://doi.org/10.1016/j.cis.2017.05.009.

[9] Bartelmess J, Milcovich G, Maffeis V, d'Amora M, Bertozzi SM, Giordani S. Modulation of Efficient Diiodo-BODIPY in vitro Phototoxicity to Cancer Cells by Carbon Nano-Onions. Front Chem 2020;8. https://doi.org/10.3389/fchem.2020.573211.

[10] Wang J, Liu X, Milcovich G, Chen TY, Durack E, Mallen S, et al. Co-reductive fabrication of carbon nanodots with high quantum yield for bioimaging of bacteria. Beilstein Journal of Nanotechnology 2018;9:137–45. https://doi.org/10.3762/bjnano.9.16.

[11] Liu Z, Robinson JT, Tabakman SM, Yang K, Dai H. Carbon materials for drug delivery & cancer therapy. Materialstoday 2011;14:316–23.

[12] Mulay MR, Chauhan A, Patel S, Balakrishnan V, Halder A, Vaish R. Candle soot: Journey from a pollutant to a functional material. Carbon N Y 2019;144:684–712. https://doi.org/10.1016/j.carbon.2018.12.083.

[13] Pagliaro M. Nano-Age How Nanotechnology Changes our Future. Wiley-VCH. 2010.

[14] Khanna V, Kumar V, Bansal SA. Effect of carbonaceous nanomaterials' reinforcement on mechanical properties of aluminium metal-based nanocomposite: A review. Mater Today Proc, vol. 38, Elsevier Ltd; 2020, p. 289–95. https://doi.org/10.1016/j.matpr.2020.07.221.

[15] Yee MJ, Mubarak NM, Abdullah EC, Khalid M, Walvekar R, Karri RR, et al. Carbon nanomaterials based films for strain sensing application—A review. Nano-Structures and Nano-Objects 2019;18. https://doi.org/10.1016/j.nanoso.2019.100312.

[16] Abedi M, Fangueiro R, Correia AG. Effects of multiscale carbon-based conductive fillers on the performances of a self-sensing cementitious geocomposite. Journal of Building Engineering 2021;43. https://doi.org/10.1016/j.jobe.2021.103171.

[17] Green DA, Lewis R, Dwyer-Joyce RS. Wear effects and mechanisms of soot-contaminated automotive lubricants. Proceedings of the Institution of Mechanical Engineers, Part J: Journal of Engineering Tribology, vol. 220, 2006, p. 159–69. https://doi.org/10.1243/13506501JET140.

[18] Naha S, Sen S, Puri IK. Flame synthesis of superhydrophobic amorphous carbon surfaces. Carbon N Y 2007;45:1702–6. https://doi.org/10.1016/j.carbon.2007.04.018.

[19] Esmeryan KD, Castano CE, Bressler AH, Abolghasemibizaki M, Mohammadi R. Rapid synthesis of inherently robust and stable superhydrophobic carbon soot coatings. Appl Surf Sci 2016;369:341–7. https://doi.org/10.1016/j.apsusc.2016.02.089.

[20] Li X, Shi H, Wang Y, Wang H, Huang J, Duan M. Liquid marbles from soot films. Soft Matter 2020;16:4512–9. https://doi.org/10.1039/c9sm02199j.

[21] Zhang B, Duan J, Huang Y, Hou B. Double layered superhydrophobic PDMS-Candle soot coating with durable corrosion resistance and thermal-mechanical robustness. J Mater Sci Technol 2021;71:1–11. https://doi.org/10.1016/j.jmst.2020.09.011.

[22] Li S, Huang J, Chen Z, Chen G, Lai Y. A review on special wettability textiles: theoretical models, fabrication technologies and multifunctional applications. J Mater Chem A Mater 2017;5:31–55. https://doi.org/10.1039/c6ta07984a.

[23] Li S, Ren Y, Biswas P, Tse SD. Flame aerosol synthesis of nanostructured materials and functional devices: Processing, modeling, and diagnostics. Prog Energy Combust Sci 2016;55:1–59. https://doi.org/10.1016/j.pecs.2016.04.002.

[24] Zheng F. Thermophoresis of spherical and non-spherical particles: a review of theories and experiments. Adv Colloid Interface Sci 2002;97:255–78.

[25] Strobel R, Pratsinis SE. Flame aerosol synthesis of smart nanostructured materials. J Mater Chem 2007;17:4743–56. https://doi.org/10.1039/b711652g.

[26] Roth P. Particle synthesis in flames. Proceedings of the Combustion Institute 2007;31 II:1773–88. https://doi.org/10.1016/j.proci.2006.08.118.

[27] Kammler HK, Mädler L, Pratsinis SE. Flame synthesis of nanoparticles. Chem Eng Technol 2001;24:583–96. https://doi.org/10.1002/1521-4125(200106)24:6<583::AID-CEAT583>3.0.CO;2-H.

[28] Wegner K, Barborini E, Piseri P, Milani P. Gas phase synthesis of nanostructured particulate films. KONA Powder and Particle Journal 2006;24:54–69.

[29] Li C, Hu Y, Yuan W. Nanomaterials synthesized by gas combustion flames: Morphology and structure. Particuology 2010;8:556–62. https://doi.org/10.1016/j.partic.2010.08.009.

[30] Teoh WY, Amal R, Mädler L. Flame spray pyrolysis: An enabling technology for nanoparticles design and fabrication. Nanoscale 2010;2:1324–47. https://doi.org/10.1039/c0nr00017e.

[31] Pratsinis SE. Aerosol-based technologies in nanoscale manufacturing: From functional materials to devices through core chemical engineering. AIChE Journal 2010;56:3028–35. https://doi.org/10.1002/aic.12478.

[32] Zhang Y, Shuiqing L, Deng S, Yao Q, Tse SD. Direct synthesis of nanostructured TiO2 films with controlled morphologies by stagnation swirl flames. J Aerosol Sci 2012;44:71–82. https://doi.org/10.1016/j.jaerosci.2011.10.001.

[33] Sano N. Formation of multi-shelled carbon nanoparticles by arc discharge in liquid benzene. Mater Chem Phys 2004;88:235–8. https://doi.org/10.1016/j.matchemphys.2004.07.018.

[34] Zhang S, Song H, Guo P, Zhou J, Chen X. Formation of carbon nanoparticles from soluble graphene oxide in an aqueous solution. Carbon N Y 2010;48:4211–4. https://doi.org/10.1016/j.carbon.2010.07.025.

[35] Alam A, Wan C, McNally T. Surface amination of carbon nanoparticles for modification of epoxy resins: plasma-treatment vs. wet-chemistry approach. Eur Polym J 2017;87:422–48. https://doi.org/10.1016/j.eurpolymj.2016.10.004.

[36] Andhika IF, Saraswati TE, Hastuti S. The structural characteristics of carbon nanoparticles produced by arc discharge in toluene without added catalyst or gases. Evergreen 2020;7:417–28. https://doi.org/10.5109/4068622.

[37] Kelesidis GA, Goudeli E, Pratsinis SE. Flame synthesis of functional nanostructured materials and devices: Surface growth and aggregation. Proceedings of the Combustion Institute 2017;36:29–50. https://doi.org/10.1016/j.proci.2016.08.078.

[38] Martin JW, Salamanca M, Kraft M. Soot inception: Carbonaceous nanoparticle formation in flames: Soot inception. Prog Energy Combust Sci 2022;88. https://doi.org/10.1016/j.pecs.2021.100956.

[39] Michelsen HA, Colket MB, Bengtsson PE, D'Anna A, Desgroux P, Haynes BS, et al. A review of terminology used to describe soot formation and evolution under combustion and pyrolytic conditions. ACS Nano 2020;14:12470–90. https://doi.org/10.1021/acsnano.0c06226.

[40] Commodo M, Sgro LA, Minutolo P, D'Anna A. Characterization of combustion-generated carbonaceous nanoparticles by size-dependent ultraviolet laser

photoionization. Journal of Physical Chemistry A 2013;117:3980–9. https://doi.org/10.1021/jp401061d.

[41] Commodo M, De Falco G, Bruno A, Borriello C, Minutolo P, D'Anna A. Physicochemical evolution of nascent soot particles in a laminar premixed flame: From nucleation to early growth. Combust Flame 2015;162:3854–63. https://doi.org/10.1016/j.combustflame.2015.07.022.

[42] Commodo M, Tessitore G, De Falco G, Bruno A, Minutolo P, D'Anna A. Further details on particle inception and growth in premixed flames. Proceedings of the Combustion Institute 2015;35:1795–802. https://doi.org/10.1016/j.proci.2014.06.004.

[43] Commodo M, De Falco G, Minutolo P, D'Anna A. Structure and size of soot nanoparticles in laminar premixed flames at different equivalence ratios. Fuel 2018;216:456–62. https://doi.org/10.1016/j.fuel.2017.12.032.

[44] Commodo M, Kaiser K, De Falco G, Minutolo P, Schulz F, D'Anna A, et al. On the early stages of soot formation: Molecular structure elucidation by high-resolution atomic force microscopy. Combust Flame 2019;205:154–64. https://doi.org/10.1016/j.combustflame.2019.03.042.

[45] Vitiello G, De Falco G, Picca F, Commodo M, D'Errico G, Minutolo P, et al. Role of radicals in carbon clustering and soot inception: A combined EPR and Raman spectroscopic study. Combust Flame 2019;205:286–94. https://doi.org/10.1016/j.combustflame.2019.04.028.

[46] De Falco G, Commodo M, Barra M, Chiarella F, D'Anna A, Aloisio A, et al. Electrical characterization of flame-soot nanoparticle thin films. Synth Met 2017;229:89–99. https://doi.org/10.1016/j.synthmet.2017.05.008.

[47] Picca F, Pietro A di, Commodo M, Minutolo P, D'Anna A. Variable Temperature Synthesis of Tunable Flame-Generated Carbon Nanoparticles. C (Basel) 2021;7:44. https://doi.org/10.3390/c7020044.

[48] Russo C, D'Anna A, Ciajolo A, Sirignano M. The effect of butanol isomers on the formation of carbon particulate matter in fuel-rich premixed ethylene flames. Combust Flame 2019;199:122–30. https://doi.org/10.1016/j.combustflame.2018.10.025.

[49] Sgro LA, D'Anna A, Minutolo P. Charge fraction distribution of nucleation mode particles: New insight on the particle formation mechanism. Combust Flame 2011;158:1418–25. https://doi.org/10.1016/j.combustflame.2010.11.010.

[50] Bockhorn H. Soot Formation in Combustion. Mechanisms and Models. vol. 59. Berlin, Heidelberg: Springer Berlin Heidelberg; 1994. https://doi.org/10.1007/978-3-642-85167-4.

[51] Schenk M, Lieb S, Vieker H, Beyer A, Gölzhäuser A, Wang H, et al. Morphology of nascent soot in ethylene flames. Proceedings of the Combustion Institute 2015;35:1879–86. https://doi.org/10.1016/j.proci.2014.05.009.

[52] D'Anna A. Combustion-formed nanoparticles. Proceedings of the Combustion Institute 2009;32 I:593–613. https://doi.org/10.1016/j.proci.2008.09.005.

[53] Russo C, Apicella B, la Rocca A, Sirignano M. Fluorescent carbon dots synthesis in premixed flames: Influence of the equivalence ratio. Carbon N Y 2023;201:659–66. https://doi.org/10.1016/j.carbon.2022.09.061.

[54] Liu C, Singh A v., Saggese C, Tang Q, Chen D, Wan K, et al. Flame-formed carbon nanoparticles exhibit quantum dot behaviors. Proc Natl Acad Sci U S A 2019;116:12692–7. https://doi.org/10.1073/pnas.1900205116.

[55] Bhunia SK, Saha A, Maity AR, Ray SC, Jana NR. Carbon nanoparticle-based fluorescent bioimaging probes. Sci Rep 2013;3. https://doi.org/10.1038/srep01473.

[56] Ray SC, Saha A, Jana NR, Sarkar R. Fluorescent carbon nanoparticles: Synthesis, characterization, and bioimaging application. Journal of Physical Chemistry C 2009;113:18546–51. https://doi.org/10.1021/jp905912n.

[57] Boakye-Yiadom KO, Kesse S, Opoku-Damoah Y, Filli MS, Aquib M, Joelle MMB, et al. Carbon dots: Applications in bioimaging and theranostics. Int J Pharm 2019;564:308–17. https://doi.org/10.1016/j.ijpharm.2019.04.055.

[58] Molkenova A, Toleshova A, Song SJ, Kang MS, Abduraimova A, Han DW, et al. Rapid synthesis of nontoxic and photostable carbon nanoparticles for bioimaging applications. Mater Lett 2020;261. https://doi.org/10.1016/j.matlet.2019.127012.

[59] Dinger N, Panzetta V, Russo C, Netti PA, Sirignano M. In vitro effects of combustion generated carbon dots on cellular parameters in healthy and cancerous breast cells. Nanotoxicology 2022:1–24.

[60] Loh KP, Ho D, Chiu GNC, Leong DT, Pastorin G, Chow EKH. Clinical Applications of Carbon Nanomaterials in Diagnostics and Therapy. Advanced Materials 2018;30. https://doi.org/10.1002/adma.201802368.

[61] Schulz F, Commodo M, Kaiser K, De Falco G, Minutolo P, Meyer G, et al. Insights into incipient soot formation by atomic force microscopy. Proceedings of the Combustion Institute 2019;37:885–92. https://doi.org/10.1016/j.proci.2018.06.100.

[62] De Falco G, Commodo M, Bonavolontà C, Pepe GP, Minutolo P, D'Anna A. Optical and electrical characterization of carbon nanoparticles produced in laminar premixed flames. Combust Flame 2014;161:3201–10. https://doi.org/10.1016/j.combustflame.2014.05.021.

[63] Dobbins RA, Megaridis CM. Morphology of flame generatd soot as determined by thermophoretic sampling. Langmuir American Chemical Society 1987;3:254–9.

[64] Maricq MM. A comparison of soot size and charge distributions from ethane, ethylene, acetylene, and benzene/ethylene premixed flames. Combust Flame 2006;144:730–43. https://doi.org/10.1016/j.combustflame.2005.09.007.

[65] Maricq MM. Size and charge of soot particles in rich premixed ethylene flames. Combust Flame 2004;137:340–50. https://doi.org/10.1016/j.combustflame.2004.01.013.

[66] Martin JW, Botero M, Slavchov RI, Bowal K, Akroyd J, Mosbach S, et al. Flexoelectricity and the Formation of Carbon Nanoparticles in Flames. Journal of Physical Chemistry C 2018;122:22210–5. https://doi.org/10.1021/acs.jpcc.8b08264.

[67] Baldelli A, Trivanovic U, Sipkens TA, Rogak SN. On determining soot maturity: A review of the role of microscopy- and spectroscopy-based techniques. Chemosphere 2020;252. https://doi.org/10.1016/j.chemosphere.2020.126532.

[68] Fuchs G, Treilleux M, Santos Aires F, Cabaud B, Melinon P, Hoareau A. Cluster-beam deposition for high-quality thin films. Phys Rev A (Coll Park) 1918;40:6128–9.

[69] Batchelor GK, Shent C. Thermophoretic Deposition of Particles in Gas Flowing over Cold Surfaces. J Colloid Interface Sci 1985;107:21–37.

[70] Zhao H, Liu X, Tse SD. Control of nanoparticle size and agglomeration through electric-field- enhanced flame synthesis. Journal of Nanoparticle Research 2008;10:907–23. https://doi.org/10.1007/s11051-007-9330-7.

[71] Zhang X, Gan Z, Li Y. Collection of particles on cold surfaces: A review. Ind Eng Chem Res 2020;59:16493–506. https://doi.org/10.1021/acs.iecr.0c02337.

[72] De Falco G, Commodo M, Minutolo P, D'Anna A. Flame aerosol synthesis and thermophoretic deposition of superhydrophilic TiO2 nanoparticle coatings. Chem Eng Trans 2019;73:37–42. https://doi.org/10.3303/CET1973007.

[73] Sirignano M, Russo C, Ciajolo A. One-step synthesis of carbon nanoparticles and yellow to blue fluorescent nanocarbons in flame reactors. Carbon N Y 2020;156:370–7. https://doi.org/10.1016/j.carbon.2019.09.068.

[74] Russo C, Apicella B, Tregrossi A, Oliano MM, Ciajolo A. Thermophoretic sampling of large PAH (C ≥ 22–24) formed in flames. Fuel 2020;263. https://doi.org/10.1016/j.fuel.2019.116722.

[75] Koirala R, Pratsinis SE, Baiker A. Synthesis of catalytic materials in flames: Opportunities and challenges. Chem Soc Rev 2016;45:3053–68. https://doi.org/10.1039/c5cs00011d.

[76] Bongiorno G, Podestà A, Ravagnan L, Piseri P, Milani P, Lenardi C, et al. Electronic properties and applications of cluster-assembled carbon films. Journal of Materials Science: Materials in Electronics 2006;17:427–41. https://doi.org/10.1007/s10854-006-8089-4.

[77] Rodríguez-Pérez D, Castillo JL, Antoranz JC. Relationship between particle deposit characteristics and the mechanism of particle arrival. Phys Rev E Stat Nonlin Soft Matter Phys 2005;72. https://doi.org/10.1103/PhysRevE.72.021403.

[78] Castillo JL, Martin S, Rodriguez-Perez D, Perea A, Garcia-Ybarra PL. Morphology and nanostructure of granular materials built from nanoparticles. KONA Powder and Particle Journal 2014;31:214–33. https://doi.org/10.14356/kona.2014012.

[79] Tolmachoff ED, Abid AD, Phares DJ, Campbell CS, Wang H. Synthesis of nano-phase TiO2 crystalline films over premixed stagnation flames. Proceedings of the Combustion Institute 2009;32 II:1839–45. https://doi.org/10.1016/j.proci.2008.06.052.

[80] Kumar M, Bhattacharya S. Flame synthesis and characterization of nanocrystalline titania powders. Processing and Application of Ceramics 2012;6:165–71. https://doi.org/10.2298/pac1203165k.

[81] Vemury S, Pratsinis SE, Kibbey L. Electrically controlled flame synthesis of nanophase TiO2 , SiO2 , and SnO2 powders. J Mater Res 1997;12:1031–42.

[82] Eisner AD, Rosner DE. Experimental Studies of Soot Particle Thermophoresis in Nonisothermal Combustion Gases Using Thermocouple Response Techniques. Combust Flame 1985;61:153–66.

[83] De Falco G, Commodo M, D’Anna A, Minutolo P. The evolution of soot particles in premixed and diffusion flames by thermophoretic particle densitometry. Proceedings of the Combustion Institute 2017;36:763–70. https://doi.org/10.1016/j.proci.2016.07.108.

[84] Botero ML, Akroyd J, Chen D, Kraft M, Agudelo JR. On the thermophoretic sampling and TEM-based characterisation of soot particles in flames. Carbon N Y 2021;171:711–22. https://doi.org/10.1016/j.carbon.2020.09.074.

[85] Messerer A, Niessner R, Pöschl U. Thermophoretic deposition of soot aerosol particles under experimental conditions relevant for modern diesel engine exhaust gas systems. J Aerosol Sci 2003;34:1009–21. https://doi.org/10.1016/S0021-8502(03)00081-8.

[86] De Falco G, Carbone F, Commodo M, Minutolo P, D’Anna A. Exploring nanomechanical properties of soot particle layers by atomic force microscopy nanoindentation. Applied Sciences (Switzerland) 2021;11. https://doi.org/10.3390/app11188448.

[87] Commodo M, De Falco G, Larciprete R, D'Anna A, Minutolo P. On the hydrophilic/hydrophobic character of carbonaceous nanoparticles formed in laminar premixed flames. Exp Therm Fluid Sci 2016;73:56–63. https://doi.org/10.1016/j.expthermflusci.2015.09.005.

[88] Migliorini F, de Iuliis S, Cignoli F, Zizak G. How "flat" is the rich premixed flame produced by your McKenna burner? Combust Flame 2008;153:384–93. https://doi.org/10.1016/j.combustflame.2008.01.007.

[89] Clauss W, Fabelinsky VI, Kozlov DN, Smirnov V v, Stelmakh OM, Vereschagin KA. Dual-broadband CARS temperature measurements in hydrogen-oxygen atmospheric pressure flames. Applied Physics B 2000;70:127–31. https://doi.org/10.1007/s003409900090.

[90] Schulz C, Kock BF, Hofmann M, Michelsen H, Will S, Bougie B, et al. Laser-induced incandescence: Recent trends and current questions. Appl Phys B 2006;83:333–54. https://doi.org/10.1007/s00340-006-2260-8.

[91] Pizzi G, Milana S, Ferrari AC, Marzari N, Gibertini M. Shear and Breathing Modes of Layered Materials. ACS Nano 2021;15:12509–34. https://doi.org/10.1021/acsnano.0c10672.

[92] Tauc J, Grigorovici R, Vancu A. Optical Properties and Electronic Structure of Amorphous Germanium. Physica Status Solidi (b) 1966;15:627–37. https://doi.org/10.1002/pssb.19660150224.

[93] Smyth KC, Shaddix CR. The Elusive History of rh = 1.57-0.56i for the Refractive Index of Soot. Combust Flame 1996;107:314–20.

[94] Griepentrog M, Krämer G, Cappella B. Comparison of nanoindentation and AFM methods for the determination of mechanical properties of polymers. Polym Test 2013;32:455–60. https://doi.org/10.1016/j.polymertesting.2013.01.011.

[95] Butt HJ, Cappella B, Kappl M. Force measurements with the atomic force microscope: Technique, interpretation and applications. Surf Sci Rep 2005;59:1–152. https://doi.org/10.1016/j.surfrep.2005.08.003.

[96] Natori K. Ballistic metal-oxide-semiconductor field effect transistor. J Appl Phys 1994;76:4879–90. https://doi.org/10.1063/1.357263.

[97] Ye PD, Wilk GD, Yang B, Kwo J, Chu SNG, Nakahara S, et al. GaAs metal-oxide-semiconductor field-effect transistor with nanometer-thin dielectric grown by atomic layer deposition. Appl Phys Lett 2003;83:180–2. https://doi.org/10.1063/1.1590743.

[98] Zhan Z, Wang WN, Zhu L, An WJ, Biswas P. Flame aerosol reactor synthesis of nanostructured SnO2 thin films: High gas-sensing properties by control of

morphology. Sens Actuators B Chem 2010;150:609–15. https://doi.org/10.1016/j.snb.2010.08.032.

[99] Kim YS, Ha SC, Yang Y, Kim YJ, Cho SM, Yang H, et al. Portable electronic nose system based on the carbon black-polymer composite sensor array. Sens Actuators B Chem, vol. 108, 2005, p. 285–91. https://doi.org/10.1016/j.snb.2004.11.067.

[100] Zhang B, Wang D, Yu B, Zhou F, Liu W. Candle soot as a supercapacitor electrode material. RSC Adv 2014;4:2586–9. https://doi.org/10.1039/c3ra42507j.

[101] Wei Z, Yan K, Chen H, Yi Y, Zhang T, Long X, et al. Cost-efficient clamping solar cells using candle soot for hole extraction from ambipolar perovskites. Energy Environ Sci 2014;7:3326–33. https://doi.org/10.1039/c4ee01983k.

[102] Saji VS. Carbon nanostructure-based superhydrophobic surfaces and coatings. Nanotechnol Rev 2021;10:518–71. https://doi.org/10.1515/ntrev-2021-0039.

[103] Baldelli A, Esmeryan KD, Popovicheva O. Turning a negative into a positive: Trends, guidelines and challenges of developing multifunctional non-wettable coatings based on industrial soot wastes. Fuel 2021;301. https://doi.org/10.1016/j.fuel.2021.121068.

[104] Yang C, Li Z, Huang Y, Wang K, Long Y, Guo Z, et al. Continuous Roll-to-Roll Production of Carbon Nanoparticles from Candle Soot. Nano Lett 2021;21:3198–204. https://doi.org/10.1021/acs.nanolett.1c00452.

[105] Cancian J, Bennett BAV, Colket MB, Smooke MD. Prediction of electron and ion concentrations in low-pressure premixed acetylene and ethylene flames. Combustion Theory and Modelling 2013;17:294–315. https://doi.org/10.1080/13647830.2012.759278.

[106] Sgro LA, D'Anna A, Minutolo P. Charge distribution of incipient flame-generated particles. Aerosol Science and Technology 2010;44:651–62. https://doi.org/10.1080/02786826.2010.483701.

[107] Majid H, Winker-Heil R, Madl P, Hofmann W, Alam K. Effect of Oral Pathway on Charged Particles Deposition in Human Bronchial Airways. J Aerosol Med Pulm Drug Deliv 2016;29:24–9. https://doi.org/10.1089/jamp.2014.1194.

[108] Carotenuto C, Di Natale F, Lancia A. Wet electrostatic scrubbers for the abatement of submicronic particulate. Chemical Engineering Journal 2010;165:35–45. https://doi.org/10.1016/j.cej.2010.08.049.

[109] Di Natale F, Carotenuto C, Parisi A, Flagiello D, Lancia A. Wet electrostatic scrubbing for flue gas treatment. Fuel 2022;325. https://doi.org/10.1016/j.fuel.2022.124888.

[110] Kuhl J, Seeger T, Zigan L, Will S, Leipertz A. On the effect of ionic wind on structure and temperature of laminar premixed flames influenced by electric fields. Combust Flame 2017;176:391–9. https://doi.org/10.1016/j.combustflame.2016.10.026.

[111] Xu KG. Plasma sheath behavior and ionic wind effect in electric field modified flames. Combust Flame 2014;161:1678–86. https://doi.org/10.1016/j.combustflame.2013.12.008.

[112] Sardari PT, Rahimzadeh H, Ahmadi G, Giddings D. Nano-particle deposition in the presence of electric field. J Aerosol Sci 2018;126:169–79. https://doi.org/10.1016/j.jaerosci.2018.09.012.

[113] Xiong G, Kulkarni A, Dong Z, Li S, Tse SD. Electric-field-assisted stagnation-swirl-flame synthesis of porous nanostructured titanium-dioxide films. Proceedings of the Combustion Institute 2017;36:1065–75. https://doi.org/10.1016/j.proci.2016.08.079.

[114] Sabzyan H, Ghalami F. Electric field effects on the growth of flame-synthesized nanosilica: a two-stage modeling. Journal of the Iranian Chemical Society 2019;16:963–78. https://doi.org/10.1007/s13738-019-01591-9.

[115] Mädler L, Roessler A, Pratsinis SE, Sahm T, Gurlo A, Barsan N, et al. Direct formation of highly porous gas-sensing films by in situ thermophoretic deposition of flame-made Pt/SnO 2 nanoparticles. Sens Actuators B Chem 2006;114:283–95. https://doi.org/10.1016/j.snb.2005.05.014.

[116] Lawton J, Payne KG, Weinberg FJ. Flame-Arc Combination. Nature 1962;193:736–8.

[117] Calcote HF, Pease RN. Electrical properties of flames. Burner Flames in Longitudinal Electric Fields. Ind Eng Chem 2021;18:2726–31.

[118] Chen B, Wang H, Wang Z, Han J, Alquaity ABS, Wang H, et al. Ion chemistry in premixed rich methane flames. Combust Flame 2019;202:208–18. https://doi.org/10.1016/j.combustflame.2019.01.009.

[119] Belhi M, Domingo P, Vervisch P. Direct numerical simulation of the effect of an electric field on flame stability. Combust Flame 2010;157:2286–97. https://doi.org/10.1016/j.combustflame.2010.07.007.

[120] Call TS, Schwartz DB. Electric fields for flame extinguishment. Florida: 1993.

[121] Calcote HF. Ion and electron profiles in flames. Symposium (International) on Combustion 1963;9:622–37.

[122] Pedersen T, Brown RC. Simulation of Electric Field Effects in Premixed Methane Flames. vol. 94. 1993.

[123] Delfau JL, Michaud P, Barassin A. Formation of small and large positive ions in rich and sooting low-pressure ethylene and acetylene premixed flames. Combustion

Science and Technology 1979;20:165–77. https://doi.org/10.1080/00102207908946906.

[124] Jaggers HC, von Engel A. The Effect of Electric Fields ou the Burning Velocity of Various Flames. Combust Flame 1971;16:275–85.

[125] Saito M, Sato M, Sawada K. Variation of flame shape and soot emission by applying electric field. vol. 39. 1997.

[126] Vinogradov J, Sher E, Rutkevich I, Mond M. Voltage-Current Characteristics of a Flame-Assisted Unipolar Corona. Combust Flame 2001;127:2041–50.

[127] Volkov EN, Sepman A v, Konnov AA, Shoshin YS, de Goey LPH. Towards the mechanism of DC electric field effect on flat premixed flames. Proceedings of the European Combustion Meeting, 2009.

[128] Wang Y, Nathan GJ, Alwahabi ZT, King KD, Ho K, Yao Q. Effect of a uniform electric field on soot in laminar premixed ethylene/air flames. Combust Flame 2010;157:1308–15. https://doi.org/10.1016/j.combustflame.2010.03.001.

[129] Biswas JC, Mitra V. High-Frequency Breakdown and Paschen Law. Applied Physics 1979;19:377–81.

[130] Ma Y, Li T, Yan J, Wang X, Gao J, Sun Z. A comprehensive review of the influence of electric field on flame characteristics. Preprints (Basel) 2020. https://doi.org/10.20944/preprints202010.0454.v1.

[131] Thomson JJ. Report of the British Association. 1910.

[132] Zigan L. Overview of electric field applications in energy and process engineering. Energies (Basel) 2018;11. https://doi.org/10.3390/en11061361.

[133] Altendorfner F, Kuhl J, Zigan L, Leipertz A. Study of the influence of electric fields on flames using planar LIF and PIV techniques. Proceedings of the Combustion Institute 2011;33:3195–201. https://doi.org/10.1016/j.proci.2010.05.112.

[134] Han J, Belhi M, Casey TA, Bisetti F, Im HG, Chen JY. The i-V curve characteristics of burner-stabilized premixed flames: Detailed and reduced models. Proceedings of the Combustion Institute 2017;36:1241–50. https://doi.org/10.1016/j.proci.2016.05.056.

[135] Primo A, Corma A, García H. Titania supported gold nanoparticles as photocatalyst. Physical Chemistry Chemical Physics 2011;13:886–910. https://doi.org/10.1039/c0cp00917b.

[136] Portillo-Vélez NS, Zanella R. Comparative study of transition metal (Mn, Fe or Co) catalysts supported on titania: Effect of Au nanoparticles addition towards CO oxidation and soot combustion reactions. Chemical Engineering Journal 2020;385. https://doi.org/10.1016/j.cej.2019.123848.

[137] Allen NS, Edge M, Ortega A, Sandoval G, Liauw CM, Verran J, et al. Degradation and stabilisation of polymers and coatings: Nano versus pigmentary titania particles. Polym Degrad Stab, vol. 85, Elsevier Ltd; 2004, p. 927–46. https://doi.org/10.1016/j.polymdegradstab.2003.09.024.

[138] Luo Y, Canning J, Zhang J, Peng GD. Toward optical fibre fabrication using 3D printing technology. Optical Fiber Technology 2020;58. https://doi.org/10.1016/j.yofte.2020.102299.

[139] Rishi K, Pallerla L, Beaucage G, Tang A. Dispersion of surface-modified, aggregated, fumed silica in polymer nanocomposites. J Appl Phys 2020;127. https://doi.org/10.1063/1.5144252.

[140] Daşdelen Z, Özcan AA, Özcan A. Preparation of anode catalysts for sorbitol electrooxidation based on the nanocomposites of fumed silica, reduced graphene oxide and gold nanoparticles. Int J Hydrogen Energy 2021;46:28121–33. https://doi.org/10.1016/j.ijhydene.2021.06.060.

[141] Liu J, Xue W, Jin G, Zhai Z, Lv J, Hong W, et al. Preparation of tin oxide quantum dots in aqueous solution and applications in semiconductor gas sensors. Nanomaterials 2019;9. https://doi.org/10.3390/nano9020240.

[142] Sharma A, Ahmed A, Singh A, Oruganti SK, Khosla A, Arya S. Review—Recent Advances in Tin Oxide Nanomaterials as Electrochemical/Chemiresistive Sensors. J Electrochem Soc 2021;168:027505. https://doi.org/10.1149/1945-7111/abdee8.

[143] Hardesty DR, Weinberg FJ. Electrical control of particulate pollutants from flames. Symposium (International) on Combustion 1973;14:907–18. https://doi.org/10.1016/S0082-0784(73)80083-9.

[144] Pratsinis SE. Flame aerosol synthesi of ceramic powders. Prog Energy Combust Sci 1998;24:197–219.

[145] Rodríguez-Pérez D, Castillo JL, Antoranz JC. Density scaling laws for the structure of granular deposits. Phys Rev E Stat Nonlin Soft Matter Phys 2007;76. https://doi.org/10.1103/PhysRevE.76.011407.

[146] Tassopoulos A O MJ, Rosner E. Simulation of Microstructure/Mechanism Relationships in Particle Deposition. AIChE Journal 1989;35:967–80.

[147] Meakin P, Ramanlal P, Sander LM, Ball RC. Ballistic deposition on surfaces. Phys Rev A (Coll Park) 1986;34:5091–103.

[148] Kardar M, Parisi G, Zhang Y-C. Dynamic Scaling of Growing Interfaces. Phys Rev Lett 1986;56:889–92.

[149] Arai H, Asami K, Ito H, Katayama N. Effect of the settings of electrospray deposition method on the structure and performance of the fuel cell catalyst layer. Current Applied Physics 2022;39:296–303. https://doi.org/10.1016/j.cap.2022.05.014.

[150] Zhao XY, Yang W, Li C, Wang X, Lim SL, Qi D, et al. Effects of Damkhöler number of evaporation on the morphology of active layer and the performance of organic heterojunction solar cells fabricated by electrospray method. Solar Energy Materials and Solar Cells 2015;134:140–7. https://doi.org/10.1016/j.solmat.2014.11.029.

[151] Conde JJ, Ferreira-Aparicio P, Chaparro AM. Electrospray Deposition: A Breakthrough Technique for Proton Exchange Membrane Fuel Cell Catalyst Layer Fabrication. ACS Appl Energy Mater 2021;4:7394–404. https://doi.org/10.1021/acsaem.1c01445.

[152] Sung DH, Doshi SM, Murray C, Rider AN, Thostenson ET. Electrophoretic deposition: Novel in situ film growth mechanism of carbon nanocomposite films within non-conductive fabrics for multi-scale hybrid composites. Compos Sci Technol 2020;200. https://doi.org/10.1016/j.compscitech.2020.108415.

Chapter 2

Materials and Methods

This chapter contains two sections. In the first one, the experimental setup and procedures used to produce CNP films by electric field-assisted flame synthesis are described. In the second, the ex-situ analytical techniques adopted for the morphological, chemical, structural, electrical, and surface-wetting characterization of the produced CNP films are discussed in detail.

This chapter refers, but is not limited, to the following papers:

1. Parisi, A., Carotenuto, C., De Falco, G., Sirignano, M., Di Natale, F. (2021). Electrophoretic deposition of carbon nanoparticles film produced in flame: a preliminary investigation. *Proceedings of the 10th European Combustion Meeting*, 884-889.
2. Parisi, A., De Falco, G., Sirignano, M., Minutolo, P., Commodo, M., Carotenuto, C., Di Natale, F. (submitted). Modelling the electrophoretically-enhanced in-flame deposition of carbon nanoparticles. *Journal of Aerosol Science*.
3. Parisi, A., Darvehi, P., De Falco, G., Commodo, M., Apicella, B., Russo, C., Di Natale, F., Minutolo, P. (under submission). Experimental findings on the electric field- assisted in-flame deposition of Carbon NanoParticle films.
4. Griffo, R., Parisi, A., De Falco, G., Sirignano, M., Di Natale, F., Minale, M., Carotenuto, C. (under submission).Wettability of carbon nanofilms with different fluids. Preliminary results.

Contents

2.1 Experimental apparatus

A sketch of the complete setup for CNP film deposition is shown in **Figure 2.1**.

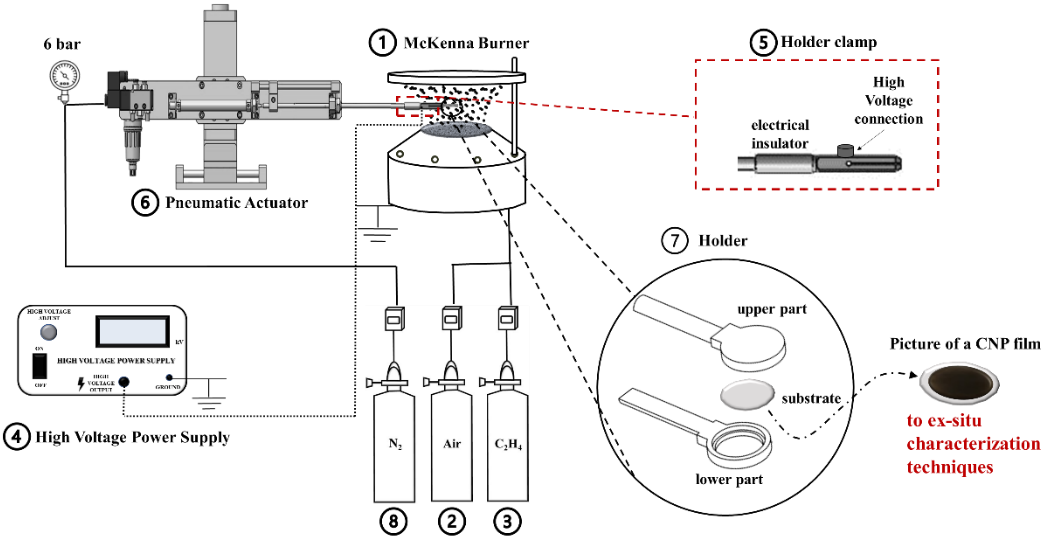

Figure 2.1. Sketch of the electric field-assisted CNP film production in flame. CNPs reactor: (1) McKenna Burner; (2)-(3) Air and Ethylene cylinders; Electrical Charging Unit: (4) High Voltage Power Supply; (5) Holder clamp; Sampling System: (6) Pneumatic Actuator, (7) Holder containing the Mica Muscovite/Borosilicate Glass/ metal-based InterDigitated Electrodes substrates for CNP film deposits, and (8) Nitrogen cylinder. A picture of a CNP film is also included on the right.

From **Figure 2.1**, it can be seen that the experimental apparatus for CNP film production consist of three main units, that are the flame reactor for CNP production, the Electrical Charging Unit, and the Sampling System.

2.1.1 Reactor for CNP production

CNPs have been generated by a flat laminar premixed ethylene-air flame which has been produced by a controlled, stabilized water-cooled McKenna burner (1) shown in **Figure 2.2**. Ethylene has been chosen because it is one of the products of the decomposition of hydrocarbons and it is usually used, together with methane, as representative of the combustion of aliphatic hydrocarbons. It can be also formed during the decomposition of oxygenated compounds [1–4].

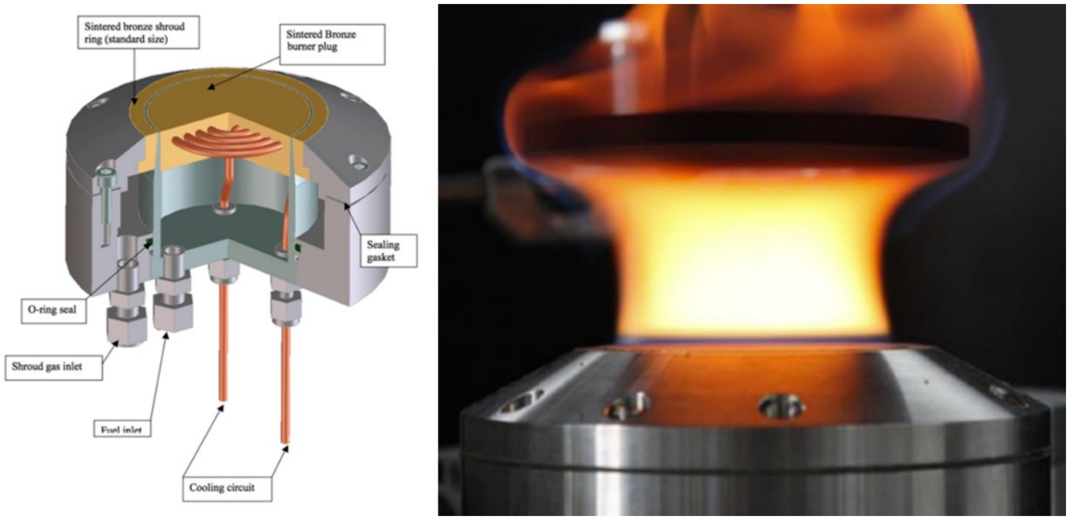

Figure 2.2. Overview of the McKenna Flat Flame Burner (left); an example of a rich ethylene/air flame stabilized above the McKenna burner (right). Adapted from Langenkamp [5].

The McKenna burner is a commercially available reactor that has long been used in combustion research [6,7]. A bronze porous sintered matrix burner disk with a diameter of 6 cm is contained in a stainless-steel housing that is fastened to the main body. The plate has an Archimedean spiral cooling circuit for water flow that minimizes radial thermal gradients. The premixed oxidizer (2) and fuel (3) are put into the bottom of the housing and distributed evenly through the burner. Cavities in the housing beneath the sintered burner plug and shroud ring guarantee a smooth fuel flow by buffering pressure surges. Furthermore, to enhance flame stability, a stabilization plate is positioned at a height above the burner equal to 22 mm. The McKenna burner provides repeatable and stable flame conditions if suitably instrumented for gas flow control. As a result, this laminar flow burner has established the gold standard for studying 1-D premixed flames [4,5,7,8], since combustion evolves only along the flame's axis. Because of the laminar character of these flames, it is also possible to accurately measure the evolution of temperature, gas concentration and particle concentrations as a function of combustion time, as it is very simple to convert the height above the burner (HAB) to a corresponding residence time. Additionally, owing to the narrow channels in the sintered burner plug, there is no risk of flashback, as flames cannot propagate through the burner deck. Moreover, the use of bronze for the burner plug offers higher heat conduction compared to other materials (*i.e* stainless steel), making it suitable for stabilizing higher-temperature flames.

To investigate the production of CNP films in slightly sooting conditions, the C/O ratio has been set to 0.67 using an air (N5.0 with 99.999% purity manufactured by Sol Group) flow rate of 13.06 L/min and an ethylene (N3.5 with 99.97% purity manufactured by Sol Group) flow rate of 1.79 L/min that have been actively maintained via flow controllers. Under these conditions, the cold gas velocity at the burner mouth is equal to 9.8 cm/s. This flame has been extensively characterized over the past decades by the Combustion Research group of the University Federico II and the STEMS-CNR of Naples [2,4,9–16]. In particular, the size distribution of the CNPs in the aerosol phase has been measured by Scanning Mobility Particle Sizer, showing that CNPs harvested at a height above the burner surface (HAB) higher than 10 mm have a typical bimodal number particle size distribution (PSD), with a first mode around 2-3 nm and a second one made by particles larger than 10 nm. This second mode is the one dominating mass-based particle size distribution.

The CNPs charge distributions are also known from previous works [15,16]. The experiments indicated an equal distribution of positively and negatively charged particles sampled from flames at atmospheric pressure and that all the particles with sizes up to 20 nm carry on at most a single electric charge [17,18]. **Figure 2.3** shows examples of Number and Volume PSD for total CNPs and the Number PSD for charged CNPs for a C/O ratio equal to 0.67 and HAB equal to 15 mm.

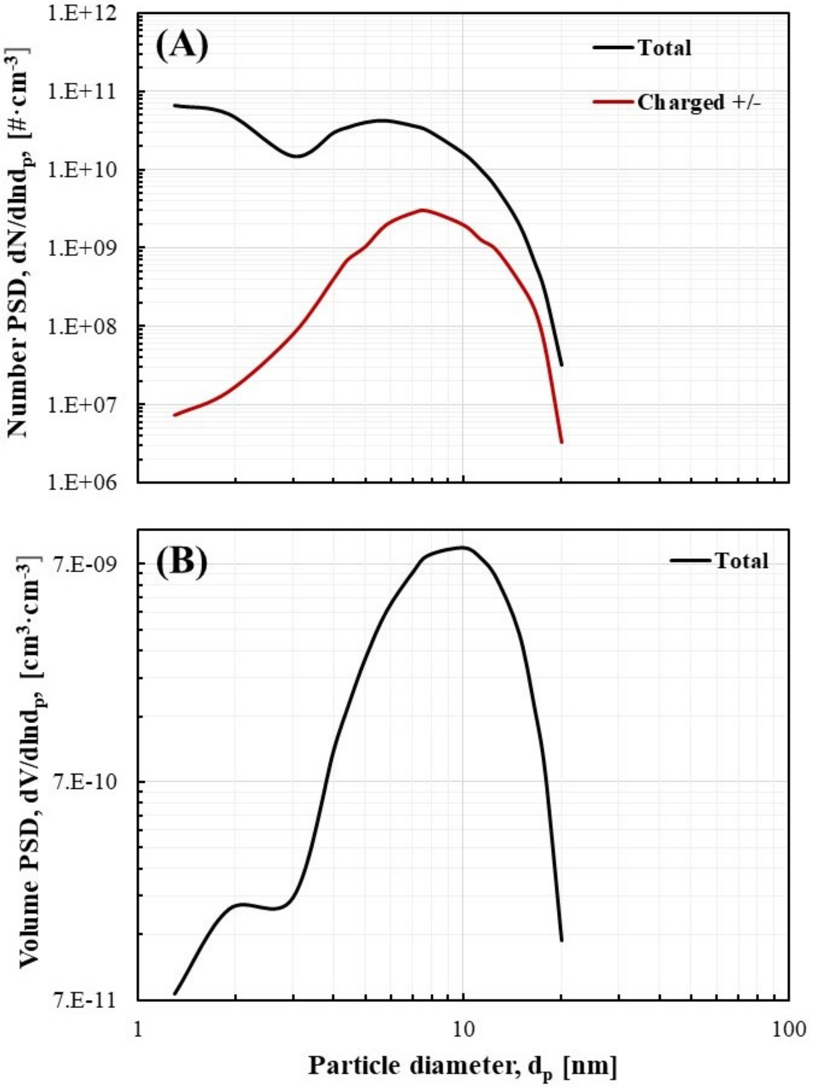

Figure 2.3. (A) Particle size distribution in number (Number PSD) of total (black line) and positively/negatively charged CNPs (red line); **(B)** Particle size distribution in volume (Volume PSD) of total CNPs produced in ethylene-air flames for C/O=0.67 and HAB=15 mm [2,4,9–16].

2.1.2 Electrical charging Unit

A High Voltage Power Supply (4) Spellmann model Bertan 230-20R with reversible polarity has been used to generate and sustain the external electric field.

In this regard, it should be specified that, strictly speaking, two different approaches could be adopted for the electric field-assisted harvesting of CNPs, schematized in **Figure 2.4**.

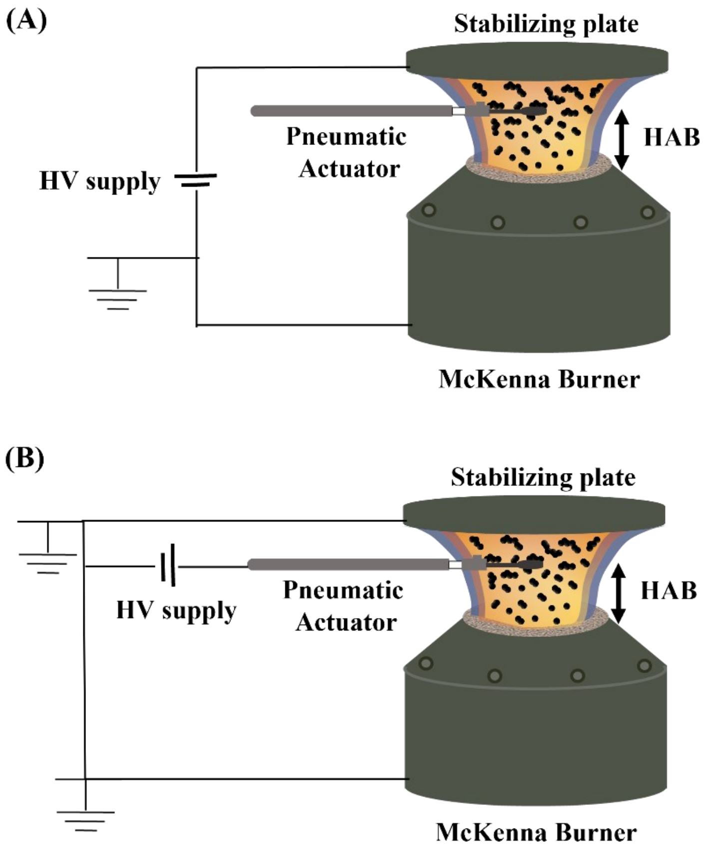

Figure 2.4. Simplified representations of the possible electric circuits that can be used to study the effects of an external electric field during the in-flame CNPs deposition in a sooting flame stabilized on a McKenna Burner: **(A)** HV power supply connected to the stabilizing plate and burner grounded; **(B)** Insertion of a substrate connected to the HV supplier in a grounded burner.

A first option is that an electric potential is applied to the stabilizing plate (panel **A Figure 2.4**), while the burner is grounded. As pointed out in **Chapter 1**, this results in significant alterations in the flame behaviour with some phenomena of flame flickering, convergence or divergence depending on the value and the polarity of the applied potential [19–23]. Moreover, there are effects on the CNPs production: positive (negative) polarity determines longer (shorter) CNPs residence time in the flame, with the production of larger (smaller) CNPs. Consequently, the amount of produced CNPs changes. Evidence of such effects for a McKenna burner is shown in **Figure 2.5**.

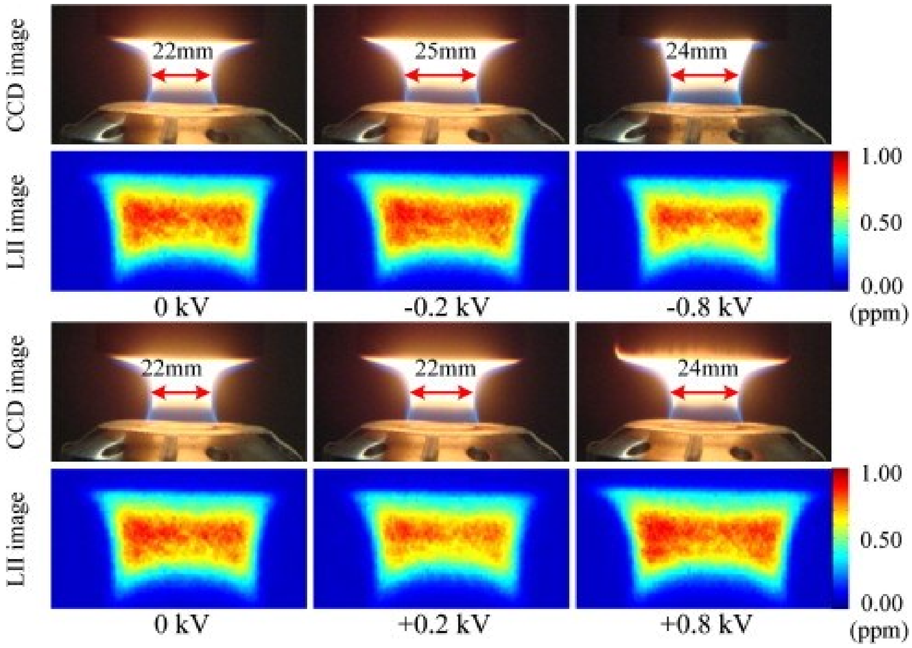

Figure 2.5. Evidence of alteration in flame behavior and soot concentration evolution in ppm obtained via laser-induced incandescence in a laminar premixed ethylene/air (C/O=0.74) flame stabilized on a McKenna Burner when a positive/negative potential is applied to the stabilizing plate. Adapted from Wang et al. [19].

In this configuration, the CNP film is produced over the stabilizing plate itself and electro/thermophoresis deposition can be produced by using a rotating stabilizing plate as reported by De Falco et al. [24].

The second option considers the electric potential applied directly to a CNPs deposition substrate, inserted in flame, maintaining both the burner and the stabilizing plate grounded (panel **B Figure 2.4**).

Theoretically, a fast enough insertion of the charged substrate in flame may affect the dynamics of particle impact with the substrate, but it is expected that neither the flame behaviour nor the kinetics of nanoparticles growth inside the flame is altered. The characteristic time of flame reactions is significantly shorter than the time of the electrical perturbation in flame: a steady-state condition for flame kinetics is achieved in the time required for a single fast insertion. In this work, the second configuration has been used, following the works made by our research group for thermophoretic deposition of CNPs [25,26].

2.1.3 Sampling system

The sampling system consists of a double-acting pneumatic cylinder (6) fed with nitrogen at 6 bar (8) equipped with a mobile extension arm, used to insert at a specific height above the burner surface (here 15 mm) a holder (7) which contains the CNP film substrate. Once the flame has stabilised within a few minutes, the user can set the time for each insertion (t_{ins}) and the time between two consecutive insertions. This sampling technique has been previously used to obtain CNP films under thermophoretic deposition [25–28] and has been shown that an insertion time of 100 ms is a good compromise between deposition rate, which allows collecting enough CNPs to estimate their size and morphology [28], and production of a quite homogeneous coating of the whole substrate, to investigate CNP film properties [25,26]. Moreover, a 10 seconds time between two consecutive insertions has been found to be sufficient to cool the substrate down to room temperature. In order to guarantee the application of the electric potential to the substrate, it has been necessary to partially modify the former pneumatic actuator. Specifically, a metallic holder clamp with a screw (5) has been designed to secure the electrical connection via high-voltage cable between the clamp itself and the HV power supply, and to ensure safety operation of the experimental apparatus, an electrical insulating support (5) has been provided for the connection between the holder clamp and the pneumatic actuator arm. Moreover, the pneumatic actuator has been equipped with an anti-rotation system to ensure that the holder always enters parallel to the burner mouth.

The holder (7) has been specially designed to accommodate circular (ID: 10 mm) substrates in mica muscovite or glass borosilicate where CNPs will be collected. The substrates used are made of dielectric materials, whose low thickness does not lead to an electric voltage drop respect to that applied to the holder.

Mica muscovite (OD:10 mm) offers a clean surface for Atomic Force Applications. This is a uniform and nearly flat surface, free of all strains, foreign inclusions, cracks, and other similar defects with a 0.251 mm thickness. All these properties make it a very good example of an ideally smooth surface [28]. Borosilicate glass discs (OD:10mm) with a thickness of 0.300 mm are lightweight, low-cost substrates that are inert enough to be proficiently used for optical characterization tests. In addition, tests have been performed with metal-based InterDigitated Electrodes, consisting of a gold thin film on a glass substrate, which have been used to evaluate the current-voltage characteristics of the CNP samples. Details on this substrate will be provided in **Paragraph 2.3.5**.

2.2 Experimental Protocol

In this paragraph, the experimental protocol for CNP films production by electric field-assisted flame synthesis is described. The operating conditions have been chosen to investigate the effects of an external electric field on CNP film deposition. To this aim, the electric potential on the substrate is varied from 0 kV up to -3kV, below the onset of corona discharge which occurs at nearly -4 kV. In this work, only negative electric potentials have been considered because in presence of positive polarities, instabilities and flame extinctions have been observed and also reported by Wang et al. [19]. Furthermore, the amount of material deposited in the presence of positive polarity was much lower than that retrieved for pure thermophoresis. For each fixed electric potential, the number of insertions in flame (N_{ins}) has been fixed to obtain CNP films either with the desired deposited mass or with comparable absorbance values. As will be shown in **Chapter 3**, in presence of a voltage, there is an increase in the harvesting rate: therefore the number of insertions required to obtain a given deposited mass or absorbance is lower when the voltage is increased. Moreover, for each electric potential, samples have been produced after a single insertion in flame, to analyse the size and shape of CNP primary particles or aggregates. **Table 2.1** resumes all the explored experimental conditions.

Table 2.1. List of the explored experimental conditions.

Description (units)	**Value**
C/O ratio (-)	0.67
Cold gas velocity (cm/s)	9.8
Sampling position *HAB* (mm)	15
Insertion time t_{ins} (ms)	100
Deposition substrates	Mica Muscovite; Borosilicate Glass; Metal InterDigitated Electrodes
Applied electric potential *V* (kV)	From 0 to -3 kV
Number of insertions N_{ins} (#)	At 0 kV: 1; from 100 to 600 At -1 kV: 1; from 40 to 200 At -2 kV:1; from 35 to 175 At -3 kV:1; from 25 to 150

The sequence of steps for producing CNP films are outlined below:

1. Examine the electrical connections in the system. Check that the burner and the stabilizing plate are properly grounded and that the high-voltage cable is connected to the holder clamp. Connect the voltage generator to the ground.

2. Using the micro-screw system, fix the holder height above the burner to HAB=15 mm. Ensure that in the end position for the extensor arm, the holder is exactly in the centre of the burner mouth to avoid edge effects.
3. Open the air and the ethylene cylinders connected to the burner, and the nitrogen cylinder connected to the pneumatic actuator.
4. Check the pressure read by the pressure gauge connected to the actuator: a value of 6 bar is required.
5. Set an ethylene flow rate of 1.79 L/min by mass flow controller. Then, using a torch, an ethylene diffusion flame is switched on.
6. Set an air flow rate of 13.06 L/min to obtain a carbon-oxygen ratio of 0.67. The later addition of air avoids highly dangerous stoichiometric flame conditions.
7. Wait a few minutes for the flame stabilization.
8. Place a substrate, after cleaning it with ethanol, inside the holder.
9. Switch on the High Voltage Power Supply and set a value V_0 of the electric potential.
10. Use the actuator control system to set the insertion time t_{ins} and the time between two insertions.
11. When finished, switch off the High Voltage Power Supply and wait for the holder to cool down.
12. Remove the substrate with the deposited CNP film from the holder and collect the samples into a polystyrene Petr dish.
13. The CNP film is ready for ex-situ characterization.
14. Repeat steps 10-13 with a different number of insertions N_{ins}.
15. Repeat steps 9-14 varying the electric potential V_0.
16. Switch off the HV potential, the pneumatic actuator and close the cylinders after tests are completed.
17. Remove carbon waste from the pneumatic arm and the stabilizing plate.

2.3 Analytical techniques

CNP films have been analysed with a number of techniques. UV-vis absorption has been performed directly on the produced CNP films [25,28]. Then, the same CNP samples have been characterized by Raman Spectroscopy [10,25,28,29], Atomic Force Microscopy [25,28], Surface texture Analysis [30–32], Current-Voltage [25], and Contact Angle measurements [33,34]. At last, these CNP samples have been completely removed from the glass substrate by dispersion in N-methyl pyrrolidone (NMP) in an ultrasonic bath (5 min, 59 kHz). Solvent-dispersed CNPs have been analysed by UV-Vis spectroscopy and size exclusion chromatography (SEC). The carbon dispersion has been filtered on an Anotop filter (Whatman) to separate the CNP agglomerates smaller than 20 nm and smaller than 100 nm. These have been analysed by UV-vis absorption, fluorescence spectroscopy, and SEC analysis [27,35,36]. The figure shows a summary of the ex-situ characterizations carried out on the CNP films.

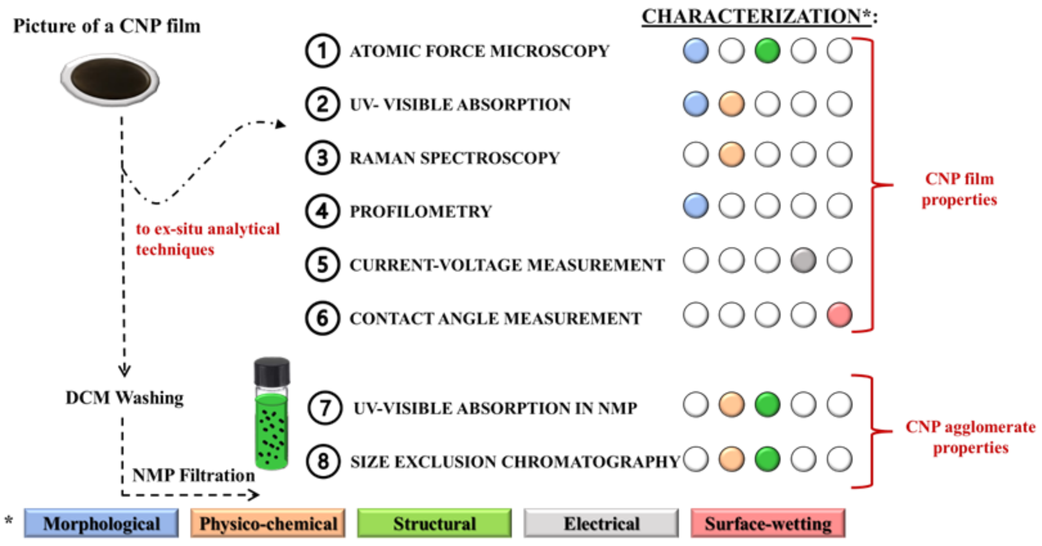

Figure 2.6. Overview of the ex-situ analytical techniques adopted for the CNP films and agglomerates characterization.

In the following sections, the different analytical techniques are presented, explaining in detail the information that can be obtained from each of them and how they can be used to characterize the CNP films and agglomerates.

2.3.1 Atomic Force Microscopy

Atomic force microscopy (AFM) measurements have been performed in the Clean Combustion Research Lab (University of Naples Federico II and CNR-STEMS) with a Scanning Probe Microscope NTEGRA Prima from NT-MDT, operated in semi-contact mode in air and equipped with NANOSENSORS^{TM} SSS-NCHR super-sharp silicon probes with a nominal tip radius of 2 nm. The AFM is a Scanning Probe Microscope that has a long history of use in determining the size and shape of isolated CNPs or CNP films [25,28,37,38]. When compared to other microscopic techniques, the AFM provides image resolution up to the Angstrom scale. A typical AFM system (**Figure 2.7**) consists of a cantilever probe with a sharp tip attached to a Piezoelectric (PZT) actuator and a position-sensitive photodetector for receiving a laser beam reflected off the beam's end-point to provide a cantilever deflection feedback.

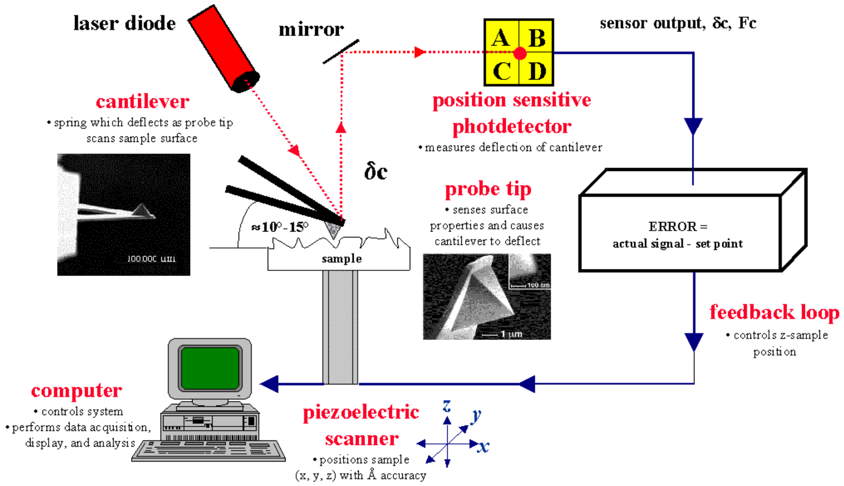

Figure 2.7. Atomic force microscopy: general components and their function.

The contact between the nanometric probe at the end of the cantilever and the sample surface is at the heart of the AFM working principle; the probe scans the surface, interacting with the sample via attractive or repulsive Van der Waals forces.

Typically, AFM is operated in a semi-contact mode to obtain surface topography measurements. The semi-contact mode requires that a distance of between 5 and 15 nm always remains between the tip and the sample surface. The van der Waals forces acting between the tip and the sample are evaluated quantitatively and a microtopographic image of the sample is produced based on this measurement. A small oscillation is applied to the tip and the weak forces involved are measured by analysing the changes in amplitude, phase, and frequency of the tip oscillations. In this way, both 3D and 2D images with a resolution of 1-2 nm in the *xy* plane and 0.1 nm along the *z* axis are obtained in low noise conditions. Mica muscovite disks (OD:10mm) are the substrates used for AFM analysis, as mentioned before, due to their features such as low roughness, elevated mechanical and chemical resistance to flame temperature and also the possibility to obtain a clean surface by cleaving process.

Figure 2.8 shows examples of 3D and 2D images for isolated CNPs obtained using the AFM software.

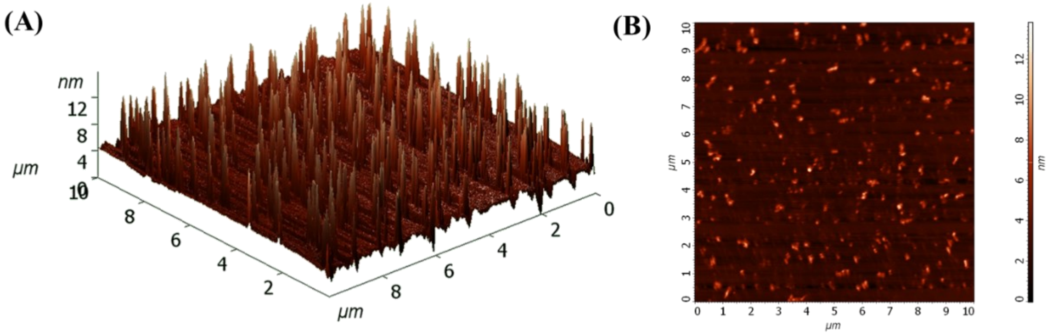

Figure 2.8. Typical 3D **(A)** and 2D **(B)** images for isolated CNPs obtained in our experimental campaign for an electric potential applied to the deposition substrate equal to V_0=0 kV and with a single insertion in flame *(C/O=0.67;* t_{ins}*=100 ms; HAB=15 mm;* N_{ins}*=1)*.

From these images, it is possible to obtain information about the CNP sizes, shapes, and spatial distribution on the substrate. In addition, when a CNP film is analysed, information about average roughness on the nanoscale ($S_{a,AFM}$), and maximum height ($S_{max,AFM}$) of the nanostructures can be obtained. Moreover, AFM also gives information about the grain size and distribution in thin films [39–41] in terms of excess Kurtosis (E_{ku}). The excess kurtosis measures how sharp the surface spikes are and how uniform they are about the mean line (zero-excess kurtosis with normal distribution for the roughness): an excess kurtosis value greater than 0 indicates a spiky surface, whereas surfaces with excess kurtosis lower than 0 are more “bumpy”.

2.3.2 UV-vis Absorption Spectroscopy

An Agilent UV-vis 8453 spectrophotometer has been used to record the UV-vis absorption spectra of CNP films deposited on glass substrates [25,28]. Ultraviolet-visible (UV-vis) absorption spectroscopy is an optical technique based on the measurement of the attenuation of electromagnetic radiation by an absorbing substance in a specific wavelength region. Typically, the UV-vis spectral range is 190-950 nm [42]. In our condition, glass borosilicate is used as a deposition substrate. This implies that all the spectra will be reliable from around 350 nm onwards, as glass causes non-negligible absorption at lower wavelengths.

From the UV-vis light absorbance, for each wavelength it is possible to obtain the fraction of absorbed light, *i.e.* the absorbance $Abs(\lambda)$, defined as the logarithm of the ratio of incident P_0 to transmitted $P(\lambda)$ radiant power through the sample [42]:

$$Abs(\lambda) = log \frac{P_0}{P(\lambda)} \tag{2.1}$$

Figure 2.9 shows examples of UV-vis Absorption spectra for CNP films obtained in our experimental campaign for a fixed value of the electric potential applied to the deposition substrate (V_0=0) and varying the number of insertions in flame (N_{ins}). In this chart, the Absorbance $Abs(\lambda)$ is reported against the wavelength λ.

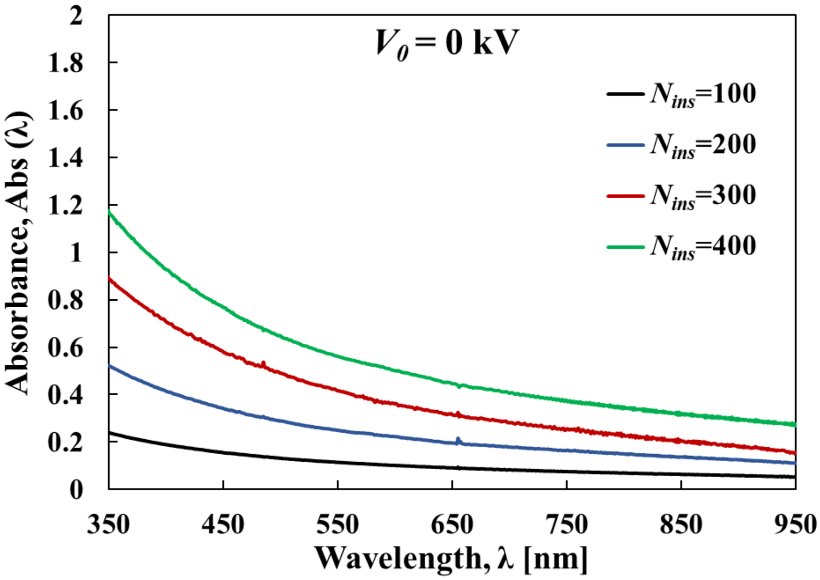

Figure 2.9. Example of UV-vis absorption spectra obtained for a fixed electric potential applied to the deposition substrate (V_0=0 kV) and varying the number of insertions N_{ins} in flame from 100 to 400 *(C/O=0.67;* t_{ins}*=100 ms; HAB=15 mm)*.

UV-vis absorption spectroscopy is one of the more widespread analytical and characterization techniques in science, and in materials research, it is used to infer [25,42–44]:

1. Qualitative analysis of the deposited mass
2. Quantitative measurement of the deposited mass in terms of film thickness
3. Optical and electronic properties of the deposited film.

From a qualitative point of view, it is possible to state that when the deposited mass increases, for example, because of the increase in the number of insertions N_{ins} as in **Figure 2.9**, there is a reduction in the transmitted radiant power through the sample $P(\lambda)$, and, consequently, there is an increase in the absorbance, resulting in an upward shift of the spectrum.

Moreover, thanks to the Beer-Lamber expression [25,43,45], it is possible to obtain a linear correspondence between the absorbance and film thickness:

$$Abs(\lambda) = log \frac{P_0}{P(\lambda)} = \alpha(\lambda)\delta \tag{2.2}$$

Where $\alpha(\lambda)$ is the light absorption coefficient; δ is the optical thickness of the homogeneous sample. The absorption coefficient is a function of the wavelength of the incident light:

$$\alpha(\lambda) = \frac{4\pi}{\lambda} k(\lambda) \tag{2.3}$$

Where $k(\lambda)$ is the extinction coefficient, namely the imaginary portion of the complex refractive index, which gives the attenuation of light as a function of wavelength as it passes through the medium. The extinction coefficient and the complex refractive index are determined by the phase velocity of the light propagating through the homogenous medium [25,46,47]. Combining **Eqs. (2.2)** and **(2.3)**, it is possible to obtain a direct correlation between the absorbance at a specific wavelength and the film thickness for a homogeneous material:

$$Abs(\lambda) = \frac{4\pi}{\lambda} k(\lambda)\delta \tag{2.4}$$

When the material is porous [45,46,48], the absorbance can be written as the sum of the absorbances due to the individual constituents. Although this is a rather strong linearity hypothesis, it is confirmed by tests on many porous materials [45,46,48]. Consequently, it is possible to write:

$$Abs(\lambda) = \frac{4\pi}{\lambda} k_s(\lambda)\delta_s + \frac{4\pi}{\lambda} k_g(\lambda)\delta_g \tag{2.5}$$

where $k_s(\lambda)$ is the extinction coefficient for the solid material; δ_s is the equivalent thickness of the solid phase; $k_g(\lambda)$ is the extinction coefficient for the air; δ_g is the equivalent thickness of the void. The refractive index of CNPs has been much studied over the years, because of its relevance for the radiative transfer problem in combustion chambers and the environment. It changes a little in the visible range for

CNPs produced under different conditions, and a typical value of k=0.56 is used, for a λ=532 nm [49]. Moreover, for the air, the complex refractive index is equal to 0. Therefore **Eq. (2.5)** becomes:

$$Abs(\lambda)=\frac{4\pi}{\lambda}k_s(\lambda)\delta_s \tag{2.6}$$

To obtain information about the total film thickness, it is possible to define the optical porosity φ, that is the ratio between void space and total volume of a porous medium [45]:

$$\varphi=\frac{\delta_g}{\delta}=\frac{\delta-\delta_s}{\delta}=1-\frac{\delta_s}{\delta} \tag{2.7}$$

Combining **Eqs. (2.6)** and **(2.7)**, it is possible to obtain:

$$Abs(\lambda)=\frac{4\pi}{\lambda}k_s(\lambda)\delta(1-\varphi) \tag{2.8}$$

This means that by knowing the porosity of the material, obtained through complementary tests, it is possible to use **Eq. (2.8)** to obtain the actual film thickness δ. In the absence of this information, it is possible to use **Eq. (2.6)** to obtain an approximate indication of the sole solid equivalent optical thickness (δ_s), that can be considered as an equivalent material thickness as proposed by [25].

Finally, the UV-vis absorption spectra can be used to obtain optical and electronic properties for the deposited films [25,42,44,50–52]. In particular, for semiconductor materials, the UV-vis spectrum can measure the optical band gap using Tauc's procedure [53]. The optical band gap in solid-state physics is defined as the energy difference between the highest occupied energy level of the valence band (HOMO) and the lowest unoccupied level of the conduction band (LUMO). In carbonaceous structures, this gap depends mainly on the different hybridization of the carbon atom wave functions, either sp^3 or sp^2, but also the size of the π-bonded clusters of sp^2 carbon atoms. Thus, the Optical band gap is a powerful indicator of the nature of the carbonaceous structures produced in rich flames and provides a physical characterization of the final CNPs: The closer the value is to zero, the greater the graphitic character of the material is. Following Tauc's equation, it is possible to write the absorption coefficient $\alpha(\lambda)$ as a function of the optical band gap energy E_g:

$$h\nu\alpha(\lambda) \propto (h\nu - E_g)^{k_r} \tag{2.9}$$

where ν is the frequency of the incident light; h is Planck's constant and k_r is a constant depending on the particular optical transition. In particular, the value of k_r can be equal to ½ or 2 for direct and indirect transition, respectively. For CNPs in the explored conditions, it has been verified that we operate under an indirect transition mode and the constant has been set to 2 [51]. Thus, the optical band gap energy E_g can be estimated by plotting the square root of $h\nu\alpha(\lambda)$ as a function of the $h\nu$, that is the energy of the incident photon, and extrapolating the linear slope in this plot to zero absorption in a range of photon energy equal to 1.5-3.5 eV [25,54]. **Figure 2.10** shows Tauc's plot obtained from the absorption spectra reported in **Figure 2.9**.

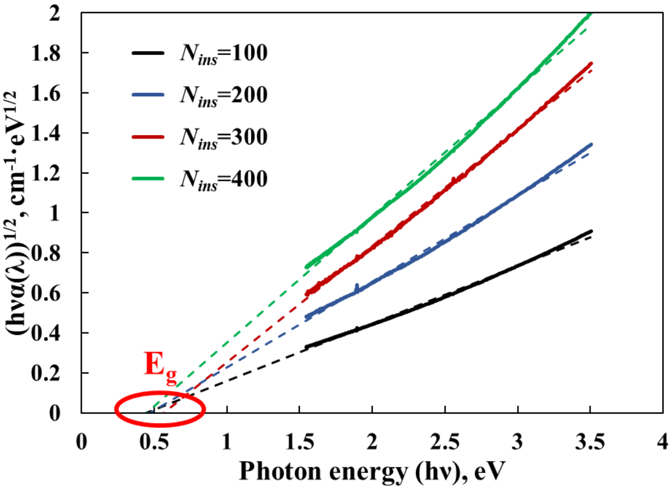

Figure 2.10. Tauc's plot for the UV-vis absorption spectra (reported in **Figure 2.9**) obtained for a fixed electric potential applied to the deposition substrate (V_0=0 kV) and varying the number of insertions N_{ins} in flame from 100 to 400 *(C/O=0.67; tins=100 ms; HAB=15 mm)*. The dotted lines represent linear extrapolations in the photon energy range 1.5-3.5 eV to obtain the E_g value at zero absorption.

2.3.3 Raman Spectroscopy

Raman spectra have been acquired by a Raman microscope (Horiba XploRA) equipped with a 100x objective (NA0.9, Olympus) available at the Clean Combustion Research Lab. The laser source has a frequency-doubled Nd:YAG laser (λ = 532 nm, 12 mW maximum laser power at the sample). The power of the excitation laser beam and the exposure time has been opportunely adjusted to avoid structural changes in the sample due to thermal decomposition. Spectra have been obtained with a laser beam power of 1%, and an accumulation-exposure time of 5 cycles of 30 s each. Several spots have been randomly selected and averaged to obtain statistically relevant Raman spectra. Finally, all the spectra have been baseline-corrected and normalized to the G peak around 1600 cm^{-1} [55–58].

Raman spectroscopy is a scattering type of molecular spectroscopy. The Raman scattering, or Raman effect, is a two-photon event that involves a change in the polarizability of the molecule about its vibrational motion in the form of scattered energy. The interaction of a molecules polarizability with the incoming light creates a dipole moment, and the light dispersed by this generated dipole incorporates Raman scattering. At this point, molecules can relax back down to the initial state and emit a photon with the same incident energy: this process is elastic and is referred to as Rayleigh scattering. Secondly, molecules can relax to a real photon state and emit a photon with less energy than the incident one (Stokes shifted Raman Scattering). Otherwise, molecules can reach a higher virtual state and relax back to the ground state emitting a photon with a higher amount of energy than the incident one: this phenomenon is called Anti-Stokes Raman scattering. Since most molecules will be found in the ground state at room temperature, Raman measurements are performed considering only the Stokes shifted light. Raman spectroscopy is a very useful technique to provide information about both the chemical characteristics and the structural characteristics of CNPs, in terms of size and internal structure [10,25,28,29,59–61]. **Figure 2.11** shows a typical Raman spectrum for a CNP film.

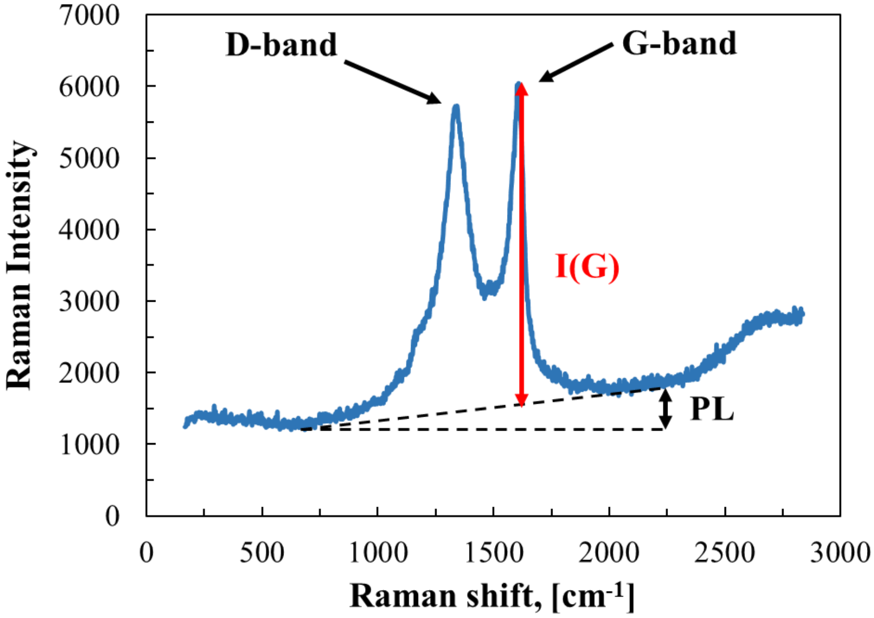

Figure 2.11. The typical shape of the Raman spectrum for a CNP film produced with *V*=-3 kV applied to the deposition substrate with 100 insertions *(C/O=0.67;tins=100 ms; HAB=15 mm)*. The two main peaks – *I*(D) and *I*(G) – and the photoluminescence background PL.

It is possible to notice that the Raman spectrum is dominated by two peaks, named D and G. In particular, the D peak is observed at about 1350 cm^{-1} and it is activated by the presence of defects in the sp^2 aromatic network, such as small crystallite sizes, grains, and vacancies, which are prohibited in the perfect hexagonal lattice. The second one, namely the G peak, is centered at about 1600 cm^{-1}, and it is due to every sp^2 bond. This feature is mostly insensitive to defects, only presenting small changes in the width and position of the maximum as a function of the different carbon structures. Moreover, the ratio between the absolute intensity of the two peaks of the spectrum, namely *I*(D)/*I*(G), gives information about the degree of ordering of the samples providing an estimation of the average size of the graphitic crystallites L_a [nm] that can be obtained as follows [25,28,59]:

$$L_a^2 = 5.4 \cdot 10^{-2} \left(E_L^4\right) \frac{I(D)}{I(G)} \tag{2.10}$$

Where E_L [eV] is the energy of the incident photon.

In addition, the Raman spectrum of CNP films often presents a photoluminescence background (PL), as shown in **Figure 2.11**. The PL intensity can be evaluated as the slope of the PL linear background, *m*, divided by the intensity of the Raman line at the G peak which is due to sp^2 in the sample. In this way, it is possible to evaluate the amount of fluorescing component with the respect to the total sp^2 carbon present in the CNP film. This ratio, moreover, is considered an indication of the relative content of organic carbon OC, with respect to the total sp^2 carbon, but it can include also the effect of the adsorbed gas-phase PAH molecules on CNPs [59].

2.3.4 Surface texture analysis

Surface texture analysis is a technique used to evaluate surface morphology in terms of roughness on a mesoscale. The surface roughness measurements have been carried out using a 3D optical profilometer, S Neox Sensor (Sensofar Metrology). Measurements are based on non-contact vertical scan confocal and interferometry techniques using Nikon 50x and 100x lenses. The instrument is connected to a vibration isolation system (Daeil System - DVIA-T56) and to a laptop equipped with a measurement analysis software, SensoVIEW. This returns surface topographic parameters following the ISO25178 standard.

Roughness measurements have been made in the laboratory "Protipazione Materiali Compositi" at University of Naples Federico II under normal ambient light conditions. For each surface analysed, the measurement output is a high-resolution 3D profile of the surface (*see* **Figure 2.12** for an example), with a field of view of 142μm × 170μm and an image size of 0.14μm/pixels.

For the calculation of the statistical roughness propriety, information taken during the vertical scan of the sample is managed, therefore the more points are acquired, the better the accuracy achieved.

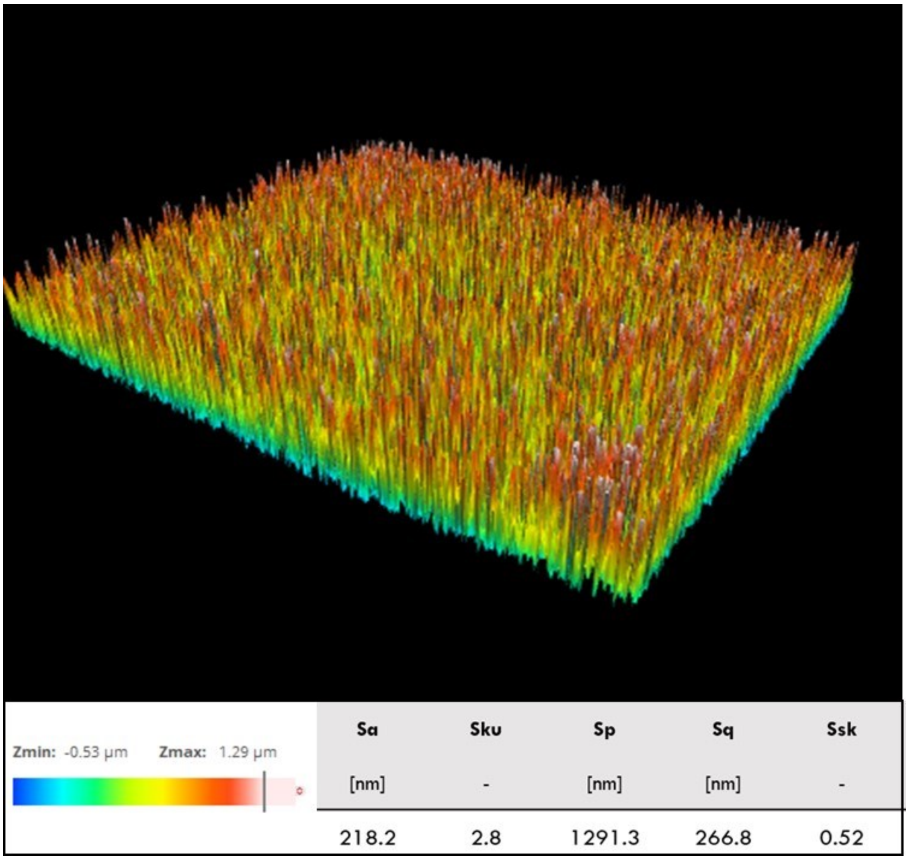
Zmin: -0.53 µm Zmax: 1.29 µm

Sa	Sku	Sp	Sq	Ssk
[nm]	-	[nm]	[nm]	-
218.2	2.8	1291.3	266.8	0.52

Figure 2.12. Example of high-resolution 3D profile of the surface for a CNP film *(C/O=0.82; HAB=1 5mm;* t_{ins}*= 100 ms;* N_{ins}*=8;* V_0*=0 kV)*. Indication about the average roughness (S_a), the Kurtosis (S_{ku}), the maximum heigh of peaks (S_p), the root mean square roughness (S_q) and the Skewness (S_{sk}) are reported. The graduated colored bar indicates the peak height between a minimum (Z_{min}) and a maximum (Z_{max}) values.

In particular, scan measurements in which at least 85% of the total points were acquired were counted as valid: the higher the percentage of scanned points is, the better the resolution of the profile obtained is. As shown in **Figure 2.12**, SensoVIEW software allows the evaluation of different parameters representative of roughness, but during our tests five different amplitude parameters have been considered to describe the mesoscale surface roughness, namely the average roughness (S_a), the Kurtosis (S_{ku}) the Skewness (S_{sk}) (*see* **Figure 2.13**), the root mean square roughness (S_q) and the maximum height of peaks (S_p).

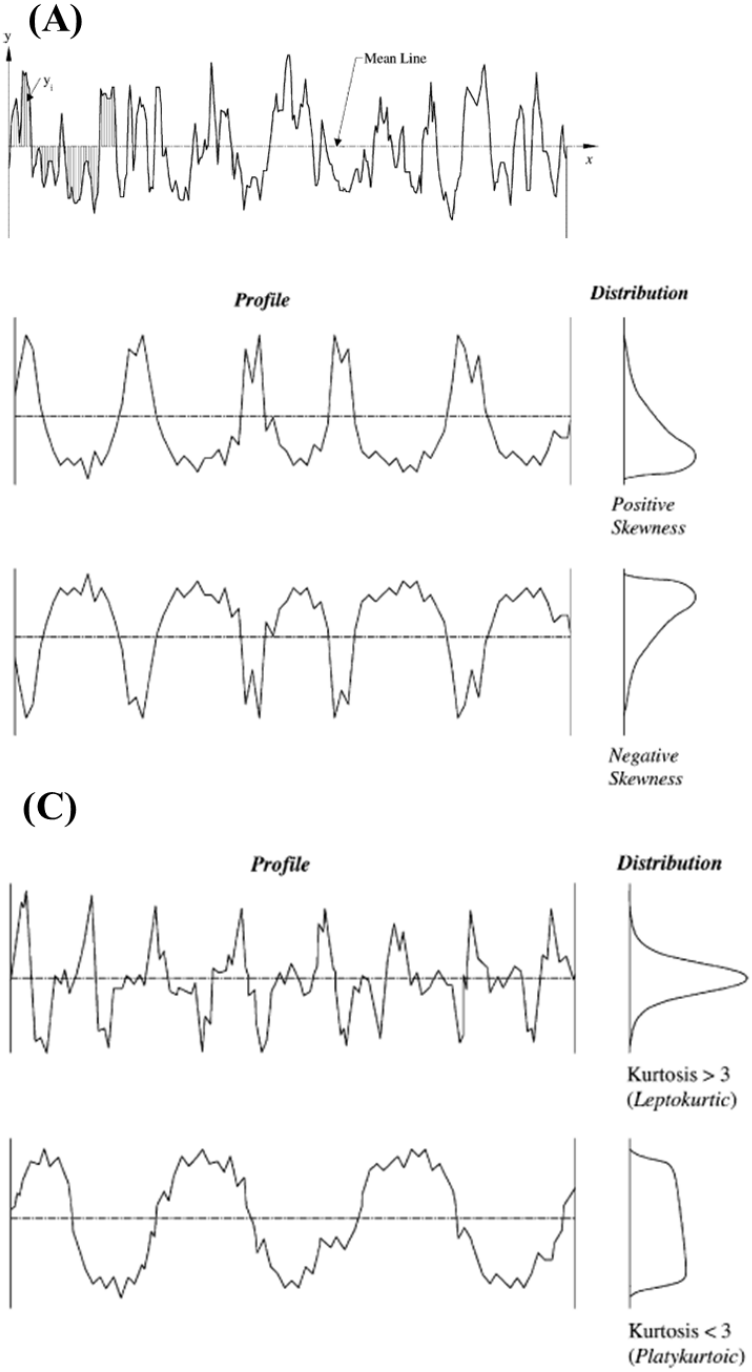

Figure 2.13. Definition and examples of **(A)** average roughness S_a, **(B)** skewness S_{sk} and **(C)** Kurtosis S_{ku}. Adapted from Giljean et al. [32].

The average roughness (S_a), also known as arithmetic average height parameter or centre line average, is the most universally used roughness parameter for general quality control. It is defined as the average absolute deviation of the roughness irregularities from the mean line of the profile, as shown in panel **(A)** of **Figure 2.13**. It is also possible to define the root mean square roughness (S_q), that represents the standard deviation of the distribution of surface heights: this parameter is more sensitive than the average roughness to large deviation from the mean line. Moreover, the maximum height of peaks (S_p) above the mean line can be typically determined.

The skewness of a profile (S_{sk}) is the third central moment of profile amplitude probability density function, measured over the assessment length. It is used to measure the symmetry of the profile around the mean line and it is sensitive to occasional deep valleys or high peaks. If there are as many peaks as valleys, the distribution has zero skewness. Profiles with small peaks or deep valleys have negative skewness, whereas profiles with small valleys filled or high peaks have positive skewness, as shown in Panel **(B)** in **Figure 2.13**.

Lastly, the Kurtosis coefficient (S_{ku}) is the fourth central moment of profile amplitude probability density functions, measured over the profile. It describes the sharpness of the probability density function of the profile and, consequently, allows evaluating deviations from an ideal Normal distribution, *i.e.* indicates the presence of disordered deep peaks/valleys. If $S_{ku}<3$ the distribution curve is said to be platykurtoic and has relatively few high peaks and low valleys. If $S_{ku}>3$ the distribution curve is leptokurtoic and has relatively many high peaks and low valleys. Panel **(C)** in **Figure 2.13** shows these two types of kurtosis.

Kurtosis coefficient and Skewness are very important parameters in distinguishing surfaces characterized by different shapes but with the same average roughness [32].

2.3.5 Current-voltage measurement

Electrical properties of CNP films can be obtained by current-voltage measurement. It is important to underline the need for a different substate for CNPs deposition including an electrode without which the amount of current passing through the CNP films could not be measured. Specifically, CNPs have been deposited on a metal-based InterDigitated Electrode produced by MicruX Technologies. It consists of a gold thin film, namely the working electrodes WE1 and WE2, deposited on a glass substrate. Each working electrode has a pad on one end to interface with the acquisition system and a comb-shaped microelectrodes on the other end, disposed in a planar, interdigitated circular pattern.

Figure 2.14 shows a picture of the electrode and its main features. The use of such a rectangular substrate required the creation of a specific holder.

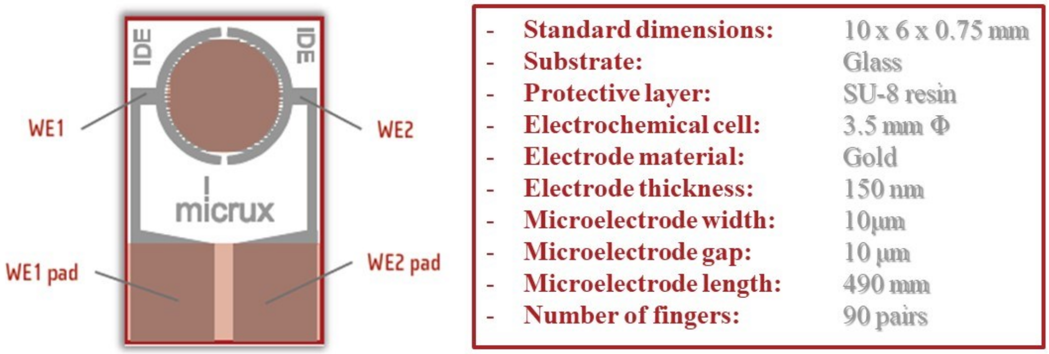

- **Standard dimensions:**	10 x 6 x 0.75 mm
- **Substrate:**	Glass
- **Protective layer:**	SU-8 resin
- **Electrochemical cell:**	3.5 mm Φ
- **Electrode material:**	Gold
- **Electrode thickness:**	150 nm
- **Microelectrode width:**	10µm
- **Microelectrode gap:**	10 µm
- **Microelectrode length:**	490 mm
- **Number of fingers:**	90 pairs

Figure 2.14. Picture of the interdigitated electrode by MicruX Technologies and its main features.

The CNP samples obtained after the in-flame deposition have been send to electrical characterization section. **Figure 2.15** shows all the devices used in the Clean Combustion Research Lab for electrical characterization of CNP samples.

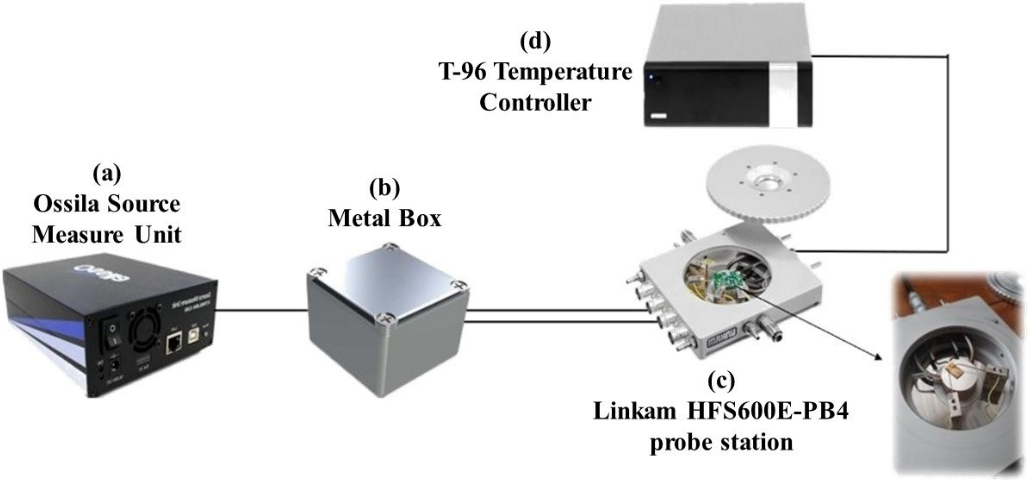

Figure 2.15. Devices used for I-V measurements carried out in Clean Combustion Research Lab.

The sequence of steps for CNP films electrical characterization are outlined below:

1. The CNP sample is positioned on a circular metal plate inside the chamber of the Linkam probe station **(c)**, where humidity and vacuum can be adjusted via gas purging, and temperature can be varied from -196°C to 600°C.
2. A fixed temperature or a heating rate is be set by using the T-96 Temperature Controller **(d)**.
3. Four positional gold-tipped tungsten probes are connected directly with the working electrodes on the sample, verifying that the electrical contact is optimal.
4. Finally, the Ossila Source Measure Unit **(a)** is used in order to set a voltage and to measure the current through the CNP sample. The maximum value applicable by the instrument for voltage is ± 10 V, whereas the maximum value for current is ± 200 mA.
5. In this way, it is possible to obtain I-V curves at a fixed temperature, as the one shown in **Figure 2.16**.

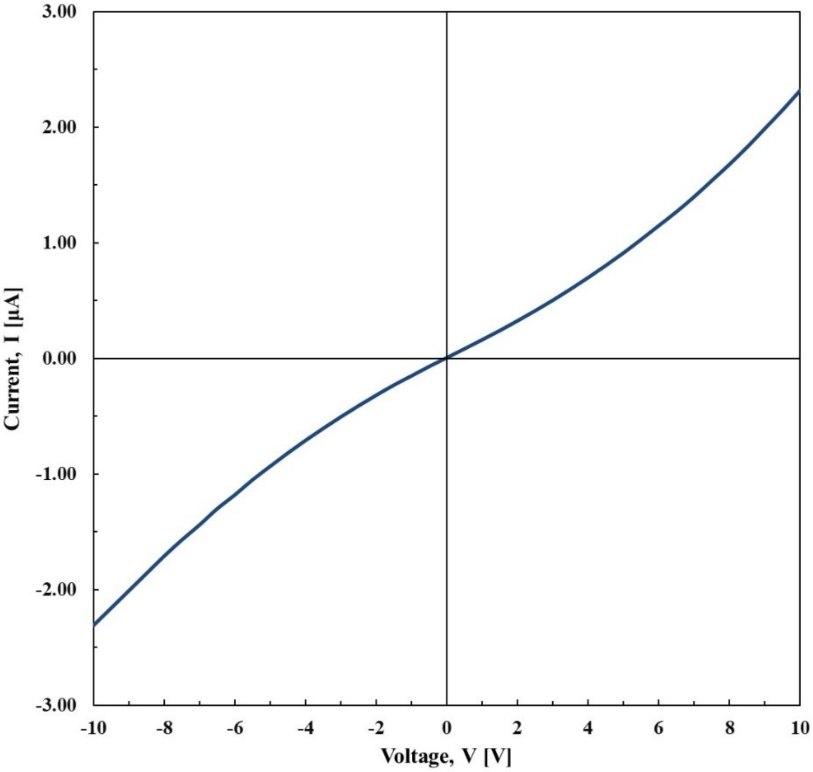

Figure 2.16. Typical I-V curve for a CNP sample at T=25°C (Operating conditions: C/O=0.67, HAB=15 mm; t_{ins}=100; N_{ins}=400; V_0= 0 kV).

Starting from the I-V curve, it is possible to evaluate the electrical conductivity (σ) for each CNP sample [25] as:

$$\sigma = G\frac{W}{L\delta_{eq}} \tag{2.11}$$

where G is the electrical conductance; W is the microelectrode width (10 μm from **Figure 2.14**); L is the microelectrode length (490 mm from **Figure 2.14**); δ_{eq} is the equivalent film thickness obtained from UV-vis absorption measurements (*see* **Eq. (2.6)**). Regarding to the electrical conductance (G), it is worth distinguishing two possibilities:

1. If the I-V curve is linear, CNP sample exhibit an ohmic behaviour and G is the slope of the I-V line.

2. If I-V curve is not linear, CNP sample exhibit a non-ohmic behaviour. In this case, it is possible to consider *G* as the slope of the I-V curve in the voltage range where it appears linear, and not close to V=0 V, that is the reversal point in our system: at 0 V, there is a high change in the current value where the voltage is very low, resulting in an unrealistic bump of the conductance with a very large error. The range between 8 and 10 V has been defined as the optimal one to obtain the I-V curve slope.

2.3.6 Contact angle measurement

Contact angle measurement is a powerful tool for surface characterization and wetting study due to its simplicity and versatility [33]. In this section, the technique used to obtain static contact angle information is described, but first a brief theoretical outline of the concept of wettability is given in order to clarify the meanings of the obtained results.

Wetting of a solid surface by a liquid can be quantitatively described from the profile of a liquid droplet deposited over it, more specifically from the tangential angle at liquid-solid-air interface. This angle of contact is defined respect to the liquid-solid contact line and is called static contact angle or Young's angle (*see* **Figure 2.17**). It is a results of a mechanical equilibrium on an ideal solid surface - being smooth, rigid, chemically homogeneous, insoluble, and non-reactive [33,34].

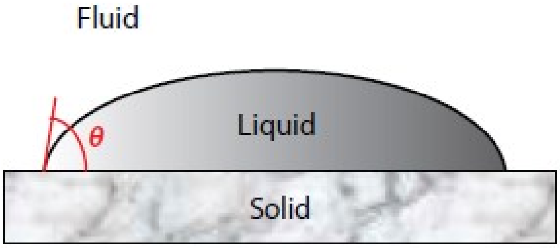

Figure 2.17. Graphical representation of the static contact angle θ for an ideal solid surface. Adapted from Marmur et al. [34].

When considering a real surface, the behaviour of the contact line is more complex. It depends on the intrinsic wettability of the solid which in turn depends on the chemical properties of solid, liquid and fluid reflected by the surface energies of the interfaces and solid. However, it also depends on the spatial properties of the roughness of the surface. In other words, the apparent wettability of the surface depends on the length scale of the roughness relative to the size of the drop as well as the physiochemical properties of the surface. In this case, it is possible to consider an apparent contact angle (θ_{ap}), that is defined as the equilibrium contact angle that the liquid makes with the projection of the solid surface as observed macroscopically [34,62] (*see* **Figure 2.18**).

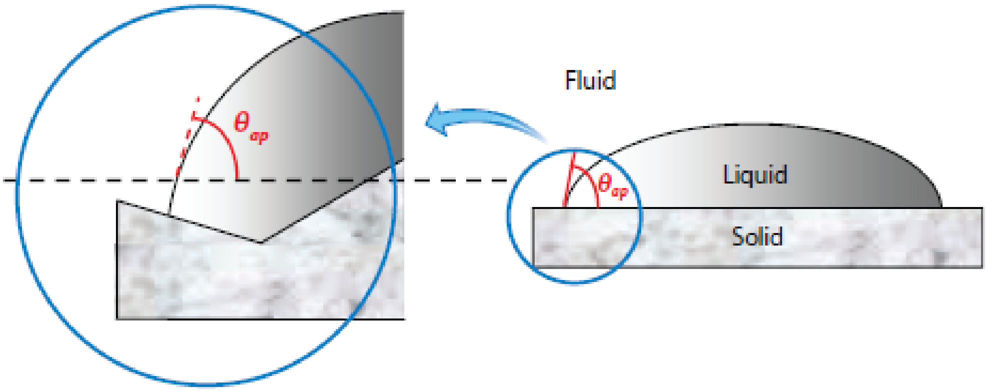

Figure 2.18. Apparent contact angle θ_{ap}. The details of roughness are not visible macroscopically. The macroscopically observable solid surface is actually the projection (black dashed line) of the real one. Adapted from Marmur et al. [34].

Because the existing methods of contact angle measurement are macroscopic, the apparent contact angle is currently the only measurable contact angle.

For an ideal solid surface, the apparent contact angle is identical to the ideal one. For real surfaces, which may be chemically and topographically heterogeneous, the apparent contact angle may change from one point to the other. **Figure 2.19** shows an overview of contact angle values as a function of the surface wettability.

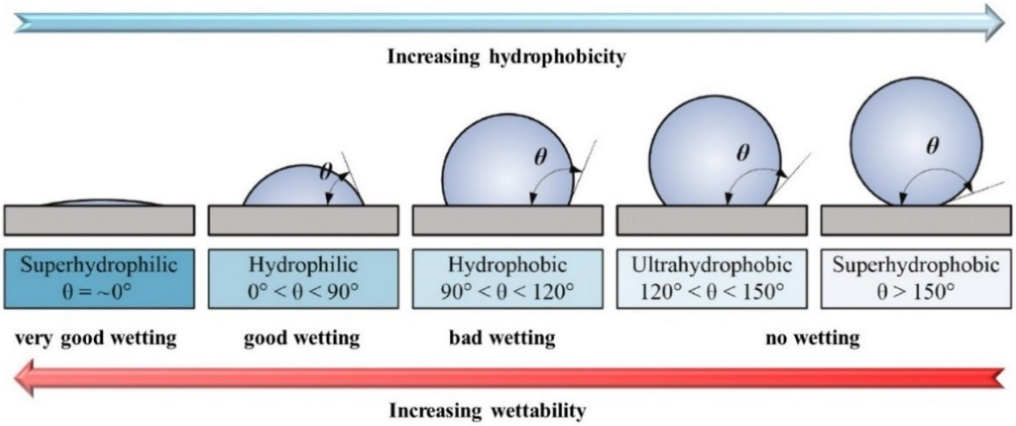

Figure 2.19. Overview of contact angle values as a function of the surface wettability. Adapted from Himma et al.[63].

If the contact angle is lower than 90°, the surface is designated hydrophilic since the forces of interaction between water and the surface nearly equal the cohesive forces of bulk water and water does not cleanly drain from the surface. If water spreads over a surface and the contact angles at the spreading front edge of the water is less than 10°, the surface is designated as Superhydrophilic.

On a hydrophobic surface, water forms distinct droplets. As the hydrophobicity increases, the contact angle of the droplets with the surface increase. Surfaces with contact angles greater than 90° are designated as hydrophobic. The theoretical maximum contact angle for water on a smooth surface is 120°.

Micro-textured or micro-patterned surfaces with hydrophobic asperities can exhibit apparent contact angles exceeding 150° and are associated with superhydrophobicity. Five typical wetting states in terms of roughness associated to superhydrophobicity are possible: a) totally wetting superhydrophobic surfaces in the Wenzel state, b) totally air-supporting superhydrophobic surfaces in the Cassie state, c) the metastable state between the Wenzel and Cassie states, known as petal state, d) surfaces in the micro/nanostructured two-tier lotus state, and e) partially wetting gecko state. Nature provides several examples of superwettability (*see* **Figure 2.20**).

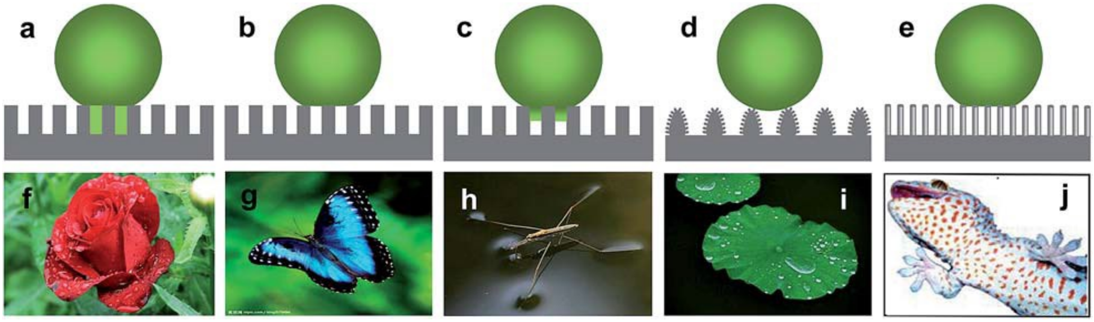

Figure 2.20. Typical cases for anti-wetting surfaces (a: Wenzel state; b: Cassie state; c: Wenzel–Cassie state; d: “lotus” state; e: “gecko” state) and examples for anti-wetting in nature. Adapted from Li et al. [64].

Generally, the wettability of rough surface is explained in a simplified way just referring to two different theories, the Wenzel model and the Cassie-Baxter model (see **Figure 2.21**), that refer to two extremely opposite rough surface wetting behaviours.

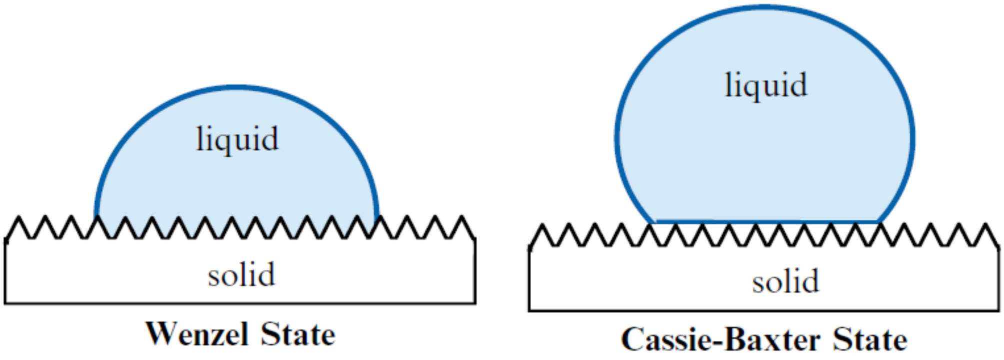

Figure 2.21. Schematic representation of the two possible wetting states on a real rough surface: Wenzel state (l*eft*) and Cassie-Baxter state (*right*) [33,64].

In particular, Wenzel revised the Young equation for ideal surfaces and suggested that the real contact area increases on a roughened surface. The liquid is considered to be in complete contact with the rough solid surface so it is difficult for the water droplet to move and roll off the surface due to the larger contact area and stronger adhesion. In Wenzel model the surface is assumed to be chemically homogeneous and rough. On the other hand, Cassie and Baxter proposed a heterogeneous contact model where the liquid is on top of the rough surface with air trapped in between: a water droplet is easy to move and roll off the surface because of the reduced contact area with the solid. Consequently, the surface is assumed to be chemically heterogeneous and rough.

Contact angle measurements have been carried out in the Rheology Lab (University of Campania L. Vanvitelli) using the tensiometer FTA1000 (First Ten Angstroms, Inc.) using the Sessile Drop procedure, shown in **Figure 2.22**.

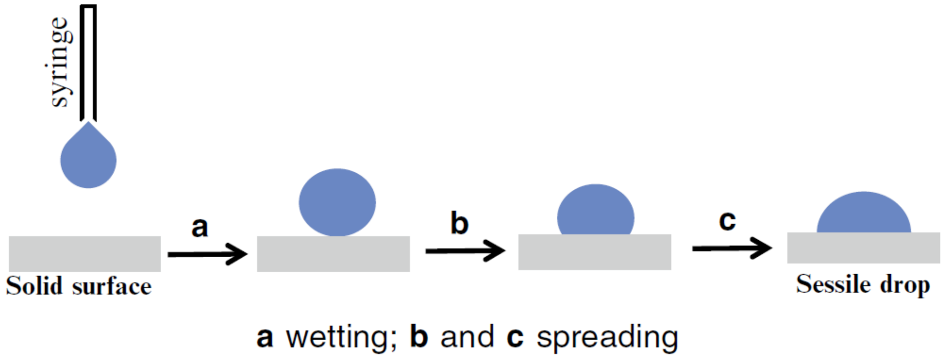

Figure 2.22. Schematization for the sessile drop procedure from the pendant to the sessile drop. Adapted from [33].

In particular, a drop volume has been dispensed very slowly through a microsyringe at 0.4 μL/s gently onto a horizontal solid surface using a motor-controlled dosing unit. The liquid having lower surface tension released from the needle may tend to ride up the outer surface of the needle during the pumping. To prevent this effect, the needle of the syringe has been rubbed with parafilm. The entire apparatus is on a vibration-free table, so that the pendant drop formation is not affected by any vibrational noise from the surrounding environment. So, firstly, a pendant drop is obtained; then the water droplet wets the surface, with a dynamic contact angle close to 180°, and finally this dynamic angle decay to the steady state contact angle in less than a second. From there, the drop side-view profile is captured and analysed using the Fta32 Video 2.1 software in order to obtain the static contact angle. Moreover, it is possible to follow and record drop evaporation from video recording of the droplet evolution. **Figure 2.23** shows a typical output of contact angle measurements.

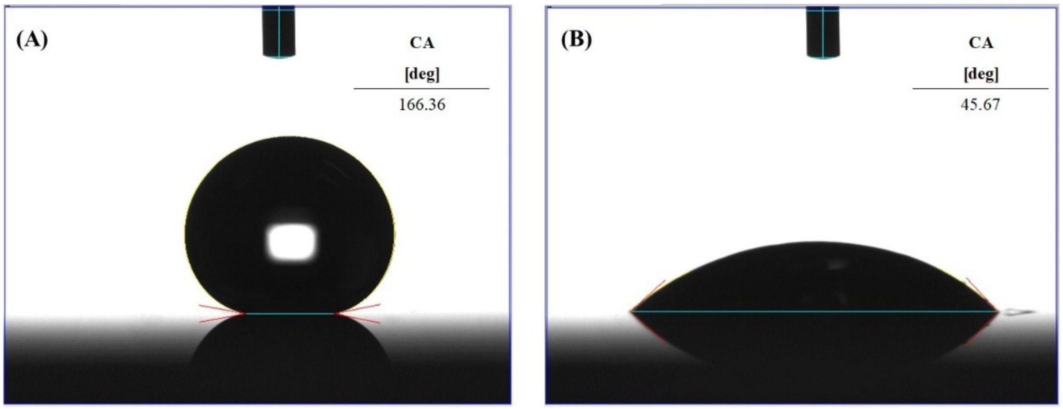

.

Figure 2.23. Typical output of static contact angle measurements: drop side-view profile and static contact angle (CA, [deg]) for **(A)** superhydrophobic CNP film and **(B)** hydrophilic CNP film. *(C/O=0.82;* t_{ins}*=100 ms; HAB=15 mm;* N_{ins}*=16 for* ***(A)*** *and 8 for* ***(B)****).*

2.3.7 UV-vis Absorption after dilution in NMP

The techniques described so far make it possible to obtain CNP films-related information. It is also interested, however in obtaining information on the chemical and physical characteristics of the primary particles and aggregates that make up the CNP film itself. For this reason, the CNP film is removed from the glass substrate by rinsing the substrate in Dichloromethane (DCM) to eliminate the condensed species (PAH) and then the CNPs powder is dispersed in N-Methyl-2-pyrrolidone (NMP) using an ultrasonic bath (5 min, 59 kHz). The NMP has proved to be a powerful dispersing agent for hard carbon materials such as coal and soot. After stabilization, it is possible to obtain the UV-vis spectra of all the suspended CNP fractions in suspension and, consequently, to evaluate the relative amount of fluorescing components and the overall optical band gap for the CNP agglomerates.

The UV-vis absorption have been measured in the 190-1100 nm wavelength range on an HP 8453 Diode Array Spectrophotometer, available in CNR-STEMS Lab, using 1 cm quartz cuvettes. In spite of the good CNPs dispersion, particles in NMP behaves as colloids, whose size is also linked to the size of the most stable agglomerates that constitute the film.

2.3.8 Size Exclusion Chromatography

Size exclusion chromatography (SEC analysis) is a useful technique for determining the molecular weight distribution in a very wide range of polymers, tars, asphaltenes, etc. In our experiment, CNP films have been removed from the glass plate and finely dispersed in NMP. A Jordi Gel DVB Solid Bead column 300 x 7.8 mm has been used to separate the carbon in a very wide molecular weight range (2000- $4\cdot10^8$ u). Then, to better separate smaller particles, a second highly cross-linked individual-pore column (Polymer Laboratories, Ltd, UK) has been used. The injection volume is 250 μL and the analyses have been performed at a temperature of 80°C with a flow rate of 0.5 mL/min. The online detection of species eluted from the SEC column has been carried out using an HP1050 UV-Vis diode array detector that measured the absorbance signal at a fixed absorption wavelength (350 nm) [27,35,36]. The output of the SEC analysis is the elution time. The attribution of a molecular weight to a specific elution time has been made on the basis of calibration curves using polystyrene standards (Polymer laboratories) in the molecular mass rang 580-$13.2\cdot10^6$ u [65–70].

Figure 2.24 shows the SEC polystyrene calibration curve. It is possible to notice that the logarithm of molecular weight versus elution time gives a straight line over an appreciable molecular weight range.

The SEC method has been efficiently used to evaluate the molecular weight distribution of CNPs obtained in flames [65,67] . A typical SEC chromatogram of a CNP samples is reported in **Figure 2.24**.

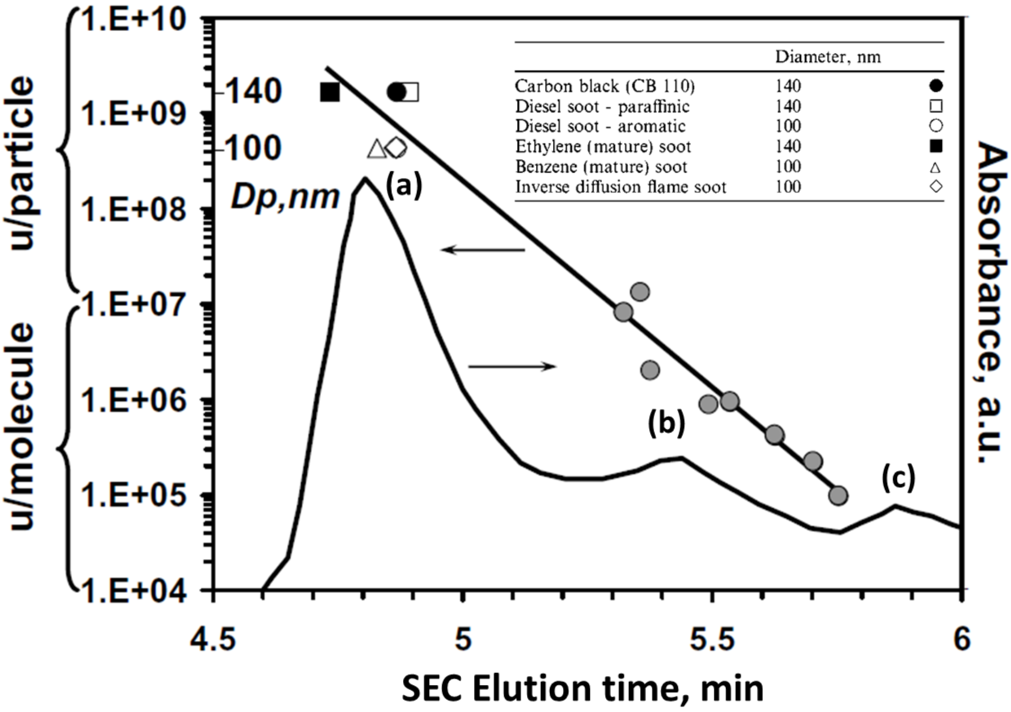

Figure 2.24. SEC polystyrene calibration curve for molecular weight evaluation based on molecular weight of polystyrene standard and for size evaluation (*Dp*) on CNP samples whose molecular weight has been evaluated from Dynamic Light Scattering particle diameter (*Dp*) considering a density of 1.8 g/cm^3 and spherical shape. A typical SEC chromatogram of soot is also reported. Grey dots refer to polystyrene. Other symbols are listed on the right legend [66].

It is possible to distinguish three different peaks in the molecular weight distribution. The first peaks **(a)** is attributed to larger soot particles/aggregates with molecular weight higher than $2 \cdot 10^5$ u, namely particles with an equivalent size ranging between 8 and 250 nm. The second peak **(b)** is due to soot precursor particles with masses between $2 \cdot 10^4$ and $2 \cdot 10^5$ u, that correspond to particles with equivalent sizes from 4 to 8 nm. Typically, these two peaks represent the particle-size region. Furthermore, the third peak **(c)** corresponds to molecular species with masses between $6 \cdot 10^2$ and $2 \cdot 10^4$ u, that correspond to particles with equivalent sizes from 1 to 4 nm. In particular, this peak is due to mechanism of aromatic addition to aromatic radicals.

Finally, in some SEC chromatograms there is also a fourth peak (not shown in **Figure 2.24**), with corresponds to high molecular mass PAHs with molecular weight between 202 and 600 u (particles with equivalent sizes of about 1 nm). These two last peaks correspond to the molecular-size region. The components eluting in the molecular region of the SEC chromatogram exhibited green fluorescence. Based on these considerations, it can be deduced that the first column results in the formation of an eluate consisting of primary particles and aggregates smaller than 100 nm, while in the second column the final eluate consists of CNP primary particles smaller than 20 nm.

Table 2.2 resumes all the tests on CNP samples, with indications about operating conditions, *e.g.* applied voltage (V_0) and number of insertions in flame (N_{ins}). Moreover, for each CNP sample, indications about the adopted substrate and analytical techniques are reported.

Table 2.2. Summary of all the produced CNP samples by electric field-assisted flame synthesis (C/O=0.67; t_{ins}=100 ms; HAB=15mm) by varying the electric potential (V_0) applied to the deposition substrate and the number of insertions (N_{ins}) in flame. Indications about the substrate and analytical techniques used for CNP characterization are reported.

V, [kV]	N_{ins}, [-]	Substrate		Analytical techniques							
		Mica	**Glass**	**Atomic Force Microscopy**	**UV-vis Absorption**	**Raman Spectroscopy**	**Surface Texture Analysis**	**Current-Voltage Measurement**	**Contact Angle Measurement**	**UV-vis Absorption in NMP**	**Size Exclusion Chromatography**
0	1	*x*		*x*	*x*	*x*					
	100		*x*		*x*	*x*					
	200		*x*		*x*	*x*	*x*		*x*		
	300		*x*		*x*	*x*					
	400	*x*	*x*	*x*	*x*	*x*		*x*		*x*	*x*
	600		*x*		*x*	*x*					
-1	1	*x*		*x*	*x*	*x*					
	25		*x*		*x*	*x*					
	50		*x*		*x*	*x*					
	100		*x*		*x*	*x*					
	150	*x*	*x*	*x*	*x*	*x*		*x*		*x*	*x*
	200		*x*		*x*	*x*	*x*		*x*		
-2	1	*x*		*x*	*x*	*x*					
	35		*x*		*x*	*x*					
	100		*x*		*x*	*x*					
	125	*x*	*x*	*x*	*x*	*x*		*x*		*x*	*x*
	175		*x*		*x*	*x*	*x*		*x*		
-3	1	*x*		*x*	*x*	*x*					
	25		*x*		*x*	*x*					
	40		*x*		*x*	*x*					
	50		*x*		*x*	*x*					
	75		*x*		*x*	*x*					
	100	x	*x*	*x*	*x*	*x*		*x*		*x*	*x*
	150		*x*		*x*	*x*	*x*		*x*		

2.4 References

[1] Martin JW, Pascazio L, Menon A, Akroyd J, Kaiser K, Schulz F, et al. π-Diradical Aromatic Soot Precursors in Flames. J Am Chem Soc 2021;143:12212–9. https://doi.org/10.1021/jacs.1c05030.

[2] Commodo M, Kaiser K, De Falco G, Minutolo P, Schulz F, D'Anna A, et al. On the early stages of soot formation: Molecular structure elucidation by high-resolution atomic force microscopy. Combust Flame 2019;205:154–64. https://doi.org/10.1016/j.combustflame.2019.03.042.

[3] Schulz F, Commodo M, Kaiser K, De Falco G, Minutolo P, Meyer G, et al. Insights into incipient soot formation by atomic force microscopy. Proceedings of the Combustion Institute 2019;37:885–92. https://doi.org/10.1016/j.proci.2018.06.100.

[4] Commodo M, De Falco G, Bruno A, Borriello C, Minutolo P, D'Anna A. Physicochemical evolution of nascent soot particles in a laminar premixed flame: From nucleation to early growth. Combust Flame 2015;162:3854–63. https://doi.org/10.1016/j.combustflame.2015.07.022.

[5] Langenkamp PN. Laser diagnostics of combustion-generated nanoparticles. Doctor of Philosophy. University of Groningen, 2018.

[6] Senser DW, Morse JS, Cundy VA. Construction and novel application of a flat flame burner facility to study hazardous waste combustion. Review of Scientific Instruments 1985;56:1279–84. https://doi.org/10.1063/1.1137992.

[7] Migliorini F, de Iuliis S, Cignoli F, Zizak G. How "flat" is the rich premixed flame produced by your McKenna burner? Combust Flame 2008;153:384–93. https://doi.org/10.1016/j.combustflame.2008.01.007.

[8] Li S, Ren Y, Biswas P, Tse SD. Flame aerosol synthesis of nanostructured materials and functional devices: Processing, modeling, and diagnostics. Prog Energy Combust Sci 2016;55:1–59. https://doi.org/10.1016/j.pecs.2016.04.002.

[9] Picca F, Pietro A di, Commodo M, Minutolo P, D'Anna A. Variable Temperature Synthesis of Tunable Flame-Generated Carbon Nanoparticles. C (Basel) 2021;7:44. https://doi.org/10.3390/c7020044.

[10] Vitiello G, De Falco G, Picca F, Commodo M, D'Errico G, Minutolo P, et al. Role of radicals in carbon clustering and soot inception: A combined EPR and Raman spectroscopic study. Combust Flame 2019;205:286–94. https://doi.org/10.1016/j.combustflame.2019.04.028.

[11] Commodo M, Sgro LA, Minutolo P, D'Anna A. Characterization of combustion-generated carbonaceous nanoparticles by size-dependent ultraviolet laser

photoionization. Journal of Physical Chemistry A 2013;117:3980–9. https://doi.org/10.1021/jp401061d.

[12] Commodo M, Tessitore G, De Falco G, Bruno A, Minutolo P, D'Anna A. Further details on particle inception and growth in premixed flames. Proceedings of the Combustion Institute 2015;35:1795–802. https://doi.org/10.1016/j.proci.2014.06.004.

[13] Commodo M, De Falco G, Minutolo P, D'Anna A. Structure and size of soot nanoparticles in laminar premixed flames at different equivalence ratios. Fuel 2018;216:456–62. https://doi.org/10.1016/j.fuel.2017.12.032.

[14] Russo C, D'Anna A, Ciajolo A, Sirignano M. The effect of butanol isomers on the formation of carbon particulate matter in fuel-rich premixed ethylene flames. Combust Flame 2019;199:122–30. https://doi.org/10.1016/j.combustflame.2018.10.025.

[15] Sgro LA, D'Anna A, Minutolo P. Charge distribution of incipient flame-generated particles. Aerosol Science and Technology 2010;44:651–62. https://doi.org/10.1080/02786826.2010.483701.

[16] Sgro LA, D'Anna A, Minutolo P. Charge fraction distribution of nucleation mode particles: New insight on the particle formation mechanism. Combust Flame 2011;158:1418–25. https://doi.org/10.1016/j.combustflame.2010.11.010.

[17] Maricq MM. A comparison of soot size and charge distributions from ethane, ethylene, acetylene, and benzene/ethylene premixed flames. Combust Flame 2006;144:730–43. https://doi.org/10.1016/j.combustflame.2005.09.007.

[18] Maricq MM. Size and charge of soot particles in rich premixed ethylene flames. Combust Flame 2004;137:340–50. https://doi.org/10.1016/j.combustflame.2004.01.013.

[19] Wang Y, Nathan GJ, Alwahabi ZT, King KD, Ho K, Yao Q. Effect of a uniform electric field on soot in laminar premixed ethylene/air flames. Combust Flame 2010;157:1308–15. https://doi.org/10.1016/j.combustflame.2010.03.001.

[20] Saito M, Sato M, Sawada K. Variation of flame shape and soot emission by applying electric field. vol. 39. 1997.

[21] Xiong G, Kulkarni A, Dong Z, Li S, Tse SD. Electric-field-assisted stagnation-swirl-flame synthesis of porous nanostructured titanium-dioxide films. Proceedings of the Combustion Institute 2017;36:1065–75. https://doi.org/10.1016/j.proci.2016.08.079.

[22] Altendorfner F, Kuhl J, Zigan L, Leipertz A. Study of the influence of electric fields on flames using planar LIF and PIV techniques. Proceedings of the

Combustion Institute 2011;33:3195–201. https://doi.org/10.1016/j.proci.2010.05.112.

[23] Kuhl J, Seeger T, Zigan L, Will S, Leipertz A. On the effect of ionic wind on structure and temperature of laminar premixed flames influenced by electric fields. Combust Flame 2017;176:391–9. https://doi.org/10.1016/j.combustflame.2016.10.026.

[24] De Falco G, Porta A, Petrone AM, del Gaudio P, el Hassanin A, Commodo M, et al. Antimicrobial activity of flame-synthesized nano-TiO2 coatings. Environ Sci Nano 2017;4:1095–107. https://doi.org/10.1039/c7en00030h.

[25] De Falco G, Commodo M, Barra M, Chiarella F, D'Anna A, Aloisio A, et al. Electrical characterization of flame-soot nanoparticle thin films. Synth Met 2017;229:89–99. https://doi.org/10.1016/j.synthmet.2017.05.008.

[26] De Falco G, Carbone F, Commodo M, Minutolo P, D'Anna A. Exploring nanomechanical properties of soot particle layers by atomic force microscopy nanoindentation. Applied Sciences (Switzerland) 2021;11. https://doi.org/10.3390/app11188448.

[27] Russo C, Apicella B, Tregrossi A, Oliano MM, Ciajolo A. Thermophoretic sampling of large PAH (C $\geq$ 22–24) formed in flames. Fuel 2020;263. https://doi.org/10.1016/j.fuel.2019.116722.

[28] De Falco G, Commodo M, Bonavolontà C, Pepe GP, Minutolo P, D'Anna A. Optical and electrical characterization of carbon nanoparticles produced in laminar premixed flames. Combust Flame 2014;161:3201–10. https://doi.org/10.1016/j.combustflame.2014.05.021.

[29] Ferrari AC, Basko DM. Raman spectroscopy as a versatile tool for studying the properties of graphene. Nat Nanotechnol 2013;8:235–46. https://doi.org/10.1038/nnano.2013.46.

[30] Abbott JPR, Zhu H. 3D optical surface profiler for quantifying leaf surface roughness. Surf Topogr 2019;7. https://doi.org/10.1088/2051-672X/ab4cc6.

[31] Spori DM, Drobek T, Zürcher S, Ochsner M, Sprecher C, Mühlebach A, et al. Beyond the lotus effect: Roughness influences on wetting over a wide surface-energy range. Langmuir 2008;24:5411–7. https://doi.org/10.1021/la800215r.

[32] Giljean S, Bigerelle M, Anselme K, Haidara H. New insights on contact angle/roughness dependence on high surface energy materials. Appl Surf Sci 2011;257:9631–8. https://doi.org/10.1016/j.apsusc.2011.06.088.

[33] Kock-Yee Law, Hing Zhao. Surface Wetting. Characterization, Contact Angle, and Fundamentals. Springer. 2016.

[34] Marmur A. Solid-surface characterization by wetting. Annu Rev Mater Res 2009;39:473–89. https://doi.org/10.1146/annurev.matsci.38.060407.132425.

[35] Sirignano M, Russo C, Ciajolo A. One-step synthesis of carbon nanoparticles and yellow to blue fluorescent nanocarbons in flame reactors. Carbon N Y 2020;156:370–7. https://doi.org/10.1016/j.carbon.2019.09.068.

[36] Russo C, Apicella B, la Rocca A, Sirignano M. Fluorescent carbon dots synthesis in premixed flames: Influence of the equivalence ratio. Carbon N Y 2023;201:659–66. https://doi.org/10.1016/j.carbon.2022.09.061.

[37] De Falco G, Commodo M, Minutolo P, D'Anna A. Flame-formed carbon nanoparticles: Morphology, interaction forces, and hamaker constant from AFM. Aerosol Science and Technology 2015;49:281–9. https://doi.org/10.1080/02786826.2015.1022634.

[38] Griepentrog M, Krämer G, Cappella B. Comparison of nanoindentation and AFM methods for the determination of mechanical properties of polymers. Polym Test 2013;32:455–60. https://doi.org/10.1016/j.polymertesting.2013.01.011.

[39] Westra KL, Thomsonb DJ. The microstructure of thin films observed using atomic force microscopy. vol. 257. 1995.

[40] Mwema FM, Oladijo OP, Sathiaraj TS, Akinlabi ET. Atomic force microscopy analysis of surface topography of pure thin aluminum films Atomic force microscopy analysis of surface topography of pure thin aluminium films. Mater Res Express 2018. https://doi.org/10.1088/2053.

[41] Serhan M, Sprowls M, Jackemeyer D, Long M, Perez ID, Maret W, et al. Total iron measurement in human serum with a smartphone. AIChE Annual Meeting, Conference Proceedings, vol. 2019- November, American Institute of Chemical Engineers; 2019. https://doi.org/10.1039/x0xx00000x.

[42] Tissue BM. Ultraviolet and Visible Absorption Spectroscopy. Optical Imaging and Spectroscopy. Characterization of Materials. John Wiley & Sons, 2012.

[43] Minutolo P, Commodo M, D'Anna A. Optical properties of incipient soot. Proceedings of the Combustion Institute 2022. https://doi.org/10.1016/j.proci.2022.09.019.

[44] Minutolo P, Gambi G, D'alessio A. THE OPTICAL BAND GAP MODEL IN THE INTERPRETATION OF THE UV-VISIBLE ABSORPTION SPECTRA OF RICH PREMIXED FLAMES. Symposium (Internation) on Combustion 1996:951–7.

[45] Mei L, Somesfalean G, Svanberg S. Light propagation in porous ceramics: Porosity and optical property studies using tunable diode laser spectroscopy. Appl

Phys A Mater Sci Process 2014;114:393–400. https://doi.org/10.1007/s00339-013-8137-x.

[46] Niskanen I, Suopajärvi T, Liimatainen H, Fabritius T, Heikkilä R, Thungström G. Determining the complex refractive index of cellulose nanocrystals by combination of Beer-Lambert and immersion matching methods. J Quant Spectrosc Radiat Transf 2019;235:1–6. https://doi.org/10.1016/j.jqsrt.2019.06.023.

[47] Minutolo P, De Falco G, Commodo M, Aloisio A, D'Anna A. Temperature Sensing with Thin Films of Flame-Formed Carbon Nanoparticles. Applied Sciences (Switzerland) 2022;12. https://doi.org/10.3390/app12157714.

[48] Bensalem M, Sommier A, Mindeguia JC, Batsale JC, Pradere C. Terahertz Measurement of the Water Content Distribution in Wood Materials. J Infrared Millim Terahertz Waves 2018;39:195–209. https://doi.org/10.1007/s10762-017-0441-7.

[49] Smyth KC, Shaddix CR. The Elusive History of rh = 1.57-0.56i for the Refractive Index of Soot. Combust Flame 1996;107:314–20.

[50] Migliorini F, Belmuso S, Maffi S, Dondè R, de Iuliis S. In-flow optical characterization of flame-generated carbon nanoparticles sampled from a premixed flame. Physical Chemistry Chemical Physics 2021;23:15702–12. https://doi.org/10.1039/d1cp01267c.

[51] Russo C, Apicella B, Tregrossi A, Ciajolo A, Le KC, Török S, et al. Optical band gap analysis of soot and organic carbon in premixed ethylene flames: Comparison of in-situ and ex-situ absorption measurements. Carbon N Y 2020;158:89–96. https://doi.org/10.1016/j.carbon.2019.11.087.

[52] Bauer FJ, Braeuer PAB, Aßmann S, Thiele MA, Huber FJT, Will S. Characterisation of the transition type in optical band gap analysis of in-flame soot. Combust Flame 2022;243. https://doi.org/10.1016/j.combustflame.2022.111986.

[53] Tauc J, Grigorovici R, Vancu A. Optical Properties and Electronic Structure of Amorphous Germanium. Physica Status Solidi (b) 1966;15:627–37. https://doi.org/10.1002/pssb.19660150224.

[54] De Falco G, Mattiello G, Commodo M, Minutolo P, Shi X, D'Anna A, et al. Electronic band gap of flame-formed carbon nanoparticles by scanning tunneling spectroscopy. Proceedings of the Combustion Institute, vol. 38, Elsevier Ltd; 2021, p. 1805–12. https://doi.org/10.1016/j.proci.2020.07.109.

[55] Martins Ferreira EH, Moutinho MVO, Stavale F, Lucchese MM, Capaz RB, Achete CA, et al. Evolution of the Raman spectra from single-, few-, and many-

layer graphene with increasing disorder. Phys Rev B Condens Matter Mater Phys 2010;82. https://doi.org/10.1103/PhysRevB.82.125429.

[56] Ferrari AC, Basko DM. Raman spectroscopy as a versatile tool for studying the properties of graphene. Nat Nanotechnol 2013;8:235–46. https://doi.org/10.1038/nnano.2013.46.

[57] Commodo M, D'Anna A, De Falco G, Larciprete R, Minutolo P. Illuminating the earliest stages of the soot formation by photoemission and Raman spectroscopy. Combust Flame 2017;181:188–97. https://doi.org/10.1016/j.combustflame.2017.03.020.

[58] Vitiello G, De Falco G, Picca F, Commodo M, D'Errico G, Minutolo P, et al. Role of radicals in carbon clustering and soot inception: A combined EPR and Raman spectroscopic study. Combust Flame 2019;205:286–94. https://doi.org/10.1016/j.combustflame.2019.04.028.

[59] Commodo M, Joo PH, De Falco G, Minutolo P, D'Anna A, Gülder ÖL. Raman Spectroscopy of Soot Sampled in High-Pressure Diffusion Flames. Energy and Fuels 2017;31:10158–64. https://doi.org/10.1021/acs.energyfuels.7b01674.

[60] Meier W, Vyrodov AO, Bergmann V, Stricker W. Simultaneous Raman/LIF measurements of major species and NO in turbulent H2/air diffusion flames. Applied Physics B Pasers and Optics 1996;63:79–90.

[61] Martins Ferreira EH, Moutinho MVO, Stavale F, Lucchese MM, Capaz RB, Achete CA, et al. Evolution of the Raman spectra from single-, few-, and many-layer graphene with increasing disorder. Phys Rev B Condens Matter Mater Phys 2010;82. https://doi.org/10.1103/PhysRevB.82.125429.

[62] Huang X, Gates I. Apparent Contact Angle around the Periphery of a Liquid Drop on Roughened Surfaces. Sci Rep 2020;10. https://doi.org/10.1038/s41598-020-65122-w.

[63] Himma NF, Prasetya N, Anisah S, Wenten IG. Superhydrophobic membrane: Progress in preparation and its separation properties. Reviews in Chemical Engineering 2019;35:211–38. https://doi.org/10.1515/revce-2017-0030.

[64] Li S, Huang J, Chen Z, Chen G, Lai Y. A review on special wettability textiles: theoretical models, fabrication technologies and multifunctional applications. J Mater Chem A Mater 2017;5:31–55. https://doi.org/10.1039/c6ta07984a.

[65] Alfà M, Apicella B, Barbella R, Tregrossi A, Ciajolo A. Distribution of soot molecular weight/size along premixed flames as inferred by size exclusion chromatography. Energy and Fuels 2007;21:136–40. https://doi.org/10.1021/ef060320p.

[66] D’Anna A, Ciajolo A, Alfè M, Apicella B, Tregrossi A. Effect of fuel/air ratio and aromaticity on the molecular weight distribution of soot in premixed n-heptane flames. Proceedings of the Combustion Institute 2009;32 I:803–10. https://doi.org/10.1016/j.proci.2008.06.198.

[67] Apicella B, Ciajolo A, Suelves I, Morgan TJ, Herod AA, Kandiyoti R. Structural characterization of products from fuel-rich combustion: An approach based on size exclusion chromatography. Combustion Science and Technology 2002;174:345–59. https://doi.org/10.1080/713712962.

[68] Apicella B, Ciajolo A, Barbella R, Tregrossi A, Morgan TJ, Herod AA, et al. Size exclusion chromatography of particulate produced in fuel-rich combustion of different fuels. Energy and Fuels 2003;17:565–70. https://doi.org/10.1021/ef020149r.

[69] Sirignano M, Russo C. Pyrene dimerization in controlled temperature environment: An experimental study. Proceedings of the Combustion Institute, vol. 38, Elsevier Ltd; 2021, p. 1173–80. https://doi.org/10.1016/j.proci.2020.06.367.

[70] Sirignano M, Ciajolo A, D’Anna A, Russo C. Chemical Features of Particles Generated in an Ethylene/Ethanol Premixed Flame. Energy and Fuels 2017;31:2370–7. https://doi.org/10.1021/acs.energyfuels.6b02372.

Chapter 3

Modelling the electric field-assisted in-flame CNPs deposition

This chapter reports a numerical model based on momentum balance on single CNPs and on a simplified model for the flame environment, which has been validated against dedicated experimental data, and provides several insights into the physical mechanisms governing the electric field-assisted flame synthesis of CNPs.

This chapter refers to the original paper:

Parisi, A., De Falco, G., Sirignano, M., Minutolo, P., Commodo, M., Carotenuto, C., Di Natale, F. (submitted). Modelling the electrophoretically-enhanced in-flame deposition of carbon nanoparticles. *Journal of Aerosol Science*.

Contents

3.1 Graphical Abstract

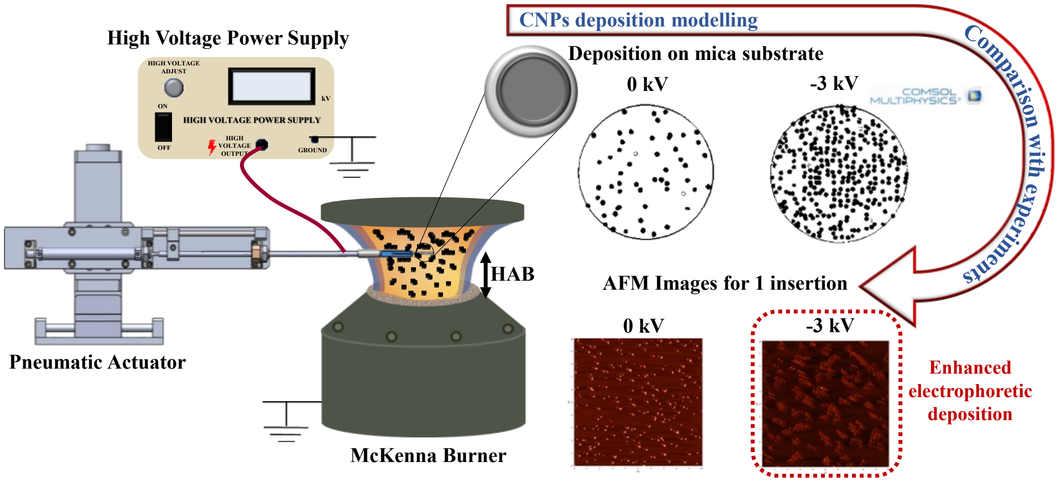

3.2 Abstract

Flame synthesis of Carbon NanoParticles (CNP) films is gaining strong interest for novel industrial applications because of the easy tuning of the operating conditions that enables accurate control of the chemical and physical properties of the produced CNPs. This work proposes a novelty in the synthesis of CNP films, namely the possibility of applying electric fields in flame to trigger electrophoretic deposition phenomena. In this way, it is possible to add another degree of freedom to the harvesting process and potentially modify the properties of the CNP films, without changing the operating flame conditions. To investigate the physical mechanisms governing the thermo-electrophoretic deposition of CNPs, a numerical model to simulate the particle dynamics close to the collecting substrate has been developed, and experiments have been carried out to provide highly controlled test conditions that can be used to support model validation. The experimental results consist of Atomic Force Microscopy (AFM) measurements to determine the number of particles deposited after a controlled harvesting condition as a function of the applied electrophoretic force, imposed on the substrate by means of a DC voltage varied from 0 to -3kV. The AFM shows that the deposited material increases up to six times

when passing from an uncharged to the -3kV charged case. The model predictions are highly consistent with the AFM measurements and pointed out that the electric field in flame significantly alters the CNPs deposition velocities and impact angles, which are likely to affect the properties of the films.

3.3 Highlights

- Proposed model is able to reproduce AFM results for particle deposition
- Electrophoresis is effective in harvesting naturally charged particles in flame
- Electrophoresis is the dominant phenomenon when active for particle deposition
- Electrophoresis increases up to 6 times collection rate of charged particles
- Electrophoresis increases impact velocity of collected particles on substrate

3.4 Introduction

Combustion-generated particles have been extensively associated with adverse health and environmental effects [1–5]. Hence, over the last decades, combustion-generated Carbon NanoParticles (CNPs) [6–10] have received increasing attention driven by the need to reduce the emission factors of combustion processes and the evolution of scientific knowledge and technological capabilities in the fields of combustion, environmental science, and toxicology.

On the other hand, CNP-based materials are gaining increasing interest in material science, due to their high specific surface area [11,12], biocompatibility [13,14], superhydrophobicity [15,16] as well as fascinating optical and electrical properties [17–21] that have encouraged their use in various fields such as bio-imaging [22–26], nanomedicine [27–29], sensor technology and energy storage [30–33].

CNPs materials are produced by a variety of methods, such as wet-chemistry, arc discharge, and gas-phase processes [34–37]. Among these latter, flame synthesis appears as a valid option since it is autothermic, operable as a one-step process, with lower cost compared to other routes, and scalable to the industrial level [38–46]. CNPs produced in flames can be collected by employing thermophoretic deposition, *i.e.,* inserting a cold substrate in the flame environment [47–49]. Large temperature gradients, up to about 10^6 K/m, appear very close to the substrate, driving particles toward the surface thanks to the unbalanced Brownian diffusion phenomena known as thermophoresis. The formation of CNPs thin films with different properties can be obtained by tuning combustion parameters and the substrate temperature [21,38–46,50].

De Falco et al. [21] have studied the morphological and electrical properties of flame-formed CNPs thin films produced by thermophoretic harvesting in a laminar premixed ethylene-air flame at a fixed equivalence C/O ratio, deposition time, and distance above the burner, HAB. A cold substrate is repeatedly inserted into the flame with a controlled insertion and cooling-down times. The experiments revealed that the film properties change with the HAB and the C/O ratio and that it is possible to fine-tune the film thickness by opportunely combining the number of substrate insertions in flame and their duration. However, a low harvesting rate has been achieved at a low C/O ratio, due to the low amount of CNPs in flame and to the intrinsic low thermophoretic deposition rate. This implies long production times and, consequently, a less efficient and scalable process. Besides, the thermophoretic deposition provides film structures with low density and the film mechanical resistance is thus scarce [21,51].

Electrophoretic forces can be used to enhance the deposition rate [50,52–60]. The use of electric fields to trigger electrophoretic effects on CNP harvesting has been largely exploited in after-treatment equipment and high-precision measurements systems [61–63] but less adopted for producing thin films, where a few examples on flame-generated titania and silica are reported [64–66].

To ignite electrophoretic deposition, an electric field must be applied to the flame. Typically, this is achieved by applying an electric potential to the stabilization plate or the collector substrate. This has several effects on particle deposition and even on flame characteristics.

The extensive knowledge of electrostatic particle capture suggests that the presence of an electric field in flame enhances deposition efficiency [53]. In fuel-rich flame conditions, a relevant fraction of the produced CNPs acquires an electric charge mainly due to thermal ionization and diffusion charging phenomena [67–69]. The charge fraction distribution of CNPs formed in flames has symmetric polarities and is in good agreement with Boltzmann's theory. The correlation between particle charge and size is at the basis of electrical mobility measurements used to infer the particle size distributions [68,69].

It was also observed that the electric fields have a noticeable effect on primary CNPs size, agglomerate size, and probably their crystallinity depending on the polarity at the electrode [70–74]. This is due to the alteration of CNP residence time in flame depending on the polarity applied to the substrate: application of a given polarity to the substrate electrode accelerates the capture of CNPs with opposite polarity, reducing their residence time, while the opposite occurs for CNPs with the same polarity applied to the substrate electrode [73]. Since CNP charge distribution is symmetric [75,76], in principle symmetric deposition rate can be expected regardless of the applied potential. Nevertheless, the effects of electric fields on the flame hydrodynamics and the ions dynamics alter this simple behaviour.

It has long been common knowledge that an external electric field has dramatic visible effects upon a flame since this is essentially a thermal plasma system: flame distortion, flame extinction, and soot suppression have been evidenced since decennia [77–79]. These phenomena are due to mechanical forces acting on the molecules as a consequence of the ionic wind, which sensibly affects the physical parameters of the flame. The ionic wind is the flow of ions and neutral gases which occurs when a flame is subjected to an external electric field. The flow of neutral gases happens because the ions, which are directly subjected to displacement caused by the electric field, transfer their momentum to the more numerous neutral particles [80,81]. Wang et al. [60] have studied the effect of a normally uniform electric field in a laminar premixed ethylene/air flames from a McKenna burner, where the burner was electrically grounded, whereas either positive or negative voltages were applied to the stabilization plate. They have shown that above a critical value for the electric field, the flame becomes unstable, firstly exhibiting flickering and then showing the onset of electric discharges. In particular, the electric breakdown potential under a negative field is about two times greater than those observed for a positive field and takes place well below the 3000 kV/m observed for dry air at ambient conditions [82].

Therefore, the motion of CNPs under the effects of an external electric field applied to a surface immersed in the flames is the result of the complex intertwining between electrostatic effects on the CNP charge, ionic wind effects and occurrence of electric breakdown. Below the electric breakdown, only flame-generated ions are present. Positive ions are formed by cations, while the negative ones are mostly composed of electrons, whose mass is far lower than the that of the cations. Therefore, the ionic wind mostly follows the direction of the cation motion in the field. For a negative polarity applied to the substrate, flame cations and positive CNPs are attracted. The cations mass generates an appreciable ionic wind that further pushes the particles towards the substrate. For a positive polarity, negatively charged CNPs are attracted to the substrate, but repelled by the ionic wind.

Xiong et al. [65] have studied the effects of a uniform external electric field and polarity on the production of titania-based films on a silicon substrate. When the applied electric potential is below 400 V, oppositely charged particles have been attracted to the substrate, increasing their electrophoretic velocity but decreasing their in-flame growth and agglomeration, resulting in smaller particle sizes and more columnar-structured films with lower packing density. For voltages above 400 V, the authors argued that particles behave as they acquired the same charge polarity as the voltage bias applied, being repelled and residing in the flame longer, thus increasing in-flame agglomeration and particle size. This turned into a more branched-structured film growth with high packing density [65].

As shown by Xiong et al. [65] the acceleration, or the deceleration of CNPs toward the charged substrate, and the resulting alteration of their velocity and impact angle with the substrate is likely to be related to a modification of the achieved film morphology. Indeed, the growth of CNP films comprises several steps: CNP collision on the substrate (or on deposit), CNP adhesion to the clean substrate or CNPS deposit, and, finally, CNP deposit/film re-structuring [83–86]. The CNP motion above the deposit can be considered as the controlling mechanism for film growth assuming a complete passive deposit, for which CNP attachment and coagulation phenomena can be neglected [86,87].

The dynamics of CNPs close to the substrate depend on field forces (*e.g.* gravitational or electromagnetic fields), particle inertia, and Brownian diffusion, which give rise to a combination of deterministic motions and random walk trajectories [83–87]. The dimensionless Peclet number measures the relative importance of the deterministic CNPs motion to the Brownian random walk and it is defined as:

$$Pe_i = \frac{v_i d_{p,i}}{D_i} \tag{3.1}$$

Where v_i is the normal component of the particle arrival velocity and D_i is the CNP diffusion coefficient. In the limit case of $Pe<<1$, a purely diffusive CNPs deposit occurs and the generated film grows with a fractal structure predicted by the diffusion-limited aggregation model [88]. On the other hand, for $Pe>>1$ there is a ballistic behaviour of the CNP and the deposits will be compact with a rough interface [89–92]. The introduction of an electric field in the flame, and the onset of an electrophoretic deposition mechanism in combination with a pure thermophoretic one, may alter the particle velocity, and thus their characteristic Peclet number, giving rise to an alteration of the film properties. Unfortunately, an experimental determination of the CNPs trajectories and velocity close to the film substrate is not available.

This paper aims to contribute to the discussion by proposing new experiments and a mathematical model for the thermo-electrophoretic deposition of CNPs in flame. A mathematical model is used to describe the CNPs dynamics close to the collector surface and aims to understand how the application of an electric field over the collecting substrate alters the velocity and the trajectories of CNPs of different sizes and charges while they are in the flame. The experimental work is thought to support and validate the modelling data, a controlled flame reactor has been equipped with a CNP collector unit which is pneumatically driven to provide a single insertion of a substrate in the flame, at a given height above the burner (HAB), with controlled residence time and speed of insertion. CNPs deposited on substrates have been analysed by atomic force microscopy (AFM). The validated model could offer useful indications to predict the morphological characteristics of CNP films obtained in the same experimental conditions with a larger number of insertions in flame.

The experimental results allow us to shed light on the amount of CNPs deposited under the effects of thermophoretic and electrophoretic forces. The model results allow us to predict CNPs collisional probability with the substrate and to identify the main controlling mechanisms of the film formation process.

The paper is divided into three main sections: the description of i) the experimental setup and methodology and ii) the model equations to describe particle motion in the flame and their adhesion to the substrate and the characteristics of the numerical model used for their resolution and iii) the presentation of experimental and model results.

3.5 Experimental methods

A sketch of the thermos-electrophoretic deposition setup is shown in **Figure 3.1**. This is an update of the thermophoretic deposition setup used by De Falco et al. [21,51,93,94], with specific improvements aimed to allow stable and steady application of a DC electric potential on the surface of the collector.

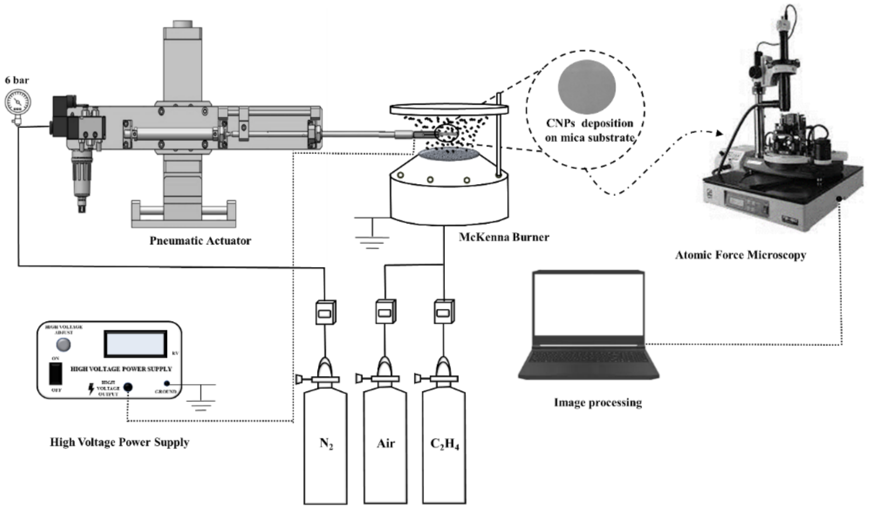

Figure 3.1. Sketch of the electrophoretic deposition setup.

A flat laminar premixed ethylene-air flame stabilized on a water-cooled McKenna burner was used as the CNPs-producing reactor. Cold gas velocity was 9.8 cm/s at the inlet of the burner and the carbon-to-oxygen ratio (C/O) was set to 0.67, which corresponds to a slightly sooting flame. These flame conditions have been extensively characterized by our research group [19,44,95–97], showing that CNPs harvested at a *HAB* higher than 10 mm have a typical bimodal number particle size distribution (PSD), with a first mode around 2-3 nm and a second one made by particles larger than 10 nm. However, CNPs of the first mode give a negligible contribution in terms of relative mass to the total population, whereas most of the mass of the total population is due to CNPs of the second mode. Moreover, CNP charge distributions are also known from previous works [68,69]. The experiments indicate an equal distribution of positively and negatively charged particles sampled from flames at atmospheric pressure and that all the particles with sizes up to 20 nm carry on at most a single electric charge [67,98]. The PSD in number and the fraction of charged particles for the experimental condition investigated therein are shown in the following **Figure 3.8B**.

CNPs were deposited on a freshly cleaved mica disk (ID= 10mm) substrate after a single rapid insertion in the flame. The insertion time t_{ins} was 100 ms, and the *HAB* was 15 mm. The probe containing the substrate was kept at a fixed electric potential, while the burner was grounded. The electric potential on the substrate varied from 0 kV up to -3kV, below the onset of corona discharge, which appears at about -4 kV. In this work, only negative electric potentials were tested, since in presence of positive polarities, instabilities and flame extinctions have been observed, leading to a more complex interpretation of the experimental and model results. Experimental setup conditions are summarized in **Table 3.1**.

Table 3.1. Experimental setup conditions.

Description (units)	Value
C/O ratio (-)	0.67
Cold gas velocity (cm/s)	9.8
Sampling position *HAB* (mm)	15
Insertion time t_{ins} (ms)	100
Applied voltage V_0 (kV)	0;-1;-2;-3
Substrate	Mica
Number of insertions N_{ins} (#)	1

AFM images were acquired over the freshly cleaved mica substrate to estimate the degree of coverage (*i.e.* the area of CNP deposits per unit area of mica substrate) and to obtain a morphological characterization of CNPs deposits as a function of the applied electric potential. AFM measurements were performed with a Scanning Probe Microscope NTEGRA Prima from NT-MDT, operated in semi-contact mode in air and equipped with NANOSENSORS SSS-NCHR super-sharp silicon probes with a nominal tip radius of 2 nm.

3.6 Model description

In this section, we report the equations used to simulate the dynamics of CNPs close to a cold substrate immersed in a flat laminar ethylene-air premixed flame.

The model simulates the exact geometrical characteristics of the McKenna burner flame space, with its stabilization plate and with the substrate steadily kept in position inside the flame, according to the experimental conditions. The mathematical domain is thus a cylindrical space between the burner exit and the stabilization plate where the substrate is immersed in. Due to the extremely fast chemical kinetics and specific harvesting conditions, we assumed that no active chemistry is involved. Accordingly, the flame is made up of air entering the burner. Temperature (1500 K) and uniform axial velocity (0.50 m/s) simulating flame-burnt gases have been assigned at the burner exit [99]. The substrate is kept at 350 K when the simulation starts. The substrate is kept at a fixed applied potential while the burner and the stabilization plate are grounded.

The particle deposition model includes the resolution of the mass, momentum and energy balance in the gas phase, the Maxwell and Gauss equations for the assessment of the electric field and the particle's momentum balance to determine particle tracing. Considerations to estimate particle rebounds and adhesion on the substrate surface have been included to allow a more appropriate comparison with the experimental results. All the equations reported in this section are in vectorial notation. Both vectors and tensors are always reported in bold.

The model adopts Navier-Stokes equations for the conservation of momentum and the continuity equation for incompressible flows, by neglecting the influence of the electric field on the stress tensor:

$$\rho_g \left(\boldsymbol{u} \cdot \nabla \boldsymbol{u} \right) = \nabla \cdot \left[-P \underline{\boldsymbol{I}} + \mu_g \left(\nabla \boldsymbol{u} + \nabla \boldsymbol{u}^T \right) \right] \tag{3.2}$$

$$\nabla \cdot \boldsymbol{u} = 0 \tag{3.3}$$

Where ρ_g is the gas density; $\boldsymbol{u}$ is the velocity vector; P is the pressure; $\underline{\boldsymbol{I}}$ is the identity tensor and μ_g is the gas viscosity; $\nabla \boldsymbol{u}$ and $\nabla \boldsymbol{u}^T$ are, respectively, the velocity gradient tensor and its transposed; $\nabla \cdot \boldsymbol{u}$ is the divergence of the velocity vector. No slip condition is assigned on the physical walls and a suppress backflow condition is imposed on the lateral surface of the domain. A uniform axial velocity simulating flame-burnt gases is assigned at the base of the cylinder in correspondence with the burner exit:

$$\begin{aligned} &\boldsymbol{u}_{wall} = \boldsymbol{0} \\ &\underline{\boldsymbol{T}} \cdot \boldsymbol{n} = -p_{out} \cdot \boldsymbol{n} \\ &\left| \boldsymbol{u}_{inlet} \right| = 50\ cm/s \end{aligned} \tag{3.4}$$

Where $\boldsymbol{u}_{wall}$ is the gas velocity vector on the physical walls; $\boldsymbol{n}$ is the outward surface normal vector; p_{out} is the pressure outside the domain, set to prevent the fluid from entering back into the domain; $|\boldsymbol{u}_{inlet}|$ is the normal inflow inlet velocity, equal to 50 cm/s at the inlet temperature of 1500 K (9.8 cm/s at ambient temperature) as in the experiments [95].

The flame temperature is modelled by solving the enthalpy balance as a boundary value problem of the form:

$$\rho_g c_{p,g} \boldsymbol{u} \cdot \nabla T + \nabla \left(-k \nabla T + q_r \right) = Q_{gen} \tag{3.5}$$

Where $c_{p,g}$ is the gas specific heat capacity at constant pressure; ∇T is the temperature gradient; k is the thermal conductivity; q_r is the heat flux by radiation estimated from our previous knowledge of the particle emissivity values [100,101]; Q_{gen} contains heat sources other than viscous dissipation such as the thermal power generated by the highly exothermic incomplete combustion reactions occurring in the flame [102–105]. Computations are preliminarily performed for the unperturbed flow in the absence of the probe and, subsequently, by introducing the probe in the flame at an imposed temperature of 350 K.

By neglecting magnetic field effects, the Maxwell and Gauss laws are solved to simulate the electric field along the flame, considering a ground boundary condition on both the burner and the stabilization plate, and a constant DC electric potential applied on the substrate, V_0:

$$\begin{aligned} &-\nabla \cdot \left(\varepsilon_m \nabla V \right) = \rho_{sc} \\ &V_p = V_b = 0 \\ &V_{sub} = V_0 \end{aligned} \tag{3.6}$$

where V_{sub} is the electric potential at the substrate; V_p and V_b are, respectively, the electric potential values at the burner and the stabilization plate; ρ_{sc} is the net space charge density -*i.e.,* the difference of positive and negative ions concentration in a flame [106–108]. Electrons, with their small mass and high mobility, have a high diffusion rate out of the flame, resulting in a spatial distribution of charge in the flame. In order to adjust the electrons and ions fluxed in flame, there is a self-induced electric field through the flame that accelerates positive ions and decelerates electrons, making them diffuse out of the flame front at an equal rate. The intrinsic electric field in the flame is described in terms of net space charge density. This parameter is a function of both flame fluid dynamics and the local Carbon-to-Oxygen ratio. An average value of the flame space-charge density is retrieved from the pertinent literature [108].

The motion of dispersed CNPs in the flame can be modelled by the Langevin equation [109,110]. For each CNPs size d_p and each value for the CNPs charge q, its translational motion under the assumption of spherical shape is modelled as:

$$m\frac{d\boldsymbol{U}}{dt} = \boldsymbol{F}_D + \boldsymbol{F}_G + \boldsymbol{F}_B + \boldsymbol{F}_T + \boldsymbol{F}_E + \boldsymbol{F}_i \tag{3.7}$$

where m is the mass of a single CNP; $\boldsymbol{U}$ is the relative velocity – *i.e.,* the difference between the particle velocity and the gas (flame) velocity at each point in the domain. $\boldsymbol{F}_D$ is the friction force on a spherical CNP:

$$\boldsymbol{F}_D = \frac{3\pi\mu_g d_p \boldsymbol{U}}{C_c} \tag{3.8}$$

where d_p is the CNP diameter, μ_g is the dynamic viscosity of the gas medium and C_c is the Cunningham correction factor.

Due to the size of CNPs considered therein, the particle's motion is also affected by Brownian diffusion. This is the irregular wiggling motion of a particle caused by random variations in the relentless bombardment of gas molecules against the CNPs. The amplitude of Brownian excitation can be modelled with the Gaussian-with noise fictitious force:

$$\boldsymbol{F}_B = \boldsymbol{\zeta}\sqrt{\frac{6\pi k_B T d_p}{\Delta t}} \tag{3.9}$$

where $\boldsymbol{\zeta}$ is a zero-mean, unit-variance independent Gaussian random number vector; k_B is the Boltzmann constant; T is the absolute temperature and Δt is the time-step for the integration of the equation of particle motion.

$\boldsymbol{F}_G$ is the gravity (and buoyancy) body force:

$$\boldsymbol{F}_G = \frac{\pi}{6} d_p^3 \left(\rho_p - \rho_g\right)\boldsymbol{g} \tag{3.10}$$

where ρ_g is the gas density; ρ_p is the CNPs density and $\boldsymbol{g}$ is the gravitational acceleration.

$\boldsymbol{F}_T$ is the thermophoretic force:

$$\boldsymbol{F}_T = -\frac{P\lambda d_p^2 \nabla T}{T} \tag{3.11}$$

valid on the free molecule regime (Knudsen number Kn>>1) limit, where P is the pressure and λ is the fluid mean free path.

In the operating conditions, CNP deposition is driven mostly by thermophoresis and friction, since inertia and body forces are negligible because of their small sizes [111–114]. This is in line with former studies on the Brownian deposition mechanism which showed that this phenomenon is relevant only when the CNPs are within 100 nm distance from the collecting surface [60].

$\boldsymbol{F}_i$ reported in **Eq.(3.7)** represent a sum of all contributions from interaction forces between pairs of particles, *i.e.* the attractive van der Waals sintering force and the electrostatic forces between charged CNPs, normal repulsive, dissipative and attractive contact forces [115,116]. For diluted systems, where the interparticle distance is higher than 5 times the CNPs diameter, these interparticle forces could be neglected. Moreover, if CNPs have sizes higher than 20 nm, the assumption of a spherical shape is not acceptable. In fact, particles larger than 20 nm appear as aggregates, which are clusters of primary particles that are chemically bonded by sinter-bridges with dimensions typically between 200 and 300 nm. For aggregated and agglomerates, the additional torque balance is needed [115,116]:

$$\boldsymbol{M} = I\frac{d\boldsymbol{\omega}}{dt} = \boldsymbol{M}_F + \boldsymbol{M}_i \tag{3.12}$$

Where I is the CNP moment of inertia, $\boldsymbol{\omega}$ is the CNP angular velocity, $\boldsymbol{M}$ is the net torque, $\boldsymbol{M}_F$ is the resulting momenta related to the external long-range field and $\boldsymbol{M}_i$ is the resulting torque acting between pair of CNPs, which can be expressed as:

$$\boldsymbol{M}_i = -\boldsymbol{F}_t \times \boldsymbol{R}_p - \boldsymbol{M}_r \tag{3.13}$$

Where $\boldsymbol{F}_t$ is the tangential component of the friction forces related to the CNP against the tangential component of the velocity; $\boldsymbol{R}_p$ is the radius vector for a CNP and $\boldsymbol{M}_r$ is the rolling friction force acting against the angular velocity $\boldsymbol{\omega}$ [116].

When an external electric field is applied, charged CNPs are affected by an electrostatic force $\boldsymbol{F_E}$ [53,117] near the deposition surface, which is given by the following expression:

$$\boldsymbol{F}_E = q\boldsymbol{E} - \frac{q^2}{16\pi\varepsilon_m z^2}\boldsymbol{n} \tag{3.14}$$

where q is the total charge carried by a CNP; **E** is the electric field vector; **n** is the unit vector orthogonal to the burner exit; ε_m is the flame permittivity. On the right-hand side of the **Eq.(3.14)**, the first term, $q\boldsymbol{E}$, is the Coulomb force due to the imposed electric field, and the second term is the image force, corresponding to the force created by an image charge of $-q$ at position $-z$ from the surface. Under the effect of an external field, the Coulomb force is dominant, the image force being relevant only at short-range very near the surface [117].

When CNPs are placed in a non-uniform electric field, they will be polarized leading to the attraction of CNPs, which are dependent on the relative polarizability of the CNPs and the surrounding medium [118–121]. According to Maxwell-Wagner-Sillars theory [122,123] such polarization occurs at the CNP medium interface on a microscopic scale, leading to the separation of charges. This gives rise to a motion of particles toward the electrode known as dielectrophoresis, DEP. The strength of the DEP force ($\boldsymbol{F_{DEP}}$) varies with the properties of these CNPs and the suspension media. The simplest theoretical model for DEP is that of a homogeneous spherical particle immersed in a dielectric medium [124], which can be calculated according to the Pohl model [118] as follows:

$$\boldsymbol{F}_{DEP} = \frac{\pi}{4} d_p^3 \varepsilon_m \operatorname{Re}\left(f_{CM}\right) \nabla \boldsymbol{E}^2 \tag{3.15}$$

Where ε_m is the medium permittivity and $\operatorname{Re}(f_{CM})$ is the real part of the Clausius-Mossotti factor (f_{CM}) [119,121], which is defined in terms of complex permittivity as follows:

$$f_{CM} = \frac{\varepsilon_p^* - \varepsilon_m^*}{\varepsilon_p^* + 2\varepsilon_m^*} \tag{3.16}$$

Where ε_p^* and ε_m^* are the complex permittivity of the CNP and the suspension medium respectively. The calculation of the complex permittivity for CNP and medium is given below[121,125]:

$$\varepsilon_p^* = \varepsilon_p - \boldsymbol{i}\left(\frac{\sigma_p}{\omega_e}\right) \tag{3.17}$$

$$\varepsilon_m^* = \varepsilon_m - \boldsymbol{i}\left(\frac{\sigma_m}{\omega_e}\right) \tag{3.18}$$

Where ε_p is the CNP permittivity; σ_p is the CNP electrical conductivity; σ_m is the medium electrical conductivity; ω_e is the angular frequency of the electric field. If the angular frequency of the electric field is equal to zero – *i.e.* direct current electric field – the real part of the complex permittivity becomes [125]:

$$\mathrm{Re}\left(f_{CM}\right) = \frac{\sigma_p - \sigma_m}{\sigma_p + 2\sigma_m} \tag{3.19}$$

The Langevin equation can be used to determine particle trajectories inside the flame, as they enter the domain through a given injection plane. The model is also able to calculate the fraction of particles that collide with the substrate, *i.e.*, the collisional probability ξ_i of each particle size.

To compare model results and experiments, it is necessary to make a direct comparison of the model result with the data in terms of the degree of coverage obtained by AFM. To this aim, it is possible to estimate the area A_i occupied by a CNP of diameter d_{pi} on the mica substrate, if the collisional probability ξ_i of each particle size is known:

$$A_i = \gamma_i \xi_i N_{i0} \frac{\pi}{4} d_{pi}^2 \tag{3.20}$$

In which N_{i0} is the number concentration of CNPs in the sampling point of the flame, as defined by the experimental data, γ_i is the sticking coefficient of a particle of diameter d_{pi}. Some clarification is needed regarding this parameter. CNPs reach the charged surface with an impact velocity $\boldsymbol{v_i}$ that is obtained by solving **Eq.(3.7)**. According to the specific characteristics of the impact dynamics, particles may either adhere or rebound after collision with the substrate. Typically, particle rebounding from a surface has been considered an unwanted phenomenon causing artifacts in inertial impactors and reduction of the effective deposited particles. This suggests the importance of studying particle-surface interaction phenomena. The interaction can be understood through four basic phenomena: adhesion, rebound, resuspension and charge transfer. An adhesion force arising from the molecular interaction of a particle and a surface affects the particle in the adhesion force field within a distance from the surface. The extension of the adhesion force field depends on the material roughness and objects involved but for flame-formed nanoparticles, it is in the order of a few atomic layers, typically near 0.4 nm [126–128].

For uncharged CNPs, the van der Waals interactions represent the main contribution to adhesion [129]. These interactions can be modelled in terms of Lennard-Jones potentials and the framework of the gas kinetic theory. In particular, it is considered that for CNP sizes smaller than 10 nm, a sticking coefficient significantly lower than 1 is expected because thermal rebound effects are likely to prevail over adhesion mechanisms due to van der Waals forces [130]. On the contrary, soot particles with a diameter larger than 10 nm are expected to stick after collision [130].

This discrepancy is likely to be neglected in presence of a voltage since the adhesion mechanism includes additional attractive electric interaction forces with a potential increase in the sticking coefficient up to 1 [130]. In this model, sticking coefficients for uncharged CNPs produced in a C/O=0.67 flame reported in D'Alessio et al. [130] are used for both charged and uncharged particles and whatever the applied potential is. The total degree of coverage φ is the ratio between the total area occupied by all the CNPs and the mica substrate area, A_s.

$$\varphi = \frac{\sum_i A_i}{A_s} \tag{3.21}$$

3.7 Numerical methods

COMSOL Multiphysics® [131] finite element solver package has been used to solve the mass, momentum, energy balances, electric field equations, and the particle tracing model, using specific integrated software libraries.

The flame environment is represented as a cylindrical three-dimensional domain (diameter 6 cm and height 22 mm, as the distance between the burner exit and the stabilizing plate), generated within the COMSOL software using the internal geometry and functionality tools. In particular, the bottom and top circular surfaces of the cylinder represent the burner exit (namely the flame inlet) and the stabilizing plate (namely the flame outlet) respectively, while the side surface of the cylinder represents the interface between the flame and the surrounding outside air.

An aluminium holder including the deposition substrate has been positioned at a distance from the burner exit equal to the height above the burner of the real system (*HAB*=15 mm) so that the centre of the deposition substrate coincides with the centre of the flame itself. A 3D CAD file for the holder has been imported to obtain its correct sizes. For the substrate, a flat disk with a 10 mm diameter and 150-micron thickness has been considered. All the physical properties of the substrate have been set equal to those of mica muscovite.

The numerical simulations for the flame have been carried out by using COMSOL Computational Fluid Dynamics, Heat Transfer, and AC/DC three-dimensional solvers. The specific physics interfaces used are Heat transfer and Laminar Flow, both of which are coupled to the Multiphysics of Non-Isothermal Flow, and Electrostatics, considering stationary conditions.

In particular, **Eqs. (3.2)** and **(3.3)** have been solved under the hypothesis of incompressible laminar flow with a reference pressure level equal to 1 atm. The fluid viscosity has been set equal to that of air, whereas the density is a simulation result. A normal inflow velocity of 50 cm/s has been considered as a boundary condition at the burner exit for the inlet flame (this corresponds to the 9.8 cm/s cold-gas velocity – 25°C – set for the experimental setup), whereas for the flame outlet an ambient reference absolute pressure equal to 0 Pa with a compensation of the hydrostatic pressure and suppression of the backflow has been considered. Regarding the lateral walls, however, the standard no-slip condition has been used.

Furthermore, **Eq.(3.5)** has been solved for the heat transfer in the flame. Here, a reference temperature equal to 293.15 K has been used, applying a consistent stabilization with streamline and crosswind diffusion. Both at the flame inlet and outlet a thermal insulation condition has been applied. Additionally, the temperature at the holder and substrate surface has been set equal to 350 K, and a volumetric heat source equal to Q_{gen}=40 W has been set to simulate the heat generated by the exothermic incomplete combustion reactions occurring in the flame [102–105]. Moreover, heat flux is added to the whole domain to consider the radiative heat losses estimated from the emissivity values for CNPs generated in flame [100,101].

Regarding electrostatics physics, the reference default impedance value of 50 Ohm for the terminals connected to grounding has been selected. A ground condition has been defined for both the flame inlet and outlet, while for the lateral walls, a zero charge condition has been considered. A net space charge density has been defined, as $4.61 \cdot 10^{-10}$ C/m^3 as retrieved in literature to ensure the flame quasi-neutrality even in presence of charged species and electrons spatial diffusion in the flame [106–108]. Finally, an adjustable electric potential condition (V_0) has been applied to the holder, considering values lower that the onset of corona discharges.

All these equations have been first discretized on the flame domain and then solved via the finite element method (FEM). The FEM technique discretized the domain into finite elements and the dependent variables have been solved at nodes connecting these elements. This is done by multiplying the governing equation by weighting functions and integrating them to obtain their weak form. The solution has been then approximated at the element level, and the entire problem can be solved by assembling the elemental equations. The main advantage of the finite element method is its capacity to treat boundary conditions on curved surfaces.

To obtain fluid temperature, velocity, pressure, electric potential, and electric field, a three-dimensional unstructured mesh with four-node tetrahedral elements has been adopted. In the region close to the holder and substrate wall, where the boundary layers develop, mesh refinement is used. The Multifrontal massively parallel sparse direct solver has been used for all the simulations, with the generalized minimum residual (GMRES) solver as a linear solver and the Newton iteration method as a nonlinear method. The relative tolerance has been set to 10^{-4}, but usually, values below 10^{-5} are reached.

Grid independence tests, from the numerical results, have been done with various grid sizes. From this process, a mesh with 807804 size elements and 39888 boundary elements has been built. This mesh is sufficient to achieve accuracy within 2% of that obtained by the maximum number of elements (820370 size elements and 43944 boundary elements).

Model results of temperature profiles and velocity streamlines with and without the probe inserted in flame and of the electric field modulus and streamlines without and with a voltage applied to the probe are reported in **Figure 3.2**.

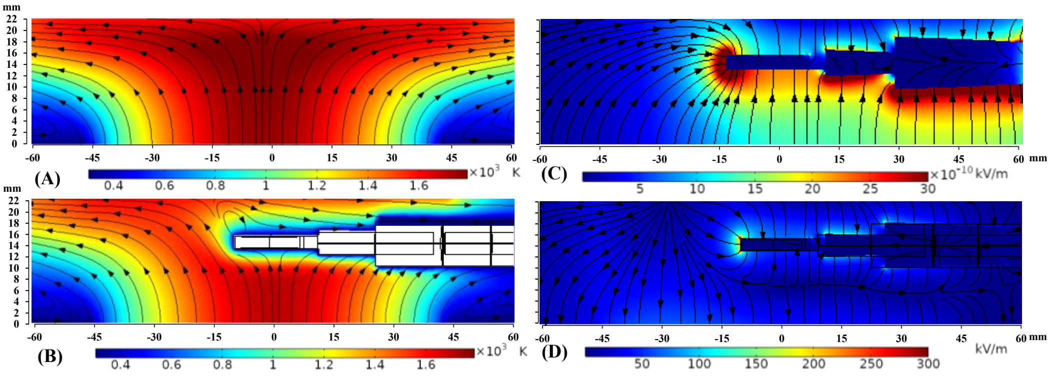

Figure 3.2. Left: Temperature profile and velocity streamlines (lines and arrows) without **(A)** and with **(B)** the probe in flame; Right: Electric field intensity and streamlines (lines and arrows) without **(C)** and with **(D)** the voltage applied to the probe. Images reported refer to the cut plane rz perpendicular to the burner plate, where r and z are the radial and axial coordinates.

The comparison between the experimental axial temperature profiles reported in [44] and the simulated one shows a very good agreement (*see* **Figure 3.3**).

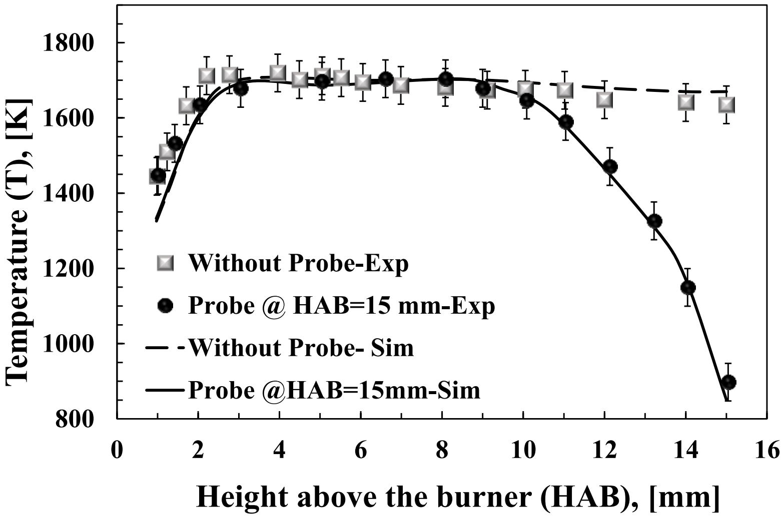

Figure 3.3. Comparison between experimental [44] and simulated temperature profile of the flame without and with the probe (HAB = 15 mm with C/O=0.67). Experimental uncertainty: ±50 K. Measurements and simulations have been performed using a cylindrical dilution probe as described in [44].

Even in the absence of an applied electric potential, the flame is characterized by an intrinsic (although very low) electric field, deriving from the imposed space-charge density. When potential is applied, a strong electric field perpendicular to the substrate establishes. The electric field has been simulated using the same mesh of the fluid dynamic field model.

CNPs are modelled with a discrete distribution, considering seven reference size bins at 2, 3, 5, 8, 10, 15 and 20 nm. The selected bins have been chosen to fully describe the experimental CNPs Size Distribution (PSD) [132–134]. The use of finer discretization does not affect the results. Modelled CNPs are considered single spheres, and this assumption is reasonable for the investigated size range [115,116]. CNPs are released from the inlet burner boundary plane with a random spatial distribution at the bottom of the particle tracing domain. To allow a proper balancing between calculation time and significance of the model results, for particles up to 10 nm, $N_{in,i} = 5 \cdot 10^3$ particles have been injected in the particle tracing domain, while this number is doubled for the 15 and 20 nm particle size, to account for their lower thermophoretic deposition efficiency.

CNP motion has been modelled using Particle Tracing for the Fluid Flow interface with a one-way coupling approach: this implies that particle dynamics do not induce effects on the external fluid. When this physics interface is added, it is important to define particle properties in terms of density, diameter, charge number, and type. CNPs have been approximated as solid spherical particles of density 1.8 g/mL [135,136], which variable diameters from 2 to 20 nm, and charge numbers (0, +1, or -1). It is important to underline that the spherical hypothesis is consistent with some experimental evidence for the selected size range [137,138]. Particle release and propagation have been modelled using the Newtonian formulation with the Langevin correction (*see* **Eq.(3.7)**). In this module, it is possible to add some default forces, but also user-defined forces can be added. In particular, the gravity, the drag with the Cunningham-Millikan-Davies model, the Brownian, dielectrophoretic and the

Coulomb electric forces have been selected from the default ones, since the COMSOL default equations are the same adopted in the model. Instead, thermophoretic and image forces have been user-defined (*see* **Eq.(3.11)** and the second addendum to the right of **Eq.(3.14)**).

To balance the physical representativeness of the model results and computational costs, particle tracing has been calculated in a portion of the overall domain: the particle tracing domain is a cylindrical volume of a given diameter, which extends vertically from the burner to the substrate horizontal surfaces. The size of this cylinder is determined according to optimization and convergence criteria, as discussed in the following paragraph. Also in this domain, the calculations are performed using the same tetrahedral mesh of the overall computational domain. **Figure 3.4** shows the projection in the x-z plane of the domain for the flame environment and the particle tracing with the adopted mesh. The mesh refinement area close to the substrate is also reported.

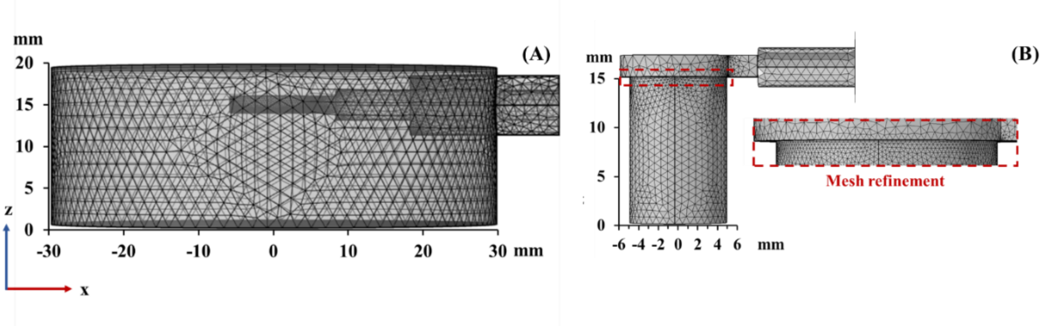

Figure 3.4. (A) Geometry domain for the flame environment and **(B)** Particle tracing domain projected in the xz plane. The unstructured mesh with four-node tetrahedral elements and the mesh refinement adopted for the boundary layer are reported.

CNPs have been released from the inlet flame boundary plane with a random spatial distribution from the bottom of the particle tracing domain. At the lateral wall of this domain, a boundary condition of disappear has been set. Instead, a freeze condition has been set on the substrate to activate the Particle Counter node.

The diameter of the particle tracing domain has been determined from the numerical simulation. In particular, the minimum size of the cylindrical volume close to the deposition substrate was found as the one which guaranteed that all the positively charged CNPs were harvested when the maximum electric potential (*i.e.* -3 kV) was applied to the deposition substrate. Similarly, it was decided to optimize the release time duration of the CNPs in the control volume by defining a minimum duration that would not alter the results. In fact, the CNPs injection in the volume could be better described as an instantaneous pulse – namely zero release time – or as a time-distributed injection – namely non-zero release time. For each domain size, the mesh is optimized to grant convergence of the results. The effects of the diameter of the particle tracing domain and the release time duration of collisional probability for positively charged particles of 10 nm are reported in **Figure 3.5** considering a standard COMSOL Fine mesh.

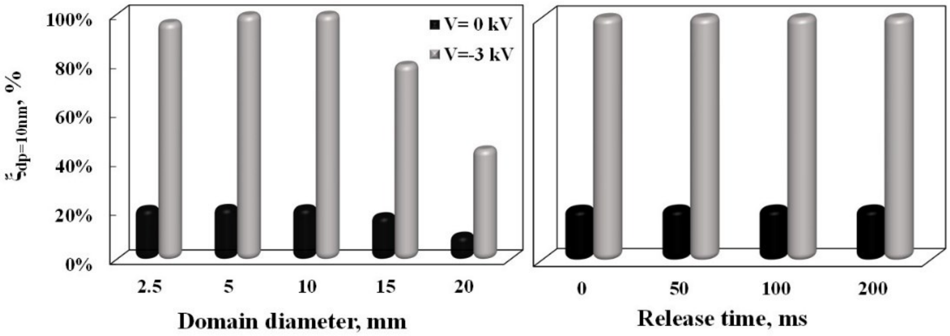

Figure 3.5. Effects of the domain diameter (left) and release time duration (right) on the collisional probability (ξ, %) of 10nm CNPs with a single positive charge in the absence (V=0 kV, black) and presence (V=-3kV, grey) of an electric potential applied to the deposition substrate. A release time of 0 ms refers to an instantaneous pulse.

Figure 3.5 shows that the duration of the release time does not affect the collisional probability, so this was minimized by assuming an instantaneous impulse. Moreover, the simulations indicate that the minimum particle tracing domain diameter is 10 mm, which is exactly the size of the deposition substrate. The computational time of the COMSOL model is greatly affected by the particle tracing step. Convergence for the steady state solution of the thermal-fluid dynamic and the electric fields requires 30 and 45 iterations respectively, while the particle tracing model requires 8000 iterations. The simulations results consist of profiles of velocity, temperature, pressure, electric potential, and electric field at each point of the domain and the different streamlines. Moreover, for CNPs it is possible to obtain information about the particle trajectories, the impact velocity vectors, and the number of particles that freeze on the substrate. Besides, the freezing position can be determined. From particle trajectory analysis, a collisional probability (ξ_i,%) – the ratio between the number of harvested CNPs ($N_{out,i}$) and the number of injected ones ($N_{in,i}$) – can be determined. The fraction of covered area for each CNP size is calculated from **Eq.(3.20)** after fixing the sticking coefficient γ_i. Finally, the total degree of coverage φ is calculated with **Eq.(3.21)**.

3.8 Experimental Results

CNPs have been collected with a single insertion on mica disks varying the electric potential from 0 kV to -3kV. **Figure 3.6** shows AFM images for selected areas of the mica disk for different applied voltages. The images show that deposited CNPs increase as the voltage increases. Using the Software Image J® to obtain image analysis, it is possible to show that the degree of coverage increases by six times, from 5% at 0kV to 30% at -3kV.

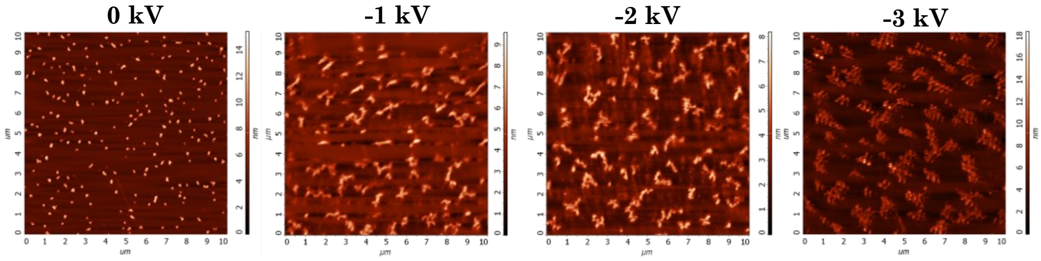

Figure 3.6. AFM 2D images of the CNPs collected on a mica substrate with a single insertion of 100 ms in flame. (C/O=0.67, HAB=15mm, t_{ins}=100ms; N_{ins}=1).

Interestingly, in the case of pure thermophoresis at 0 kV, CNPs are distributed uniformly on the substrate and appear mostly as single spherical entities or small aggregates of a few particles. This effect is consistent with former observations of the thermophoretic deposition mechanism [95,139], according to which particles fall sequentially at apparently random points towards an initially flat surface and each particle sticks to the first point of contact. On the other hand, in presence of applied potential, CNPs are organized as fractal petal-like structures. It is beyond the scope and the limit of the proposed model to delve into details of the morphology of the deposits, that will be specific object of further investigation. However, literature studies, suggest that the formation of the deposits can be described by using a diffusion-limited cluster aggregation (DLCA) model [140,141], according to which single CNPs deposited on the substrate after impacting on the surface, diffuse and aggregate to form larger fractal structures. Also polarization effects should be considered as well [142,143]: positively charged CNPs are deposited on the negatively charged substrate as a result of Coulomb interactions [110]. CNPs reach the negative charge at equilibrium with the substrate. While other positively charged particles can be attracted by Coulomb interactions, the neutral CNPs in the flame – the majority – can be polarised by the applied field determining stronger adhesion over the already deposited particles due to the higher chemical affinity [68,69]. Indeed, CNPs fractal-like structures are also observed in other works for similar reasons [144,145].

3.9 Modelling Results

To understand the controlling mechanism and the role of the electric field in the harvesting for each class of CNPs, simulations have been conducted considering both uncharged and charged CNPs with and without the application of an electric field.

Figure 3.7 shows the contribution to the collisional probability related to Brownian, thermophoresis, Coulomb, and dielectric electrophoresis of uncharged and single (positive) charged CNPs over a substrate kept at – 3kV, as a function of their size. These are obtained by applying the particle tracing model (**Eq.(3.7)**) with one single force plus the drag, $\boldsymbol{F}_D$, and interaction forces, $\boldsymbol{F}_i$, at a time.

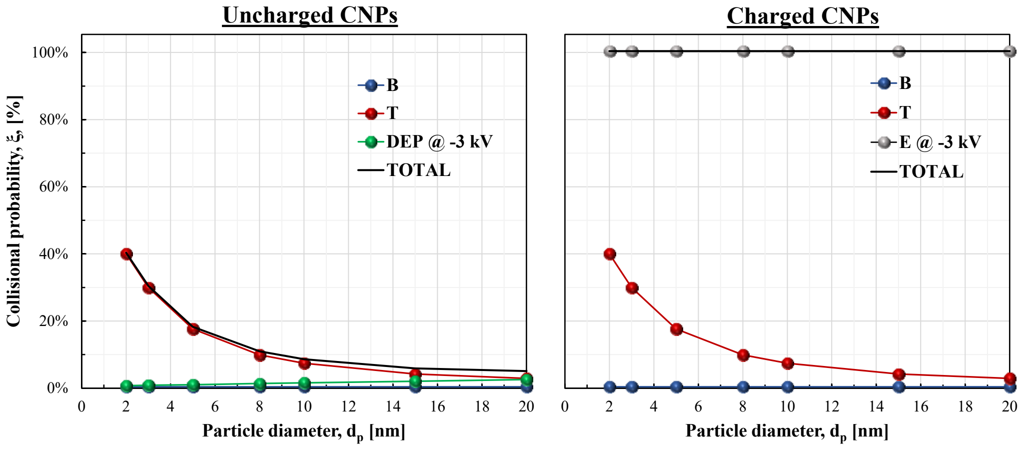
Uncharged CNPs

Charged CNPs

Figure 3.7. Contribution to the collisional probability of CNPs of different sizes for uncharged (left) and a single positive charge (right) CNPs. B: Brownian motion; T: Thermophoretic force; DEP: Dielectrophoretic force for uncharged CNPs with an applied voltage equal to -3 kV; E: Electrostatic force for charged CNPs with an applied voltage equal to -3 kV.

Figure 3.7 shows that for uncharged CNPs the resulting total collision probability (dark line) has a decreasing trend with CNPs sizes, passing from 40% to 1% for CNPs size increasing from 2 to 20 nm. Moreover, the contribution to the collisional probability due to the Brownian motion (B) is negligible for all CNPs classes. In the presence of an external electric field – when a voltage is applied to the deposition substrate – polarisation phenomena are activated on the uncharged CNPs, determining the onset of dielectrophoretic force (DEP). This contribution becomes non-negligible only for CNPs larger than 5 nm, but it is still <4% of the total collisional probability. Indeed, for uncharged CNPs thermophoresis is the controlling mechanism for the harvesting, favouring the deposition of smaller CNPs, characterised by higher thermal mobility, and disfavouring the larger ones, whose inertia is higher and thermal mobility is lower. Thermophoresis favours the harvesting of smaller CNPs, both for the lower fraction of charged particles and for the higher thermal mobility. The fluid dynamic field and the Brownian motion allow small CNPs to randomly approach the substrate zone. At a distance < 1 mm from the deposition substrate, due to the very high-temperature gradient (about 10^6 K/m) thermophoresis becomes larger than Brownian motion and CNPs motion becomes non-chaotic and directional.

For charged CNPs (**Figure 3.7**, right), Brownian motion remains negligible and the effect of thermophoresis is similar to that obtained for uncharged CNPs. Ionic wind effects and dielectrophoretic forces have low effects on the deposition rate, but Coulomb electrophoresis provides a significant increase in the collisional probability, which reaches 100% for an applied potential of -3 kV. Moreover, the effect of the electric field is CNPs size-independent, being mostly influenced by the CNP charge (equal to a single cation in this calculation).

The calculated collisional probability can be applied to the actual particle size and charge distribution of flame CNPs at the sampling point, to compare with the experimental deposition data (C/O=0.67, HAB= 15 mm).

To this aim, **Figure 3.8** shows (from the top to the bottom) the total collisional probability values for uncharged CNPs and charged ones varying the voltages applied to the deposition substrate; the actual fraction of positively charged and uncharged CNPs and the resulting collisional probability values for CNPs weighted against the CNP size and charge distributions.

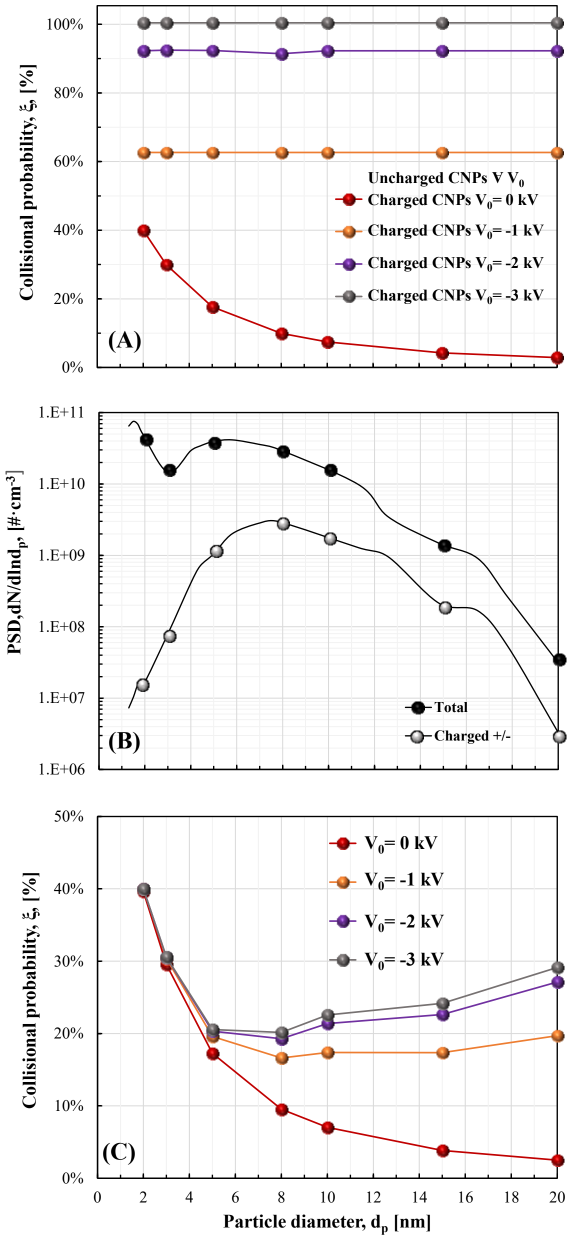

Figure 3.8. (A): Total collisional probability for uncharged and for single charged CNPs varying the voltage applied to the deposition substrate from 0 kV to -3 kV. Note that for uncharged CNPs the collisional probability is always equal to that at 0 kV. **(B)**: Particle size distribution (PSD) in number for total (black) and single-charged CNPs (grey). **(C)**: Collisional probability (ξ,%) weighed against the size and charge distribution of CNPs adapted from [75,76] as a function of the particle diameter varying the electric potential applied to the deposition substrate.

Figure 3.8A reports the total collisional probability for each CNPs size on the deposition substrate as a function of the applied potential. As discussed in the comments of **Figure 3.7**, for uncharged CNPs, thermophoresis is stronger than dielectrophoresis and ionic wind effects and therefore, the curve 0 kV refers to the harvesting of charged CNPs in absence of an external electric field but is also very close to that of uncharged CNPs for a charged substrate. For charged CNPs, there is an increase in the total collisional probability, which reaches 65% for an electric potential applied to the deposition substrate of -1 kV and up to 100% for an applied potential of -3 kV. **Figure 3.8B** reports the PSD of CNPs used as input for this work together with the size distribution of single-charged (both positive and negative) CNPs achieved in the same experimental conditions tested in this work [68,69]. It is possible to see how below 8 nm the fraction of charged CNPs is less than 10% while reaching nearly 30% for CNPs larger than 10 nm. Modelling results on the collisional probability for each CNPs size as a function of the applied potential are reported in panel **(C)** of **Figure 3.8** taking into account the fraction of charged CNPs.

Figure 3.8C shows that, due to the small fraction of CNPs smaller than 5 nm that is charged (**Figure 3.8B**), the collisional probability for these particles is not affected by the applied electric field. On the other hand, thanks to the higher fraction of charged particles (**Figure 3.8B**), a significant increase in the collision probability for CNPs larger than 5 nm appears after the application of the electric field. This increase is not linear: the collisional probability increases significantly in the transition from pure thermophoresis to an applied potential of -1 kV. For higher potentials, there is a weaker increase since mainly all particles are collected within the insertion time and saturation is reached for the system.

On the basis of the collisional probability data for the CNPs in the experimental flame conditions, and after the application of **Eqs.(3.20)** and **(3.21)**, the surface coverage can be estimated. **Figure 3.9** resumes on the left the estimated degree of coverage as a function of the electric potential applied to the mica substrate and on the right the comparison between simulation and experimental values of the degree of coverage without and with the sticking coefficient correction.

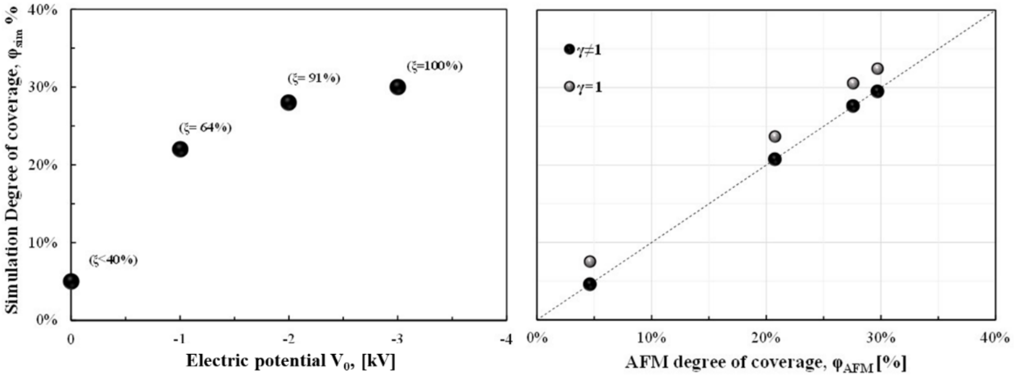

Figure 3.9. Left: simulation results in terms of the degree of coverage as a function of the electric potential applied to the mica substrate. Values in brackets represent the corresponding values for the collisional probability if all the CNPs are positively charged. Right: Comparison between the simulation and the AFM degree of coverage without (grey) and with (black) the sticking coefficient correction. (C/O=0.67, HAB=15mm, t_{ins}=100ms; N_{ins}=1).

From **Figure 3.9** it is possible to understand that there is a good agreement between the simulation and the experimental values for the degree of coverage, which goes from 5% to 30% passing from 0 to -3 kV. The increase in the degree of coverage is not linear, but it seems to reach an asymptotic value, also confirmed by the collisional probability values. Moreover, the sticking coefficient model of D'Alessio et al. [130] valid for uncharged CNPs seems to be efficient in describing experimental results. It is worth noticing, indeed, that the sticking coefficient model can solve an error of estimation of the model which is exactly the same for thermophoretic and electrophoretic depositions, suggesting that particle rebounding is mostly related to the thermal agitation velocity of the CNPs rather than to the electrophoretic velocity.

Finally, the model allows the estimation of particle velocity trajectories and modulus in the particle tracing domain, and, in particular, when they impact the substrate.

Table 3.2 summarizes the mean and standard deviations of the velocity modulus and the impact angle distributions for the CNPs at 0 and -3 kV for 2, 5 and 10 nm particles.

Table 3.2. Mean and standard deviation (St.dev.) of CNPs impact velocity and impact angle for the CNPs at 0 kV (either charged or uncharged) and the single-charged CNPs at -3 kV.

Parameter	**Descriptor**	**d_p= 2 nm**		**d_p = 5 nm**		**d_p = 10 nm**	
		0 kV	**-3 kV**	**0 kV**	**-3 kV**	**0 kV**	**-3 kV**
		q=0, +1e	**q=+1e**	**q=0, +1e**	**q=+1e**	**q=0, +1e**	**q=+1e**
Impact velocity	Mean, m/s	0.50	20.19	0.50	20.33	0.50	20.24
	St. dev., -	7.3%	2.1%	7.4%	1.7%	9.4%	1.4%
Impact angle	Mean, °	83.84	88.77	82.36	88.89	81.72	89.10
	St.dev., °	4.48	1.36	4.05	0.83	3.56	0.67
Peclet number	Mean, -	$3.45\cdot10^{-4}$	$1.41\cdot10^{-2}$	$5.53\cdot10^{-3}$	0.225	$4.51\cdot10^{-2}$	1.66
	St.dev., -	$4.98\cdot10^{-5}$	$1.86\cdot10^{-3}$	$8.16\cdot10^{-4}$	0.031	$5.18\cdot10^{-3}$	0.63

The model results indicate that at 0 kV, the impacts of CNPs with the substrate is independent on their charge, since thermophoretic forces are dominant in both cases, as shown in **Figure 3.6**. Instead, the charged CNPs impacts the substrate at a far larger velocity when the electric field is applied to the substrate. This is related to the component of velocity perpendicular to the substrate, while other components are scarcely affected by the potential. As a consequence, the impact angle becomes closer to the perpendicular, following the direction of the electric field, and the standard deviations of both the velocity and the angle are smaller. It is indeed relevant to notice that the impact velocity of uncharged particles is very similar for both charged and uncharged substrates. Therefore, following the indications of Castillo et al. [83–87,146], the model results indicate that uncharged particles are deposited according to a diffusional model, while for charged particles larger than 6 nm a ballistic deposition model is likely to take place. The role of this different impact velocity on the morphology of the CNPs films requires further investigations and will be the subject of following works.

3.10 Conclusions

CNPs harvesting and deposition on a substrate in flame with and without the presence of an electric field has been modelled by implementing all the force fields involved in the process in a commercial CFD software. The proposed model is able to identify the controlling mechanism for the CNPs harvesting, as their size and charge vary.

For uncharged CNPs, or for an uncharged substrate, thermophoresis is the controlling mechanism of the harvesting process, theoretically favoring the deposition of smaller CNPs with higher thermal mobility. For uncharged CNPs, results are similar even in presence of an external electric field since polarization phenomena and dielectrophoretic forces are negligible. For charged CNPs, electrophoresis is the controlling mechanism for the harvesting process in presence of an external electric field with a resulting collisional probability that is size-independent.

Considering the PSD in the actual flame and the actual fractions of charged CNPs, Collisional probability is higher for small CNPs under pure thermophoretic conditions. However, the presence of resuspension and rebounding phenomena in particles smaller than 10 nm leads to a reduction in the actual number of particles adhering to the substrate. Furthermore, the presence of external electric fields determines a significant increase in the collisional probability for CNPs larger than 5 nm. A non-linear trend with the electric potential applied to the deposition substrate due to saturation phenomena is observed. The good agreement between modelling and AFM experimental results in terms of the degree of coverage provides a validation criterion for the model.

Model is also able to retrieve information on particle impact velocities. It suggests that electrophoretic harvesting implies higher impact velocities and more perpendicular impact angles, consequently, a partial transition from a diffusion-controlled to a ballistic deposition mechanism is expected. Further experimental and numerical investigations on this aspect can shed light on the nature of deposited films and their possible applications.

3.11 Acknowledgements

This work was financially supported by the PRIN project 2017PJ5XXX: “MAGIC DUST”.

3.12 List of Symbols

A_i	Area occupied by a single CNP
A_s	Mica Substrate area
AFM	Atomic Force Microscopy
C_c	Cunningham correction factor
CNP	Carbon nanoparticle
C/O	Carbon to oxygen ratio
$c_{p,g}$	Gas specific heat capacity at constant pressure
D_i/D	CNP diffusivity
d_p/d_{pi}	CNP diameter

$\boldsymbol{E}$	Electric field vector
f	Peclet number distribution
f_w	Peclet number distribution weighted considering the CNPs mass distribution
$\boldsymbol{F}_B$	Brownian excitation amplitude
$\boldsymbol{F}_D$	Friction force on a spherical CNP
$\boldsymbol{F}_{DEP}$	Dielectrophoretic force for uncharged CNP
$\boldsymbol{F}_E$	Electrostatic force for charged CNP
$\boldsymbol{F}_i$	Interaction forces
$\boldsymbol{F}_G$	Gravity and buoyancy body force
$\boldsymbol{F}_T$	Thermophoretic force
$\boldsymbol{F}_t$	Tangential component of the friction forces to the CNP against the tangential component of velocity
$\boldsymbol{f}_{CM}$	Clausius-Mossotti factor
$\boldsymbol{g}$	Gravitational acceleration
HAB	Height above the burner
I	Moment of inertia
$\underline{\boldsymbol{I}}$	Identity tensor
k	Thermal conductivity
k_B	Boltzmann constant
$\boldsymbol{M}$	Net torque
m	Mass of a single CNP

$\boldsymbol{M}_F$	Resulting momenta related to the external long-range field
$\boldsymbol{M}_i$	Resulting torque acting between pair of CNPs
$\boldsymbol{M}_r$	Rolling friction force acting against the angular velocity
$N_{in,i}$	Number of injected CNPs
N_{i0}	Number of inlet CNPs in the real flame
N_{ins}	Number of insertions in flame
$N_{out,i}$	Number of harvested CNPs
$\boldsymbol{n}$	Outward surface normal unit vector
P	Pressure
Pe_i	Peclet dimensionless number of each CNP
p_{out}	Pressure outside the domain
PSD	Particles sized distribution
q	Total charged carried by a CNP
q_r	Heat flux by radiation
Q_{gen}	Heat sources other than viscous dissipation
$\mathrm{Re}(f_{CM})$	Real part of the Clausius-Mossotti factor
$\boldsymbol{R}_p$	Radius vector
T	Absolute Temperature
t_{ins}	Insertion time- time for a single insertion
$\boldsymbol{U}$	Relative CNP velocity
$\boldsymbol{u}$	Flame velocity vector

$\boldsymbol{u}_{\text{inlet}}$	Normal inflow inlet velocity vector
$\boldsymbol{u}_{\text{wall}}$	Flame velocity vector on the physical walls of the domain
V	Electric potential
V_0	Electric potential applied to the deposition substrate
V_b	Electric potential at the burner exit
V_p	Electric potential at the stabilization plate
v_i	CNP impact velocity modulus
z	Distance from the deposition surface
Δt	Time-step for the integration of the equation of particle motion
φ_{AFM}	Experimental degree of coverage obtained by AFM
φ_{sim}	Simulation degree of coverage
ε_m	Medium (flame) permittivity
ε_p	CNP permittivity
ε^*_m	Complex permittivity for the flame
ε^*_p	Complex permittivity for CNP
λ	Fluid mean free path
∇	Nabla operator
∇T	Temperature gradient
$\nabla \boldsymbol{V}$	Electric potential gradient
$\nabla \boldsymbol{u}$	Velocity gradient tensor
$\nabla \boldsymbol{u}^{\boldsymbol{T}}$	Transposed velocity gradient tensor

$\nabla\cdot\boldsymbol{u}$	Divergence of the velocity vector
ξ_i	Collisional probability
ρ_g	Gas mass density
ρ_{sc}	Net space charge density
σ_m	Flame electrical conductivity
σ_p	CNP electrical conductivity
ω	CNP Angular velocity
ω_e	Angular frequency of the electric filed
$\boldsymbol{\zeta}$	Zero-mean, unit-variance independent Gaussian random vector number

3.13 References

[1] De Falco G, Terlizzi M, Sirignano M, Commodo M, D'Anna A, Aquino RP, et al. Human peripheral blood mononuclear cells (PBMCs) from smokers release higher levels of IL-1-like cytokines after exposure to combustion-generated ultrafine particles. Sci Rep 2017;7. https://doi.org/10.1038/srep43016.

[2] Thompson JE. Airborne Particulate Matter: Human Exposure and Health Effects. J Occup Environ Med 2018;60:392–423. https://doi.org/10.1097/JOM.0000000000001277.

[3] Magnani ND, Muresan XM, Belmonte G, Cervellati F, Sticozzi C, Pecorelli A, et al. Skin damage mechanisms related to airborne particulate matter exposure. Toxicological Sciences 2016;149:227–36. https://doi.org/10.1093/toxsci/kfv230.

[4] Bernasconi S, Angelucci A, Aliverti A. A Scoping Review on Wearable Devices for Environmental Monitoring and Their Application for Health and Wellness. Sensors 2022;22. https://doi.org/10.3390/s22165994.

[5] Wang M, Yao G, Sun Y, Yang Y, Deng R. Exposure to construction dust and health impacts – A review. Chemosphere 2023;311. https://doi.org/10.1016/j.chemosphere.2022.136990.

[6] Michelsen HA. Probing soot formation, chemical and physical evolution, and oxidation: A review of in situ diagnostic techniques and needs. Proceedings of the Combustion Institute 2017;36:717–35. https://doi.org/10.1016/j.proci.2016.08.027.

[7] Michelsen HA, Colket MB, Bengtsson PE, D'Anna A, Desgroux P, Haynes BS, et al. A review of terminology used to describe soot formation and evolution under combustion and pyrolytic conditions. ACS Nano 2020;14:12470–90. https://doi.org/10.1021/acsnano.0c06226.

[8] Martin JW, Salamanca M, Kraft M. Soot inception: Carbonaceous nanoparticle formation in flames: Soot inception. Prog Energy Combust Sci 2022;88. https://doi.org/10.1016/j.pecs.2021.100956.

[9] Bauer FJ, Braeuer PAB, Aßmann S, Thiele MA, Huber FJT, Will S. Characterisation of the transition type in optical band gap analysis of in-flame soot. Combust Flame 2022;243. https://doi.org/10.1016/j.combustflame.2022.111986.

[10] D'Anna A. Combustion-formed nanoparticles. Proceedings of the Combustion Institute 2009;32 I:593–613. https://doi.org/10.1016/j.proci.2008.09.005.

[11] Chen T, Dai L. Carbon nanomaterials for high-performance supercapacitors. Materials Today 2013;16:272–80. https://doi.org/10.1016/j.mattod.2013.07.002.

[12] Zhang LL, Zhou R, Zhao XS. Graphene-based materials as supercapacitor electrodes. J Mater Chem 2010;20:5983–92. https://doi.org/10.1039/c000417k.

[13] Kümmerer K, Menz J, Schubert T, Thielemans W. Biodegradability of organic nanoparticles in the aqueous environment. Chemosphere 2011;82:1387–92. https://doi.org/10.1016/j.chemosphere.2010.11.069.

[14] Souza VGL, Fernando AL. Nanoparticles in food packaging: Biodegradability and potential migration to food-A review. Food Packag Shelf Life 2016;8:63–70. https://doi.org/10.1016/j.fpsl.2016.04.001.

[15] Seo K, Kim M, Kim DH. Candle-based process for creating a stable superhydrophobic surface. Carbon N Y 2014;68:583–96. https://doi.org/10.1016/j.carbon.2013.11.038.

[16] Khan SA, Ganeev RA, Boltaev GS, Alnaser AS. Wettability modification of glass surfaces by deposition of carbon-based nanostructured films. Fullerenes Nanotubes and Carbon Nanostructures 2021;29:576–87. https://doi.org/10.1080/1536383X.2021.1871897.

[17] Minutolo P, Commodo M, D'Anna A. Optical properties of incipient soot. Proceedings of the Combustion Institute 2022. https://doi.org/10.1016/j.proci.2022.09.019.

[18] Veronesi S, Commodo M, Basta L, De Falco G, Minutolo P, Kateris N, et al. Morphology and electronic properties of incipient soot by scanning tunneling microscopy and spectroscopy. Combust Flame 2022;243. https://doi.org/10.1016/j.combustflame.2021.111980.

[19] De Falco G, Commodo M, Bonavolontà C, Pepe GP, Minutolo P, D'Anna A. Optical and electrical characterization of carbon nanoparticles produced in laminar premixed flames. Combust Flame 2014;161:3201–10. https://doi.org/10.1016/j.combustflame.2014.05.021.

[20] De Falco G, Mattiello G, Commodo M, Minutolo P, Shi X, D'Anna A, et al. Electronic band gap of flame-formed carbon nanoparticles by scanning tunneling spectroscopy. Proceedings of the Combustion Institute, vol. 38, Elsevier Ltd; 2021, p. 1805–12. https://doi.org/10.1016/j.proci.2020.07.109.

[21] De Falco G, Commodo M, Barra M, Chiarella F, D'Anna A, Aloisio A, et al. Electrical characterization of flame-soot nanoparticle thin films. Synth Met 2017;229:89–99. https://doi.org/10.1016/j.synthmet.2017.05.008.

[22] Bhunia SK, Saha A, Maity AR, Ray SC, Jana NR. Carbon nanoparticle-based fluorescent bioimaging probes. Sci Rep 2013;3. https://doi.org/10.1038/srep01473.

[23] Ray SC, Saha A, Jana NR, Sarkar R. Fluorescent carbon nanoparticles: Synthesis, characterization, and bioimaging application. Journal of Physical Chemistry C 2009;113:18546–51. https://doi.org/10.1021/jp905912n.

[24] Boakye-Yiadom KO, Kesse S, Opoku-Damoah Y, Filli MS, Aquib M, Joelle MMB, et al. Carbon dots: Applications in bioimaging and theranostics. Int J Pharm 2019;564:308–17. https://doi.org/10.1016/j.ijpharm.2019.04.055.

[25] Molkenova A, Toleshova A, Song SJ, Kang MS, Abduraimova A, Han DW, et al. Rapid synthesis of nontoxic and photostable carbon nanoparticles for bioimaging applications. Mater Lett 2020;261. https://doi.org/10.1016/j.matlet.2019.127012.

[26] Dinger N, Panzetta V, Russo C, Netti PA, Sirignano M. In vitro effects of combustion generated carbon dots on cellular parameters in healthy and cancerous breast cells. Nanotoxicology 2022.

[27] Loh KP, Ho D, Chiu GNC, Leong DT, Pastorin G, Chow EKH. Clinical Applications of Carbon Nanomaterials in Diagnostics and Therapy. Advanced Materials 2018;30. https://doi.org/10.1002/adma.201802368.

[28] Zhang Y, Petibone D, Xu Y, Mahmood M, Karmakar A, Casciano D, et al. Toxicity and efficacy of carbon nanotubes and graphene: The utility of carbon-based nanoparticles in nanomedicine. Drug Metab Rev 2014;46:232–46. https://doi.org/10.3109/03602532.2014.883406.

[29] Liu Z, Robinson JT, Tabakmar SM, Yang K, Dai H. Carbon materials for dryg delivery & cancer therapy. Materials Today 2011;14:316–23.

[30] Saini D, Gunture N, Kaushik J, Aggarwal R, Tripathi KM, Sonkar SK. Carbon Nanomaterials Derived from Black Carbon Soot: A Review of Materials and Applications. ACS Appl Nano Mater 2021;4:12825–44. https://doi.org/10.1021/acsanm.1c02840.

[31] Islam N, Saikia BK. An overview on atmospheric carbonaceous particulate matter into carbon nanomaterials: A new approach for air pollution mitigation. Chemosphere 2022;303. https://doi.org/10.1016/j.chemosphere.2022.135027.

[32] Xiao J, Momen R, Liu C. Application of carbon quantum dots in supercapacitors: A mini review. Electrochem Commun 2021;132. https://doi.org/10.1016/j.elecom.2021.107143.

[33] Miao L, Song Z, Zhu D, Li L, Gan L, Liu M. Recent advances in carbon-based supercapacitors. Mater Adv 2020;1:945–66. https://doi.org/10.1039/d0ma00384k.

[34] Sano N. Formation of multi-shelled carbon nanoparticles by arc discharge in liquid benzene. Mater Chem Phys 2004;88:235–8. https://doi.org/10.1016/j.matchemphys.2004.07.018.

[35] Zhang S, Song H, Guo P, Zhou J, Chen X. Formation of carbon nanoparticles from soluble graphene oxide in an aqueous solution. Carbon N Y 2010;48:4211–4. https://doi.org/10.1016/j.carbon.2010.07.025.

[36] Alam A, Wan C, McNally T. Surface amination of carbon nanoparticles for modification of epoxy resins: plasma-treatment vs. wet-chemistry approach. Eur Polym J 2017;87:422–48. https://doi.org/10.1016/j.eurpolymj.2016.10.004.

[37] Andhika IF, Saraswati TE, Hastuti S. The structural characteristics of carbon nanoparticles produced by arc discharge in toluene without added catalyst or gases. Evergreen 2020;7:417–28. https://doi.org/10.5109/4068622.

[38] Zheng F. Thermophoresis of spherical and non-spherical particles: a review of theories and experiments. Adv Colloid Interface Sci 2002;97:255–78.

[39] Roth P. Particle synthesis in flames. Proceedings of the Combustion Institute 2007;31 II:1773–88. https://doi.org/10.1016/j.proci.2006.08.118.

[40] Kammler HK, Mädler L, Pratsinis SE. Flame synthesis of nanoparticles. Chem Eng Technol 2001;24:583–96. https://doi.org/10.1002/1521-4125(200106)24:6<583::AID-CEAT583>3.0.CO;2-H.

[41] Li S, Ren Y, Biswas P, Tse SD. Flame aerosol synthesis of nanostructured materials and functional devices: Processing, modeling, and diagnostics. Prog Energy Combust Sci 2016;55:1–59. https://doi.org/10.1016/j.pecs.2016.04.002.

[42] Nersisyan HH, Lee JH, Ding JR, Kim KS, Manukyan K v., Mukasyan AS. Combustion synthesis of zero-, one-, two- and three-dimensional nanostructures: Current trends and future perspectives. Prog Energy Combust Sci 2017;63:79–118. https://doi.org/10.1016/j.pecs.2017.07.002.

[43] De Falco G, Commodo M, Minutolo P, D'Anna A. Flame aerosol synthesis and thermophoretic deposition of superhydrophilic TiO2 nanoparticle coatings. Chem Eng Trans 2019;73:37–42. https://doi.org/10.3303/CET1973007.

[44] Commodo M, De Falco G, Bruno A, Borriello C, Minutolo P, D'Anna A. Physicochemical evolution of nascent soot particles in a laminar premixed flame: From nucleation to early growth. Combust Flame 2015;162:3854–63. https://doi.org/10.1016/j.combustflame.2015.07.022.

[45] Sirignano M, Russo C, Ciajolo A. One-step synthesis of carbon nanoparticles and yellow to blue fluorescent nanocarbons in flame reactors. Carbon N Y 2020;156:370–7. https://doi.org/10.1016/j.carbon.2019.09.068.

[46] Kelesidis GA, Goudeli E, Pratsinis SE. Flame synthesis of functional nanostructured materials and devices: Surface growth and aggregation. Proceedings of the Combustion Institute 2017;36:29–50. https://doi.org/10.1016/j.proci.2016.08.078.

[47] Zheng F. Thermophoresis of spherical and non-spherical particles: a review of theories and experiments. Adv Colloid Interface Sci 2002;97:255–78.

[48] Zhao H, Liu X, Tse SD. Control of nanoparticle size and agglomeration through electric-field- enhanced flame synthesis. Journal of Nanoparticle Research 2008;10:907–23. https://doi.org/10.1007/s11051-007-9330-7.

[49] Messerer A, Niessner R, Pöschl U. Thermophoretic deposition of soot aerosol particles under experimental conditions relevant for modern diesel engine exhaust gas systems. J Aerosol Sci 2003;34:1009–21. https://doi.org/10.1016/S0021-8502(03)00081-8.

[50] Kumar M, Bhattacharya S. Flame synthesis and characterization of nanocrystalline titania powders. Processing and Application of Ceramics 2012;6:165–71. https://doi.org/10.2298/pac1203165k.

[51] De Falco G, Carbone F, Commodo M, Minutolo P, D'Anna A. Exploring nanomechanical properties of soot particle layers by atomic force microscopy nanoindentation. Applied Sciences (Switzerland) 2021;11. https://doi.org/10.3390/app11188448.

[52] Ho PY, Chen CK, Huang KH. Combined effects of thermophoresis and electrophoresis on particle deposition in mixed convection flow onto a vertical wavy plate. International Communications in Heat and Mass Transfer 2019;101:116–21. https://doi.org/10.1016/j.icheatmasstransfer.2018.12.019.

[53] Sardari PT, Rahimzadeh H, Ahmadi G, Giddings D. Nano-particle deposition in the presence of electric field. J Aerosol Sci 2018;126:169–79. https://doi.org/10.1016/j.jaerosci.2018.09.012.

[54] Jaworek A, Sobczyk AT, Marchewicz A, Krupa A, Czech T, Śliwiński, et al. Two-stage vs. two-field electrostatic precipitator. J Electrostat 2017;90:106–12. https://doi.org/10.1016/j.elstat.2017.10.006.

[55] Boccaccini AR, Cho J, Roether JA, Thomas BJC, Jane Minay E, Shaffer MSP. Electrophoretic deposition of carbon nanotubes. Carbon N Y 2006;44:3149–60. https://doi.org/10.1016/j.carbon.2006.06.021.

[56] Zhitomirsky I. Electrophoretic deposition of organic-inorganic nanocomposites. J Mater Sci, vol. 41, 2006, p. 8186–95. https://doi.org/10.1007/s10853-006-0994-7.

[57] Cohen E, Lifshitz M, Gladkikh A, Kamir Y, Ben-Barak I, Golodnitsky D. Novel one-step electrophoretic deposition of the membrane-electrode assembly for flexible-battery applications. J Mater Chem A Mater 2020;8:11391–8. https://doi.org/10.1039/d0ta02328k.

[58] Sung DH, Doshi SM, Murray C, Rider AN, Thostenson ET. Electrophoretic deposition: Novel in situ film growth mechanism of carbon nanocomposite films within non-conductive fabrics for multi-scale hybrid composites. Compos Sci Technol 2020;200. https://doi.org/10.1016/j.compscitech.2020.108415.

[59] Diba M, Fam DWH, Boccaccini AR, Shaffer MSP. Electrophoretic deposition of graphene-related materials: A review of the fundamentals. Prog Mater Sci 2016;82:83–117. https://doi.org/10.1016/j.pmatsci.2016.03.002.

[60] Wang Y, Nathan GJ, Alwahabi ZT, King KD, Ho K, Yao Q. Effect of a uniform electric field on soot in laminar premixed ethylene/air flames. Combust Flame 2010;157:1308–15. https://doi.org/10.1016/j.combustflame.2010.03.001.

[61] Amer Cid Í, Ussembayev YY, Neyts K, Strubbe F. Measurement of the amplitude and phase of the electrophoretic and electroosmotic mobility based on fast single-particle tracking. Electrophoresis 2021;42:1623–35. https://doi.org/10.1002/elps.202100030.

[62] Carotenuto C, Di Natale F, Lancia A. Wet electrostatic scrubbers for the abatement of submicronic particulate. Chemical Engineering Journal 2010;165:35–45. https://doi.org/10.1016/j.cej.2010.08.049.

[63] Di Natale F, Carotenuto C, Parisi A, Flagiello D, Lancia A. Wet electrostatic scrubbing for flue gas treatment. Fuel 2022;325. https://doi.org/10.1016/j.fuel.2022.124888.

[64] Sabzyan H, Ghalami F. Electric field effects on the growth of flame-synthesized nanosilica: a two-stage modeling. Journal of the Iranian Chemical Society 2019;16:963–78. https://doi.org/10.1007/s13738-019-01591-9.

[65] Xiong G, Kulkarni A, Dong Z, Li S, Tse SD. Electric-field-assisted stagnation-swirl-flame synthesis of porous nanostructured titanium-dioxide films. Proceedings of the Combustion Institute 2017;36:1065–75. https://doi.org/10.1016/j.proci.2016.08.079.

[66] Vemury S, Pratsinis SE, Kibbey L. Electrically controlled flame synthesis of nanophase TiO 2 , SiO 2 , and SnO 2 powders. 1997.

[67] Maricq MM. Size and charge of soot particles in rich premixed ethylene flames. Combust Flame 2004;137:340–50. https://doi.org/10.1016/j.combustflame.2004.01.013.

[68] Sgro LA, D'Anna A, Minutolo P. Charge fraction distribution of nucleation mode particles: New insight on the particle formation mechanism. Combust Flame 2011;158:1418–25. https://doi.org/10.1016/j.combustflame.2010.11.010.

[69] Sgro LA, D'Anna A, Minutolo P. Charge distribution of incipient flame-generated particles. Aerosol Science and Technology 2010;44:651–62. https://doi.org/10.1080/02786826.2010.483701.

[70] Kammler HK, Jossen R, Morrison PW, Pratsinis SE, Beaucage G. The effect of external electric fields during flame synthesis of titania. Powder Technol 2003;135–136:310–20. https://doi.org/10.1016/j.powtec.2003.08.023.

[71] Tolmachoff ED, Abid AD, Phares DJ, Campbell CS, Wang H. Synthesis of nano-phase TiO2 crystalline films over premixed stagnation flames. Proceedings of the Combustion Institute 2009;32 II:1839–45. https://doi.org/10.1016/j.proci.2008.06.052.

[72] Zhao H, Liu X, Tse SD. Control of nanoparticle size and agglomeration through electric-field- enhanced flame synthesis. Journal of Nanoparticle Research 2008;10:907–23. https://doi.org/10.1007/s11051-007-9330-7.

[73] Wang Y, Nathan GJ, Alwahabi ZT, King KD, Ho K, Yao Q. Effect of a uniform electric field on soot in laminar premixed ethylene/air flames. Combust Flame 2010;157:1308–15. https://doi.org/10.1016/j.combustflame.2010.03.001.

[74] Xiong G, Kulkarni A, Dong Z, Li S, Tse SD. Electric-field-assisted stagnation-swirl-flame synthesis of porous nanostructured titanium-dioxide films. Proceedings of the Combustion Institute 2017;36:1065–75. https://doi.org/10.1016/j.proci.2016.08.079.

[75] Sgro LA, D'Anna A, Minutolo P. Charge fraction distribution of nucleation mode particles: New insight on the particle formation mechanism. Combust Flame 2011;158:1418–25. https://doi.org/10.1016/j.combustflame.2010.11.010.

[76] Sgro LA, D'Anna A, Minutolo P. Charge distribution of incipient flame-generated particles. Aerosol Science and Technology 2010;44:651–62. https://doi.org/10.1080/02786826.2010.483701.

[77] Volkov EN, Sepman A v, Kornilov VN, Konnov AA, Shoshin YS, de Goey LPH. Towards the mechanism of DC electric field effect on flat premixed flames. Proceedings of the European Combustion Meeting, 2009.

[78] Zigan L. Overview of electric field applications in energy and process engineering. Energies (Basel) 2018;11. https://doi.org/10.3390/en11061361.

[79] Altendorfner F, Kuhl J, Zigan L, Leipertz A. Study of the influence of electric fields on flames using planar LIF and PIV techniques. Proceedings of the Combustion Institute 2011;33:3195–201. https://doi.org/10.1016/j.proci.2010.05.112.

[80] Park DG, Chung SH, Cha MS. Visualization of ionic wind in laminar jet flames. Combust Flame 2017;184:246–8. https://doi.org/10.1016/j.combustflame.2017.06.011.

[81] Kuhl J, Seeger T, Zigan L, Will S, Leipertz A. On the effect of ionic wind on structure and temperature of laminar premixed flames influenced by electric fields. Combust Flame 2017;176:391–9. https://doi.org/10.1016/j.combustflame.2016.10.026.

[82] Biswas JC, Mitra V. High-Frequency Breakdown and Paschen Law. Applied Physics 1979;19:377–81.

[83] Tassopoulos A O MJ, Rosner E. Simulation of Microstructure/Mechanism Relationships in Particle Deposition. AIChE Journal 1989;35:967–80.

[84] Meakin P, Ramanlal P, Sander LM, Ball RC. A Ballistic deposition on surfaces. Phys Rev A (Coll Park) 1986;34:5091–103.

[85] Kardar M, Parisi G, Zhang Y-C. Dynamic Scaling of Growing Interfaces. Physical Reniew Letters 1986;56:889–92.

[86] Rodríguez-Pérez D, Castillo JL, Antoranz JC. Density scaling laws for the structure of granular deposits. Phys Rev E Stat Nonlin Soft Matter Phys 2007;76. https://doi.org/10.1103/PhysRevE.76.011407.

[87] Rodríguez-Pérez D, Castillo JL, Antoranz JC. Relationship between particle deposit characteristics and the mechanism of particle arrival. Phys Rev E Stat Nonlin Soft Matter Phys 2005;72. https://doi.org/10.1103/PhysRevE.72.021403.

[88] Liu D, Zhou W, Qiu Z, Song X. Fractal simulation of flocculation processes using a diffusion-limited aggregation model. Fractal and Fractional 2017;1:1–14. https://doi.org/10.3390/fractalfract1010012.

[89] Castillo JL, Martin S, Rodriguez-Perez D, Perea A, Garcia-Ybarra PL. Morphology and nanostructure of granular materials built from nanoparticles. KONA Powder and Particle Journal 2014;31:214–33. https://doi.org/10.14356/kona.2014012.

[90] Arai H, Asami K, Ito H, Katayama N. Effect of the settings of electrospray deposition method on the structure and performance of the fuel cell catalyst layer. Current Applied Physics 2022;39:296–303. https://doi.org/10.1016/j.cap.2022.05.014.

[91] Zhao XY, Yang W, Li C, Wang X, Lim SL, Qi D, et al. Effects of Damkhöler number of evaporation on the morphology of active layer and the performance of organic heterojunction solar cells fabricated by electrospray method. Solar Energy Materials and Solar Cells 2015;134:140–7. https://doi.org/10.1016/j.solmat.2014.11.029.

[92] Conde JJ, Ferreira-Aparicio P, Chaparro AM. Electrospray Deposition: A Breakthrough Technique for Proton Exchange Membrane Fuel Cell Catalyst Layer Fabrication. ACS Appl Energy Mater 2021;4:7394–404. https://doi.org/10.1021/acsaem.1c01445.

[93] De Falco G, Commodo M, Bonavolontà C, Pepe GP, Minutolo P, D'Anna A. Optical and electrical characterization of carbon nanoparticles produced in laminar premixed flames. Combust Flame 2014;161:3201–10. https://doi.org/10.1016/j.combustflame.2014.05.021.

[94] Minutolo P, Commodo M, D'Anna A. Optical properties of incipient soot. Proceedings of the Combustion Institute 2022. https://doi.org/10.1016/j.proci.2022.09.019.

[95] De Falco G, Commodo M, Barra M, Chiarella F, D'Anna A, Aloisio A, et al. Electrical characterization of flame-soot nanoparticle thin films. Synth Met 2017;229:89–99. https://doi.org/10.1016/j.synthmet.2017.05.008.

[96] Commodo M, De Falco G, Minutolo P, D'Anna A. Structure and size of soot nanoparticles in laminar premixed flames at different equivalence ratios. Fuel 2018;216:456–62. https://doi.org/10.1016/j.fuel.2017.12.032.

[97] De Falco G, Commodo M, D'Anna A, Minutolo P. The evolution of soot particles in premixed and diffusion flames by thermophoretic particle densitometry. Proceedings of the Combustion Institute 2017;36:763–70. https://doi.org/10.1016/j.proci.2016.07.108.

[98] Maricq MM. A comparison of soot size and charge distributions from ethane, ethylene, acetylene, and benzene/ethylene premixed flames. Combust Flame 2006;144:730–43. https://doi.org/10.1016/j.combustflame.2005.09.007.

[99] Carbone F, Gleason K, Gomez A. Probing gas-to-particle transition in a moderately sooting atmospheric pressure ethylene/air laminar premixed flame. Part I: gas phase

and soot ensemble characterization. Combust Flame 2017;181:315–28. https://doi.org/10.1016/j.combustflame.2017.01.029.

[100] Maquin B, Goyhénèche J-M, Goyhén G, Goyhénèche G, Derré A, Derré D, et al. Thermal conductivity of submicrometre particles: carbon blacks and solid solutions containing C, B and N. J Phys D Appl Phys 2000;33:8–17.

[101] De Falco G, Commodo M, D'Anna A, Minutolo P. The evolution of soot particles in premixed and diffusion flames by thermophoretic particle densitometry. Proceedings of the Combustion Institute 2017;36:763–70. https://doi.org/10.1016/j.proci.2016.07.108.

[102] Yang Y, Zhang H, Li C, Li C, Yu Z, Yu K. Diffusion charging of nanometer-sized liquid aerosol particles. J Phys D Appl Phys 2021;54. https://doi.org/10.1088/1361-6463/abdefd.

[103] D'Anna A. Detailed kinetic modeling of particulate formation in rich premixed flames of ethylene. Energy and Fuels 2008;22:1610–9. https://doi.org/10.1021/ef700641u.

[104] Balthasar M, Frenklach M. Detailed kinetic modeling of soot aggregate formation in laminar premixed flames. Combust Flame 2005;140:130–45. https://doi.org/10.1016/j.combustflame.2004.11.004.

[105] D'Anna A, Violi A, D'alessio A, Sarofim AF. A Reaction Pathway for Nanoparticle Formation in Rich Premixed Flames. Combust Flame 2001;127:1995–2003.

[106] Calcote HF. Ion and electron profiles in flames. Combust Flame 1957;9.

[107] Guo J, Goodings JM, Hayhurst AN, Taylor SG. A simple method for measuring positive ion concentrations in flames and the calibration of a nebulizer/atomizer. Combust Flame 2003;133:335–43. https://doi.org/10.1016/S0010-2180(03)00020-8.

[108] Calcote HF, Pease RN. Electrical Properties of flames. Burner Flames in Longitudinal Electric Fields. Ind Eng Chem 1951;43:2726–31.

[109] Kim MM, Zydney AL. Effect of electrostatic, hydrodynamic, and Brownian forces on particle trajectories and sieving in normal flow filtration. J Colloid Interface Sci 2004;269:425–31. https://doi.org/10.1016/j.jcis.2003.08.004.

[110] Vishnyakov VI, Kiro SA, Oprya M v., Ennan AA. Coagulation of charged particles in self-organizing thermal plasmas of welding fumes. J Aerosol Sci 2014;76:138–47. https://doi.org/10.1016/j.jaerosci.2014.06.010.

[111] Hwang SH, Okumura T, Kamataki K, Itagaki N, Koga K, Shiratani M. Size and flux of carbon nanoparticles synthesized by Ar+CH4 multi-hollow plasma chemical vapor deposition. Diam Relat Mater 2020;109. https://doi.org/10.1016/j.diamond.2020.108050.

[112] Bongiorno G, Podestà A, Ravagnan L, Piseri P, Milani P, Lenardi C, et al. Electronic properties and applications of cluster-assembled carbon films. Journal of Materials Science: Materials in Electronics 2006;17:427–41. https://doi.org/10.1007/s10854-006-8089-4.

[113] Fuchs G, Treilleux M, Santos Aires F, Cabaud B, Melinon P, Hoareau A. Cluster-beam deposition for high-quality thin films. Physical Review A- The Americal Physical Society 1989;40:6128–30.

[114] Hinds W. Aerosol Technology. Properties, Behavior and Measurement of Airborne Particles. Second Edi. 1999. https://doi.org/10.1080/17449200600935521.

[115] Qian W, Kronenburg A, Hui X, Lin Y, Karsch M. Effects of agglomerate characteristics on their collision kernels in the free molecular regime. J Aerosol Sci 2022;159. https://doi.org/10.1016/j.jaerosci.2021.105868.

[116] Endres SC, Ciacchi LC, Mädler L. A review of contact force models between nanoparticles in agglomerates, aggregates, and films. J Aerosol Sci 2021;153. https://doi.org/10.1016/j.jaerosci.2020.105719.

[117] Li A, Ahmadi G. Dispersion and deposition of spherical particles from point sources in a turbulent channel flow. Aerosol Science and Technology 1992;16:209–26. https://doi.org/10.1080/02786829208959550.

[118] Pohl HA. The motion and precipitation of suspensoids in divergent electric fields. J Appl Phys 1951;22:869–71. https://doi.org/10.1063/1.1700065.

[119] Markx GH, Pethig R. Dielectrophoretic separation of cells: Continuous separation. Biotechnol Bioeng 1995;45:337–43. https://doi.org/10.1002/bit.260450408.

[120] Jungmann F, Kruss M, Teiser J, Wurm G. Aggregation of sub-mm particles in strong electric fields under microgravity conditions. Icarus 2022;373. https://doi.org/10.1016/j.icarus.2021.114766.

[121] Jones TB. Basic Theory of Dielectrophoresis and Electrorotation. IEEE Engineering in Medicine and Biology Magazine 2003;22:33–42. https://doi.org/10.1109/MEMB.2003.1304999.

[122] Xia X, Zhong Z, Weng GJ. Maxwell–Wagner–Sillars mechanism in the frequency dependence of electrical conductivity and dielectric permittivity of graphene-polymer nanocomposites. Mechanics of Materials 2017;109:42–50. https://doi.org/10.1016/j.mechmat.2017.03.014.

[123] McKenzie R, Zurawsky W, Mijovic J. A molecular interpretation of Maxwell-Wagner-Sillars processes. J Non Cryst Solids 2014;406:11–21. https://doi.org/10.1016/j.jnoncrysol.2014.09.035.

[124] Akihiko Irimajiri, Tetsuya Hanai, Akira Inouye. A Dielectric Theory of “Multi-Stratified Shell” Model with its Application to a Lymphoma Cell. Journal of Theoretical Biology 1979;78:251–69.

[125] Kirby B (Brian J). Micro- and nanoscale fluid mechanics : transport in microfluidic devices. Cambridge University Press; 2010.

[126] Kuuluvainen H, Arffman A, Saukko E, Virtanen A, Keskinen J. A new method for characterizing the bounce and charge transfer properties of nanoparticles. J Aerosol Sci 2013;55:104–15. https://doi.org/10.1016/j.jaerosci.2012.08.007.

[127] Kweon H, Yiacoumi S, Tsouris C. The role of electrostatic charge in the adhesion of spherical particles onto planar surfaces in atmospheric systems. Colloids Surf A Physicochem Eng Asp 2015;481:583–90.

[128] Takeuchi M. Adhesion forces of charged particles. Chem Eng Sci, vol. 61, 2006, p. 2279–89. https://doi.org/10.1016/j.ces.2004.06.051.

[129] De Falco G, Commodo M, Minutolo P, D’Anna A. Flame-formed carbon nanoparticles: Morphology, interaction forces, and hamaker constant from AFM. Aerosol Science and Technology 2015;49:281–9. https://doi.org/10.1080/02786826.2015.1022634.

[130] D’Alessio A, Barone AC, Cau R, D’Anna A, Minutolo P. Surface deposition and coagulation efficiency of combustion generated nanoparticles in the size range from 1 to 10 nm. Proceedings of the Combustion Institute, vol. 30, Elsevier Ltd; 2005, p. 2595–603. https://doi.org/10.1016/j.proci.2004.08.267.

[131] Chaurasia AS. Computational Fluid Dynamics and Comsol Multiphysics: A Step-by-Step Approach for Chemical Engineers. First Edition. Palm Bay (USA): Apple Academy Press; 2022.

[132] Commodo M, Sgro LA, Minutolo P, D’Anna A. Characterization of combustion-generated carbonaceous nanoparticles by size-dependent ultraviolet laser photoionization. Journal of Physical Chemistry A 2013;117:3980–9. https://doi.org/10.1021/jp401061d.

[133] Sirignano M, Bartos D, Conturso M, Dunn M, D’Anna A, Masri AR. Detection of nanostructures and soot in laminar premixed flames. Combust Flame 2017;176:299–308. https://doi.org/10.1016/j.combustflame.2016.10.009.

[134] Vitiello G, De Falco G, Picca F, Commodo M, D’Errico G, Minutolo P, et al. Role of radicals in carbon clustering and soot inception: A combined EPR and Raman spectroscopic study. Combust Flame 2019;205:286–94.

[135] Alfà M, Apicella B, Barbella R, Tregrossi A, Ciajolo A. Distribution of soot molecular weight/size along premixed flames as inferred by size exclusion

chromatography. Energy and Fuels 2007;21:136–40. https://doi.org/10.1021/ef060320p.

[136] Apicella B, Ciajolo A, Suelves I, Morgan TJ, Herod AA, Kandiyoti R. Structural characterization of products from fuel-rich combustion: An approach based on size exclusion chromatography. Combustion Science and Technology 2002;174:345–59.

[137] Endres SC, Ciacchi LC, Mädler L. A review of contact force models between nanoparticles in agglomerates, aggregates, and films. J Aerosol Sci 2021;153.

[138] Morán J, Henry C, Poux A, Yon J. Impact of the maturation process on soot particle aggregation kinetics and morphology. Carbon N Y 2021;182:837–46. https://doi.org/10.1016/j.carbon.2021.06.085.

[139] Buzio R, Gnecco E, Boragno C, Valbusa U, Piseri P, Barborini E, et al. Self-affine properties of cluster-assembled carbon thin films. vol. 444. 2000.

[140] Morán J, Henry C, Poux A, Yon J. Impact of the maturation process on soot particle aggregation kinetics and morphology. Carbon N Y 2021;182:837–46. https://doi.org/10.1016/j.carbon.2021.06.085.

[141] Celardo GL, Archetti D, Ferrini G, Gavioli L, Pingue P, Cavaliere E. Evidence of diffusive fractal aggregation of TiO2 nanoparticles by femtosecond laser ablation at ambient conditions. Mater Res Express 2017;4. https://doi.org/10.1088/2053-1591/aa50e9.

[142] Olevanov MA, Mankelevich YuA, Rakhimova TV. Coagulation and Growth Mechanisms for Dust Particles in a Low-Temperature Plasma. Journal of Experimental and Theoretical Physics 2004;98:287–304.

[143] Xiong G, Kulkarni A, Dong Z, Li S, Tse SD. Electric-field-assisted stagnation-swirl-flame synthesis of porous nanostructured titanium-dioxide films. Proceedings of the Combustion Institute 2017;36:1065–75. https://doi.org/10.1016/j.proci.2016.08.079.

[144] Liu BG, Wu J, Wang EG, Zhang Z. Two-dimensional pattern formation in surfactant-mediated epitaxial growth. Phys Rev Lett 1999;83:1195–8.

[145] Nie M, Mete T, Ellmer K. Morphology and structure evolution of tin-doped indium oxide thin films deposited by radio-frequency magnetron sputtering: The role of the sputtering atmosphere. J Appl Phys 2014;115. https://doi.org/10.1063/1.4871810.

[146] Castillo JL, Martin S, Rodriguez-Perez D, Perea A, Garcia-Ybarra PL. Morphology and nanostructure of granular materials built from nanoparticles. KONA Powder and Particle Journal 2014;31:214–33. https://doi.org/10.14356/kona.2014012.

Chapter 4

Results and Discussion

In this chapter, the results obtained using the different analytical techniques, described in **Chapter 2**, are reported. This chapter aims to exploit the morphological, physicochemical, structural, electrical and wettability properties of the CNP films produced by electric field-assisted flame synthesis, and the potential applications of these CNPs.

This chapter refers, but is not limited, to the following papers:

1. Parisi, A., Carotenuto, C., De Falco, G., Sirignano, M., Di Natale, F. (2021). Electrophoretic deposition of carbon nanoparticles film produced in flame: a preliminary investigation. *Proceedings of the 10th European Combustion Meeting*, 884-889.
2. Parisi, A., De Falco, G., Sirignano, M., Minutolo, P., Commodo, M., Carotenuto, C., Di Natale, F. (submitted). Modelling the electrophoretically-enhanced in-flame deposition of carbon nanoparticles. *Journal of Aerosol Science*.
3. Parisi, A., Darvehi, P., De Falco, G., Commodo, M., Apicella, B., Russo, C., Di Natale, F., Minutolo, P. (under submission). Experimental findings on the electric field- assisted in-flame deposition of Carbon NanoParticle films.
4. Griffo, R., Parisi, A., De Falco, G., Sirignano, M., Di Natale, F., Minale, M., Carotenuto, C. (under submission).Wettability of carbon nanofilms with different fluids. Preliminary results.

Contents

Figure 4.1 recaps the analytical techniques adopted in this work to characterize CNP film and their agglomerates in terms of morphological, chemical, structural, electrical, or surface-wetting properties.

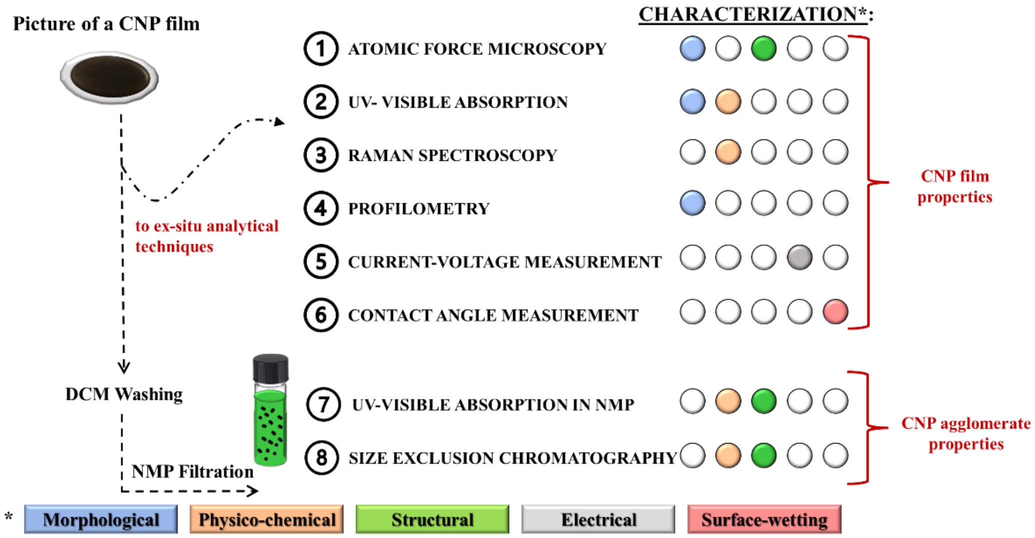

Figure 4.1. Overview of the ex-situ analytical techniques adopted for the CNP films and agglomerates characterization in terms of morphological, physico-chemical, structural, electrical and surface-wetting features.

4.1 Morphological characterization

UV-vis absorption spectra of CNP films deposited on glass substrates provide the first piece of information about possible changes in the morphology of the CNP films caused by the application of an external electric field to their flame synthesis. It is good to remind that there is a direct proportionality between the absorbance measured for a specific wavelength and the equivalent film thickness. In particular, an increase in absorbance, *i.e.* an upward shift in the absorption spectrum, corresponds to an increased thickness of the deposited material. As discussed in **Chapter 2**, it is possible to use the Beer-Lambert equation to estimate an equivalent CNP film optical thickness (δ_{eq}), which considers the film as made by pure CNP in the absence of voids. This approach does not take into account any structural or porosity properties of the produced CNP film and their possible effects on the UV-vis absorbance. **Figure 4.2** shows the values for the equivalent film thickness (δ_{eq}) as a function of the number of insertions in flame (N_{ins}), parametric with the electrical potential applied to the deposition substrate.

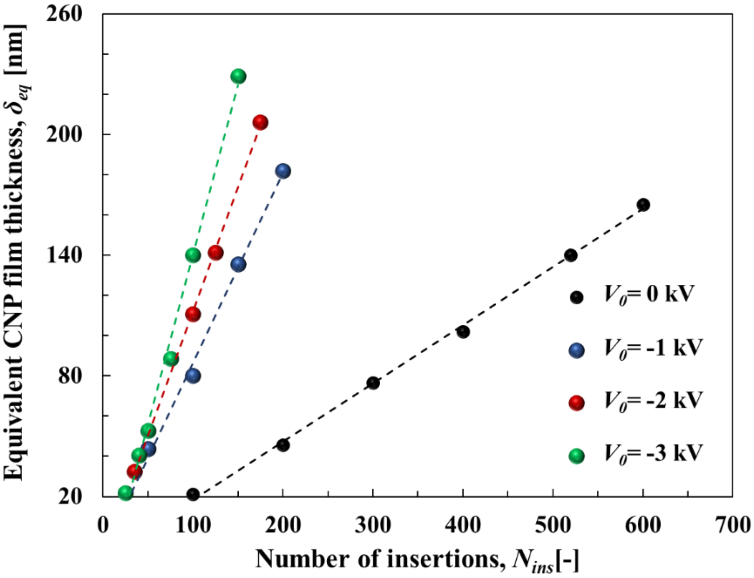

Figure 4.2. Equivalent CNP film thickness (δ_{eq}) as a function of the number of insertions in flame (N_{ins}), varying the electric potential (V_0) applied to the deposition substrate from 0 to -3 kV. Linear extrapolations of the observed trends are shown as a dashed line, showing a coefficient of determination R^2 higher than 0.994. Each point is obtained as the average of at least 20 values.

From **Figure 4.2**, it can be understood that for a fixed electric potential, V_0, the equivalent CNP film thickness increases linearly with the number of insertions (N_{ins}): In fact, the linear interpolations (dashed lines in **Figure 4.2**) return always a coefficient of determination R^2 higher than 0.994. This result is in line with the experimental evidence reported in former works [1–4].

Furthermore, it is evident that in the presence of electrical potential, a lower number of insertions N_{ins} is required to achieve a fixed equivalent thickness: a CNP film with a thickness of 153±18 nm is obtained at V_0=-3 kV with 6 times fewer insertions that at V_0=0 kV (pure thermophoresis). Consequently, thanks to the presence of an electric field it is possible to ensure the deposition of CNP films of the desired thicknesses with reduced production times. These findings are perfectly in line with the increases (by six times) in the harvesting rate predicted by the deposition model described in **Chapter 3**.

It is worth noting that the reduction in the number of insertions required to obtain a fixed equivalent thickness is very marked in the transition from 0 kV to -1 kV (reduction: 75%), even though it becomes gradually irrelevant – an additional increase of 10% – in the transition from -1 kV to -3 kV. This observation is very important as it demonstrates a non-linear increase in the equivalent thickness with the electric potential and the existence of a plateau representative of a saturation condition for the process, which the deposition model correlates to the chosen residence time of insertion of the CNP film support in the flame (*see* **Chapter 3**).

Although the equivalent optical film thickness is not an accurate measure of the actual film thickness, it is a clear indication of the amount of deposited CNPs, and this parameter can be a useful normalization method, used to compare the properties of CNP films produced at different voltages for a similar mass of the deposits: the films are produced at a given number of insertions which corresponds to the desired equivalent optical film thickness. For example, for a film thickness of 140 nm, the required insertions go from 520 at 0 kV to around 100 at – 3 kV.

Further information on film morphology can be obtained from AFM images. The electric field effect has been analysed by selecting two samples obtained at 0 kV and -3 kV, with 520 and 100 insertions in flame, respectively (*see* panels **(A)** and **(B)** in **Figure 4.3**). As suggested before, these two films show the same optical film thickness of 140 nm.

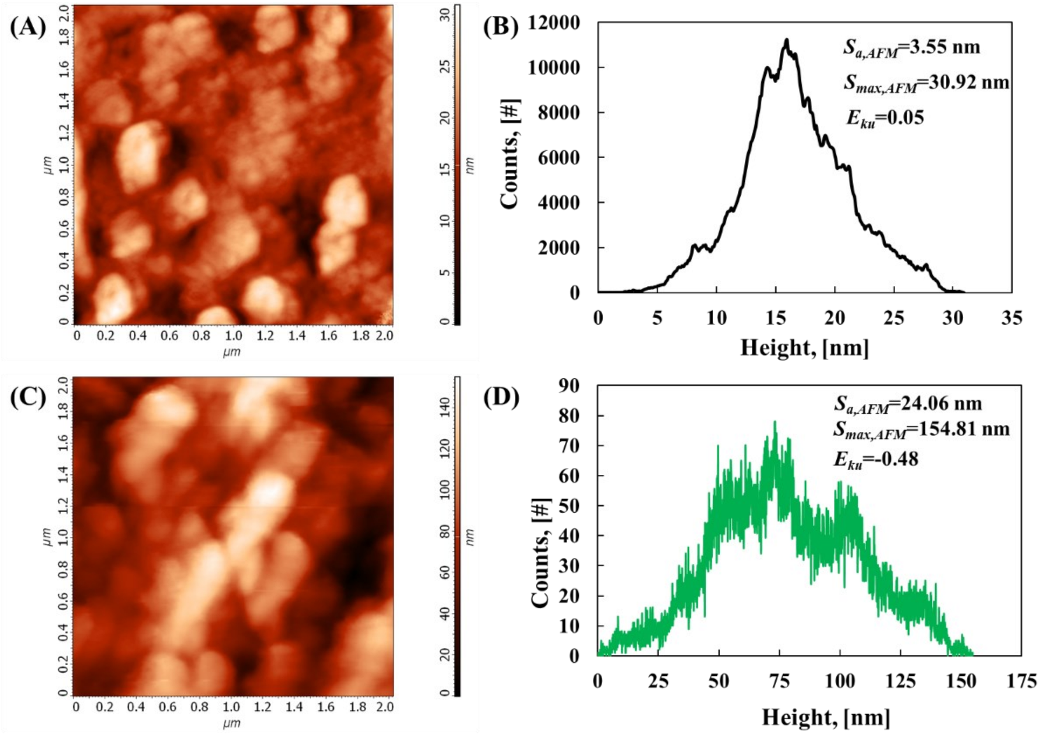

Figure 4.3. AFM Images and roughness parameters (average roughness $S_{a,AFM}$, maximum peak height $S_{max,AFM}$, and excess kurtosis E_{ku}) for CNP films obtained at 0 kV **(A-B)** and – 3 kV **(C-D)**, characterized by the same optical equivalent thickness of 140 nm. Pictures **(A)** and **(C)** refer to a scan area of 2 μm x 2 μm.

As can be seen, AFM images provide useful information on changes in the CNP film morphology at the nano-microscale due to the presence of the electrical potential applied to the deposition substrate. In particular, the analysis of the AFM images reveals the increase of the CNPs agglomerate size from 71±15 nm to 125±25 nm when the voltage increases from 0 to -3 kV. Moreover, in the presence of -3 kV voltage, a significant increase in the nanoscale average surface roughness $S_{a,AFM}$ is also observed. Finally, there is a change in the roughness distribution (panels **(B)** and **(C)** in **Figure 4.3**): at 0 kV the excess kurtosis E_{ku} is close to 0, suggesting a uniform distribution for the roughness. On the contrary, at -3 kV, the excess kurtosis is negative, suggesting the formation of a more “bumpy” surface, and confirming the presence of larger CNP agglomerates.

Information on the morphology of the first CNPs deposits on mica, as obtained after a single insertion is also shown in **Figure 3.6**, which indicates that the deposition rate largely increases thanks to the electrophoretic forces and that the morphology of the deposits is likely to change with respect to the pure thermophoretic deposition.

Finally, Surface texture analysis profilometry provides information about the mesoscale surface morphology of the CNP films. **Figure 4.4** shows the 3D and 2D surface profiles for the CNP films for the different values of electric potential V_0.

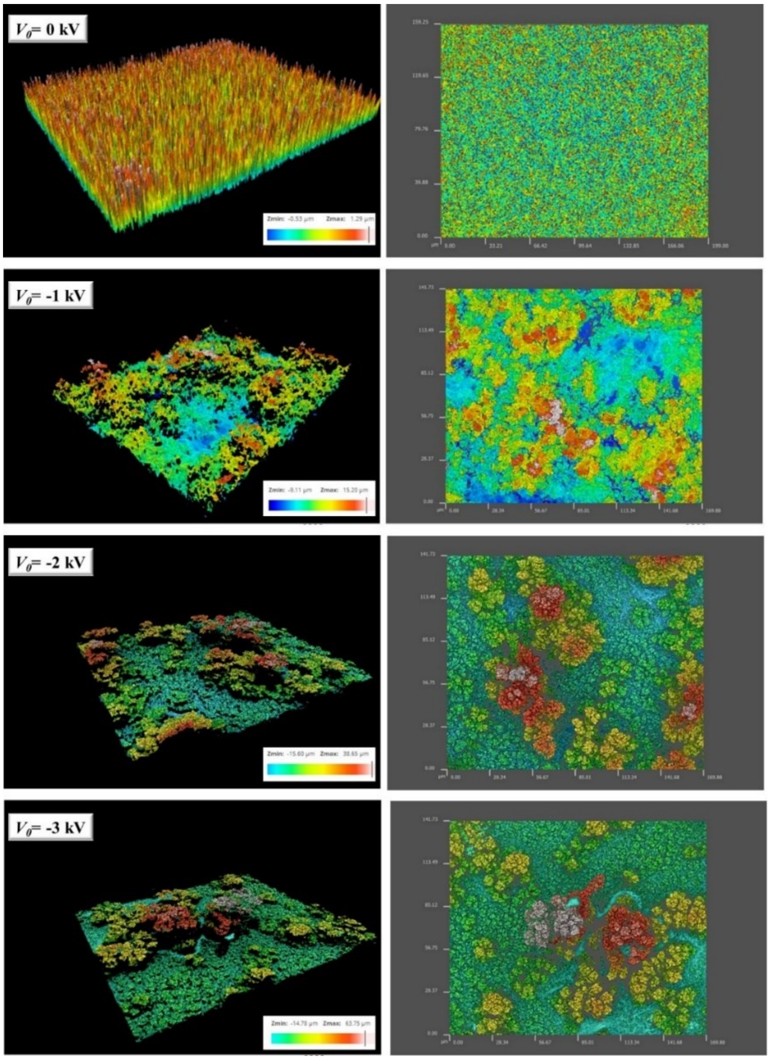

Figure 4.4. From the top to the bottom: Examples of 3D (left) and 2D (right) CNP film surface textures varying the electric potential applied to the deposition substrate.

Additionally, **Table 4.1** resumes the surface roughness descriptive parameters, obtained by using the ISO 25178-2:2022 standard for surface texture analysis for CNP samples with an equivalent optical thickness of 202±20 nm.

Table 4.1. Surface texture analysis of the CNP films obtained varying the voltage V_0 applied to the deposition substrate and the number of insertions N_{ins} in flame in terms of average roughness (S_a), Kurtosis (S_{ku}), Skewness (S_{sk}), the maximum height of peaks (S_p), and the root mean square roughness (S_q). An approximate estimation of the film thickness as the difference between the maximum (Z_{max}) and the minimum (Z_{min}) height peaks for each CNP film is also reported. The equivalent optical film thickness is 202±20 nm.

V_0, [kV]	0	-1	-2	-3
N_{ins}, [-]	600	200	175	150
Actual δ_{eq}, *[μm]*	0.19	0.18	0.20	0.22
S_a, [μm]	0.22	2.78	9.28	10.15
S_{ku}, [-]	2.8	3.44	3.38	7.06
S_{sk}, [-]	0.52	0.58	1.09	1.99
S_p, [μm]	1.29	15.20	38.65	63.76
S_q, [μm]	0.27	3.47	11.45	13.91
$\|Z_{max}-Z_{min}\|$,[μm]	1.82	24.31	54.25	78.53

It should be noted that measurements are affected by the intrinsic roughness equal to 1.9 nm of the glass coverslip used as a deposition substrate. The surface texture analysis provides relevant information on the effect of the electric field on the CNP film deposition and growth. In particular, at V_0= 0 kV, the CNP film is characterized by an average roughness of 0.22 μm and the 3D-2D CNP film surface textures show that the roughness appears quite homogenous with a Kurtosis near 3: a roughness probability density distribution very similar to a Normal one is, and the CNP film profile is characterized by the presence of as many peaks as valleys. This profile is consistent with previous observations [4]. The authors suggest that during the early stages of deposition, CNPs tend to attach evenly on the substrate and on the CNPs deposits, and hence favour three-dimensional or island growth. As the deposition time increases, they coagulate to form a CNP film characterized by a highly symmetric structure. This growth mechanism is known as the Volmer-Weber mode [5–7]. For this kind of morphology, AFM and surface texture analysis provide similar indications, since the flat texture of the films allows us to provide a good estimation of their morphology at the submicrometric scale. In contrast, CNP films obtained in the presence of an electric field show far higher roughness, up to 10.15 µm, which increases with the applied electric potential. Furthermore, the Skewness is positive, and the Kurtosis is greater than 3, suggesting the existence of extremely irregular surface textures, with flat valleys and many high and spiked peaks, as suggested by the 2D-3D CNP film profile in **Figure 4.4**. It is worth mentioning that the texture analysis for such kind of surface is not able to provide an accurate indication of the microscale morphology of the film: due to the high irregularity of the texture, the details of surface roughness in a smaller spot of the sample cannot be determined from this techniques, but can be only inferred with the AFM analysis. These results are in line with other experimental and theoretical evidence [8–10], stating that the presence of an intense electric field at the deposition substrate determines a surface energy instability and a polarization effect, with resulting preferential particle deposition in some specific points on the surface: this results in the formation of aligned particle structures, as branches protruding out of the deposit, in the same direction of the main electric field, with increased roughness [8] and a more irregular texture, but also a higher surface area. In order to illustrate the process, we can consider the 2D representation shown in **Figure 4.5**.

The McKenna burner mouth and the charged deposition substrate form a capacitator and an electrostatic field $E = V_0/d$ is approximately established between them. In the initial surface geometry (panel **A** in **Figure 4.5**), d is equal to HAB. The presence of an electric field induces a perturbation in the energy to the deposition substrate, which can be considered for graphical simplicity as a small sinusoidal one (panel **B** in **Figure 4.5**).

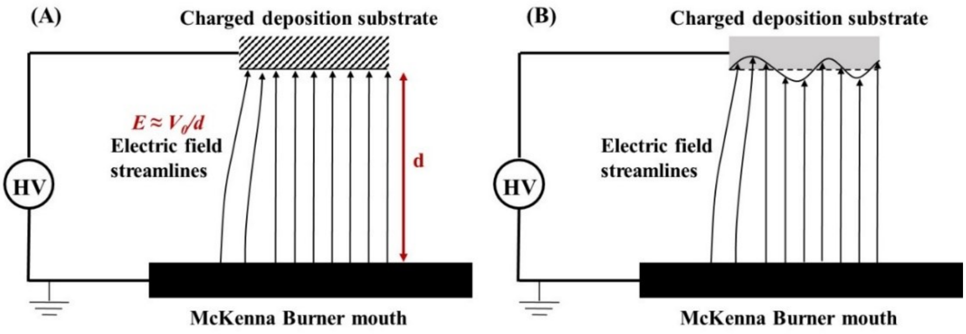

Figure 4.5. Electric field induced surface instability in the McKenna Burner-Deposition Substrate system. **(A)** Initial surface geometry. **(B)** Perturbed geometry of the surface. The electric field streamlines are higher close to the peaks than in the valleys.

Consequently, some randomly distributed points on the deposition surface are at a lower distance than HAB. These are preferential points of adhesion for CNPs of charge polarity opposite to that applied to the deposition substrate, both due to the higher field intensity and of the need to obtain a minimization of the total elastic energy in the system. This is consistent with the results of Gill et al. [8] which is shown in **Figure 4.6**.

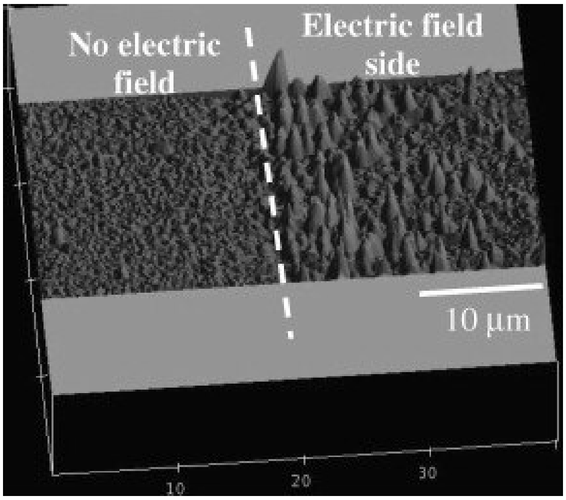

Figure 4.6. Experimental results obtained by Gill et al. [8] showing increase of the surface roughness produced under the effect of an external electric filed on a titanium electrode. The preferential sharp points for adhesion are clearly visible.

This results in the formation of 3D islands with an increase in the overall roughness. However, it should be noted that in flame there is a higher amount of uncharged CNPs: thanks to polarization phenomena and thermophoretic diffusion processes, these particles can also deposit in less energetically favoured points. It is known that polarization effects are likely to favour chain-branched deposits, as those shown from image analysis of particles deposited on electrostatic filters [11–15] which is described by the Stranski-Krastanov growth model.

On the overall, the mechanism of film growth in the presence of an electric field changes leading to a transition from a Volmer-Weber to a Stranski-Krastanov growth mechanism (*see* **Figure 4.**7) [7,8,16].

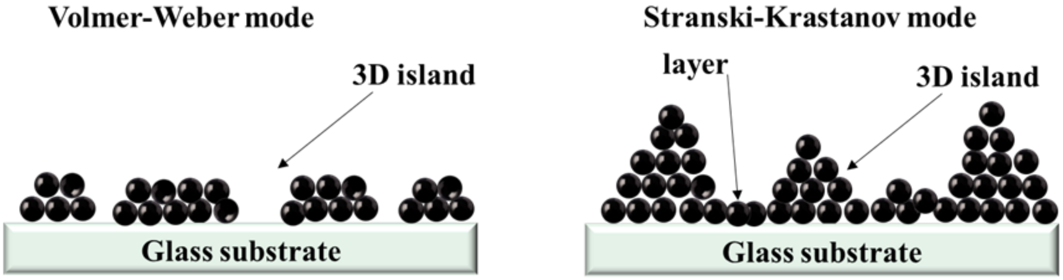

Figure 4.7. Representation of (A) 3D island growth according to the Volmer-Weber mode and (B) layer plus 3D island growth according to Stranski-Krastanov mode. Adapted from [7].

As can be seen in **Figure 4.4**, in presence of an electric field it is possible to notice the presence of small 3D islands evenly distributed throughout the CNP sample, and larger 3D islands, favoured by the presence of the electric field. Consequently, the average roughness increases and the peaks are heterogeneously distributed over the substrate. It is worth noting that semiconductor films growing according to the Stranski-Krastanov mechanism exhibit electronic, optical and wettability properties that make them extremely interesting for various industrial applications [16–23]. In the following paragraphs, information obtained through the different characterization techniques will be useful to verify the validity of this statement also for electrophoretically-produced CNP films.

4.2 Physico-chemical characterization

In this section, we report the information retrieved from the experiments related to the physical/chemical properties of CNP films produced by electric field-assisted flame synthesis. The first experimental result considered in this discussion is the analysis of the Raman spectra obtained for all the produced CNPs. The most prominent features in each spectrum are the ratio between the *I*(D) and *I*(G) peaks, I(D)/I(G), and the ratio between the slope of the linear photoluminescence background, *m*, and the intensity *I*(G) obtained by Raman spectroscopy. **Figure 4.8** shows the *I*(D)/*I*(G) and the *m*/*I*(G) values as a function of the equivalent optical film thickness and parametric with the applied potential.

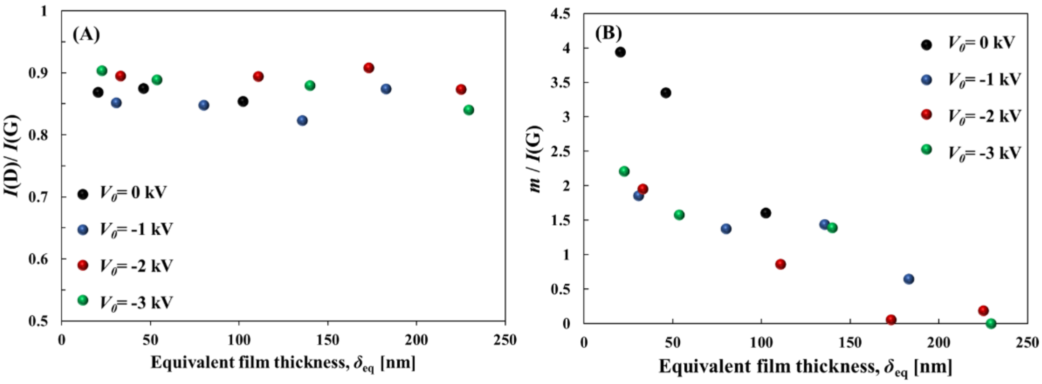

Figure 4.8. Values of *I*(D)/*I*(G) ratio **(A)** and the *m*/*I*(G) ratio **(B)** from the Raman spectra as a function of the equivalent film thickness δ_{eq} and the applied potential V_0.

From **Figure 4.8A** it is possible to notice that the *I*(D)/*I*(G) ratio is not dependent on the number of insertions – the equivalent film thickness – and on the electric potential applied to the deposition substrate: All the CNP films are characterized by a *I*(D)/ *I*(G) ratio equal to 0.87±0.02, meaning that Raman spectra are completely superimposable [4]. The *I*(D)/*I*(G) ratio can be used to estimate the in-plate correlation length of the aromatic island, L_a, that is the size of the polyaromatic units contained in each particle [24]. These aromatic structures can be viewed as small nanographene sheets containing both zigzag and armchair edges [25]. In particular, the I(D)/I(G) ratio is proportional to the probability of finding aromatic sp^2 hybridized carbon with respect to the total sp^2 hybridized carbon, which is proportional to L_a^2. Various expressions have been proposed by different authors to estimate L_a [26,27]. When this is smaller than 2 nm, it is possible to use the empirical expression reported in **Chapter 2**. For our CNP samples, the values of L_a are almost constant with the electric potential and equal to 1.36±0.38 nm. This demonstrates that the presence of an electric field in flame for an insertion time equal to 100 ms has no effect on the growth chemistry of CNPs in flame.

Furthermore, **Figure 4.8B** shows the m/I(G) ratio, which is a way to estimate the fluorescence of the samples with respect to the total sp^2 carbon. Interestingly, there is a reduction of the fluorescence as the equivalent film thickness increases, and this reduction is higher for CNP films obtained in the presence of an electric field. This effect can be easily observed from **Figure 4.9**, where the m/I(G) ratio for four different CNP films obtained by varying the electric potential at the same optical equivalent thickness (*see* **Table 4.2**) is reported.

Table 4.2. Resume of the information for the CNP films in terms of the electric potential applied to the deposition substrate V_0, [kV]; the number of insertions in flame N_{ins} [-]; Absorbance at a wavelength equal to 532 nm $Abs(\lambda=532$ nm) and equivalent CNP film thickness δ_{eq}, [nm]. Nominal average equivalent film thickness: 139.24 ± 2.52 nm.

SAMPLE	V, [kV]	N_{ins}, [-]	$Abs(\lambda$=532nm), [-]	*Actual* δ_{eq}, [nm]
A	0	520	0.79	140.02
B	-1	150	0.78	135.62
C	-2	125	0.81	141.45
D	-3	100	0.80	139.88

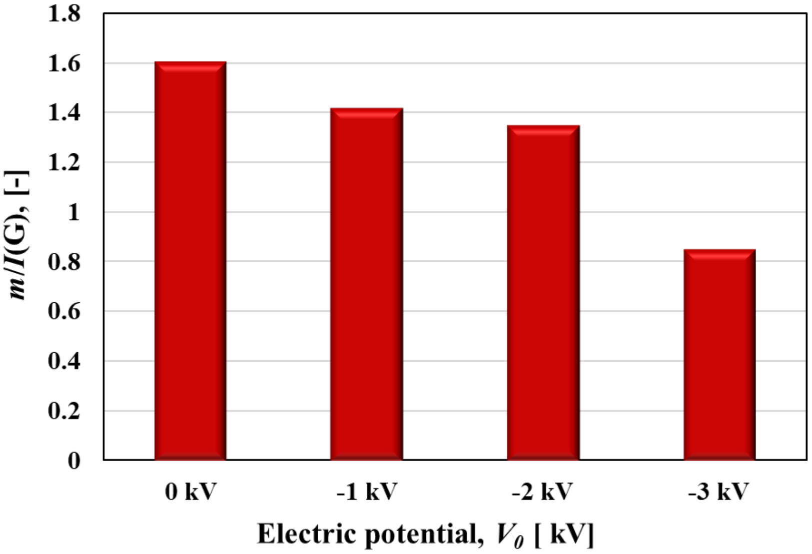

Figure 4.9. m/I(G) ratio as a function of the electric potential V_0 applied to the deposition substrate for four different CNP films characterized with an equivalent optical thickness of 139.24 ± 2.52 nm.

The m/I(G) ratio reduction can be explained by considering that the measured photoluminescence background is associated with the PAH molecular compounds, but also with CNPs with molecular-like electronic energy levels, *e.g.* the CNPs smaller than 5 nm, belonging to the first mode of the numerical PSD typical in our flame conditions (*see* **Figure 2.3** and **Figure 3.8B**). Otherwise, CNPs of the second Mode of the numerical PSD [28–30]. As predicted by the model discussed in **Chapter 3**, the m/I(G) ratio shows that CNP films produced by electric field-assisted flame synthesis are characterised by a smaller relative amount of CNP fluorescent particles, confirming that electric field induces selective harvesting of CNPs formed in the flame.

The same observation can be deduced by considering the absorption spectra normalised with respect to the absorbance value at 532 nm for CNP films (*see* **Table 4.2**) obtained by varying the voltage applied to the deposition substrate with the same equivalent optical thickness of 139.24 ± 2.52 nm (*see* **Figure 4.10**).

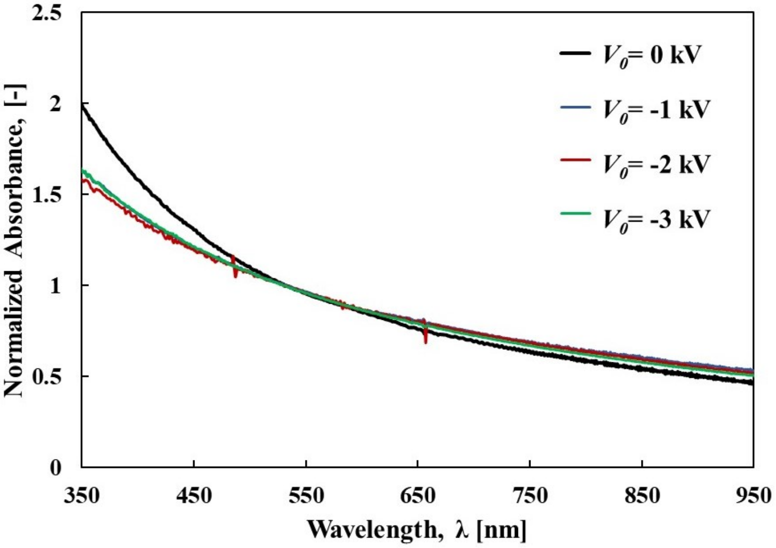

Figure 4.10. Normalized absorption spectra at 532 nm for CNP films of equivalent optical thickness of 139.24 ± 2.52 nm obtained varying the electric potential applied to the deposition substrate.

It is possible to notice that the features of the normalized spectra measured for the CNP films produced by electric field assisted flame synthesis are significantly different to those produced by pure thermophoretic flame synthesis. In particular, the light absorption remains the same above 520 nm, suggesting that the structure of large CNPs aggregates is not affected by the electric potential [31]. Otherwise, there is a decrease in the blue region (λ<500 nm) for all the applied potentials. As suggested by Sirignano et al. [31,32], this change is related to a shift of fluorescence in the CNP films, and in particular to the reduction of the fluorescent primary particles finer than 5 nm. These results are consistent with those obtained from the Raman spectra and with our model prediction.

The UV-vis absorption technique can be also used as an easy and forthright way to accurately estimate the optical band gap of inorganic π-conjugated materials. The optical band gap denotes the energy separation between the highest occupied molecular orbital (HOMO) and the lowest unoccupied molecular orbital (LUMO), that for inorganic materials represents the valence and the conduction bands, respectively [33,34]. For a semiconductor, this value is lower than 3 eV and it becomes close to zero for a conducting material. The control of the HOMO-LUMO band gap is a critical task to obtain materials with interesting electronic properties, useful for the semiconductive and nanomaterial industries. In carbonaceous structures, the HOMO-LUMO band gap depends mainly on the hybridization level of the carbon atoms and it becomes a powerful indicator of the nature of the carbonaceous structures produced in rich flames and of the physical properties of the CNPs. Investigations on soot reveal a band gap of 1.3±0.2 eV for CNPs of the first mode (< 5nm), which usually decreases to 0.6±0.2 eV for young soot, and to 0.2±0.2 eV for mature soot with high graphitization and conductive behavior [34–39]. However, the optical band gap for a carbonaceous film depends not only on the nature of single particles, but also on its structural arrangement [19,31,32].

As described in **Chapter 2**, starting from the UV-vis spectra and following Tauc's plot, it is possible to obtain the optical band gap values (E_g) for the CNP films. **Figure 4.11** shows the optical band gap as a function of the equivalent film thickness, parametric with the electric potential applied to the deposition substrate.

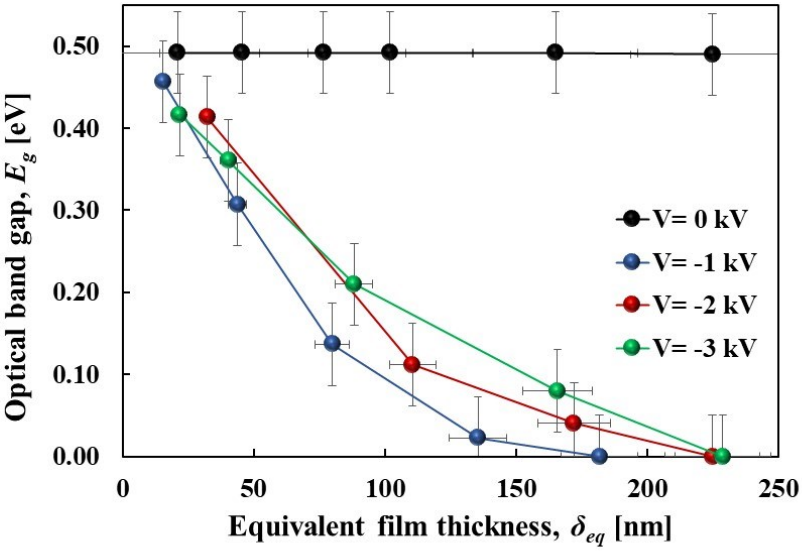

Figure 4.11. Optical band gap E_g as a function of the equivalent film thickness δ_{eq} varying the electric potential V_0 from 0 to -3 kV. Error bars are reported.

It is possible to notice that at 0 kV, the optical band gap remains almost constant as the equivalent optical thickness of the film varies. The value is equal to 0.5±0.05 eV, similar to other CNP films produced by thermophoresis for a C/O ratio lower than 0.72 [4].

On the contrary, the CNP films obtained in the presence of electric potential show a different trend, with a marked reduction of the optical band gap as the absorbance increases, from 0.5±0.05 to 0 eV. It is worth emphasizing that the optical band gap reduction obtained for the three electric potentials is essentially identical. The observed reduction may be partly due to the increase in the relative amount of the CNPs larger than 5 nm, which have a more graphitic behaviour. However, this it may also be related to the different arrangements of CNPs and the specific film surface texture, which can affect the UV-vis results.

To fully understand this, one can proceed to analyze the effects that the electric field has on the optical band gap of the CNP agglomerates, irrespective of how they are then arranged in making the film.

To this aim, as described in **Chapter 2**, four different CNP films (*see* **Table 4.2**) have been removed from the glass substrate, dispersed in DCM and then in NMP. After the suspension stabilization, UV-vis spectra have been analyzed to obtain the optical band gap for the CNP agglomerates (CNP_{TOT}). Moreover, CNP agglomerates have been filtered in order to obtain two different CNP fractions: CNP agglomerates smaller than 100 nm (CNP_{100}), and then those smaller than 20 nm (CNP_{20}). Even for these two fractions, spectra have been acquired and analyzed to obtain information on the corresponding optical band gaps.

Figure 4.12 shows the optical band gap value for the total CNP agglomerates, for the agglomerates smaller than 100 nm, and for those smaller than 20 nm as a function of the electric potential applied to the deposition substrate V_0.

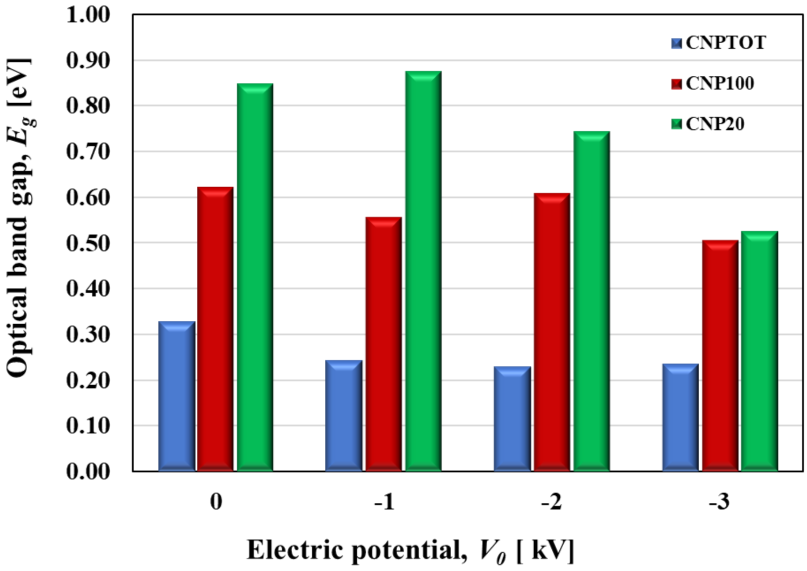

Figure 4.12. Optical band gap from the UV-visible absorption spectra for CNP films after dissolution in NMP containing all the CNP agglomerates (CNP_{TOT}), those smaller than 100 nm (CNP_{100}) 20 nm (CNP_{20}).

It is possible to notice that CNP agglomerates obtained in presence of an electric field (blue bars in **Figure 4.12**) show an optical band gap of 0.23 eV, which is lower than that for CNP agglomerates in the sample produced at 0 kV (0.33 eV). This suggests the presence of a smaller amount of fluorescent particles and a more graphitic behaviour for CNP agglomerates. However, it should be noted that CNP agglomerates smaller than 100 nm (red bars in **Figure 4.12**) exhibit a similar variation of the optical band gap, within 0.1 eV passing from 0 to -3kV, whereas the optical band gap values for CNP agglomerates finer than 20 nm (green bars in **Figure 4.12**) shows a marked reduction from 0.8±0.1 to 0.5±0.1 eV. These results are in agreement with the indications obtained from the Normalized Absorption Spectra (*see* **Figure 4.10**): the electric field-assisted flame synthesis gives rise to an overall reduction in the relative amount in the range of CNP agglomerates smaller than 20 nm, which are likely to represent large primary particles or smaller aggregates, including the fluorescent particles finer than 5 nm obtained by electrophoresis.

However, reduced fraction of smaller CNP agglomerates does not seem to explain the drastic reduction in the optical band gap of CNP films shown in **Figure 4.11**. In particular, as suggested by surface texture analysis, in the presence of an electric field there is a transition from 3D island growth (Volmer-Weber) to layer plus 3D island growth (Stranski-Krastanov mode, *see* **Figure 4.7**) [6,7,10,16].

Consequently, also in light of the produced alteration of charged particles impact velocity and the tested modification of the film morphology, we argue that the CNP film in presence of an external electric field is characterised by a rearrangement of the internal skeleton with the formation of lower porosity films with stronger preferential channels with higher conductivity (tunnelling effects). This is an exciting phenomenon, the so-called Giant Stark effect, observed in other semiconductor thin films [19,21,23,40–42].

Ultimately, electrophoretic harvesting allows increasing the amount of non-fluorescent larger CNPs and change the film growth pattern, resulting in a reduction in the overall CNP film optical band gap of the film with a transition from a semiconductive to a metal-like behaviour.

4.3 Structural characterization

Information on the size of CNPs constituting the deposited film, as already mentioned, can be obtained, indirectly, on the basis of the particles size distribution of the pristine CNPs in flame and by optical measurements. In particular, it has been shown that the UV-fluorescence spectral signal (with $\lambda \approx 330$ nm) can be attributed to high-molecular-mass oligomers with sizes of 2-3 nm constituted by 2-3 fused-rings species connected by aliphatic bonds. Instead, the Visible fluorescence signal (with $\lambda \approx 400$-450 nm) refers to carbon nanoparticles with sizes up to 5 nm constituted by oligomers of larger PAHs or by highly-packed, sandwich-like structural clusters of PAHs held together by van der Waals forces. Finally, the incandescence signal (with $\lambda \approx 550$ nm) is associated to CNPs larger than 10 nm with a strong solid-state feature

[29,30]. These results of the optical classification of CNPs have been confirmed by Atomic Force Microscopy and Particle Differential Mobility Analysis [29,43].

This implies that in the presence of an applied electrical potential, the reduction of the fluorescent component for λ< 450 nm observed in Raman and UV spectra results in a reduction of the relative proportion of CNPs characterised by a size smaller than 5 nm. This is consistent with the model prediction reported in **Chapter 3**: the activation of superior electrophoretic forces occurs only for charged particles and results in a significant increase in collision probability compared to thermophoresis mostly for CNPs larger than about 5 nm.

A direct measure of this CNP size classification can also be obtained from the results of the Size Exclusion Chromatography (SEC). **Figure 4.13** shows the normalised absorbance of single and agglomerated CNPs at 350 nm as retrieved from CNP films dissolved in NMP and analyzed by SEC methods (*see* **Table 4.2**). The normalization is needed to account for differences in the concentration of dissolved particles in the NMP liquid sample.

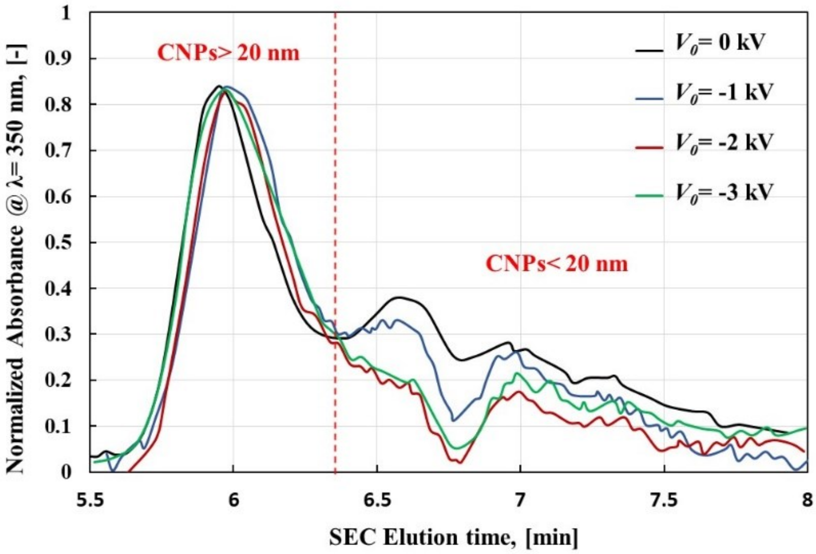

Figure 4.13. SEC chromatogram for CNP suspensions in NMP.

As explained in **Chapter 2**, the SEC elution time is inversely proportional to the CNPs aggregate size passing through the SEC column: the longer the SEC elution time, the lower is the molecular weight of the eluting species.

Figure 4.13 shows that the first peak at about 6 minutes has been used to normalize the signals and the similarities of the absorbance curved before 6.38 min indicated that no major differences in the relative size distribution of particles larger than 20 nm can be observed in the investigated conditions. Otherwise, the second region of the diagram reveals that CNPs finer than 20 nm are more abundant in the sample produced under thermophoretic conditions (V_0=0 kV), further confirming the results of film morphology and structural characterization and the model findings.

Moreover, as mentioned in the **Paragraph 4.2**, CNP agglomerates have been filtered in order to obtain two different CNP fractions: CNP agglomerates smaller than 100 nm (CNP100), and then those smaller than 20 nm (CNP20).

It is worth mentioning that it is not easy to discriminate between CNP aggregates or agglomerates in these experiments. Indeed, the analysis of pristine flame CNPs indicate that only primary particles with sizes finer than 20 nm are found in the flame. When they are collected, the primary particles agglomerate. Upon dissolution, the most stable of these agglomerates remain in the liquid as colloidal particles. Nevertheless it is not possible to guarantee that the colloids are agglomerates or aggregates. The UV-vis spectra have been acquired and analyzed also for these fractions.

Figure 4.14 shows the UV-vis absorption spectra for total CNP agglomerates (**A**), for CNP agglomerates smaller than 100 nm - CNP100 (**B**) - and for CNP agglomerates smaller than 20 nm - CNP20 (**C**) - for electric potentials equal to 0 kV, -2 kV, and -3 kV.

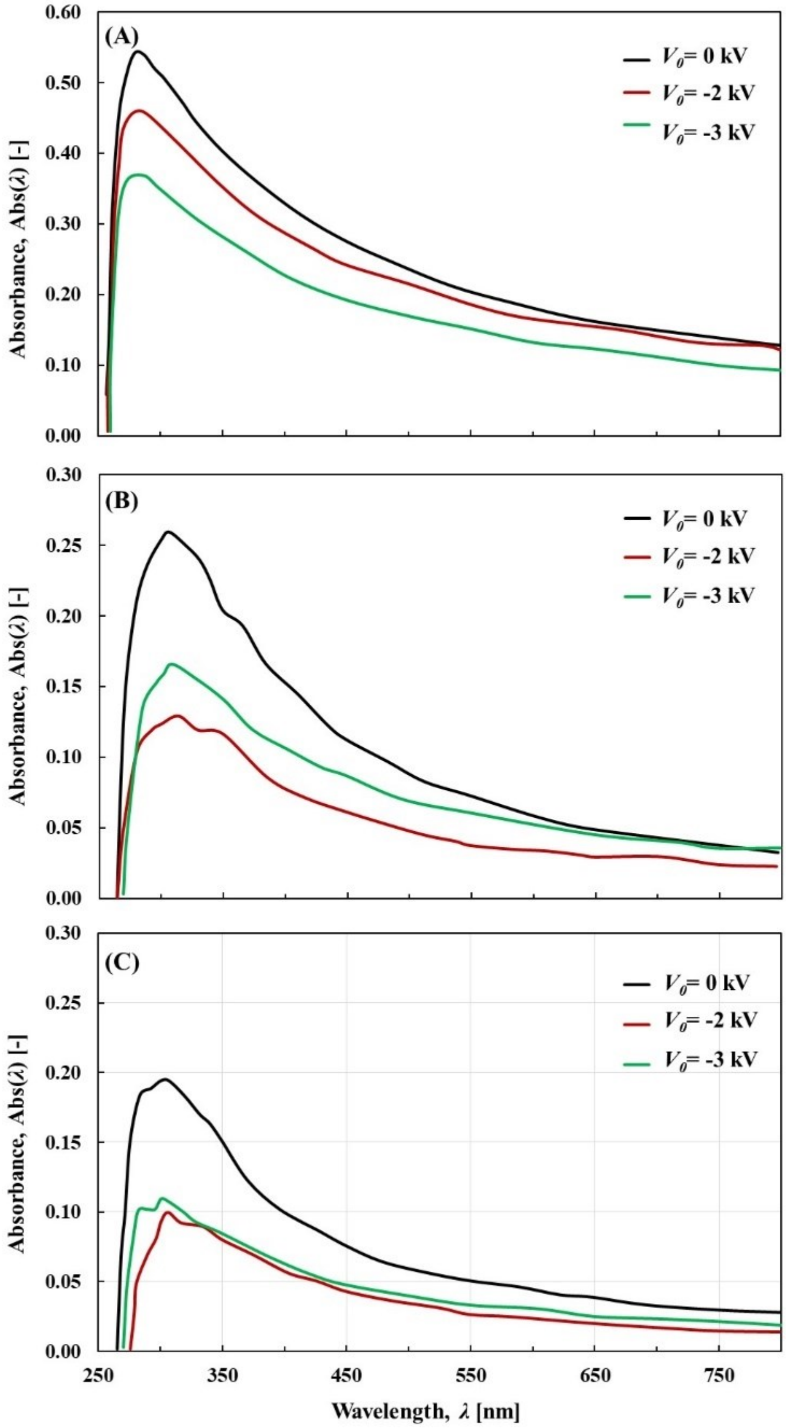

Figure 4.14. UV-vis absorption spectra for **(A)** total CNP aggregates, **(B)** CNP aggregates smaller than 100 nm (CNP100), and for **(B)** CNP aggregates smaller than 20 nm (CNP20) after dissolution in NMP and filtration.

The panel **A** in **Figure 4.14** shows that UV-vis signals of the total dissolved CNPs is not affected by the electric field. However, for each CNP sample at a fixed electric potential, it is possible to obtain information on the relative amount of CNP100 and CNP20 as the ratio between the absorbance at λ=350 nm or at λ=550 nm [32,39,44] for each sample in panel **B** and the corresponding value in panel **C**. It should be noted that the same values can be obtained considering the ratio between the area under the absorbance spectrum for each sample in panel **B** and the corresponding value in panel **C**. **Table 4.3** shows both the absorbance values at λ=350 nm and 550 nm for CNP100, and for CNP20 and the corresponding ratio for each electric potential.

Table 4.3. Values of absorbance at 350 nm - *Abs*(λ= 350 nm), *Abs*(λ=550nm) - for CNP aggregates smaller than 100 nm (CNP100) and those smaller than 20 nm (CNP20) and corresponding ratio (CNP100/CNP20) for each CNP sample obtained at a fixed electric potential V_0 (0, -2, -3) kV.

	V_0= 0 kV	**V_0= - 2 kV**	**V_0= -3 kV**
Abs(λ=350nm) for:			
CNP100 (panel **B Figure 4.14**)	0.20	0.12	0.14
CNP20 (panel **C Figure 4.14**)	0.15	0.08	0.09
CNP100/CNP20	**1.35**	**1.45**	**1.65**
Abs(λ=350nm) for:			
CNP100	0.07	0.04	0.06
CNP20	0.05	0.02	0.03
CNP100/CNP20	**1.28**	**1.49**	**1.82**

It is possible to notice that from 0 kV to -3 kV there is an increase in the CNP100/CNP20 ratio for both wavelengths, showing the increase of the amount of larger agglomerates in presence of an electric potential. This may be associated with increased interparticle electrical cohesive forces. More stable agglomerates stabilised by electrostatic forces rather than the pure Van der Waals and dielectric forces which characterize thermophoretic flame synthesis agglomerates, and that the dissolution procedure is unable to separate.

Moreover, the ratio between the absorbance at λ=550 nm and the absorbance at 350 nm – Abs(λ=550 nm)/Abs(λ=350 nm) can give information about the level of graphitisation for each CNP fraction. From **Figure 4.14** this ratio can be obtained, and it is possible to notice that both for CNP100 and CNP20 agglomerates there is an increase from 32% up to 40% for electric potentials going from 0 kV to – 3 kV. CNP agglomerates in presence of an electric field have a more graphitic behaviour, confirming all our previous observations.

The structural characterisation of the CNP agglomerates constituting each film can be concluded by reproducing the AFM images of aged samples obtained considering a single insertion (N_{ins}=1) of a mica muscovite substrate in flame. We can assume that these images represent a portrait of the individual units deposited on the substrate (*see* **Figure 4.15**).

As can be seen, the CNP agglomerates observed in the presence of electric potential are completely different in terms of shape, distribution and size. Interestingly, in the case of V_0=0 kV, CNPs are distributed uniformly on the substrate and appear mostly as single spherical entities or small aggregates of a few particles. On the other hand, in presence of applied potential, CNPs are organized as fractal petal-like structures of larger sizes.

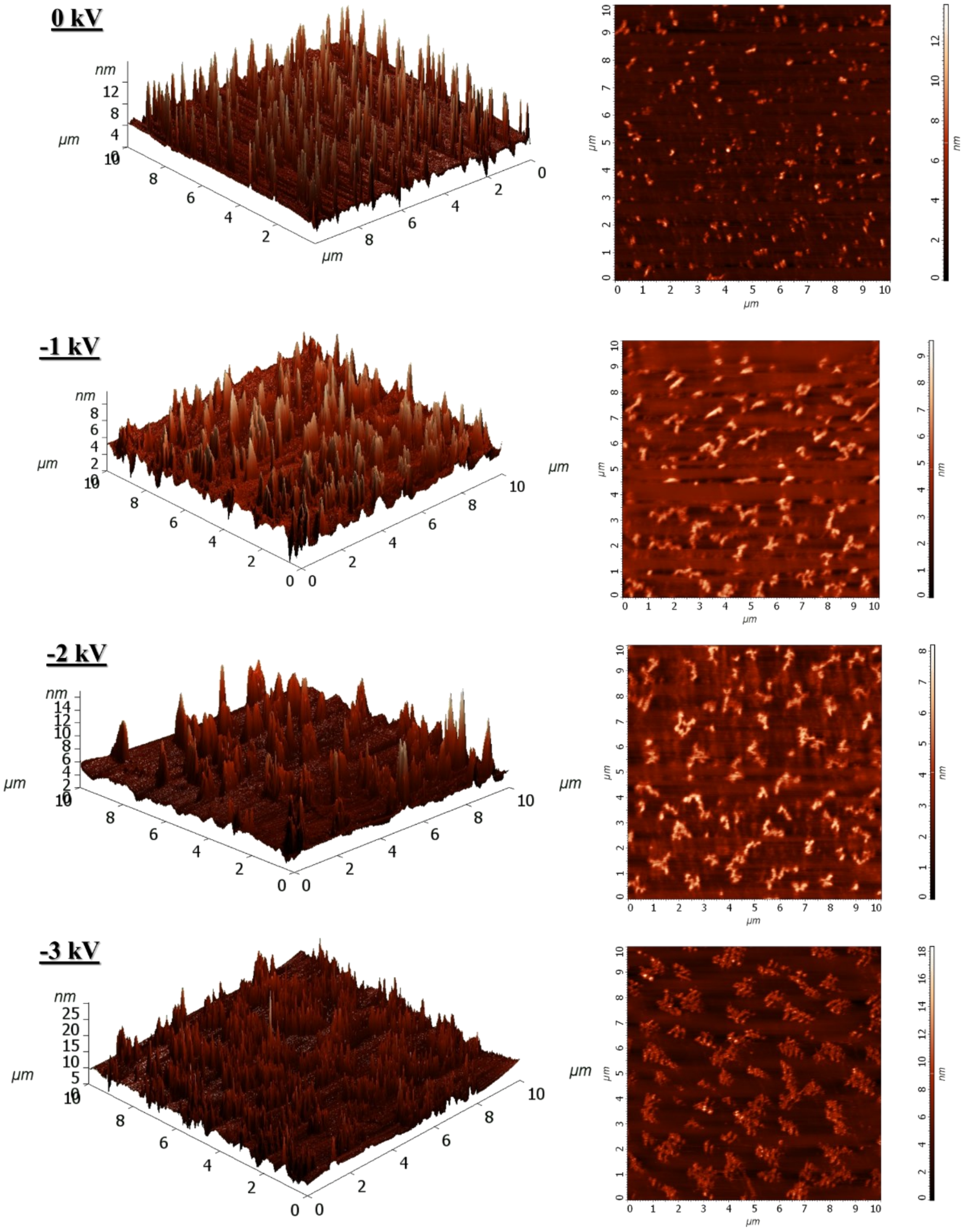

Figure 4.15. AFM 3D and 2D images obtained after a single insertion in flame (N_{ins}=1) by varying the electric potential V0 from 0 to -3 kV.

4.4 Possible technological applications of CNP films

Carbon-based amorphous materials, including graphene, candle soot, and carbon black, play important parts in progress of civilization, because of their applications in many technical areas [45,46] . No alternatives are known to simultaneously exhibit nano-sized dimensions, large specific surface area, high electrical conductivity, good chemical stability and mechanical strength with such a cost effective production cost in the industry [47,48]. Among the interesting properties of these materials, the aspects associated with electrical and wettability properties will be discussed in more detail below. The electrical conductivity is the key parameter for applications in renewable energy storage/conversion devices. Kumar et al. [47] reviewed the fabrication of electrodes based on graphene for application in energy storage and conversion, including relevant performance data for real devices, as supercapacitors, lithium-ion battery, fuel cells, solar cells, and wearable and portable electronics among others [45,47–49]. The analysis of the State-of-art shows that some issues remain unresolved, including controllable preparation of graphene-based materials with desired quality, size distribution of flakes, conductivity, porosity, high specific surface area and electrochemical activity at low cost and high yield [47]. The same considerations can be extended to the use of candle soot. Its high mass activity along with good conductivity, high surface area to volume ratio and easy processability makes candle soot an ideal candidate for PEM fuel cell catalyst support [50]. Candle soot has been also explored as a cheap electrocatalyst for water splitting [51]. Moreover, the fractal-like interconnected morphology leading to shortest diffusion pathways makes it an ideal anode material for Li-ion batteries [52]. All these advantageous characteristics can also be applied in the field of high power density supercapacitors [53]. Carbon nanomaterials have been considered as a practical component of superhydrophobic coatings with self-cleaning, anti-corrosion, anti-icing, anti-reflective properties due to the their hydrophobic coatings and the microroughness of these surfaces [49,54]. Moreover, starting from hydrophobic materials, it is possible to obtain hydrophilic materials either by deposition of a molecular film of a new hydrophilic inorganic material or by modification of the substrate surface chemistry. Glass/anti-fogging surfaces, anti-biofouling biomedical devices, and enhanced boiling heat transfer in nuclear power plants, cooling of electronics and chemical reactors are just some of the applications of hydrophilic materials that have been achieved [55]. **Figure 4.16** resumes the most important applications of carbon-based nanomaterials based on electrical and wettability properties.

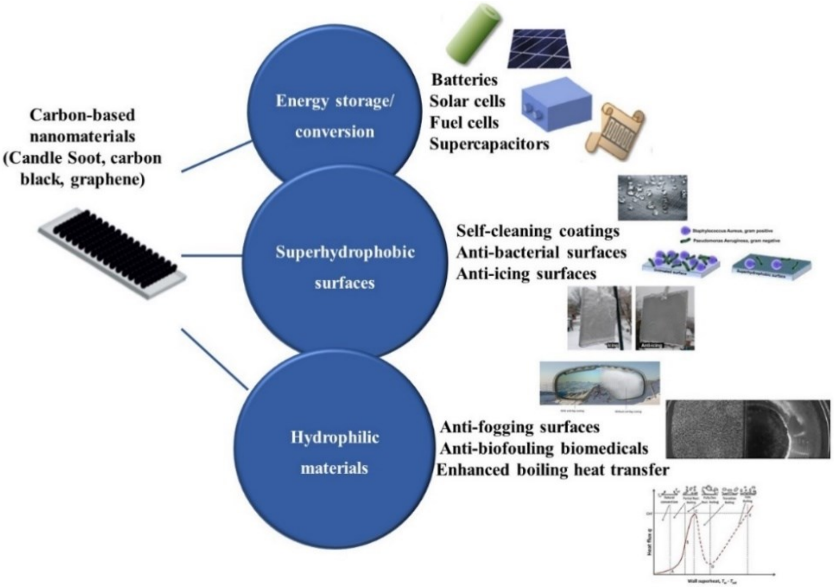

Figure 4.16. Summary of the applications for Carbon-based nanomaterials (carbon black, candle soot, and graphene) based on electrical and wettability properties: energy storage/conversion, superhydrophobic surfaces, and hydrophilic materials.

The quasi-graphitic structure of CNP films, very similar to that of carbon black, have suggested their promising potential for the industry, and some works [4,56] reviewed in **Chapter 1** have shown its feasibility. Moreover, the production of CNP films in controllable and tunable conditions allow to overcome some limitations encountered in the production of other carbon-based materials. The following sections aim to revise the morphological, structural, and physico-chemical properties of electric field-assisted flame synthesis CNP films and suspensions to exploit their electrical and wettability properties and their potential technological applications.

4.4.1 Electrical properties

In this section, the I-V curves and electrical conductivity data for the CNP films listed in **Table 4.2** are reported.

Figure 4.17 shows the I-V curves at 25°C obtained for CNP samples by varying the electric potential from 0 to -3 kV. In particular, the x-axis reports the voltage, *V* in Volts, applied to the probe station, and the y-axis the output recorded current, *I* in μA. Note that in view of the differences of orders of magnitude in the values obtained for the - 3V sample, for this sample a secondary scale on the right is added.

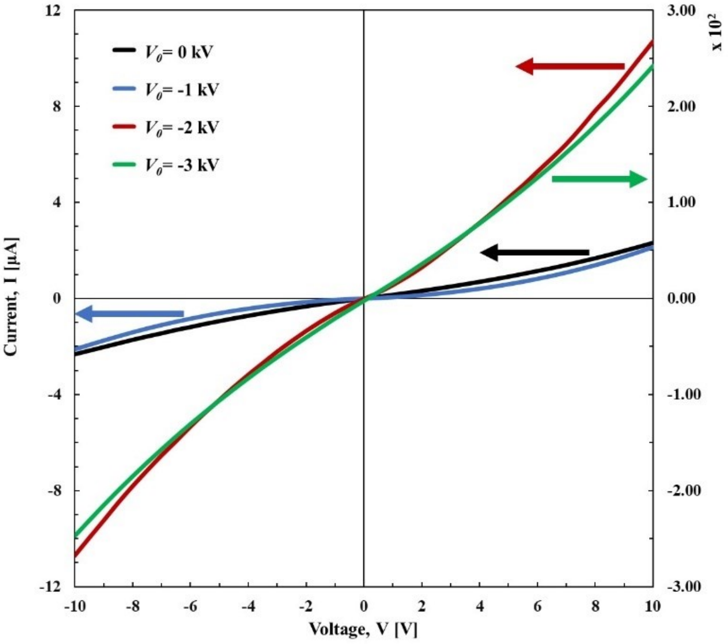

Figure 4.17. *I-V* curves of CNP samples with optical equivalent thickness of 139.24 ± 2.52 nm (*see* **Table 4.2**). by varying the electric potential applied to the deposition substrate V_0. For -3 kV refer to the secondary scale on the right for the y-axis.

It is possible to notice that for all the CNP samples, the I-V curve appear symmetrical respect to the reversal potential (V=0), exhibiting a non-linearity. This means that CNP films have a non-Ohmic behaviour. Moreover, from the maximum values of the output current and the slope of the *I-V* curves, it is possible to underline that there is an increase in the conductance of CNP samples with the electric potential applied to the deposition substrate.

As suggested in **Chapter 2**, in case of non-Ohmic behaviour, the conductance can be evaluated as the slope of the I-V curve for V ranging from 8 V to 10 V. **Figure 4.*18*** shows the electrical conductivity for the CNP samples as a function of the electric potential applied to the deposition substrate.

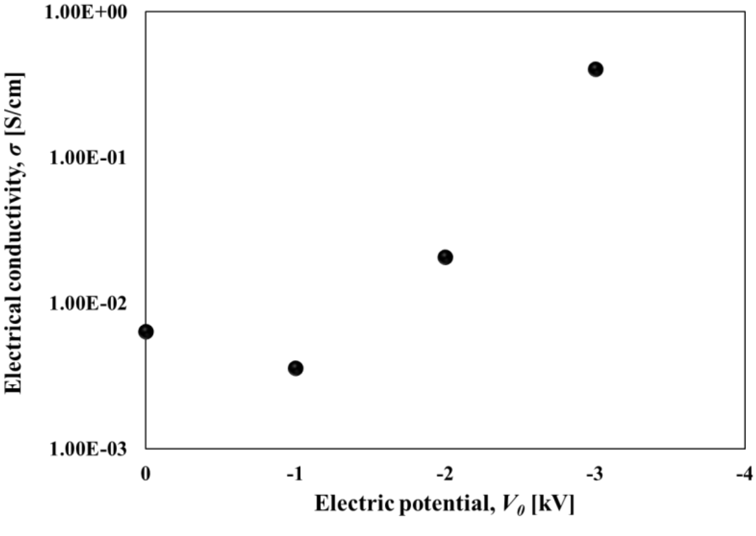

Figure 4.18. Electrical conductivity σ for CNP samples varying the electric potential applied to the deposition substrate.

First, it is important to underline that the electrical conductivity at 0 kV is equal to 10^{-3} S/cm and this value is very similar to those measured by De Falco et al. [4]

where the substrate employed for electrical characterization is completely different, suggesting the consistency of these measurements. Moreover, starting from -1 kV there is a nonlinear increase in the electrical conductivity from 10^{-3} S/cm to 10^{-1} S/cm. This increase may be partly related to the more graphitic behaviour of CNPs [46], as suggested by Optical band gap values, but it is also related to the higher electric interactions between the agglomerates, as suggested by SEC analysis.

Lastly, the effect of a temperature variation from 25 to 100°C is explored. **Figure 4.19** shows the results in terms of electrical conductivity ratio – the ratio between the electrical conductivity value at the temperature, T, and the corresponding value at 25°C – as a function of the temperature, parametric with the electric potential applied to the collector.

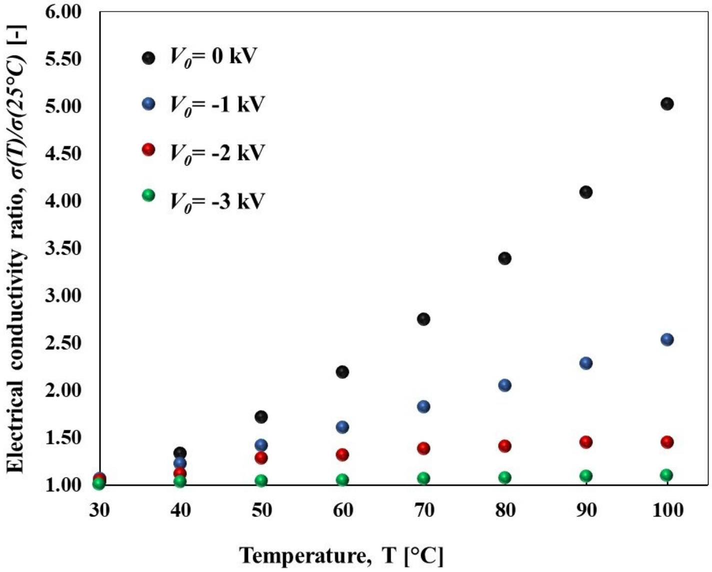

Figure 4.19. Electrical conductivity ratio as a function of the temperature varying the electric potential applied to the substrate during CNP film deposition.

It is clear that the electrical conductivity increases with the temperature, and this phenomenon is less and less relevant for electric field-assisted flame synthesis CNP films being negligible for V_0= - 3 kV. In fact, σ at 100°C is six times higher than the value at 25°C when V_0=0 kV, but this increase becomes equal to 45% at -2 kV and only 10% at – 3kV.

The difference in the strong correlation between the voltage applied for the electric field-assisted flame synthesis and the CNP film conductivity as well as the effect of temperature can be explained considering that the tunnelling of electrons between neighbouring nanoparticles is higher in presence of electric potential. At 0 kV, the CNP film is a semiconductor with an optical band gap equal to 0.5 eV. The increase of temperature determines a reduction of the activation energy required by electrons to transfer from one particle to another. Consequently, as the temperature increases, there is a linear reduction of the energy band gap, as shown in [57,58], and, thus, an increase of the films conductivity. Otherwise, CNP films obtained in presence of electric potential show reduced values for the optical band gap, which is close to 0 eV above a certain number of insertions (*see* **Figure 4.*11***). Therefore, the increasing temperature cannot affect significantly the electrical conductivity. Moreover, the increased roughness and electrostatic cohesive forces between agglomerates amplificate this effect [59]: both the activation energy required by electrons to transfer from one particle to another and the tunnelling distance are close to 0.

4.4.2 Surface- wettability properties

In this section, we study the surface-wettability properties of the CNP films produced by electric field-assisted flame synthesis. In particular, we refer to the CNP samples reported in **Table 4.1**, characterized by the same optical equivalent thickness (220±20 nm), whose morphology has been previously investigated by surface texture analysis (*see* **Figure 4.4**), and whose physicochemical properties are described in **Section 4.2**. **Figure 4.20** shows the samples pictures of the contact angle measurements carried out at the Department of Engineering at University of Campania L. Vanvitelli using the sessile drop procedure described in the **Chapter 2**. Indications about the apparent contact angles are also reported.

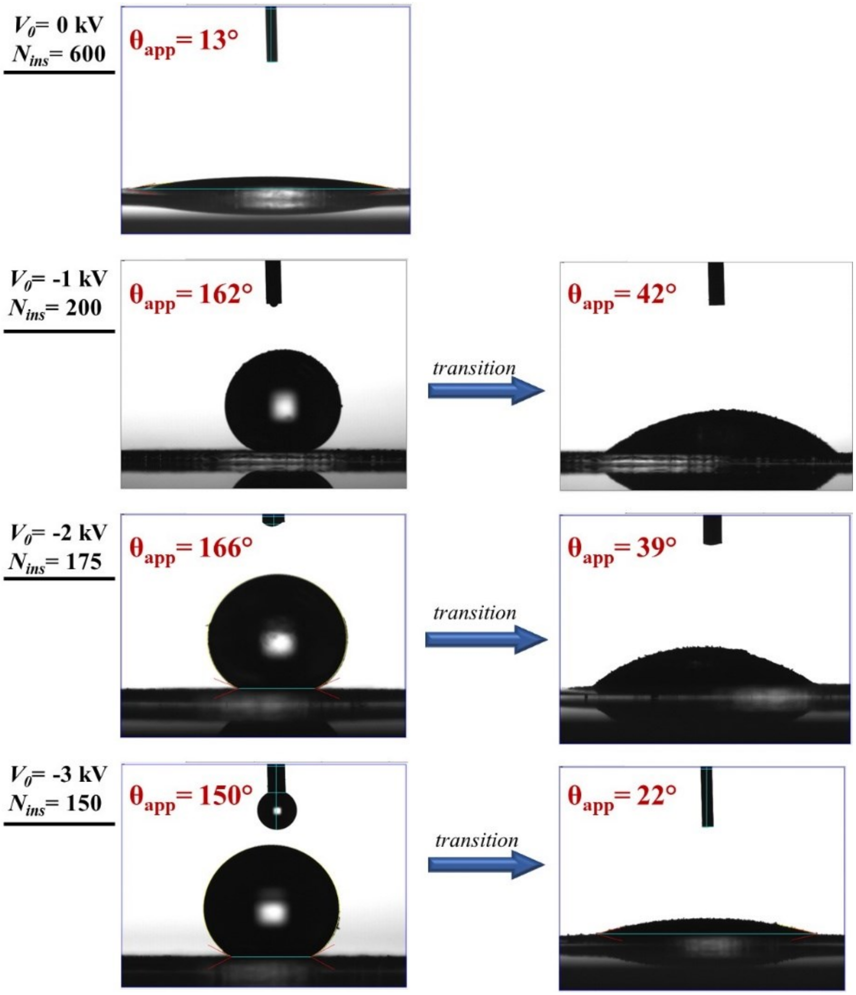

Figure 4.20. Sessile drop procedure and apparent contact angle measurements for CNP films deposited on glass substrates produced by varying the electric potential applied to the deposition substrate and the number of insertions in flame in order to obtain comparable equivalent thickness.

It is possible to notice that the CNP film produced at 0 kV appears instantaneous hydrophilic with an apparent static contact angle of 13°. As suggested by Commodo et al. [60], which observed a similar behaviour for CNPs produced by flame synthesis at C/O=0.63, finer CNPs exhibit intrinsically an hydrophilic behaviour due to large amounts of organic carbon on the surface. Moreover, the very low roughness (S_a=0.22 µm) and the uniform distribution of peaks and valleys on the surface (S_{ku}=2.8; S_{sk}=0.52) observed by surface texture analysis further discourages the onset of roughness-driven hydrophobicity of the CNP samples which preserves the chemical affinity between the finer CNPs and water droplet. The increase in the graphitic character observed in electrified samples, suggested by the results of the physicochemical characterization, might lead to an increase in the hydrophobic character of the CNP material, favoring the shift toward lower hydrophilicity. Indeed, this is what is observed for carbon black, candle soot and films with particle sizes larger than 10 nm [48,60,61]. However, under our conditions, apart from the initial instants when the contact angle is greater than 150°, an apparent contact angle less than 40° is then reached for all the electrified CNP samples, demonstrating an hydrophilic behaviour of the film. Besides, the apparent contact angle reduces with the applied potential suggesting that surface morphology play a role in the wettability. To better understand this phenomenon, **Figure 4.21** shows snapshots referred to the superhydrophobic/hydrophilic transition for two CNP samples, obtained at -1 kV and -3 kV.

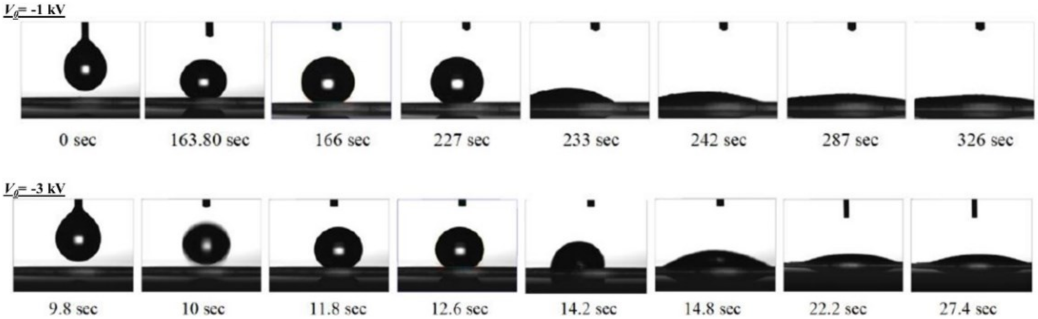

Figure 4.21. Snapshots for the superhydrophobic/hydrophilic transition of CNP films obtained at -1 kV and -3 kV. At 0 kV the CNP sample is instantaneously hydrophilic.

Indeed, this evidence can be explained considering the surface morphology of these CNP films, with larger roughness (from 2 µm at -1 kV to 10 µm at -3 kV) and the non-uniform distribution of peaks on the sample (S_{ku}>3 and S_{sk}>0). Specifically, the drop falling onto the film first makes contact with the peaks of the CNP film due to the high roughness of the sample. It is a graphitic material, and consequently there is a contact angle greater than 150 degrees, characteristic of a superhydrophobic behaviour. In the subsequent stages, the water droplet tends to reach a condition of energy minimization, whereby it penetrates into the valleys of the sample of a size comparable to that of the droplet itself, resulting in low contact angles less than 40 degrees, making the sample hydrophilic.

Furthermore, it is observed that the higher the applied electrical potential, the lower the final contact angle reached (**Figure 4.20**) and the faster (from 326 s at -1 kV to 27 s at -3 kV) the transition (**Figure 4.21**). This result is consistent with other works [62,63] showing that increasing the mesoroughness of the sample causes intrinsically hydrophobic materials to become hydrophilic according to the Wenzel model. In this perspective, CNP films obtained by electric-field in-flame synthesis possess attractive physical/chemical properties including high conductivity, large specific surface area and chemical stability as the other carbon-based materials, but a unique hydrophilic behaviour achievable without the need for additional chemical superficial treatments during the same flame synthesis process.

Lastly, **Figure 4.22** shows an interesting feature of the CNP achieved from a zoom of the drop profiles on the substrate as a function of V_0, for the samples shown in **Figure 4.20**.

It is possible to notice that for electrified samples, on the other hand, the drop profile is characterized by the presence of the film itself on the drop profile in the form of flakes. At the end of the evaporation of the drop, the film is perfectly deposited on the glass substrate. This confirms the greater cohesion of the aggregates constituting the film due to the electric forces, which are stronger than the weak van der Waals interactions.

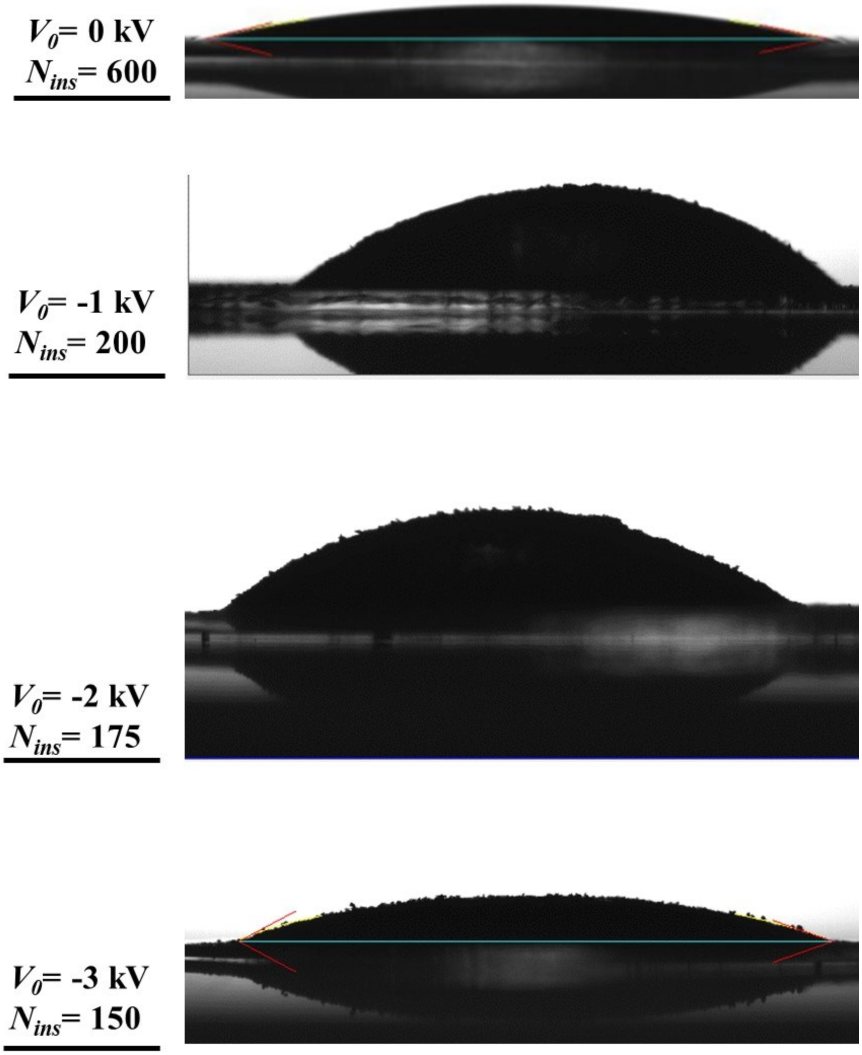

Figure 4.22. Zoom on the drop profile obtained from contact angle measurement for the CNP samples shown in **Figure 4.20**.

4.6 References

[1] Kim JH, Kil DS, Yeom SJ, Roh JS, Kwak NJ, Kim JW. Modified atomic layer deposition of Ru O2 thin films for capacitor electrodes. Appl Phys Lett 2007;91. https://doi.org/10.1063/1.2767769.

[2] Porcel C, Lavalle P, Ball V, Decher G, Senger B, Voegel JC, et al. From Exponential to Linear Growth in Polyelectrolyte Multilayers. Langmuir 2006;22:4376–83. https://doi.org/10.1021/la053218d.

[3] De Falco G, Porta A, Petrone AM, del Gaudio P, el Hassanin A, Commodo M, et al. Antimicrobial activity of flame-synthesized nano-TiO2 coatings. Environ Sci Nano 2017;4:1095–107. https://doi.org/10.1039/c7en00030h.

[4] De Falco G, Commodo M, Barra M, Chiarella F, D'Anna A, Aloisio A, et al. Electrical characterization of flame-soot nanoparticle thin films. Synth Met 2017;229:89–99. https://doi.org/10.1016/j.synthmet.2017.05.008.

[5] Li D, Liu GL, Yang Y, Wu JH, Huang ZR. Nucleation and growth mechanism of si amorphous film deposited by PIAD. J Nanomater 2013;2013. https://doi.org/10.1155/2013/383867.

[6] Lee WJ, Li C, Gunning J, Burke N, Patel J. Is the structure of anisotropic pyrolytic carbon a consequence of growth by the Volmer-Weber island growth mechanism? Carbon N Y 2012;50:4773–80. https://doi.org/10.1016/j.carbon.2012.05.052.

[7] Ta HQ, Perello DJ, Duong DL, Han GH, Gorantla S, Nguyen VL, et al. Stranski-Krastanov and Volmer-Weber CVD Growth Regimes to Control the Stacking Order in Bilayer Graphene. Nano Lett 2016;16:6403–10. https://doi.org/10.1021/acs.nanolett.6b02826.

[8] Gill V, Guduru PR, Sheldon BW. Electric field induced surface diffusion and micro/nano-scale island growth. Int J Solids Struct 2008;45:943–58. https://doi.org/10.1016/j.ijsolstr.2007.09.010.

[9] Kim D, Lu W. Three-dimensional model of electrostatically induced pattern formation in thin polymer films. Phys Rev B Condens Matter Mater Phys 2006;73. https://doi.org/10.1103/PhysRevB.73.035206.

[10] Chiu CH, Poh CT, Huang Z. Morphological stability of the Stranski-Krastanow systems under an electric field. Appl Phys Lett 2006;88. https://doi.org/10.1063/1.2212052.

[11] Chang Q, Zheng C, Yang Z, Fang M, Gao X, Luo Z, et al. Electric agglomeration modes of coal-fired fly-ash particles with water droplet humidification. Fuel 2017;200:134–45. https://doi.org/10.1016/j.fuel.2017.03.033.

[12] Jaworek A, Marchewicz A, Sobczyk AT, Krupa A, Czech T. Two-stage electrostatic precipitators for the reduction of PM2.5 particle emission. Prog Energy Combust Sci 2018;67:206–33. https://doi.org/10.1016/j.pecs.2018.03.003.

[13] Sobczyk AT, Marchewicz A, Krupa A, Jaworek A, Czech T, Śliwiński, et al. Enhancement of collection efficiency for fly ash particles (PM2.5) by unipolar

agglomerator in two-stage electrostatic precipitator. Sep Purif Technol 2017;187:91–101. https://doi.org/10.1016/j.seppur.2017.06.039.

[14] Jaworek A, Sobczyk AT, Krupa A, Marchewicz A, Czech T, Śliwiński L. Hybrid electrostatic filtration systems for fly ash particles emission control. A review. Sep Purif Technol 2019;213:283–302. https://doi.org/10.1016/j.seppur.2018.12.011.

[15] Hautanen J, Kilpeläinen M, Kauppinen EI, Jokiniemi J, Lehtinen K. Electrical agglomeration of aerosol particles in an alternating electric field. Aerosol Science and Technology 1995;22:181–9. https://doi.org/10.1080/02786829408959739.

[16] Prieto JE, Markov I. Stranski–Krastanov mechanism of growth and the effect of misfit sign on quantum dots nucleation. Surf Sci 2017;664:172–84. https://doi.org/10.1016/j.susc.2017.05.018.

[17] Deng S, Jia S, Deng X, Qing Y, Luo S, Wu Y. New insight into island-like structure driven from hydroxyl groups for high-performance superhydrophobic surfaces. Chemical Engineering Journal 2021;416. https://doi.org/10.1016/j.cej.2021.129078.

[18] O'Masta MR, Clough EC, Martin JH. Island formation and the heterogeneous nucleation of aluminum. Comput Mater Sci 2021;192. https://doi.org/10.1016/j.commatsci.2021.110317.

[19] Song J, Zhang Z, Feng N, Wang J. Electric field induced twisted bilayer graphene infrared plasmon spectrum. Nanomaterials 2021;11. https://doi.org/10.3390/nano11092433.

[20] Wang L, Dimitrijev S, Fissel A, Walker G, Chai J, Hold L, et al. Growth mechanism for alternating supply epitaxy: The unique pathway to achieve uniform silicon carbide films on multiple large-diameter silicon substrates. RSC Adv 2016;6:16662–7. https://doi.org/10.1039/c5ra24797g.

[21] Yakimov AI, Dvurechenskii A v., Nikiforov AI, Ulyanov V v., Milekhin AG, Govorov AO, et al. Stark effect in type-II Ge/Si quantum dots. Phys Rev B Condens Matter Mater Phys 2003;67. https://doi.org/10.1103/PhysRevB.67.125318.

[22] Tao K, Wang J, Jia R, Sun Y, Jin Z, Liu X. Ultralow temperature epitaxial growth of silicon-germanium thin films on Si(001) using GeF4. Diam Relat Mater 2016;68:138–42. https://doi.org/10.1016/j.diamond.2016.06.017.

[23] Damilano B, Grandjean N, Massies J, Semond F. GaN and GaInN quantum dots: an efficient way to get luminescence in the visible spectrum range. vol. 164. 2000.

[24] Raman V, Fox RO. Modeling of Fine-Particle Formation in Turbulent Flames. Annu Rev Fluid Mech 2016;48:159–90. https://doi.org/10.1146/annurev-fluid-122414-034306.

[25] Vitiello G, De Falco G, Picca F, Commodo M, D'Errico G, Minutolo P, et al. Role of radicals in carbon clustering and soot inception: A combined EPR and Raman spectroscopic study. Combust Flame 2019;205:286–94. https://doi.org/10.1016/j.combustflame.2019.04.028.

[26] Minutolo P, Commodo M, Santamaria A, De Falco G, D'Anna A. Characterization of flame-generated 2-D carbon nano-disks. Carbon N Y 2014;68:138–48. https://doi.org/10.1016/j.carbon.2013.10.073.

[27] Commodo M, De Falco G, Bruno A, Borriello C, Minutolo P, D'Anna A. Physicochemical evolution of nascent soot particles in a laminar premixed flame: From nucleation to early growth. Combust Flame 2015;162:3854–63. https://doi.org/10.1016/j.combustflame.2015.07.022.

[28] Minutolo P, Gambi G, D'alessio A, D'Anna A. Optical and Spectroscopic Characterization of Rich Premixed Flames Across the Soot Formation Threshold. Combustion Science and Technology 1994;101:311–25. https://doi.org/10.1080/00102209408951879.

[29] D'Anna A, Commodo M, Sirignano M, Minutolo P, Pagliara R. Particle formation in opposed-flow diffusion flames of ethylene: An experimental and numerical study. Proceedings of the Combustion Institute 2009;32 I:793–801. https://doi.org/10.1016/j.proci.2008.06.200.

[30] Salamanca M, Sirignano M, D'Anna A. Particulate formation in premixed and counter-flow diffusion ethylene/ethanol flames. Energy and Fuels 2012;26:6144–52. https://doi.org/10.1021/ef301081q.

[31] Russo C, Apicella B, la Rocca A, Sirignano M. Fluorescent carbon dots synthesis in premixed flames: Influence of the equivalence ratio. Carbon N Y 2023;201:659–66. https://doi.org/10.1016/j.carbon.2022.09.061.

[32] Sirignano M, Russo C, Ciajolo A. One-step synthesis of carbon nanoparticles and yellow to blue fluorescent nanocarbons in flame reactors. Carbon N Y 2020;156:370–7. https://doi.org/10.1016/j.carbon.2019.09.068.

[33] Costa JCS, Taveira RJS, Lima CFRAC, Mendes A, Santos LMNBF. Optical band gaps of organic semiconductor materials. Opt Mater (Amst) 2016;58:51–60. https://doi.org/10.1016/j.optmat.2016.03.041.

[34] Bauer FJ, Braeuer PAB, Aßmann S, Thiele MA, Huber FJT, Will S. Characterisation of the transition type in optical band gap analysis of in-flame soot. Combust Flame 2022;243. https://doi.org/10.1016/j.combustflame.2022.111986.

[35] Minutolo P, Gambi G, D'alessio A. THE OPTICAL BAND GAP MODEL IN THE INTERPRETATION OF THE UV-VISIBLE ABSORPTION SPECTRA OF RICH PREMIXED FLAMES. Symposium (Internation) on Combustion 1996:951–7.

[36] De Falco G, Commodo M, Bonavolontà C, Pepe GP, Minutolo P, D'Anna A. Optical and electrical characterization of carbon nanoparticles produced in laminar premixed flames. Combust Flame 2014;161:3201–10. https://doi.org/10.1016/j.combustflame.2014.05.021.

[37] Migliorini F, Belmuso S, Dondè R, de Iuliis S, Altman I. To optical properties of carbon nanoparticles: A need in comprehending Urbach energy. Carbon Trends 2022;8. https://doi.org/10.1016/j.cartre.2022.100184.

[38] Commodo M, D'Anna A, De Falco G, Larciprete R, Minutolo P. Illuminating the earliest stages of the soot formation by photoemission and Raman spectroscopy. Combust Flame 2017;181:188–97. https://doi.org/10.1016/j.combustflame.2017.03.020.

[39] Russo C, Apicella B, Tregrossi A, Ciajolo A, Le KC, Török S, et al. Optical band gap analysis of soot and organic carbon in premixed ethylene flames: Comparison of in-situ and ex-situ absorption measurements. Carbon N Y 2020;158:89–96. https://doi.org/10.1016/j.carbon.2019.11.087.

[40] Feng XQ, Lu HX, Shi DN, Jia JM, Wang CS. Semiconductor-metal transition induced by combined electric field and external strain in bilayer phosphorene. Solid State Commun 2021;337. https://doi.org/10.1016/j.ssc.2021.114434.

[41] Chaves A, Azadani JG, Alsalman H, da Costa DR, Frisenda R, Chaves AJ, et al. Bandgap engineering of two-dimensional semiconductor materials. NPJ 2D Mater Appl 2020;4. https://doi.org/10.1038/s41699-020-00162-4.

[42] Sie EJ, McIver JW, Lee Y-H, Fu L, Kong J, Gedik N. Optical Stark effect in 2D semiconductors. Ultrafast Bandgap Photonics, vol. 9835, SPIE; 2016, p. 983518. https://doi.org/10.1117/12.2223462.

[43] D'Alessio A, Barone AC, Cau R, D'Anna A, Minutolo P. Surface deposition and coagulation efficiency of combustion generated nanoparticles in the size range from 1 to 10 nm. Proceedings of the Combustion Institute, vol. 30, Elsevier Ltd; 2005, p. 2595–603. https://doi.org/10.1016/j.proci.2004.08.267.

[44] D'Anna A, Ciajolo A, Alfè M, Apicella B, Tregrossi A. Effect of fuel/air ratio and aromaticity on the molecular weight distribution of soot in premixed n-heptane flames. Proceedings of the Combustion Institute 2009;32 I:803–10. https://doi.org/10.1016/j.proci.2008.06.198.

[45] Xie P, Yuan W, Liu X, Peng Y, Yin Y, Li Y, et al. Advanced carbon nanomaterials for state-of-the-art flexible supercapacitors. Energy Storage Mater 2021;36:56–76. https://doi.org/10.1016/j.ensm.2020.12.011.

[46] Liu Y, Song C, Lv G, Fan C, Zhang X, Qiao Y. Relationships between the electrical properties and nanostructure of soot particles in a laminar inverse diffusion flame.

Proceedings of the Combustion Institute 2019;37:1185–92. https://doi.org/10.1016/j.proci.2018.06.090.

[47] Kumar R, Joanni E, Singh RK, Singh DP, Moshkalev SA. Recent advances in the synthesis and modification of carbon-based 2D materials for application in energy conversion and storage. Prog Energy Combust Sci 2018;67:115–57. https://doi.org/10.1016/j.pecs.2018.03.001.

[48] Mulay MR, Chauhan A, Patel S, Balakrishnan V, Halder A, Vaish R. Candle soot: Journey from a pollutant to a functional material. Carbon N Y 2019;144:684–712. https://doi.org/10.1016/j.carbon.2018.12.083.

[49] Yang C, Li Z, Huang Y, Wang K, Long Y, Guo Z, et al. Continuous Roll-to-Roll Production of Carbon Nanoparticles from Candle Soot. Nano Lett 2021;21:3198–204. https://doi.org/10.1021/acs.nanolett.1c00452.

[50] Khalakhan I, Fiala R, Lavková J, Kúš P, Ostroverkh A, Václavů M, et al. Candle Soot as Efficient Support for Proton Exchange Membrane Fuel Cell Catalyst. Fuel Cells 2016;16:652–5. https://doi.org/10.1002/fuce.201600016.

[51] Zhang Z, Hao J, Yang W, Lu B, Tang J. Modifying candle soot with FeP nanoparticles into high-performance and cost-effective catalysts for the electrocatalytic hydrogen evolution reaction. Nanoscale 2015;7:4400–5. https://doi.org/10.1039/c4nr07436j.

[52] Kakunuri M, Sharma CS. Candle Soot derived Fractal-like Carbon Nanoparticles Network as High-Rate Lithium Ion Battery Anode Material. Electrochim Acta 2015;180:353–9. https://doi.org/10.1016/j.electacta.2015.08.124.

[53] Zhang B, Wang D, Yu B, Zhou F, Liu W. Candle soot as a supercapacitor electrode material. RSC Adv 2014;4:2586–9. https://doi.org/10.1039/c3ra42507j.

[54] Baldelli A, Esmeryan KD, Popovicheva O. Turning a negative into a positive: Trends, guidelines and challenges of developing multifunctional non-wettable coatings based on industrial soot wastes. Fuel 2021;301. https://doi.org/10.1016/j.fuel.2021.121068.

[55] Ahmad D, van den Boogaert I, Miller J, Presswell R, Jouhara H. Hydrophilic and hydrophobic materials and their applications. Energy Sources, Part A: Recovery, Utilization and Environmental Effects 2018;40:2686–725. https://doi.org/10.1080/15567036.2018.1511642.

[56] De Falco G, Carbone F, Commodo M, Minutolo P, D’Anna A. Exploring nanomechanical properties of soot particle layers by atomic force microscopy nanoindentation. Applied Sciences (Switzerland) 2021;11. https://doi.org/10.3390/app11188448.

[57] Caglar M, Caglar Y, Aksoy S, Ilican S. Temperature dependence of the optical band gap and electrical conductivity of sol-gel derived undoped and Li-doped ZnO films. Appl Surf Sci 2010;256:4966–71. https://doi.org/10.1016/j.apsusc.2010.03.010.

[58] Fan HY. Temperature Dependence of the Energy Gap in Semiconductors. Phyisical Review 1951;82.

[59] Palasantzas G, Barnas J. Surface-roughness fractality effects in electrical conductivity of single metallic and semiconducting films. Phys Rev B 1997;56.

[60] Commodo M, De Falco G, Larciprete R, D'Anna A, Minutolo P. On the hydrophilic/hydrophobic character of carbonaceous nanoparticles formed in laminar premixed flames. Exp Therm Fluid Sci 2016;73:56–63. https://doi.org/10.1016/j.expthermflusci.2015.09.005.

[61] Can EM, Mufundirwa A, Wang P, Iwasaki S, Kitahara T, Nakajima H, et al. Superhydrophobic fluorinated carbon powders for improved water management in hydrogen fuel cells. J Power Sources 2022;548. https://doi.org/10.1016/j.jpowsour.2022.232098.

[62] Lee HY, Park YH, Ko KH. Correlation between surface morphology and hydrophilic/hydrophobic conversion of MOCVD-TiO2 films. Langmuir 2000;16:7289–93. https://doi.org/10.1021/la9915567.

[63] Tokudome Y, Nakane K, Takahashi M. Mesostructured carbon film with morphology-induced hydrophilic surface through a dewetting-free coating process. Carbon N Y 2014;77:1104–10. https://doi.org/10.1016/j.carbon.2014.06.028.

Chapter 5

Conclusions

This chapter resumes the final remarks, the outcomes and the future perspective for this PhD Thesis work.

Contents

5.1 Final remarks

The industrial application of carbon particles, either in the form of dispersed elements, fibers, or films dates back to the 1900s. Carbon black is the major source of particles and consists of mature soot in the form of primary particles, with sizes from 10 to 40 nm, and stable aggregates that can be larger than 500 nm.

Carbon black is superhydrophobic, has a large surface area, good conductivity, and capacity to absorb ultraviolet light and for these properties, it is largely used as an additive for the production of pigments, pneumatics, UV-resistant plastics, rubbers, inks, electrodes and many others.

Among the most finely divided materials known, carbon blacks vary widely in particle size depending on the process by which they are made. There are several types of carbon blacks, distinguished in terms of the production processes. Among them, the most common are channel or impingement black, furnace black, thermal black, Lampback, and acetylene black. Despite their differences, the essence of the production process is the exposure of a surface to a rich, smoky flame. Several fuels, mostly liquid and solids, but also gaseous ones, are used in this scope.

In the last years, the scientific discovery of the many special features of nanoparticles has driven the research toward the production of carbon nanoparticles, CNPs.

Carbon nanoparticles can be produced with a number of treatments of the carbon black particle, following a top-bottom approach. However, combustion science and technology provide sufficient know-how and facilities to produce CNPs with virtually tunable size and properties, under a more efficient and green bottom-up approach: using a gas fuel with low molecular weight to sustain a highly controlled flame condition, and with an accurate positioning and geometry of the CNP collector inside the flame, it is possible to drive the chemical processes that regulate the formation of aromatic structures, the nucleation of nascent organic carbon particles and the formation of primary particles until the formation of CNPs of desired size range and, virtually, surface C/O/H ratio can be achieved. On top of that, the process involves a highly efficient combustion process, with very low production of polluting by-products and the production of energy.

A similar bottom-up approach, which goes under the name of flame synthesis, has been largely used to produce metal or inorganic nanoparticles but its application to the production of CNPs has been the subject of a few studies.

The physics underpinning the typical production process involves the use of thermophoretic forces to deposit CNPs on cold support immersed in the flame. This can either be a flame stabilization plate or a small external substrate immersed in the core of the flame at a given height above the burner to harvest particles of a desired size range.

The thermophoretic deposition is easy and tunable and gives rise to high porosity, low-density deposits of agglomerates composed of the pristine CNPs found in the flame at the harvesting position of the substrate. This process is very effective if a tiny amount of CNPs must be evenly dispersed on the collector and, besides, the CNPs can be easily detached from the collector and suspended in liquids or other means, since they are deposited in the form of unstable agglomerates. On the other hand, the deposits are characterized by low mechanical resistance and low conductivity (highly dependent on the temperature) which limit their direct application as coating films.

Regardless of the specific applications, one of the main limits of the thermophoretic deposition process is the low harvesting rate, which may be a benefit for the control of film size but is a relevant limit for the overall process productivity. This limit becomes unsustainable when early-formed CNPs are desired. Indeed, particles finer than 5 nm are characterized by several peculiar properties, which make them similar to quantum dots. The CNPs produced by bottom-up thermophoretic methods, having size closer to 10-20 nm have the characteristics of being structurally similar to the primary particles that can be produced from carbon black but have a higher oxygen content that makes them more hydrophilic, a unique property that can be used for specific surface coatings for heat exchangers, antifouling surfaces and specific water sensors.

These can be formed by working at C/O flames slightly higher than the stoichiometric one (C/O >0.33) or placing the collector at a very low distance above the burner and the low particle concentration makes the thermophoretic deposition rate extremely low.

The longstanding experience in the field of particle filtration by electrostatic forces suggested that the superimposition of an electric field to the flame can fasten the deposition rate of CNPs overcoming the rate limitations of conventional thermophoretic-driven flame synthesis. The new process is named Electric field-assisted flame synthesis.

The pertinent literature indicates very few examples of a similar process, with a couple of papers related to the production of metal and inorganic nanoparticles and only one specifically referring to the production of CNPs. These pieces of evidence indicate that an electric field increases the deposition rate, but an alteration of the flame characteristics also takes place.

This work is part of a larger research activity, the PRIN 2017 MAGIC DUST project, which is devoted to the production of new CNPs with improved technological properties and a better understanding of the physical and chemical mechanisms underpinning this process. The PhD project has been carried out in cooperation with the Clean Combustion Research Lab of Naples (CNR STEMS and University Federico II laboratories) and with the Rheology Lab of the Department of Engineering of the University of Campania L. Vanvitelli. This work aims to improve the state of the art concerning the electric field-assisted flame synthesis applied to the production of CNPs in a low C/O ethylene air flame and to characterize the properties of the CNP films produced with this new methodology.

To this end, this PhD thesis includes a dedicated analysis of the state of the art on the deposition of CNPs in flame synthesis and the effect of electric field on the characteristics of the flame and the deposition process.

The pertinent literature indicates that the application of an external electric field to the flame gives rise to an alteration of flame morphology, which also includes macroscopic phenomena such as flame flickering and flame extinction, and an alteration of CNPs size distribution as a function of the height above the burner. The external electric field superimposes to the natural electric field existing in a flame: in the case of an electric field with a negative polarity imposed on a surface placed above the burner (*i.e.* with the burner acting as the anode), the flame speed is slightly accelerated due to the ionic wind effects, which involves the cations in the flame tip, and the particle residence time decreases, thus reducing the CNP size at a given height above the burner; in case of an electric field with positive polarity imposed on a surface placed above the burner, which acts as a cathode, the ionic wind flow in a direction opposite to the flame front, flickering and extinction may take place, but CNP residence times increase and larger particles are observed at a given height above the burner. Besides, the pertinent literature indicated an alteration of flame chemistry related to the effects of the electric field on the spatial distribution of ions and electrons.

The research work has been developed considering a specific model condition: the production of CNPs by repeated insertions of a cold substrate kept at a desired electric potential, from 0 to -3 kV, and placed 15 mm above the mouth of a McKenna burner feed with a laminar, premixed ethylene air flame. This reference condition has been chosen both because of its technological relevance and for the extensive amount of data regarding the characteristics of this flame, and the produced particles, available within the research groups involved in this project.

To investigate the dynamics of particle deposition under the effect of the electric field, a mathematical model has been developed on the bases of the Langevin equation for momentum balance over a single particle and extensive knowledge of the flame properties in the investigated conditions. The application of the electric field ignites the onset of two additional forces with respect to the hydrodynamic and thermal Brownian motion which characterize the conventional thermophoretic deposition: Coulomb, electrophoretic forces, acting on charged particles, and image, dielectrophoretic, forces acting on uncharged particles. Indeed, electrophoretic forces also act between charged particles and grounded collectors in the conventional deposition process, but they are less relevant than the dominating thermophoretic forces.

The model reveals that the Coulomb electrophoretic force dwarfs the thermophoretic forces and gives rise to faster and more perpendicular impacts of the charged particles with the collector. The dielectrophoretic force is relevant only for particles larger than 20 nm, but they are a negligible fraction of the total CNPs found in the flame under the experimental conditions, so they become irrelevant in the investigated conditions. Since the fraction of charged particles becomes appreciable only above 5 nm, the electric field-assisted flame synthesis is more effective for these kinds of particles than for the finer ones.

In summary, compared with the conventional thermophoretic deposition, the model predictions indicate that the electric field-assisted flame synthesis has a faster deposition rate, preferentially captures particles larger than 5 nm, and produces more compact films.

The experimental results provide an extensive and brand-new set of data on the characteristics of aged CNP films and agglomerates that can be formed with the electric field-assisted flame synthesis: Optical band gaps, Raman spectra, fluorescence, the morphology of the agglomerates, surface texture, wettability and conductivity are reported for pure thermophoretic and electric field-assisted films, highlighting the similitudes and the differences of the produced films and the CNPs agglomerates.

The experimental data confirm the model predictions and shed new light on the process development. The Raman spectra indicate that the crystallite size of the CNPs is unaffected by the presence of the electric field, confirming that the chemistry of CNP formation is not modified by the electric field. The AFM and the surface texture analysis indicate that the morphology is more irregular than that observed for pure thermophoretic deposition, with the formation of large mesoscopic structures of micrometric or submicrometric sizes. While under thermophoretic flame synthesis, the film grows following the Volmer-Weber model, the electric field-assisted flame synthesis produces films which grow following the Stranski-Krastanov model. This result is probably related to the onset of polarization effects in the agglomeration phenomena that gives rise to a preferential orientation of particles in the direction of the electric field, which is often observed for the deposition of charged particles in electrets. The AFM and the UV-Vis spectra indicate faster deposition rates, which are consistent with the model predictions. The conductivity and the optical band gap data prove the higher compactness of the deposits formed by electric field-assisted flame synthesis as predicted from the CNPs deposition model: the analysis of agglomerates UV-Vis spectra indicates that the agglomerates are on average much larger and stable for the electric field -assisted flame synthesis and their optical band gap is lower than that of pure thermophoretic flame synthesis. However, the optical band gap for the film indicates that its compactness greatly contributes to the conductivity of the deposits. Another indirect proof of the higher compactness of the electric field-assisted flame synthesis deposits comes from the wettability tests, where the presence of large and stable agglomerates moving on the free surface of the droplets is observed.

The experiments also indicate that the hydrophilic character of the thermophoretic deposits is preserved in the electric field-assisted flame synthesis deposits, despite their larger roughness. This suggests that surface roughness is represented by morphology which agrees with a Wenzel wettability model rather than a Cassie

Baxter one. On the other hand, this roughness is also representative of a higher surface area of the deposits that are beneficial for superficial processes.

Besides, the higher stability of the agglomerates (which are a consequence of the onset of electric interactions between the primary particles and polarization effects that are much stronger than the conventional Van der Waals forces acting on thermophoretic deposited particles) indicate that the electric field-assisted flame synthesis is probably less useful for the production of CNPs suspension compared with the conventional thermophoretic flame synthesis.

The model and experimental results suggest the possible application of the electric field-assisted flame synthesis deposits to the production of smart surfaces with enhanced wettability and higher conductivity, stably preserved at temperatures up to 90°C. The films can be proficiently used to produce electrodes for fuel cells and hydrolyze, as heat exchange surfaces for reboilers, as scaffolds for active phases, and as noble metal catalysts.

In conclusion, electric field-assisted flame synthesis emerges as a technology able to overcome the limits of conventional flame synthesis methods and to add new degrees of freedom in the synthesis of nanoparticles and thin films with new and tunable properties. Despite the overall success of the work carried out so far, several efforts are still needed to acquire a comprehensive knowledge of the electric field-assisted flame synthesis: in particular, new models are necessary to explain the electrical properties of the thin films and it is crucial to develop new models to describe the restructuring of the CNPs deposits over time.

For its advantages in terms of enhanced productivity and the possibility to exploit new features compared with conventional carbon black particles, electric field-assisted flame synthesis is worth future investigation and further technological development.

Table 5.1 summarizes the similarities and differences between CNP films and their constituent agglomerates produced by conventional thermophoretic and electric field-assisted flame synthesis.

Table 5.1. Overview of the CNP films and agglomerates properties, when manufactured by conventional thermophoretic or electric field-assisted flame synthesis.

	Thermophoretic flame synthesis	**Electric field-assisted flame synthesis**
Length of aromatic islands	1.36 nm	1.36 nm
Harvesting rate	Very low for C/O=0.67	Six-times higher
Selective harvesting?	NO	YES, CNPs larger than 5 nm
Surface texture/Roughness	Low both on nano and mesoscale, with uniform peaks and valleys. Volmer-Weber growth mode	Very high, with irregularities both on nano and mesoscale (flat valleys and many high spiked peaks). Stranski-Krastanov growth mode
Fluorescence	Higher	Lower
CNP agglomerates	Small and unstable Van der Waals's cohesive forces	Larger, stable with higher compactness Electrostatic forces and polarization effects
Optical band gap	0.5 eV	Thickness-dependent, from 0.5 eV to 0 eV
Electrical conductivity	Low and temperature-dependent 10^{-3} S/cm at 25°C	Higher and temperature-independent 10^{-1} S/cm
Wettability/ Contact Angle	Hydrophilic CA=13°	Transition, Hydrophilic even if graphitic CA<40°

5.2 Acknowledgements

This work was financially supported by the PRIN project 2017PJ5XXX: “MAGIC DUST”.

I would like to acknowledge the researchers of the CNR-STEMS and the Clean Combustion Research Group at the University of Federico II in Naples, and the Rheology Lab of the Department of Engineering of the University of Campania L.Vanvitelli, for their fundamental contribution to the experimental campaign included in this PhD thesis.